4D-Nanoparticle Tracking Combined with Real-Time Fluorescence Lifetime Imaging

Thomas Kellerer

München 2024

4D-Nanoparticle Tracking Combined with Real-Time Fluorescence Lifetime Imaging

Thomas Kellerer

Dissertation
an der Fakultät für Physik
der Ludwig–Maximilians–Universität
München

vorgelegt von
Thomas Kellerer
aus München

München, den 17.12.2024

Erstgutachter: Prof. Dr. Joachim O. Rädler
Zweitgutachter: Prof. Dr. Thomas Hellerer
Tag der mündlichen Prüfung: 11.02.2025

Abstract

Fluorescence lifetime imaging microscopy (FLIM) allows imaging of living cells while providing functional insights into local microenvironments, making it invaluable for studying structure-function relationships in biology. Lipid nanoparticle (LNP)-based nucleic acid delivery systems show great potential for curing genetic diseases and cancer. However, mechanisms of LNP uptake, transport, and cargo delivery remain poorly understood. Endosomal escape, closely linked to pH changes, is particularly elusive, as imaging fusion events at subcellular levels with high temporal resolution has yet to be achieved. Combining single-particle tracking (SPT) with environmental sensing, such as intracellular pH measurements, is crucial to gaining deeper insights. This thesis advances FLIM and SPT to address the needs of LNP studies in live-cell imaging, where current methods are mostly 2D and fail to integrate microenvironmental data.

Two novel microscopy methods are introduced to overcome these limitations. The first enables particle tracking by modifying the point spread function of two-photon excited fluorescence microscopy (TPEFM). By introducing a spatial shift between two focal volumes of different wavelengths along the optical axis, it generates a spectral-signed error signal for centering the Z-position while tracking motion in the XY-plane. Using laser scanning, this approach provides real-time 2D diffraction-limited imaging with the particle always in the field of view. It also retains key TPEFM advantages, such as deep tissue penetration and reduced photobleaching.

The second method accelerates FLIM with a digital lock-in amplifier, enabling real-time streaming of intensity-, lifetime-, and phasor data. This improves detection speed by a factor of 30 over state-of-the-art methods while preserving diffraction-limited resolution. It integrates seamlessly into laser-scanning microscopy systems and combines with other fluorescence methods, such as fluorescence correlation spectroscopy or the new tracking method. This combination allows for simultaneous tracking of a particle and its environment's lifetime, previously unachievable with traditional single-particle tracking.

These advancements allowed LNP pathways to be tracked in live-cell experiments at 7.6 fps with 1024x1024 pixel resolution, revealing distinct diffusion properties in the extracellular space, cell interior, and membrane. Static imaging over an hour showed mRNA-loaded LNP acidification, indicating transitions from early to late endosomes and degradation via lysosomes. These techniques highlight the potential of integrating fast fluorescence lifetime extraction with real-time particle tracking to advance LNP research.

Zusammenfassung

Die Fluoreszenzlebensdauer-Mikroskopie (FLIM) ermöglicht die bildgebende Darstellung lebender Zellen und liefert detaillierte Informationen über deren Mikroumgebung, was sie zu einem unverzichtbaren Werkzeug für die Untersuchung von topografischer Struktur und funktionaler Beziehungen in der Biologie macht. Nukleinsäure-Transportsysteme, die auf Lipid-Nanopartikel (LNP) basieren, besitzen großes Potenzial zur Behandlung genetischer Erkrankungen sowie Krebs. Die Mechanismen der LNP-Aufnahme, des Transports und der Freisetzung sind jedoch bisher kaum verstanden. Besonders die endosomale Freisetzung der Wirkstoffe, die eng mit Änderung des pH-Werts verbunden ist, bleibt auf subzellulärer Ebene mit der erforderlich hohen Detailtiefe in ihrem zeitlichen Ablauf unerforscht. Zur Klärung solcher Prozesse ist die Fähigkeit der Einzelpartikelverfolgung unter gleichzeitigen Messungen intrazellulärer Parameter wie dem pH-Wert entscheidend. Die vorliegende Arbeit zielt darauf ab, eine entsprechende Methodik weiterzuentwickeln, welche einzelne Partikel verfolgen und zusätzlich durch die Ermittlung der Fluoreszenz-Lebensdauer Informationen über deren Mikroumgebung ermitteln kann, um die Anforderungen der LNP-Forschung in der Lebendzell-Bildgebung zu unterstützen.

Dabei werden zwei neuartige Mikroskopie-Methoden vorgestellt, welche bisher bestehende Einschränkungen überwinden. Die erste Methode modifiziert die Punktspreizung eines Zwei-Photonenmikroskops, indem sie eine räumliche Verschiebung zwischen Fokalvolumen unterschiedlicher Wellenlängen entlang der optischen Achse einführt. Dadurch entstehen drei Anregungsregionen, die somit ein Fehlersignal zur präzisen Verfolgung der Z-Position generieren. Dies ermöglicht die Echtzeit-Bildgebung mit hoher Auflösung.

Die zweite Methode beschleunigt die Lebensdauermessung durch den Einsatz eines digitalen Lock-in-Verstärkers, der Echtzeitübertragungen von Intensitäts-, Lebenszeit- und Phasordaten ermöglicht. Dies steigert die Detektionsrate um den Faktor 30 gegenüber etablierten Methoden bei gleichzeitiger Aufrechterhaltung der optischen Auflösung. Diese Methode lässt sich nahtlos in Laserscanning-Mikroskope integrieren und mit anderen Techniken wie der Fluoreszenzkorrelationsspektroskopie kombinieren. Die Integration dieser Technik in den Tracking-Ansatz erlaubte die gleichzeitige Verfolgung eines Partikels sowie die Messung seiner Lebensdauer und seiner Umgebung, was bis dato ein Novum darstellt.

Mit diesen Fortschritten konnten die Wege von einzelnen LNP-Partikeln in Lebendzell-Experimenten mit einer Geschwindigkeit von 7,6 Bildern pro Sekunde und einer Auflösung von 1024x1024 Pixeln verfolgt werden. Es wurden damit unterschiedliche Diffusionseigenschaften im extrazellulären Raum, Zellinneren und auf der Membran sichtbar gemacht. Das Ansäuern von mRNA-beladenen LNP zeigte Übergänge von frühen zu späten Endosomen und deren Abbau durch Lysosomen. Diese Ergebnisse zeigen eindrucksvoll das Potenzial der Integration von Fluoreszenzlebensdauermessungen und Echtzeit-Einzelpartikelverfolgung in der LNP-Forschung.

Contents

Publications

Peer Review Articles

Previous Publications

1. Polzer, C., Ness, S., Mohseni, M., **Kellerer, T.**, Hilleringmann, M., Rädler, J., and Hellerer, T. (2019): "Correlative Two-Color Two-Photon (2C2P) Excitation STED Microscopy,"Biomed. Opt. Express 10, 4516-4530.

2. Ness, S., Polzer, C., **Kellerer, T.**, Hellerer, T., and Hilleringmann, M. (2019): "Catcher-tag modified pneumococcal pilus subunits as novel strategy for optimized analysis of pilus cell surface biology"(in preparation).

3. Sroka, R., Dominik, N., Eisel, M., Esipova, A., Freymüller, C., Heckl, C., Hennig, G., Homann, C., Hoehne, N., Kammerer, R., **Kellerer, T.**, et al. (2017): "Research and Developments of Laser Assisted Methods for Translation into Clinical Application,"Front. Optoelectron. 10, 239–254. https://doi.org/10.1007/s12200-017-0724-6.

Publications as PhD

1. **Kellerer, T.**, Grawert, T., Schorre, F., Müller, J.A., Rädler, J.O., and Hellerer, T. (2024): Spectrally Encoded Multiphoton Particle Tracking (SEMPA-Track): A Real-Time 4D-Single Particle Tracking Fluorescence Lifetime Imaging Microscope. (Submitted to Nature Communication)

2. **Kellerer, T.**, Moser, L., Müller, J.A., Rädler, J.O., and Hellerer, T. (2024): Speed-Up Phase-Resolved Fluorescence Lifetime Imaging (SUPER-FLIM). (Submitted to Nature Light: Science and Applications)

3. Byers, P., **Kellerer, T.**, Li, M., Chen, Z., Huser, T., and Hellerer, T. (2024): Super-Resolution Upgrade for Deep Tissue Imaging Featuring Easy Implementation. (Submitted to Nature Communication)

4. **Kellerer, T.**, Sailer, B., Byers, P., Barnkob, R., Hayden, O., and Hellerer, T. (2024): Two-Photon Microscopy of Acoustofluidic Trapping for Highly Sensitive Cell Analysis. Lab on a Chip.

5. Müller, J.A., Schäffler, N., **Kellerer, T.**, Schwake, G., Ligon, T.S., and Rädler, J.O. (2024): Kinetics of RNA-LNP Delivery and Protein Expression. European Journal of Pharmaceutics and Biopharmaceutics, 114222.

6. Stöberl, S., Balles, M., **Kellerer, T.**, and Rädler, J.O. (2023): Photolithographic Microfabrication of Hydrogel Clefts for Cell Invasion Studies.

7. **Kellerer, T.**, Janusch, J., Freymüller, C., Rühm, A., Sroka, R., and Hellerer, T. (2022): Comprehensive Investigation of Parameters Influencing Fluorescence Lifetime Imaging Microscopy in Frequency- and Time-Domain Illustrated by Phasor Plot Analysis. Int. J. Mol. Sci. 23, 15885. https://doi.org/10.3390/ijms232415885

8. Erben, A., **Kellerer, T.**, Lissner, J., Eulenkamp, C., Hellerer, T., Sudhop, S., and Heymann, M. (2022): Engineering Principles and Algorithmic Design Synthesis for Ultracompact Bio-Hybrid Perfusion Chip. bioRxiv, 2022-03. (Preprint).

Conference Papers

1. Byers, P., **Kellerer, T.**, Huser, T., and Hellerer, T. (2024): Two-Photon Line-Scanning Structured Illumination Microscopy (LIL-SIM) for Super-Resolution Imaging in Deep Tissue. In BIO Web of Conferences (Vol. 129, p. 15002). EDP Sciences.

2. **Kellerer, T.**, Grawert, T., Schorre, F., Moser, L., Byers, P., Rädler, J., and Hellerer, T. (2024): An Image-Based Real-Time 3D Particle Tracking Fluorescence Lifetime Imaging Microscope to Follow Lipid Nanoparticles. In Microscopy Histopathology and Analytics (pp. MM5A-6). Optica Publishing Group.

3. **Kellerer, T.**, Janusch, J., Moser, L., Grawert, T., Byers, P., Spellauge, T., Rädler, J., and Hellerer, T. (2024): Rigorous Investigation and Comparison of Different Fluorescence Lifetime Imaging Microscopy (FLIM) Techniques Analyzed Using the Phasor Plot. Proc. SPIE 12847, Multiphoton Microscopy in the Biomedical Sciences XXIV, 128470O. https://doi.org/10.1117/12.3002648.

Books & Bookchapters

1. **Kellerer, T.**, Janusch, J., Freymüller, C., Rühm, A., Sroka, R., and Hellerer, T. (2024): Comprehensive Investigation of Parameters Influencing Fluorescence Lifetime Imaging Microscopy in Frequency- and Time-Domain Illustrated by Phasor Plot Analysis. In: Sławomir Lach, editor. Prime Archives in Molecular Sciences: 5th Edition. Hyderabad, India: Vide Leaf.

2. **Kellerer, T.**, Kiderlen, S., Mikhaylov, V., and Krainer, L. (2023): FXS-Dual - Ultrafast Femtosecond Laser for CARS Microscopy - Whitepaper.

3. Kellerer, A., Schulz, T., and **Kellerer, T.** (2016): Die Allmacht digitaler Ablenkung? - Ein Konzentrationstraining für MINT Fächer. (Books on Demand, ISBN-10: 3739243538).

Posters

1. **Kellerer, T.**, and Hellerer, T. (2024): SEMPA-Track: Spectrally Encoded Multiphoton Particle Tracking, BMBF.

2. **Kellerer, T.**, Moser, L., Janusch, J., Byers, P., Rädler, J., and Hellerer, T. (2024): Advancements in FLIM: Comparative Analysis and New Methods for High-Resolution, Rapid Microenvironmental Imaging, ICOB 2024.

3. **Kellerer, T.**, Janusch, J., Moser, L., Byers, P., Spellauge, T., Rädler, J., and Hellerer, T. (2024): Rigorous Investigation of Influences on Fluorescence Lifetime Measured with Three Different FLIM Techniques and Analyzed Using the Phasor Plot, SPIE.

4. Lehertshuber, C.A., Jia, S., Rudolph, M., Lorentschk, M., Li, S., **Kellerer, T.**, et al. (2023): Tissue Engineering of a Three-Layered Artery.

5. Kirchmaier, B., Müller, J., **Kellerer, T.**, and Rädler, J. (2023): Quantification of mRNA and siRNA Content of Lipid Nanoparticles Using Fluorescence Correlation Spectroscopy.

6. **Kellerer, T.**, Schorre, F., Rädler, J., and Hellerer, T. (2022): Development of a Novel Time-Resolved Tracking Microscopy to Track Intracellular Release of Nucleic Acid by Lipid Nanoparticles, BayWISS Verbandtreff, München.

7. Sailer, B., **Kellerer, T.**, Barnkob, R., Hellerer, T., and Hayden, O. (2021): Micro-TAS, Hybrid, Poster Presentation No. W4B-510.c.

Oral Presentation

1. 'SEMPA-Track: Spectrally Encoded Multiphoton Particle Tracking Microscopy' Focus On Microscopy, 2024, Genua, Italy

2. 'An Image Based Real-Time 3D Particle Tracking Fluorescence Lifetime Imaging Microscope to Follow Lipid Nanoparticles' Optica Biophotonics Congress: Biomedical Optics 2024, Fort Lauderdale, USA

Conferences

1. Focus on Microsocopy (FOM) 2024, Genua, Italy

2. 7th International Congress on Biophotonics (ICOB) 2024, Jena, Germany
3. SPIE 2024, San Francisco, USA
4. Optica Biophotonics Congress: Biomedical Optics 2024, Fort Lauderdale, USA

Awards

1. BayWISS-Preis für eine herausragende oder zukunftsweisende Forschungsleistung im jeweiligen Wissenschaftsbereich 2024

Supervised Projects

1. 1x Research Project
2. 4x Project Study
3. 6x Bachelor Thesis
4. 4x Master Thesis

Abbreviations

1P	**S**ingle-**P**hoton
2P	**T**wo-**P**hoton
3D-SMART	**3D S**ingle-**M**olecule **A**ctive **R**eal-time **T**racking
A549	Adenocarcinomic human alveolar basal epithelial cells
AI	**A**rtificial **I**ntelligence
APD	**A**valanche **P**hoto**d**iode
AUX	**Aux**iliary
BNC	**B**ayonet **N**eill **C**oncelman
CARS	**C**oherent **A**nti-Stokes **R**aman **S**cattering
CLSM	**C**onfocal **L**aser-**S**canning **M**icorsocpy
Cy3	**Cy**anine**3**
cw	**c**ontinuous **w**ave
DAQ	**D**ata **Aq**uisition
DC	**D**irect **C**urrent
DNA	**D**eoxyribo**N**ucleic **A**cid
DSPC	1,2-**D**istearoyl-**s**n-glycero(3)**p**hospho**c**holin
DSPE	1,2-**D**istearoyl-**s**n-glycero-3-**P**hospho**e**thanolamine
ECU	**E**lectronic **C**ontrol **U**nit
EOL	**E**lectro **O**ptical **L**ens
FCS	**F**luorescence **C**orrelation **S**pectroscopy

FD-FLIM	**F**requency **D**omain **FLIM**
FOV	**F**ield **o**f **V**iew
FLCS	**F**luorescence **L**ifetime **C**orrelation **S**pectroscopy
FLIM	**F**luorescence **L**ifetime **I**maging **M**icroscopy
FRET	**F**örster **R**esonance **E**nergy **T**ransfer
HOMO	**H**ighest **O**ccupied **M**olecular **O**rbital
IC	**I**nternal **C**onversion
ISC	**I**nter**s**ytem **C**rossing
LISCA	**L**ive-Cell **I**maging on **S**ingle **C**ell **A**rrays
LNP	**L**ipid **N**ano**p**article
LSM	**L**aser-**S**canning **M**icorsocpy
LUMO	**L**owest **U**noccupied **M**olecular **O**rbital
MINFLUX	**Min**imal photon **flux**es
ml-FCS	**m**ulti-**l**ifetime-**FCS**
mRNA	**m**essenger **R**ibo**N**ucleic **A**cid
MSD	**M**ean **S**quared **D**isplacement
NIR	**N**ear-**I**nfrared **R**ange
PALM	**P**hoto**a**ctivated **l**ocalization **M**icroscopy
PEG	**P**oly**e**thylen**g**lykol
PMT	**P**hoto**m**ultiplier **T**ube
PSF	**P**oint **S**pread **F**unction
Rab	**Ra**s-related in **b**rain
RBC	**R**ed **B**lood **C**ells
RESOLFT	**RE**versible **S**aturable **O**ptica**L** **F**luorescence **T**ransitions
RNA	**R**ibo**N**ucleic **A**cid
SEMPA-Track	**S**pectrally **E**ncoded **M**ultiphoton **PA**rticle-**Track**ing

SFG	**S**um-**F**requency **G**eneration
SHG	**S**econd **H**armonic **G**eneration
SIM	**S**tructured **I**llumination **M**icroscopy
siRNA	**s**mall **i**nterfering **R**ibo**N**ucleic **A**cid
SLM	**S**patial **L**ight **M**odulator
SMC	**S**pherical **M**icro**c**hamber
SNR	**S**ignal to **N**oise **R**atio
SPT	**S**ingle **P**article **T**racking
SSM	**S**ample-**S**canning **M**icorsocpy
STED	**S**timulated **E**mission **D**epletion
STORM	**S**tochastic **O**ptical **R**econstruction **M**icroscopy
SUPER-FLIM	**S**peed-**U**p **P**has**E** **R**esolved **F**luorescence **L**ifetime **I**maging **M**icroscopy
TCSPC	**T**ime **C**orrelated **S**ingle **P**hoton **C**ounting
TD-FLIM	**T**ime **D**omain **FLIM**
THG	**T**hird **H**armonic **G**eneration
TIA	**T**rans**i**mpedance **A**mplifier
TPEFM	**T**wo-**P**hoton **E**xcited **F**luorescence **M**icroscopy
TSUNAMI	**T**racking **S**ingle particles **U**sing **N**onlinear **A**nd **M**ultiplexed **I**llumination

Chapter 1

Introduction

Physics plays a fundamental role in advancing technology and understanding the complexities of our world. This is especially evident in interdisciplinary research, where physical principles drive transformative innovations in biology and medicine. Biophotonics exemplifies this synergy by combining the physics of light with the study of biological systems, enabling observations and analyses at unprecedented scales [1, 2]. At the heart of Biophotonics lies the microscope, which has evolved from early optical instruments consisting of single lenses to highly complex optical systems. However, microscopy faces persistent challenges, especially when studying dynamic nanoscale biological systems in three dimensions: tracking fast-moving particles, achieving precise 3D localization, and measuring subtle environmental changes, such as pH shifts are crucial for understanding cellular processes [3].

A compelling example illustrating these challenges is the study of **L**ipid **N**ano**p**article (LNP)-based drug delivery systems [4]. Prominent during the COVID-19 pandemic, LNPs are also being explored for cancer therapy and other applications [5, 6, 7, 8, 9]. Delivering **m**essenger **R**ibo**N**ucleic **A**cid (mRNA) into cells depends on intricate mechanisms, such as pH-mediated endosomal escape [10]. Existing techniques can independently analyze LNP pathways [11] and microenvironmental changes [12, 13]. However, they lack the spatial and temporal resolution needed to study these processes simultaneously and in detail. Thus, new tools are needed to track LNPs and quantify parameters like pH dynamics in real-time, highlighting a critical gap in current methodologies. This can be proven by the fact that although the three dimensional behavior of LNP is important only one publication showed 3D-trajectory's for mRNA-LNP [14]. This dissertation addresses these challenges by developing two innovative microscopy techniques: **S**pectrally **E**ncoded **M**ultiphoton **PA**rticle-**Track**ing (SEMPA-Track), a real-time image-based **S**ingle **P**article **T**racking (SPT) system, and **S**peed-**U**p **P**has**E** **R**esolved **F**luorescence **L**ifetime **I**maging **M**icroscopy (SUPER-FLIM), an advanced **F**luorescence **L**ifetime **I**maging **M**icroscopy (FLIM) system. These methods independently offer groundbreaking capabilities and can be combined to further enhance their utility.

Speed-**U**p **P**has**E** **R**esolved **F**luorescence **L**ifetime **I**maging **M**icroscopy redefines flu-

orescence lifetime measurement by enabling ultra-fast, real-time acquisition of intensity-, lifetime-, and phasor data. It achieves a 30-fold speed increase over conventional **T**ime **C**orrelated **S**ingle **P**hoton **C**ounting (TCSPC) techniques, reducing acquisition times to 100 ns, while maintaining high spatial resolution. This is achieved using digital lock-in detection [15] combined with laser scanning excitation, enabling 3D live-imaging of rapidly changing sample environments. By merging the advantages of **T**ime **D**omain **FLIM** (TD-FLIM) and **F**requency **D**omain **FLIM** (FD-FLIM), SUPER-FLIM provides unparalleled speed without sacrificing resolution, opening new paths for investigating dynamic biological processes.

Spectrally **E**ncoded **M**ultiphoton **PA**rticle-**Track**ing introduces a novel SPT approach that combines trajectory measurements with image acquisition. This hybrid strategy overcomes limitations of traditional feedback-loop-based SPT methods, which struggle with rapid particle behavior changes or boundary interactions [16, 17]. SEMPA-Track uses two axially shifted laser foci to create three excitation regions, allowing precise localization of a particle's 3D motion. This technique not only tracks particle trajectories but also provides contextual information about their surroundings. Its compatibility with two-photon excitation makes it an ideal partner for SUPER-FLIM, enabling simultaneous particle tracking and environmental sensing.
The integration of SEMPA-Track and SUPER-FLIM represents a major advancement, demonstrated through proof of principle experiments on LNP systems. These experiments reveal LNP intracellular dynamics and pH changes, underscoring the techniques' capabilities. While LNPs serve as an exemplary application, the focus of this dissertation is the development of these technologies, which are versatile and broadly applicable in biological and biomedical research [18]. For example, SUPER-FLIM has already shown potential in advanced **F**luorescence **C**orrelation **S**pectroscopy (FCS), generating lifetime-filtered autocorrelation functions for improved analysis.

This cumulative dissertation begins in **Chapter 2** with an introduction to LNP-based drug delivery systems, outlining the basic principles, unresolved questions, and current microscopic methods. This chapter establishes the biological context and motivation for the technological innovations developed here. While LNPs are a timely and relevant case study, the experimental measurements serve as proof of principle demonstrations rather than exhaustive biological investigations, emphasizing the techniques' broader applicability. In **Chapter 3**, the dissertation leads to the technological foundation, introducing two-photon excited fluorescence microscopy (**T**wo-**P**hoton **E**xcited **F**luorescence **M**icroscopy (TPEFM)) as the basis for the developed methods. Practical applications of TPEFM are demonstrated using an acoustofluidic trap to analyze particle movement in 3D and at video-rate [19]. **Chapter 4** details fluorescence lifetime concepts, including the physical and photophysical factors influencing lifetime measurements [20]. Two measurement approaches are compared, highlighting their respective advantages and limitations. These foundational insights sets the stage for the advanced methods developed later. In **Chapter 5**, the capabilities of SUPER-FLIM are presented, focusing on its application in

measuring the endosomal acidification of LNPs. This chapter also includes benchmark experiments and supporting materials, such as the mathematical framework and open-source software, provided in **Appendix A.1**. **Chapter 6** explores the development and application of SEMPA-Track, showcasing its utility in characterizing LNP dynamics in intra- and extracellular environments, as well as on membranes. Supplementary materials in **Appendix B.1** further demonstrate the method's robustness and potential. The results and broader implications of these advancements are discussed in **Chapter 7** and **8**, with additional technical details of the experimental setup provided in **Appendix C**.

Chapter 2

Lipid Nanoparticles

„I love nature because it never hides the truth.“

Nikolaus Lenau

This quote reflects humans' never-ending quest to make the obvious truths of nature comprehensible to their minds. In the realm of science, this principle resonates strongly, as advances in technology and methodology enable us to delve deeper into nature's complexities.

This pursuit of understanding finds inspiration in nature itself, where countless examples demonstrate the ability of organisms to adapt to, and overcome diseases or environmental challenges. By observing and studying these natural mechanisms, we have developed groundbreaking therapies that address human illnesses. For instance, modern pharmaceutical products derived from the venom of snakes and lizards have revolutionized treatments for diabetes, heart attacks, and high blood pressure by decoding their mechanisms of action for medical use [21, 22]. While such approaches often effectively address symptoms, they rarely tackle the underlying causes of disease. To achieve true cures, we must probe deeper into the origins of the most common diseases — many of which lie hidden within our genetic code [23].

Modern physics equips us with the tools to design experiments that unravel the fundamental structure of our genetic code. These advancements not only help us map its intricate architecture but also enable the detection of damage within it, providing a basis for classifying various diseases. A well-known example is cancer, often understood as the result of damaged sequences in **D**eoxyribo**N**ucleic **A**cid (DNA)—damage that can be triggered by factors such as radiation from excessive sun exposure [23, 24]. As a natural defense, cells attempt to repair themselves during division, a process that is usually successful. However, when these repairs fail, the repeated cycles of division can lead to the formation of a tumor [25].

While traditional therapies often focus on addressing symptoms or like the chemotherapy eradicating cancerous and healthy cells, they can cause significant collateral damage

to the body, requiring long recovery periods even when treatments succeed. Emerging approaches, such as personalized therapies, aim to address the root causes by targeting the damaged DNA itself [26]. Gene therapy [27] exemplifies this promise by delivering mRNA directly into cells [10]. Once inside, ribosomes read this mRNA, which carries instructions for repairing or countering the underlying problem (**Figure 2.1**). This technique is a cornerstone of modern medicine, offering hope for more effective treatments for conditions ranging from cancer [6, 7] to viral infections like SARS-CoV-2 [5].

However, this approach raises many questions: How can mRNA be efficiently targeted to specific cells? What mechanisms enable cells to recognize and process mRNA? What factors influence the speed and success of this process? Where do these techniques find their most impactful applications? And most critically, can these advances enhance the efficacy of therapies for diseases that remain among the most challenging to treat?

In this chapter, the biological background is outlined to provide the context and motivation for this dissertation. While lipid nanoparticles (LNPs) served as an inspiration due to their biological and therapeutic relevance, the measurements conducted in this work were performed on a proof of principle level. The focus lies on demonstrating the feasibility and potential of the two novel techniques developed here, rather than providing comprehensive biological insights into LNP behavior.

2.1 Lipid Nanoparticle Based Drug Delivery Systems

In 1958, Francis Crick introduced the central dogma of molecular biology, describing the unidirectional flow of genetic information: from DNA to **R**ibo**N**ucleic **A**cid (RNA) to proteins [28]. Mutations or damage to genes (DNA) can result in altered or dysfunctional proteins, often leading to disease [23]. Leveraging this dogma, modern science offers ways to intervene at different steps to address these genetic anomalies. For example, in the case of the coronavirus, an mRNA sequence can be designed to produce a protein that inhibits viral entry into cells [5]. This principle extends to various genetic disorders, providing a promising outlook for therapeutic applications [6, 7, 8, 9].

However, while identifying mutations and synthesizing mRNA are significant challenges, delivering mRNA into cells poses its own set of difficulties. Freely diffusing DNA or mRNA would be rapidly degraded by the body's defense systems, necessitating a robust delivery mechanism. This is achieved using so called vectors or in other words transportation vehicles —initially viral in nature, but now more commonly non-viral, such as LNPs, which are formed from specific lipid components [4, 10, 29]. LNPs act as carriers, safeguarding mRNA and delivering it into target cells (**Figure 2.1 - A**). Despite their lipid composition, which mimics natural cellular components, the body often recognizes them as foreign. Once at the cellular surface, LNPs are internalized via endocytosis, forming an endosome (**B**). Inside the cell, endosomes take various intracellular pathways, but for successful mRNA delivery, endosomal escape is crucial [30] like shown in **F**. This process involves proton pumps lowering the endosomal pH, altering the lipid composition of the LNP and endosomal

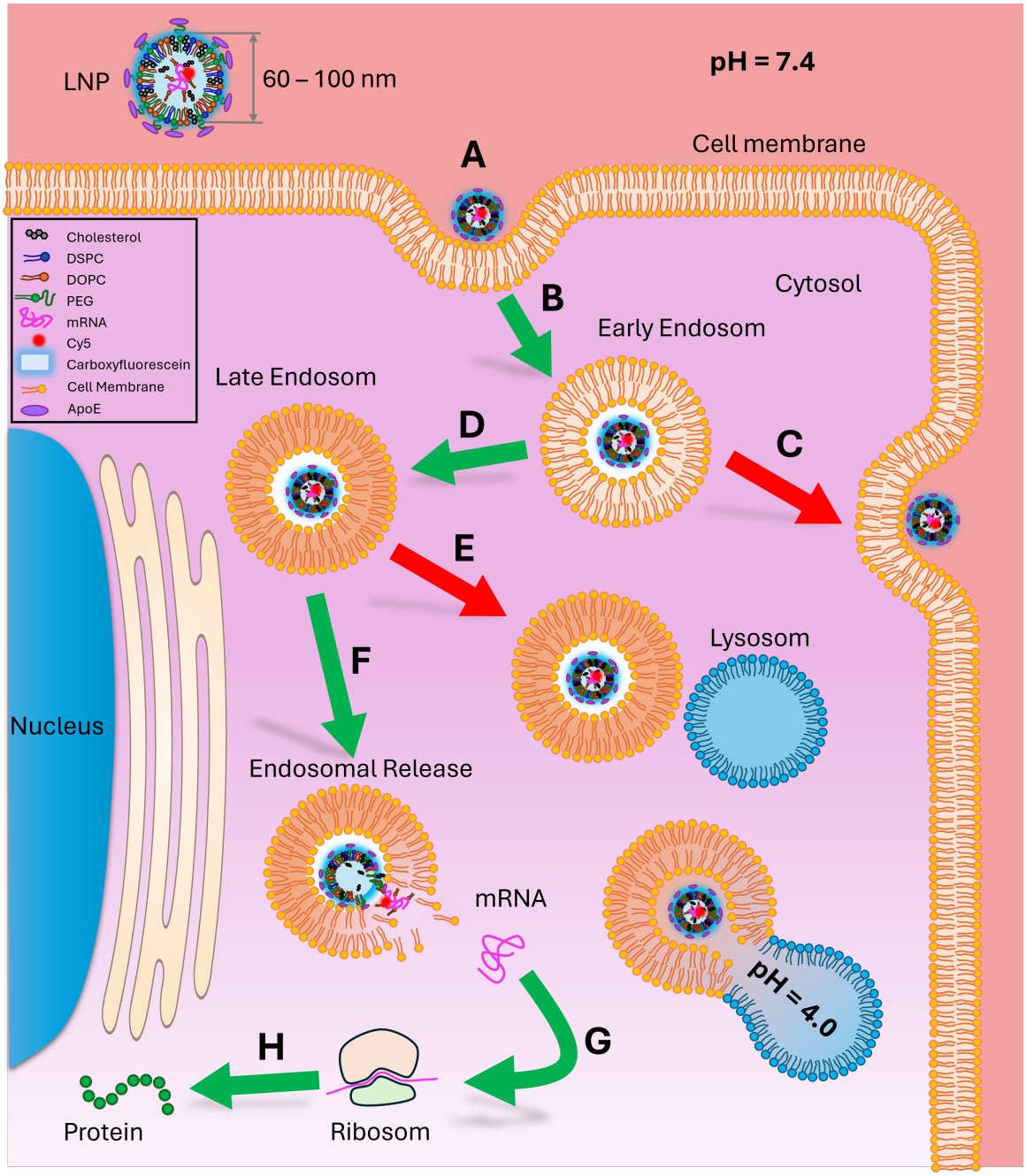

Figure 2.1: The Transfection Process and Endosomal Pathways: Following injection, the LNP are taken up via endocytosis (**A**). Once internalized, the LNPs become entrapped in endosomes, where they may follow various pathways: recycling through exocytosis (**C**), maturation into late endosomes (**D**) followed by degradation in lysosomes (**E**), or release of their contents into the cytosol (**F**). Upon successful endosomal release, the mRNA enters the cytosol, where it is translated by ribosomes (**G**) into proteins (**H**) that can perform a variety of cellular functions.

membranes [31]. These structural changes facilitate fusion of the LNP with the endosome, releasing the mRNA cargo (**G** and **H**) into the cytosol, where the central dogma begins its course, leading to protein production [10]. This entire process describes the transfection mechanism.

Understanding the kinetics of mRNA delivery, endosomal transport, and release has become an area of increasing focus [18]. Especially because the time has an drastic influence if the endosomal release is happening or not [32]. Despite progress, many aspects remain poorly characterized, particularly the endosomal escape mechanisms. Fluorescence-based techniques, including live-cell imaging and spectroscopic approaches, hold great potential for unraveling these processes [13]. In our research group, we aim to address these gaps by conducting experiments, statistical analyses, and simulations to investigate the kinetics of LNP-mediated mRNA delivery. Judith Müller *et al.* have reviewed the current state of knowledge, highlighting the critical steps and identifying areas where data are scarce [18]. Building on this foundation, the work presented in this dissertation seeks to develop and apply a framework of fluorescence-based methods to study these mechanisms in detail, offering time-resolved and trajectory-based insights into the complex process of transfection.

2.1.1 Pathways of LNP and Endosomes

Lipid nanoparticles navigate complex pathways both outside and inside target cells, which are critical to their effectiveness as mRNA delivery vehicles [31]. After injection, the LNPs traverse the extracellular matrix and their movement is influenced by size, charge and surface properties [33, 34]. For example, LNPs with diameters of 80-100 nm typically have diffusion coefficients of 2 - 10 $\mu m^2\,s^{-1}$ in aqueous environments, estimated according to the well-known Stokes-Einstein diffusion law [35, 36]. However, in denser tissue matrices, their diffusion slows considerably, often falling within the range of 0.1 – 1 $\mu m^2\,s^{-1}$ (see **Chapter 6**).

Upon reaching cells, LNPs are predominantly internalized via clathrin-mediated endocytosis, becoming enclosed within early endosomes [37, 38]. These vesicles, marked by the **Ra**s-related in **b**rain (Rab)-5 protein, maintain a mildly acidic environment (pH 5.5–6.5) [39, 40] and have slower diffusion coefficients due to the bigger diameter and the cytoplasmic viscosity [41]. Within these endosomes, the ionizable lipids in LNPs, such as Dlin-MC3-DMA, are protonated in response to the acidic pH, acquiring a positive charge [16, 42]. This facilitates interactions with the endosomal membrane, aiding the release of mRNA into the cytosol.

Late endosomes, characterized by the Rab-7 protein, are more acidic (pH 5.0-5.5) and exhibit slower mobility [43, 44]. These larger, less dynamic vesicles may fuse with lysosomes (**Figure 2.1 - E**), leading to the degradation of both LNPs and their cargo. Alternatively, late endosomes can release their contents into the cytosol via back-fusion with the membrane. The progression from early to late endosomes and the potential fusion with lysosomes constitutes a major bottleneck in mRNA delivery, as only a small fraction of mRNA avoids degradation and reaches the cytoplasm [31].

Advancing our understanding of LNP diffusion in various environments and their intracellular dynamics will help refine these systems for improved therapeutic efficacy. Thereby the differentiation between late and early endosomes can be done by the observation of the pH-value and the pathway through single particle tracking.

2.1.2 Endosomal Release

Endosomal escape is a pivotal step in the delivery of mRNA via LNPs, as it determines whether the mRNA is successfully released into the cytosol for translation, or not. Following endocytosis, LNPs are encapsulated within endosomes, where they encounter significant barriers to escape. Two principal mechanisms have been proposed to explain how LNPs overcome these barriers: the proton sponge effect [45] and pH-triggered lipid structural reorganization [46]. The proton sponge effect is a extensively studied hypotheses and strongly dependend on the buffering property of the ionizable lipid, acidification of the endosomes, chloride accumulation, and endosome bursting [31, 47]. This mechanism hinges on the behavior of ionizable lipids, such as Dlin-MC3-DMA, which become protonated in the acidic environment of the endosome (pH 5.5–6.0). Protonation leads to an influx of protons, counterions, and water into the endosome, increasing osmotic pressure. This swelling can stress the endosomal membrane to the point of rupture, enabling the mRNA to escape into the cytosol. While the proton sponge effect offers a compelling explanation, experimental evidence of direct membrane rupture due to this mechanism is limited. Moreover, some studies suggest that it may not entirely account for the observed efficiency of LNP-mediated delivery [31]. An alternative but complementary mechanism involves the pH-driven reorganization of lipid structures. Ionizable lipids exhibit a conical shape at neutral pH, which supports the spherical architecture of LNPs [48, 49]. Under acidic conditions, however, protonation alters their charge, prompting a transition from an inverse micellar (L_{II}) phase to an inverse hexagonal phase (H_{II}) [50]. This structural rearrangement destabilizes the LNP membrane and facilitates fusion with the endosomal membrane. Such fusion results in lipid bilayer mixing and the direct release of mRNA into the cytosol [31].

These mechanisms likely operate in tandem. The proton sponge effect may destabilize the endosomal membrane transiently, creating an environment conducive to lipid fusion, which offers a more controlled release pathway. A deeper understanding of the interplay between the proton sponge effect and lipid fusion will be essential for further improving the efficiency of LNP-based mRNA delivery systems and expanding their therapeutic potential. Additionally, the composition of the LNP influences its efficiency in endosomal escape. Helper lipids such as 1,2-**D**istearoyl-**s**n-glycero(3)**p**hospho**c**holin (DSPC) and cholesterol regulate membrane stability, curvature, and fluidity, which are crucial for effective fusion. PEGylated lipids, while essential for stabilizing LNPs during systemic circulation, must shed or rearrange to facilitate interactions with endosomal membranes. The detail behind the used LNP formulation for this dissertation is given in the following subsection.

2.1.3 Lipid Nanoparticle Composition

The lipid composition used to produce LNPs determines their size, shape, stability, and efficiency in delivering their cargo, such as mRNA, into cells. In this study, the LNPs were formulated using four lipid components: Dlin-MC3-DMA, DSPC, Cholesterol, and DSPE-PEG, in a molar ratio of 50:10:38.5:1.5. Each lipid serves a specific function in the LNP structure and performance, with distinct physicochemical properties such as charge and shape contributing to their role.

Dlin-MC3-DMA: The Ionizable Lipid
Dlin-MC3-DMA is an ionizable lipid, meaning its charge depends on the pH of its environment [51]. At physiological pH (~ 7.4), it remains neutral, reducing potential off-target interactions and minimizing toxicity. In acidic conditions, such as those encountered during LNP formation (pH $\sim 3-4$), it becomes positively charged. This allows Dlin-MC3-DMA to interact electrostatically with the negatively charged mRNA, encapsulating and stabilizing it within the LNP. Its conical molecular shape is critical for the spherical structure of the LNP, as it facilitates curvature and compact packing [52].

DSPC: The Helper Lipid
DSPC is a zwitterionic helper lipid with a cylindrical shape [53]. It contributes to the structural integrity and overall stability of the LNP by forming a lipid bilayer-like environment. DSPC also improves the biocompatibility of the LNPs, reducing their toxicity to cells. Its inclusion can influence particle size and help tune the physical properties of the LNPs.

Cholesterol: The Membrane Stabilizer
Cholesterol plays a pivotal role as a membrane stabilizer, enhancing the fluidity and packing density of the lipid components. It ensures that the LNP maintains its structural integrity at physiological temperatures (37°C) and provides a robust barrier against external stressors. Cholesterol's cylindrical shape complements other lipids, contributing to membrane stability. Being uncharged, it also avoids unnecessary electrostatic interactions within the LNP.

DSPE-PEG: The Shielding Lipid
1,2-**D**istearoyl-**s**n-glycero-3-**P**hospho**e**thanolamine (DSPE)-**P**oly**e**thylen**g**lykol (PEG) forms a hydrophilic shell around the LNPs. This "stealth" layer helps protect the nanoparticles from rapid clearance by the immune system (stealth effect), prolonging their circulation time in the bloodstream [54]. DSPE-PEG also prevents LNP aggregation, ensuring colloidal stability. Like DSPE and cholesterol, DSPE-PEG has a cylindrical shape and is neutral in charge. Its PEGylated headgroup extends into the aqueous environment, providing steric hindrance against immune recognition and particle clumping [55, 56].

The carefully chosen composition of Dlin-MC3-DMA, DSPC, Cholesterol, and DSPE-

PEG ensures optimal LNP properties for efficient drug delivery. The ionizable lipid Dlin-MC3-DMA is essential for mRNA encapsulation and endosomal escape, DSPC enhances stability and biocompatibility, Cholesterol regulates membrane fluidity, and DSPE-PEG provides immune evasion and prevents aggregation. Together, these components create LNPs with precise size, shape and functionality, critical for their application in therapeutic mRNA delivery systems.

2.1.4 Dynamic Microsocpy for Intracellular LNP

Once the biological question and motivation have been stated, we can choose from a variety of techniques the one that is best suited for this purpose. LNPs are small in size (60-100 nm), well below the resolution limit of light microscopes. Thus, at first, advanced electron microscopy could reveal the precise localization of particles within the cell [57]. While many measurements on LNPs have already been carried out, these methods are limited for characterization purposes [58, 33]. A deeper understanding of the transfection process and its pathway is only possible by considering random timestamps resulting from the various sample preparation steps involved. To extract this coherent single particle pathways or real kinetics is sadly not possible. This is why most research groups have focused on fluorescence-based techniques [59].

Initially, super-resolved techniques like **S**timulated **E**mission **D**epletion (STED) [60], **P**hoto**a**ctivated **l**ocalization **M**icroscopy (PALM) [61], **S**tochastic **O**ptical **R**econstruction **M**icroscopy (STORM) [62], or **S**tructured **I**llumination **M**icroscopy (SIM) [63] come to mind to resolve small particles. While some of these techniques have been used, they are not standard tools for LNP research and come with certain limitations [64]. For example, while SIM can theoretically double the resolution, it is not enough to resolve 80 nm LNP particles. Additionally, the number of images needed for super-resolution calculations is time-consuming for live-cell imaging setups. STORM and PALM belong to the **RE**versible **S**aturable **O**ptica**L** **F**luorescence **T**ransitions (RESOLFT) family, where resolution improvement is achieved by using so called photoswitchable molecules [65, 66]. These specific fluorophores can be turned "on" and "off" with particular wavelengths, limiting the use of sensor-based fluorophores that can reveale for example the pH-value. Furthermore, localization cannot be calculated if particles move too quickly, making it unsuitable for tracking individual particles in live-cell experiments although great progress was already achieved [67].

STED is a viable tool for live-cell experiments and can resolve LNPs sufficiently but was only shown for lipid droplets [33]. However, the number of usable fluorophores is limited to achieve an adequate depletion process without applying excessive power of the depletion laser, which could damage the sample [68]. Although there are ways to increase axial resolution in STED, such as through 3D-STED [69], there is still no suitable method to track nanoparticles in three dimensions. But still by combining STED with FCS the excitation volume is reduced to study lipid membrane movement with nanometer resolution [70].

The most common techniques to study LNP are with **C**onfocal **L**aser-**S**canning **M**icorsocpy

(CLSM), wide-field approaches and spectroscopic techniques [18]. Although the LNP can not be fully resolved the gained information is sufficient to extract needed information's and kinetics. Especially the characterization is done with this type of microscopy and helps for example to understand the changes for different lipid compositions or uptake efficiency [11, 71].

The state-of-the-art SPT techniques will be addressed in **Chapter 6**. Although, LNP are a promising sample systems only one publication could be found tracking mRNA loaded LNP in three dimension. The **3D S**ingle-**M**olecule **A**ctive **R**eal-time **T**racking (3D-SMART) method [17, 72] was used to study the dynamic moving of LNP in mucus like solution [14].

To study kinetics also the sample can be modified to use commonly available and high throughput microscopy approaches [73]. Here **L**ive-Cell **I**maging on **S**ingle **C**ell **A**rrays (LISCA) shows great potential and resulted in great insights of mRNA kinetics [74, 75, 76]. Another example is a microscopy technique that uses a specific convex lens in combination with a microwell patterned sample. By pushing the lens onto the sample system the LNPs are trapped into the microwells. Due to the small sample volume the particles cant escape and their motion and behavior can be studied giving great insights into LNP-LNP fusion [77, 12].

With the two new microscope techniques SUPER-FLIM (**Chapter 5**) and SEMPA-Track (**Chapter 6**) it was tried to generate a further tool in LNP research.

2.2 Kinetics of RNA-LNP delivery and protein expression

Authors	Judith A. Müller, Nathalie Schäffler, **Thomas Kellerer**, Gerlinde Schwake, Thomas S. Ligon and Joachim O. Rädler
Title	*Kinetics of RNA-LNP delivery and protein expression*
Journal	European Journal of Pharmaceutics and Biopharmaceutics (IF: 5.6 - 2020)
DOI	`https://doi.org/10.1016/j.ejpb.2024.114222`

The review article *"Kinetics of RNA-LNP delivery and protein expression"* explores the complex mechanisms involved in mRNA delivery via lipid nanoparticles and the subsequent protein expression. The focus is on the temporal dynamics of the transfection process, which is mathematically described as a series of stochastic steps. The review discusses the influence of factors such as lipid composition, particle size, and other physicochemical properties on the efficiency of this process. The theoretical framework is supported by experimental data, including results generated as part of this dissertation (see 3 - B in [18]).

Additionally, the paper reviews the techniques used to study transfection processes and the types of model systems employed. A significant emphasis is placed on single-particle studies, which are currently underutilized, despite their potential to provide deeper insights [14]. For example, while 2D tracking is commonly used for virus studies, it often focuses solely on the XY-plane and bulk measurements, neglecting the third spatial dimension (Z). Advanced methodologies that enable 3D single-particle tracking are still lacking, yet they could illuminate the intracellular movement patterns of LNPs.

A major challenge in this area is the rapid movement of particles due to their small size (less than 100 nm), which limits the ability to perform time-resolved measurements such as fluorescence lifetime imaging to sense the microenvironment. These limitations highlight the need for innovative imaging techniques to capture detailed kinetic data.

Another critical focus of the publication is the co-delivery of different genetic materials, such as mRNA and **s**mall **i**nterfering **R**ibo**N**ucleic **A**cid (siRNA), for combinatorial therapeutic approaches. This strategy enables simultaneous suppression of one gene while producing the necessary proteins from another, offering a versatile tool for advanced gene therapies.

In conclusion, the paper underscores the importance of understanding the kinetics of LNP-facilitated mRNA delivery for the development of precise gene therapies. The insights gained could advance the rational design of combinatorial therapies and support the establishment of personalized therapeutic approaches. Moreover, integrating kinetic models into therapy development holds significant promise for improving the predictability and efficiency of mRNA-based applications.

2.2.1 Contribution

In this review paper, Thomas Kellerer was responsible for conducting the extensive literature research and for writing the section focused on single nanoparticle studies. Additionally, he contributed to the acquisition of supplementary measurements and developed the evaluation software used to present labeled LNP on HuH7 cells, as shown in Figure 3 in [18]. This work involved not only designing and implementing the analysis tools, but also integrating the experimental data with the software to ensure a clear and informative presentation of the results. The section on single nanoparticle studies reflects a thorough understanding of the relevant methods and their application in the context of fluorescence microscopy and nanoparticle tracking.

European Journal of Pharmaceutics and Biopharmaceutics 197 (2024) 114222

Contents lists available at ScienceDirect

European Journal of Pharmaceutics and Biopharmaceutics

journal homepage: www.elsevier.com/locate/ejpb

Kinetics of RNA-LNP delivery and protein expression

Judith A. Müller [a], Nathalie Schäffler [a], Thomas Kellerer [b], Gerlinde Schwake [a], Thomas S. Ligon [c], Joachim O. Rädler [a,*]

[a] Faculty of Physics and Center for NanoScience, Ludwig Maximilians-University, Munich, Germany
[b] Multiphoton Imaging Lab, Munich University of Applied Sciences, Munich, Germany
[c] Independent Researcher

A B S T R A C T

Lipid nanoparticles (LNPs) employing ionizable lipids are the most advanced technology for delivery of RNA, most notably mRNA, to cells. LNPs represent well-defined core–shell particles with efficient nucleic acid encapsulation, low immunogenicity and enhanced efficacy. While much is known about the structure and activity of LNPs, less attention is given to the timing of LNP uptake, cytosolic transfer and protein expression. However, LNP kinetics is a key factor determining delivery efficiency. Hence quantitative insight into the multi-cascaded pathway of LNPs is of interest to elucidate the mechanism of delivery. Here, we review experiments as well as theoretical modeling of the timing of LNP uptake, mRNA-release and protein expression. We describe LNP delivery as a sequence of stochastic transfer processes and review a mathematical model of subsequent protein translation from mRNA. We compile probabilities and numbers obtained from time resolved microscopy. Specifically, live-cell imaging on single cell arrays (LISCA) allows for high-throughput acquisition of thousands of individual GFP reporter expression time courses. The traces yield the distribution of mRNA life-times, expression rates and expression onset. Correlation analysis reveals an inverse dependence of gene expression efficiency and transfection onset-times. Finally, we discuss why timing of mRNA release is critical in the context of codelivery of multiple nucleic acid species as in the case of mRNA co-expression or CRISPR/Cas gene editing.

1. Introduction

Lipid nanoparticles (LNPs) provide a facilitating platform for mRNA-based delivery [1–3]. The tremendous success of mRNA based vaccination during the SARS-CoV2 pandemic also boosted the perspectives of mRNA-LNP-based therapies in a wide range of applications, including cancer immunotherapies [4,5], CAR-T cell-based immunotherapies [6] and CRISPR-based gene editing [7]. As personalized gene therapies advance, the demand for an efficient, broadly applicable and reliable mRNA delivery platform grows. LNP formulations stand out by unique properties such as defined size, colloidal stability, low immunogenicity and the possibility of cell-specific delivery via surface functionalization. These properties are in parts the result of rational design approaches [8] and high-throughput screening of libraries of lipid-like compounds [9,10]. Current LNP formulations are composed of four lipid components: (i) ionizable lipid, (ii) helper lipids, e.g., DSPC (1,2-distearoyl-*sn*-glycero-3-phosphocholine), (iii) PEG (polyethylene glycol)-lipid, and (iv) cholesterol. It is understood that the favourable properties come about by optimal choice of these lipid components that ensure self-assembly into a well-defined core–shell architecture. Typically, PEG-lipid and helper lipids, such as DSPC and cholesterol, form a surface monolayer that stabilizes LNP size, while the ionizable lipid, cholesterol and nucleic acids reside in the core [2,11,12]. LNP manufacturing employs efficient condensation and encapsulation of negatively charged nucleic acid cargo with ionizable lipid at low pH via rapid microfluidic mixing, which promotes homogeneous self-assembly of lipid nanoparticles by fast solvent exchange [13]. Particle size and stability is adjusted via modification of core-lipids to shell-lipids ratio [12]. LNP formulations govern their ability to efficiently mediate cellular uptake via plasma proteins and subsequent release of nucleic acid to the cytosol. The LNPs were developed and first optimized for siRNA delivery [8,14,15]. Interestingly the same LNP formulations with only small adjustments proved also highly efficient for mRNA delivery [9,16]. In this review we will focus on mRNA-LNPs, but refer to siRNA-LNPs for comparison or in cases where corresponding data are not available for mRNA-LNPs. Over the past decade substantial progress has been made in optimizing LNP formulations turning both siRNA and mRNA LNP-based delivery into a manageable platform technology. However, quantitative pharmacokinetic modelling of LNP delivery and profound understanding of the delivery mechanism at the molecular level are still in their infancy.

The aim of the present review is to present a quantitative reaction kinetic framework of gene delivery and to collect kinetic rates for the various sub-steps leading to gene expression. We begin with an

* Corresponding author.
E-mail address: raedler@lmu.de (J.O. Rädler).

https://doi.org/10.1016/j.ejpb.2024.114222
Received 29 November 2023; Received in revised form 23 January 2024; Accepted 8 February 2024
Available online 20 February 2024

abstraction of nucleic acid delivery as a chain of transfer processes. Next, we introduce common reporter readouts and single-cell time lapse imaging. We then show that time courses of reporter gene expression reflect the reaction kinetics of a simple translation model. Single-cell expression exhibits distinct onset-times that indicate the delivery time as the period from LNP administration to mRNA release. We highlight factors that influence the uptake-rates and the existence of a window of opportunity in endosomal release. Experiments using multiple fluorescence markers or multiple mRNAs reveal distinct event-time correlations. We discuss codelivery of different mRNA reporter constructs and provide an outlook how timing can be modulated to achieve controlled gene expression.

2. Modelling LNP-based mRNA delivery

Quantitative modelling aspires to describe mRNA-LNP delivery as a sequence of discrete stochastic transfer processes [17–20]. As demonstrated in our earlier work [21] it is useful to dissect delivery in sub-steps as shown in Fig. 1. After administration of LNPs, rapid exchange of PEG-lipid and plasma proteins leads to the formation of a LNP protein corona. The protein corona enables LNPs to bind to the cell surface in a binding reaction followed by receptor mediated endocytosis. As discussed later in section 5 and 6, various pathways of endosomal uptake and endosomal processing exist. Most prominently, some endosomes are guided to undergo exocytosis, while other endosomes acidify due to the action of proton pumps and evolve into lysosomes. As a consequence, ionizable lipids become protonated and engender endosomal escape via LNP fusion with the endosomal membrane [9,20–23]. This crucial and still fairly unexplored step is subsumed in a single "escape" rate, k_L (Fig. 1). Subsequently mRNA is released from the remaining LNP shell into the cytosol. At this point, translation is initiated by ribosome binding and mRNA translation into protein, which in the case of a reporter protein like enhanced green fluorescent protein (eGFP) leads to a fluorescence readout (trajectories in Fig. 1). As detailed in section 4, eGFP fluorescence requires an additional chemical reaction known as maturation (with rate k_m). Each of the intracellular interstage products are continuously exposed to the risk of degradation. A further complication is the fact that many loaded endosomes differ in their number of LNPs as LNPs may enter endosomes either alone or as a cluster. The latter case has been addressed in multilevel modeling in reference [21]. For the sake of simplicity, we restrict ourselves to the linear model shown in Fig. 1. It is challenging, however, to reinforce the delivery cartoon by actual numbers. Only few of the kinetic rates have been measured. Furthermore most, if not all, parameters must be considered cell-type dependent. In order to provide data for quantitative modelling, single-cell time courses need to be recorded. Studying single cells allows us to get beyond the population average and to access cellular heterogeneity and subpopulations [18,24,25]. In more detail, single cell trajectories resolve rare events [26], event-time correlations [26,27], fluctuations and noise [28]. Fluctuations are seen in terms of cell-to-cell variability as well as intrinsic noise in expression trajectories, caused by stochastic nature of the underlying molecular processes. In any case, time-resolved microscopic observation is crucial to access LNP delivery and expression kinetics.

3. Reporter genes and time resolved microscopy

GFP provides the most convenient quantitative time-resolved measurement of protein expression [29]. GFP-reporters based on mRNA or plasmid vectors are widely used to signal the efficiency of nucleic acid transfer [30]. Moreover, the dynamics and spatial distribution of protein expression is readily observed in live-cell imaging. Variants of GFP exist that show enhanced or color shifted fluorescence allowing for monitoring protein expression of multiple genes in parallel [31]. Recently, more advanced reporters in terms of maturation speed, brightness and quantum yield became available such as mGreenLantern [32] or mScarlet [33]. In order to follow the fate of exogenous reporter genes during transfection, the nucleic acids can be labelled themselves using various nucleotide-bound cyanine dyes or dyes binding to 3′ UTRs of synthetic mRNAs [34,35]. Together with countless markers for live imaging of cell compartments and processes, high-resolution fluorescence imaging is a powerful method to unravel gene delivery pathways.

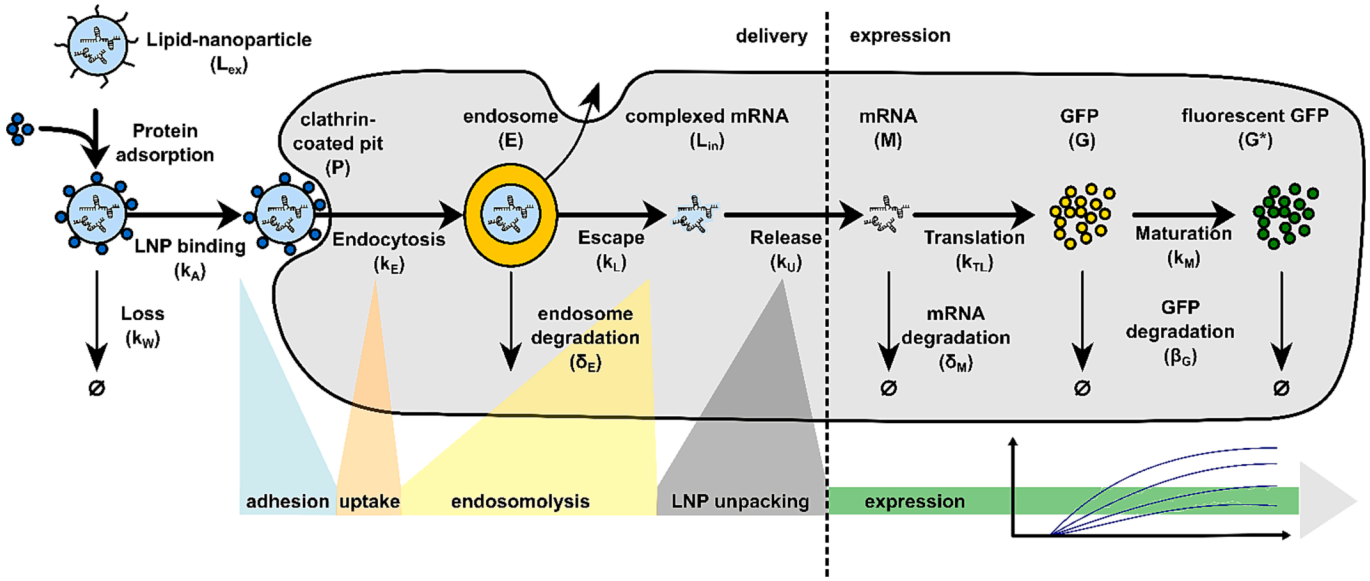

Fig. 1. Reaction pathway of mRNA-LNP delivery and expression: After incubation of LNPs to cell medium or blood serum PEG-lipid desorbs and protein adsorption decorates the LNP with proteins. The protein corona mediates LNP adhesion to the plasma membrane (blue timescale) and facilitates uptake (orange timescale). Subsequently, LNPs either undergo endosomal recycling (exocytosis), lysosomal degradation or endosomal escape (yellow timescale). Those endosomal escape events then result in cytosolic particles consisting of mRNA and residing lipids that can release their nucleic acid cargo (grey timescale). After those delivery steps, RNA is ready for cellular processing, here: mRNA translation for protein expression is depicted including steps of translation, protein maturation and potential degradation of both mRNA and protein species (green timescale). In case of reporter proteins, expression can be captured (inset with traces). Adapted from Ligon et al. [21] (© 2014 Ligon et al.). (For interpretation of the references to color in this figure legend, the reader is referred to the web version of this article.)

In particular, specific antibody labelling against clathrin or caveolin are available to follow endocytosis and intracellular processing of endosomes [34]. In addition to imaging of individual uptake and endosomal escape events, automated live-cell imaging is frequently employed to follow reporter gene expression over time. However, in order to obtain high-quality time resolved single-cell transfection data, platforms that provide identical local microenvironments are convenient. Micropatterned substrates enable us to collect high-quality fluorescence trajectories with sufficient statistics. Live-cell imaging on single cell arrays (LISCA) as described in Reiser, Krzysztoń, Murschhauser or Müller allows for high-throughput measurement of time resolved single-cell imaging and combines the above-mentioned techniques [26,36–38]. In short, arrays with cell-adhesive squares and a cell-repellent surrounding are produced and allow for cells to self-assemble to the single-cell pattern as depicted in Fig. 2a. Imaging under physiologic conditions over time (Fig. 2b) allows measurement of hundreds of single-cell fluorescence trajectories in parallel (Fig. 2c). This high statistic together with fine time-resolution allows modelling of gene expression as for example with a three-stage-maturation model described by Krzysztoń et al. (Fig. 2d) [37]. Further, this isolation of cells in defined adhesion sites results in standardized cell shape and hence area. However, it is to be noted that the lack of direct cell–cell contacts might result in adverse effects. Therefore, it is important to track cell division, survival rates and morphology as an indicator for vitality.

To quantify LNP uptake and release, real-time 3D particle tracking microscopy approaches [39] and analysis methods can help to obtain quantitative data over a large timespan. Tracking analysis led to great advancement in the field of virus-based vaccination [40,41]. In the case of LNPs, the molecular components, mRNA or lipids, can be labeled independently, revealing potentially different kinetics [42–44]. In recent studies, super resolution techniques like Stochastic Optical Reconstruction Microscopy (STORM), Stimulated Emission Depletion

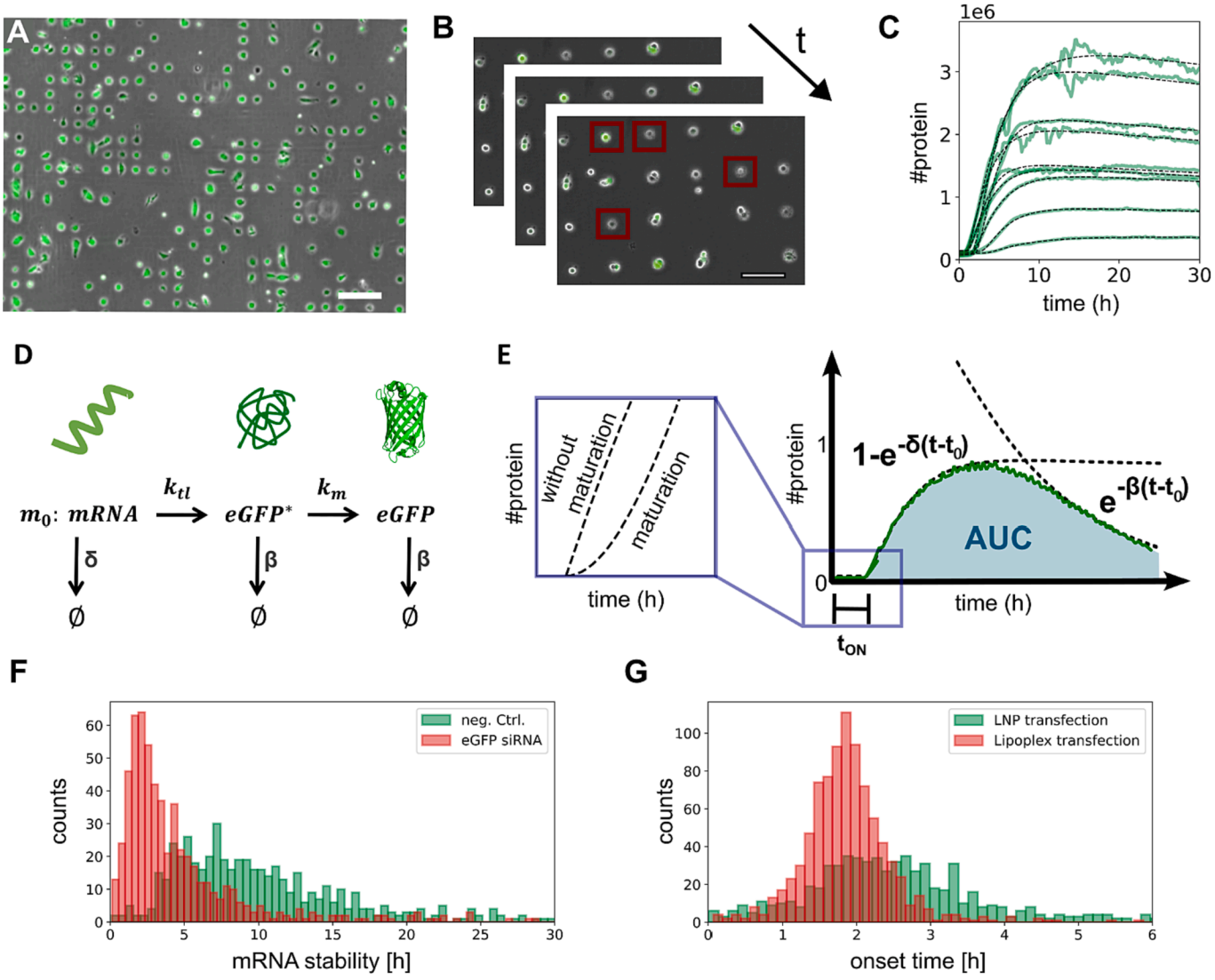

Fig. 2. Live Cell Imaging on Single Cell Arrays (LISCA) monitoring single cell reporter protein expression. (A) Micropatterned structures allowing for self-sorting of single cells on isolated adhesion sites. (B) Time-lapse movies under physiologic conditions generate (C) single cell fluorescence trajectories (green lines) which then can be fitted to quantitative models (black dashed lines). (D) translation-maturation model for GFP-mRNA expression according to Krzysztoń et al. [37]; adapted from Müller et al. [38]. (E) Predicted time course of GFP expression. Protein production and protein degradation are separately depicted by exponential functions with mRNA degradation rate δ and protein degradation b as respectively. The total transient protein expression is shown as shaded region (AUC) and calculated from the fit as described in section 3. Correct determination of the expression onset-time distribution requires consideration of the GFP maturation step. (F) Distributions of mRNA stabilities with and without siRNA (Dharmacon, GFP Duplex I siRNA) mediated knockdown. (G) Distributions of onset-times from fits of hundreds of trajectories shows faster transfection mediated via cationic lipoplexes compared to LNPs. (For interpretation of the references to color in this figure legend, the reader is referred to the web version of this article.)

Microscopy (STED) or the Structured Illumination Microscopy (SIM) are used to observe the trajectory of endosomes inside eucaryotic cells [45], the release of siRNA loaded nanovectors [46], the shape of nanocarriers [47] and the clustering of LNPs inside the early endosome [48]. As the release mechanism is little understood, it is beneficial to record the endosomal trajectories simultaneously with information about the microenvironment, a feature that most current imaging techniques lack [49].

To enhance our understanding of endosomal release kinetics and trajectories, more sophisticated imaging methodologies are needed. Among these, fluorescence lifetime imaging microscopy (FLIM) stands out as a useful technique. Fluorescence lifetime, the average time a fluorescent molecule spends in its excited state, is highly sensitive to the fluorophore's immediate biochemical environment. Variations in photophysical properties, such as those induced by fluctuations in pH-Value, temperature, or the solvent polarity, are detectable through changes in fluorescence lifetime [50,51]. This sensitivity exceeds the capabilities of traditional intensity-based microscopy techniques, which is constrained by morphological details. The specificity of this parameter to environmental factors has pushed extensive research into creating specialized fluorophores. Such probes are engineered to respond to changes within microenvironments, like subcellular pH levels within cytosolic regions of endosomes and lysosomes [52]. Fluorescence lifetime measurements can also be used to incorporate techniques like the förster resonance energy transfer (FRET) [53–55]. FRET's sensitivity to subnanometer-scale changes allows for detailed examination of lipid membrane dynamics [56] crucial to endosomal release, offering precise insights into the details of cellular trafficking processes. By incorporating fluorescence lifetime measurements simultaneously with other techniques, a richer understanding of the multifaceted mechanisms of the endosomal release can be achieved.

4. Mathematical model of mRNA-LNP mediated protein expression

When mRNA is released into the cytosol, protein expression is turned on (green area in Fig. 1). In a coarse-grained view, mRNA translation is described as a biochemical reaction and a corresponding mathematical model is readily set up. As described in the original work by Leonhardt in 2014 [18] the rate of protein (P) production in an individual cell is given by

$$\frac{d}{dt}P = k_{TL}\cdot m - \beta\cdot P \tag{1}$$

where k_{TL} is the translation rate, m the number of accessible mRNA molecules in the cytosol and β the degradation rate of protein. As mRNA has a finite life-time the concurrent decay of mRNA is described by

$$\frac{d}{dt}mRNA = -\delta\cdot m \tag{2}$$

where δ denotes the degradation rate of mRNA. Eq. (1) and Eq. (2) can be solved yielding the following analytical expression for the time course of the number of proteins

$$P(t) = \frac{m_0\cdot k_{TL}}{\delta-\beta}\cdot\left(1 - e^{-(\delta-\beta)(t-t_0)}\right)\cdot e^{-\beta(t-t_0)} \tag{3}$$

where m_0 denotes the number of mRNA molecules that are in an idealized view instantly released at a given point in time, t_0. Eq. (3) provides a prediction for the time course of number of proteins in a single cell. In the case of eGFP reporter genes, P(t) is proportional to the total eGFP fluorescence emanating from a single cell (Fig. 2c). Fig. 2d explicates the characteristic features of the expression dynamics resulting from Eq. (3). At time point t_0, which we term the onset-time, fluorescence sets in and shows an initial linear increase with slope m_0k_{tl}. The onset-time hence is an idealized time point when m_0 mRNA molecules are thought to be concurrently set free and bound by ribosomes for consecutive production of protein. The rate of fluorescence increase exponentially slows down as mRNA is degraded. As indicated by the dashed line in Fig. 2e, the protein level would saturate at a constant value, if proteins were stable ($\beta = 0$). With finite protein stability, eGFP fluorescence reaches a maximum and approaches a regime dominated by exponential decay at long time scales. We recall the protein half-life, i.e., the time when half of the initial protein is left over, is given by $\tau_{GFP} = \ln(2)/\beta$. Likewise, the half-life of mRNA is defined as $\tau_{mRNA} = \ln(2)/\delta$. Note that τ_{mRNA} represents the functional life-time of mRNA, i.e., the time until mRNA translation ends, which is different from molecular degradation or the time until mRNA can no longer be detected e.g., via FISH probes. As a rule of thumb, τ_{mRNA} is equal to the time the expression needs to reach half-maximum of the expression level and τ_{GFP} the time scale of expression decay. Without loss of generality, we can assume that the degradation rate of mRNA is larger than the degradation rate of eGFP protein, $\delta > \beta$. This is confirmed by measuring the protein degradation in an independent experiment. To this end, after some initial expression, the drug cycloheximide is added, which immediately inhibits translation. In this case, the single exponential fluorescence decay is solely determined by protein degradation [37].

Due to the finite life-time of both mRNA and protein, the expression of protein is transient. In this context the measured "area under the curve" (AUC) is generally used to describe the overall pharmaceutical protein availability. We obtain the theoretical AUC of the expression model by integration of Eq. (3)

$$AUC = (ln2)^2\cdot m_0\cdot k_{TL}\cdot\tau_{mRNA}\cdot\tau_{EGFP} \tag{4}$$

Eq. (4) is astoundingly insightful. It states that the AUC, and hence pharmaceutical efficacy, is equally dependent on four factors, the number of mRNA molecules delivered, the translation rate, the mRNA life-time and the protein life-time. Each of these factors is equally important in order to maximize efficiency. In fact, single-cell time courses can be used to screen for optimal rate constants such as increased mRNA life-time using stabilizing UTR sequences as demonstrated by Ferizi et al. [57]. Fitting experimental fluorescence time courses yields single-cell values for four parameters: the two degradation rates (β and δ), the expression rate m_0k_{tl} and the onset-time t_0. Note the expression rate, i.e., the speed of protein production, is determined by both the initial number of mRNA molecules and the translation rate, and it is not possible to separate these two factors from the analysis of the fluorescence time courses alone. Fig. 2f shows a two-color histogram of single-cell eGFP-mRNA stabilities. The histogram reflects the effect of decreasing mRNA stability in the presence of targeting siRNA (Dharmacon, GFP Duplex I siRNA) (Fig. 2g). Another meaningful histogram is the distribution of expression onset-times dependent on the carrier as shown in Fig. 2f. In this case, another subtle effect needs to be considered. GFP fluorescence appears somewhat delayed after completion of protein translation. This is due to the fact that GFP undergoes an additional autocatalytic chemical reaction, known as maturation, that leads to the formation of the cyclic chromophore inside the protein barrel [30]. Including maturation into the system of chemical rate equations (see Fig. 2d) results in time course P(t) with slightly delayed onset as shown in the inset of Fig. 2e. In the work of Krzyszton *et al.* we showed that inclusion of maturation improves the overall quality of best fits of the mathematical model to experimental time courses [37]. Note that including protein maturation in the mathematical description of mRNA translation fits experimental fluorescence time courses very well (dashed line in Fig. 2c). However, deviations from Eq. (3) can be seen at very high expression levels, when the expression burden on the organism is high [58]. Interestingly, the experimental single cell time courses are well described by a model which assumes that all mRNA is released at a particular time, t_0. This fact supports the notion that, most likely, all mRNAs are released from a few endosomal fusion events occurring in a narrow time window. Moreover, in the case of relatively stable mRNAs

and proteins the heterogeneity in transfection onset times is less prominent and ensemble average data exhibit a similar time course as described by Eq. (3). For example, time resolved plate reader data could be fitted with the same model yielding estimates of average protein lifetime and translation rate. However, single cell analysis clearly is the preferred access to expression kinetics as it not only yields the full distribution of rates across the population, but also allows us to correlate kinetic rates and event times as discussed below. The question, what causes cellular heterogeneity in expression onset suggests itself. As shown in Fig. 1, the transfer of LNPs into the cellular cytosol is dissected into at least three stochastic processes, namely uptake, endosomal fusion and mRNA release and will be discussed in the following sections.

5. Endosomal uptake

RNA loaded LNPs are internalized by cells via endocytosis [59]. Various endocytic pathways can be classified: the receptor-mediated caveolin or clathrin-mediated endocytosis (CME) as well as the receptor-independent micropinocytosis and phagocytosis [60–62]. The intracellular fate and hence the cytosolic delivery efficiency of internalized particles is determined by the path of entry [63,64]. The uptake path is further dependent on the particle characteristics as well as cell type [65]. The dominant path of entry is the receptor-mediated endocytosis [23]. Specifically, CME uptake requires receptor binding that is mediated via the passively formed protein corona consisting of ApoE targeting low-density lipoprotein (LDLR) interaction [66], high-density lipoprotein (HDL) coating as recently described by Liu [67], Lipoprotein-D coating (Fig. 3a) [68] or tumor cell type specific coating with albumin [69]. LNP uptake in particular is mediated by PEG-lipid dissociation and concomitant protein adsorption [70]. Enhanced uptake via protein corona is a frequently occurring phenomenon on nanoparticle-cell interactions. In case of positively charged polyplexes, the negatively charged serum proteins assemble around the polyplex and facilitate uptake via CME [71]. In applications where highly specific targeting is required, uptake can be promoted by addition of targeting ligands to the LNP shell [66] or adapt lipid composition to target different tissues [72]. For example, T-cell targeting LNPs have recently reached clinical studies for next generation CAR-T cell therapies [6,73,74].

Time estimates for how long uptake after receptor binding takes, vary in the literature. Table 1 provides an overview of uptake time data from selected works varying in the proposed mechanism as well as type of studied particle and cargo. In general, literature proposes uptake times for mRNA LNPs from several minutes [18,69,75] to several hours [42,76,77]. Based on fluorescent labelling and confocal microscopy Gilleron *et al.* reported a timing for the uptake of siRNA LNPs ranging from 0.5 to 1.5 h for CME and 2–6 h in case of micropinocytosis [60]. For comparison, the well-studied viral uptake in case of CME is in the range of seconds (e.g. AAV-2 s) to minutes (e.g. HIV-1 s) [78]. Studies using smFISH showed a high uptake rate during the first 4 h after transfection and subsequent slow-down of uptake [42]. Advanced imaging setups as two-photon microscopy (Fig. 3b) or single particle tracking (SPT) allows to distinguish between random movement and active transport and showed that uptake can be distinguished in 3 phases that strongly depend on carrier and cell type [44,64]. It is generally believed that uptake and hence efficiency is dependent on nanoparticle composition [79] and size. Large particles in the μm-range enter the cell via micropinocytosis [80], for particles smaller than 500 nm the caveolae-dependent pathways appeared to be dominant in accordance with the finding that CME has an upper size limit of 200 nm [81]. Theoretical considerations lead to predictions of an optimal size for entry of 30 to 60 nm [82], which is in accordance with theoretical findings for polymer nanoparticles [83], whereas the maximal efficiency for mRNA-LNP based vaccines was found for 100 nm sized particles

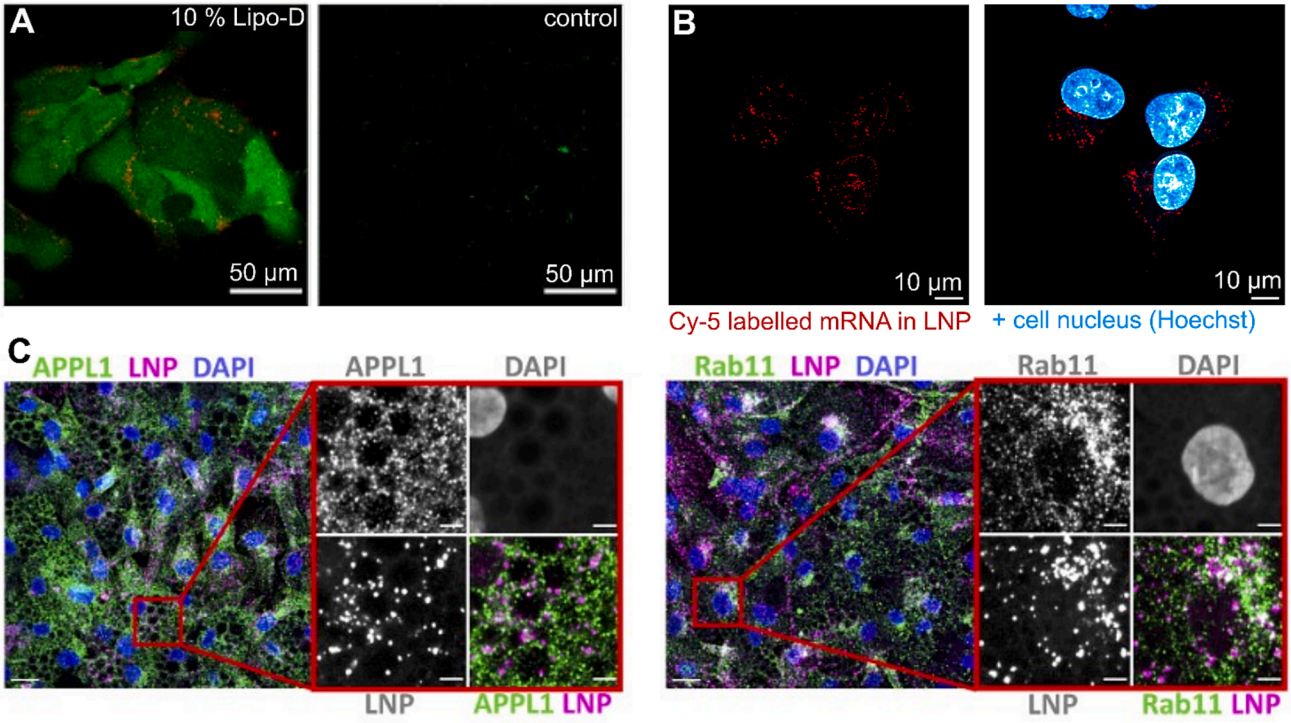

Fig. 3. Imaging of kinetics of LNP-RNA uptake and release: (A) HuH7 expressing eGFP upon transfection with LNPs encapsulating Cy5-eGFP-mRNA. LNPs were pre-incubated with or without 10 % Lipo-D protein. Cells were fixed and imaged with confocal microscopy [68] (© 2022 Aliakbarinodehi et al.). (B) Two-photon microscopy images recorded with a 60x water immersion objective. An ultrashort pulsed laser at 80 MHz with wavelengths of 1034 nm 780 nm was used as excitation source. Image analysis was performed using Fiji and Huygens software (unpublished data). (C) Human primary adipocytes after incubation with LNPs encapsulating fluorescently labeled mRNA. After 2 h cells were fixed and antibody labeled for endosomal markers (shown here: early endosomal marker APPL1 and late endosomal marker Rab11). Reprinted with permission from Ref. [79] (© 2021 Paramasivam et al).

Table 1
List of uptake times and corresponding uptake mechanism.

First Author	Year	Estimated Time	Proposed mechanism	Type of particle	Method
Dahlman [76]	2017	Maximum after 2 h	n/a		DNA barcodes *in vivo*
Miao [69]	2020	15 min	CME or micropinocytosis		Fluorescence microscopy
Miao [69]	2020	15 min	CME or micropinocytosis		Fluorescence microscopy
Patel [42]	2020	Within 4 h	n/a		3D Single particle tracking
Gallud [75]	2021	17 min (+2h if no serum incubation)	PEG shedding + LDLR receptor dependent	**LNP + mRNA**	Single NP imaging, NMR diffusometry, SANS, Proteomics, DLS
Munson [77]	2021	4–10 h	n/a		Live-cell imaging
Paramasivam [79]	2022	2–24 h (i-lipid dependent)	n/a		Super resolution microscopy
Liu [67]	2023	n/a	HDLR dependent		Multiomics
Aknic [66]	2010	n/a	LDLR dependent		Automated spinning disc confocal microscopy (fixed or live cells)
Gilleron [60]	2013	1.5 h	CME	**LNP + siRNA**	Blocking or knock out of respective components, Colocalization experiments of LNP and Rab5, EM
Hunter [103]	2023	n/a	Receptor mediated endocytosis	70 nm LNP + siRNA	Confocal microscopy + machine learning
		2–6 h	Micropinocytosis	larger LNP + siRNA	
Leonhardt [18]	2014	10–30 min	n/a	Lipoplex + DNA	LISCA
Rensen [131]	2001	n/a	GalNAc/ASGPR dependent uptake	Liposomes	Radiactive labelling and live-cell fluorescence microscopy

[84]. Interestingly, a CME endosome is only about 100 nm in diameter and hence has limited LNP capacity [62]. A recent study also showed that LNP shape matters, observing a higher uptake for star-shaped LNPs compared to round LNPs [85].

6. Endosomal fusion and mRNA release

Next, we discuss the timing of endosomal escape, considered as the bottleneck in LNP-based delivery of mRNA [86]. Following receptor-mediated uptake, LNPs are trapped in early endosomes with an internal pH ranging from 5.5 to 6.5 followed by maturation into late acidic endosomes with a pH of 5–5.5 [77,87,88]. Acidification of endosomes is likely to be crucial for fusion of LNPs with the endosomal membrane [89]. LNPs that do not escape the endosome at this stage are degraded or exocytosed [86,90,91]. Degradation through lysosomal fusion enriches the endosome with degrading enzymes while Rab-mediated signaling transports endosomes towards the plasma membrane and enables fusion for exocytosis. In fact, the majority of LNPs undergo one of the later pathways and hence do not deliver mRNA to the cytosol [59]. Escape efficiency is generally defined in terms of percentage of trapped LNPs that escape from the endosome. Some measurements of escape efficiencies are listed in Table 2 ranging from 2 % [60] to 3.5 % [92] for siRNA-LNPs and for mRNA LNPs from 1 % [93] up to 15 % with Moderna's own ionizable lipid 5 [94], similar to theoretical calculations predicting 14 % escape [95].

The timing of endosomal fusion is a key factor for delivery efficiency. It appears that only within a narrow window of opportunity the conditions allow LNPs to escape through endosomal fusion [86]. A correlation between fast endosomal trafficking and expression efficiency was described [88]. Different timescales were reported (Table 3), ranging from 0 to 1 h in case of small endosomes [79] or more general, 5 to 15 min [96] and up to 4 h [88]. Gilleron et al. described a gradual increase of siRNA-LNPs in the endosome within the first 4 h after uptake with a maximum co-localization of siRNA-LNPs in the endosome after 1 h [60].

Since the discovery of cationic lipid-mediated nucleic acid delivery, an extensive search for factors affecting endosomal escape efficiencies has been conducted. In early studies on DNA-lipoplexes it was demonstrated that cationic lipids complex into liquid crystalline nucleic acid–lipid complexes [97] and that inverse hexagonal mesophases showed higher delivery efficiency than lamellar phases [98]. LNPs made from cationic ionizable lipid likewise condense nucleic acid at low pH during the microfluidic mixing process. LNPs exhibit electron-dense core structures in cryo-TEM with a wide range of polymorphism. In the work by Arteta *et al.* using X-ray scattering it was shown that in the case of DLin-MC3-DMA the core phase consists of an inverse hexagonal phase [12]. Other LNP forming lipids exhibit cubic phases [99]. Recent X-ray studies revealed that the LNP core phase undergoes structural changes as a function of pH [100–102]. It is hypothesized that acidification-induced structure evolution inside LNPs leads to endosomal destabilization. pH driven lipid head group charge as well as release of elastic membrane energy favor membrane fusion. Local pH change as a prerequisite of LNP fusion and acidification of the endosome is a rate limiting factor in

Table 2
List of estimated times of endosomal release.

First Author	Year	Estimated Time	Type of Nanoparticle	Method
Miao	2020	15–30 min	LNP + mRNA	Confocal microscopy, qPCR
Gallud	2021	12 min	LNP + mRNA	
Alakbarinodehi	2022	5–15 min	LNP + mRNA	Live-cell TIRF, supported membranes
Kirschmann	2017	5 h	Lipoplex + mRNA	Spinning disc confocal microscopy
Gilleron	2013	Up to 6 h	LNP + siRNA	Quantitative light and electron microscopy
Wittrup	2015	5–10 min 5–15 min	LNP + siRNA Lipoplex + siRNA	Gal9 recruitment, Fluorescence imaging in two modi (long and short exposure)
Wrobel&Collins	1995	1–2 min	Liposomes + DNA	Fluorescence microscopy
Sonawane	2003	30–75 min	PEI + DNA	Cl- sensing fluorescenct probes

Table 3
Endosomal release efficiencies in percent of LNPs that are released into the cytosol from the total taken up.

First Author	Year	Estimated Efficiency	Type of Nanoparticle	Method
Sabnis	2018	15 %	LNP + mRNA	Fluorescence microscopy, Moderna lipid
Maugeri	2019	1 %	LNP + mRNA	EV extraction, qPCR, UPLC
Gilleron	2013	1–2 %	LNP + siRNA	Quantitative light and electron microscopy
Wittrup	2015	3.5 %	LNP + siRNA	Gal9 recruitment, Fluorescence imaging in two modi (long and short exposure)

endosomal release. Endosomal escape is favored at late stages when the LNP reaches the cytosolic area around the nucleus [103] and their active transport seems to be higher for small endocytosed particles [71]. Also, the number of LNPs in the endosome is relevant as several particles per endosome were discussed to block required acidification possibly due to the buffering effect of the ionizable lipid [68,79]. Furthermore, the optimal pH for endosomal escape is lowered by the protein corona, dependent on its composition [68]. Whereas Paramasivam et al. [79] described an independency of the type of ionizable lipid and timing, many others tackled the influence of the ionizable lipid on escape efficiency [94,104]. Cholesterol and analogues enhance membrane fusion [42] and stabilize high curvature regions [105]. PEG type and ratio change not only the expression level but also the expression kinetics [76,106]. Release of mRNA into the cytosol requires phase separation and membrane fusion. Therefore, the protein corona needs to be removed at least partially [107]. Apart from the lipid composition, also the type of RNA cargo might interfere with endosomal escape. Endosomal escape differs for mRNA compared to siRNA: The amount of co-localization of siRNA-LNPs with small endosomes reduces after 1 h whereas the amount of mRNA in large endosomes saturates after 1 h with no decrease until 2 h after uptake [60,79]. This leads to the general question if there is a relation between uptake pathway and release efficiency, respectively degradation. It was observed that there are at least two different types of endosomes (e.g. RAb11 positive vs. ACU22 positive as depicted in Fig. 3c) with different escape probabilities [79]. Maugeri et al showed that the endocytosis and the packaging into extracellular vesicles (EVs) for secretion are linked [93]. Furthermore, an influence of endosomal size and endosomal escape was described [108] and endosomal size is dependent on the endocytic pathways [62]. Peetla *et al.* discussed that the interaction of LNPs with artificial plasma and endosomal membranes differs [109]. Reiser *et al.* studied uptake kinetics and transfection efficiency for different cell media and found a concerted population correlation dependent on serum concentration (see also Fig. 4a) [110]. Similarly, Aliakbarinodehi found that the protein corona enhances cellular uptake and, at the same time, shifts the endosomal escape towards lower pHs and therefore to later timepoints and lower probabilities [68]. These opposing trends were also described by Miao *et al.* [69]. Nevertheless, it is to be noted that maximum protein expression does not necessarily increase in a linear manner with enhanced endosomal escape as cellular resources are limited but a more efficiently escaping drug might lower dose requirements [77,79]. Further, the linear delivery model as described in Fig. 1 includes a step where the mRNA escapes from residual lipids to become available for the translation machinery. To access this step, mRNA can be labelled and tracked over time to observe an increase of fluorescence upon unpacking. Simultaneous tracking of reporter protein expression allows to measure the time window between release and start of protein expression as shown in Fig. 4b [102].

7. Codelivery of different nucleic acid agents

Codelivery of multiple distinct elements is an increasingly relevant necessity in advanced rational design gene therapy. For example, codelivery of mRNA and siRNA allows for more effective targeting of cancer cells by simultaneous knockdown of oncogenes and overexpression of tumor suppressor genes [111]. Likewise mRNA/siRNA codelivery improves CAR-T cell engineering by expressing chimeric antigen receptor (CAR) mRNA together with siRNA knockdown of the programmed cell death protein (PD-1) in primary human T cells [112]. Also the expression of a pDNA mediated transgene was shown to be prolonged by simultaneous codelivery of anti- inflammatory siRNAs [113]. The relevance of nucleic acid codelivery was recognized at the latest with the rise of CRISPR/Cas based therapies, which typically require Cas9 protein and single guide RNA (sgRNA). These components are commonly delivered via adeno-associated viruses (AAVs) [114] but face limitations due to the limited packing size of AAVs [115] and redosing challenges [116]. LNP-based codelivery allows for selectable combinations of synthetic Cas-mRNA and sgRNA [117–120] or Cas RNP, sgRNA plus donor DNA [121]. In all these examples, codelivery of different nucleic acid elements is expected to unfold a synergistic effect. To this end, however, it is important to ensure synchronized release kinetics and action. Time-resolved single-cell studies employing two-color fluorescence enable to scrutinize the timing in codelivery [122].

In general, LNP-based codelivery of two RNA species can be achieved by two strikingly unlike mixing protocols: Each delivery agent can be encapsulated independently prior to combined administration (post-mixing protocol) or all components are jointly encapsulated in mixed nanoparticles (pre-mixing protocol). The first bears the advantage that each component can be encapsulated in its ideal vehicle and dosing can, if required, happen in cascades [37]. Yet, there is a remarkable difference between pre-mixing and post-mixing codelivery efficiency. In case of codelivery of two different GFP reporter genes, both for pDNA-lipoplex [95,122] as well as mRNA-LNP delivery [95], the percentage of cells that express both genes is higher for pre-mixing compared to

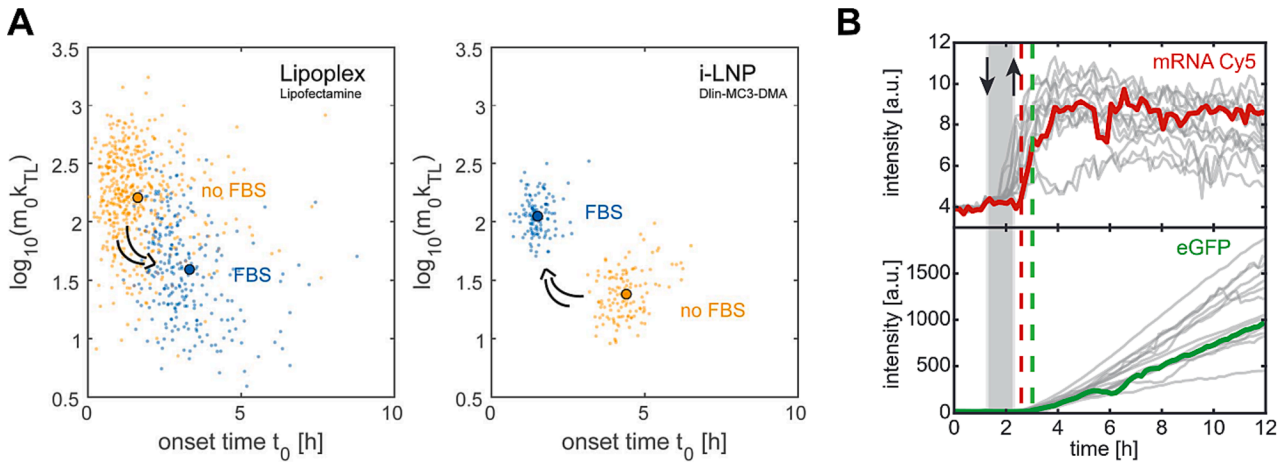

Fig. 4. Measuring rates of uptake and unpacking (A) Correlation plot of single cell onset times versus expression rates m_0k_{tl} of LNP-mediated and lipoplex mediated GFP expression measured independently with LISCA in presence and absence of serum. Reprinted with permission from Ref. [110] (© 2019 Reiser et al.). (B) Fluorescence trajectories of Cy5-labelled mRNA and eGFP protein expression signal during MC3-LNP mediated transfection. Time difference indicates a distinct time difference between endosomal release and mRNA unpacking. Grey bar marks the incubation period, red lines the respective onsets. Reprinted with permission from Ref. [102] (© 2023 National Academy of Science). (For interpretation of the references to color in this figure legend, the reader is referred to the web version of this article.)

post-mixing. Fig. 5a,b provides an example from Ref. [95] that shows the red-green fluorescence co-expression outcome as a function of the molar ratios of red/green encoding mRNAs in single RNA LNPs (S_R and S_G) compared to mingled LNPs (M_{RG}). In the regime of equimolar delivery post-mixing, i.e., delivery of either red or green encoding LNPs the percentage of co-expression is lower as seen by the heterogeneous distribution of cells that express only red or green. The experimental red/green likelihoods are quantitatively explained by stochastic mRNA-LNP uptake in the limit of small success rates of endosomal escape LNPs [95,122]. In recent work also the kinetics of co-expression were studied with the interesting observation, that differences in red/green onset-timing exist despite the fact that red and green encoding mRNAs were delivered in pre-mixed LNPs [37]. Fig. 5c shows exemplary single-cell fluorescence time courses for eGFP and CayRFP respectively, with clearly time shifted onsets, which also manifests in the onset-time correlation plot showing the entire population of single data (Fig. 5d). Possible reasons for this yet unexplained mRNA specific expression onset shift might be different release times, i.e., mRNA unpacking kinetics after endosomal release or different translation timing. While the former might be possible due to different secondary structure of the two distinct mRNA constructs, the latter could be caused by different untranslated region (UTR) and initiation site design. Also, base modification introduced to reduce the immunogenicity of mRNA were shown to influence uptake of LNPs in a tissue specific manner [123] and therefore needs to be considered in codelivery.

The issue of delayed expression gains further complexity as more than one type of nucleic acid species is encapsulated. It was discovered previously that mRNA and siRNA form different internal structures within an LNP [27] which has the potential to affect release and therefore expression timing. siRNA was found to be complexed into aqueous pockets by the phospholipids in the LNP. This leads to several questions regarding the molar ratio in codelivery of two species that have different physico-chemical properties: Are premixed LNPs homogenous in composition and if so, does the LNP nucleic acid content mirror the molar ratio that was set during LNP preparation? How many nucleic acid molecules are exactly contained in a single LNP? Based on SAXS structural data the number of mRNAs in LNPs varies as a function of size ranging from 10 molecules in LNPs of 50 nm diameter up to 200 molecules in LNPs with 140 nm [12,95]. Interestingly the number of functional mRNA molecules derived from statistical analysis of red/green fluorescence in codelivery was found to be 27 for 300 nm sized lipoplexes [95,122].For siRNA/mRNA no equivalent studies exist but an enhanced overall siRNA-mediated knockdown was reported for siRNA when codelivered with mRNA [111]. Little is known about discriminating or synergetic effects in endosomal escape and subsequent depacking in siRNA/mRNA codelivery. Furthermore, each species has

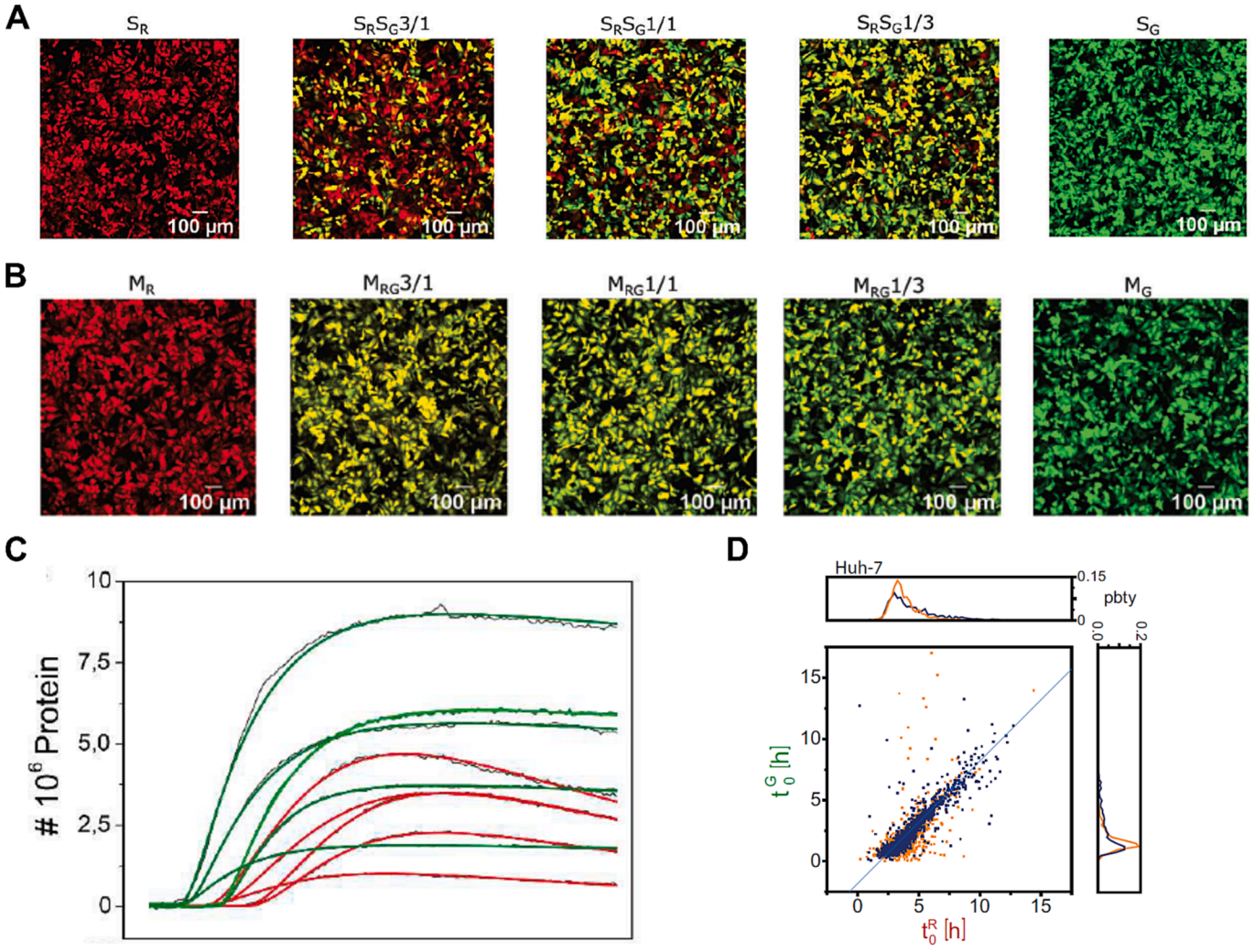

Fig. 5. Co-Delivery of RNA. (A) Co-delivery of LNPs with different ratios of mCherry-mRNA to GFP-mRNA encapsulated in single lipoplexes (S_{RG}) (B) different ratios of mRNA encapsulated in mingled lipoplexes (M_{RG}). (C) Single cell traces of HuH7 cells transfected with co-encapsulated RFP-mRNA and GFP-mRNA show shifted onset of protein expression. (D) correlation plot of GFP vs. RFP onset time distribution. (A)&(B) reprinted with permission from Ref. [95] (© 2021 Zhang et al.), (C)& (D) reprinted with permission from Ref.[37] (© 2019 Krzysztoń et al.).

different dynamics that need to be taken into account. Protein expression upon mRNA delivery is dependent on translation initiation, translational speed and protein maturation which is of special interest if the readout is a fluorescence reporter protein [37]. In contrast, siRNA needs to be spliced by the Ago Protein, assemble the RNA-induced silencing complex (RISC) and trigger mRNA degradation.

In case of CRISPR/Cas gene editing the cargo conveyed by the delivery vehicles consists of Cas protein and guide RNA (gRNA). Three discernible cargo options can be chosen: pDNA, mRNA, and ribonucleoproteins (RNPs). pDNA entails the delivery of genetic material in plasmid form, necessitating its entry into the nucleus for subsequent expression. This approach offers stability and prolonged expression but is associated with increased off-target effects and challenges in controlling the number of plasmids per cell [124]. Transfection can be done with one plasmid encoding for both Cas and gRNA, which ensures co-expression, simplifying the process but requiring cloning in large plasmids for each gRNA and/or Cas protein. However transfecting Cas and gRNA on separate plasmids allows independent control but necessitates co-transfection, introducing additional complexities [122]. In contrast to pDNA, mRNA is directly translated upon delivery, bypassing the nuclear entry step. This method possibly enables faster edits. However, it suffers from lower stability and delivery limitations due to the size of the Cas mRNA [125]. Timing differences were for example observed in Cas9 expression maxima that were measured after 36 h [118] whereas expression maxima for eGFP or CayRFP were found to peak after 15 to 20 h [37]. A difference in mRNA length (approx. 1000 nt for eGFP and CayRFP and 4500 nt for Cas9) is known but which part of the expression kinetics this impacts in which way is unknown up to date. Further to be mentioned is the timescale of sgRNA whose efficiency is described with the whole CRISPR process and is therefore ultimately extended. Apart from the different timescales of the various processes, also the different stabilities of for example mRNA and sgRNA relevant for CRISPR systems need to be taken into account [118]. RNPs, on the other hand, are preassembled complexes consisting of the Cas protein and gRNA. This structure renders them immediately functional within the cellular environment, allowing for prompt and precise genome editing actions. Challenges here include the protein extraction [125] and the missing continued production of Cas and gRNA [126]. Further considerations should also be given to the possibility of mixing cargo and delivery methods, i.e., Cas pDNA and later transfected gRNA as mRNA, which could offer timed advantages, but also strain cells more with multiple transfection periods [124,127]. Selecting the optimal CRISPR delivery method is crucial for achieving efficient and accurate genome editing. The best choice of a specific cargo delivery strategy with regards to stability, control, and efficiency is still a matter of current research. Rational design approaches will have to take the delivery kinetics into account.

8. Summary and perspective

In this paper we reviewed the kinetics of LNP mediated delivery of RNA. Uptake, escape and RNA release of LNPs can be effectively modeled as a series of discrete stochastic transfer processes, wherein each step can be described by distinct rates. We discussed those rates that have been measured in isolated studies using advanced time resolved microscopy techniques. In particular, the time course of mRNA mediated reporter gene expression is well documented in single-cell time-lapse studies and found to be in full agreement with reaction kinetics of translation, GFP maturation and associated degradation rates of mRNA and protein. Kinetic modelling contributed a substantial progress in our mechanistic understanding and consequently predictive power. Quantification of underlying rates and timescales is the basis for systematic screening approaches that aim to improve transfection and transient expression at every level of the multistep process. Time courses determine AUCs and have tangible implications in clinical applications [128]. The kinetic model of protein expression is universal and hence the analytic expression is widely useful. For example, in the work of Sabnis et al [94] the level of secreted protein hEPO and IGG protein was measured over days showing a qualitatively similar asymmetric time course as described in our model albeit with different, protein specific, life-times. Also, the time courses of SARS CoV-2 spike protein after mRNA Covid vaccination should follow the predicted behavior although in different timescales [129,130]. For future mRNA-based therapies, that follow rational design strategies for combinatorial therapies, the delivery of multiple protein and RNAs will become important. We showed that consideration of timelines in codelivery of multiple species is potentially complex, not necessarily strictly synchronized and dependent on physical–chemical properties of the different nucleic acid components. Firstly, the molar packing efficiency in codelivery is an open problem. Secondly, very little is known about the fate of nucleic acids in the time window after endosomal escape and before measurable action, like GFP expression. We would like to call this time window the dark hour of transfection (see Fig. 1). Modern single molecule fluorescent techniques could bring light into mechanisms of mRNA release from remaining ionizable lipid, the intracellular transport and degradation processes and the details of codon-specific binding and processing via ribosomes. The challenge is the detection of rare events, since, only a small fraction of LNP particles and mRNA molecules are active, as well as the detection of correlations that could elicit the mode of action. To this end it will be crucial to develop novel fluorescent probes, that signal the state of the mRNA or the microenvironment as well as automated image analysis tools that detect correlations and rare events. In principle, combinatorial delivery based on RNA-LNPs could be extended to a larger number of different nucleic acid components. LNP formulations are compatible with nucleic acid molecules in general, including pDNA, mRNA, siRNA as well as sgRNA. Multiple synthetic nucleic acid molecules enable the execution of transiently expressed synthetic circuits and open the possibility of LNP based synthetic biology [58]. Regulation of mRNA life-time via micro-RNAs is a prominent motif in natural gene regulation, correspondingly complex synthetic gene manipulation via LNP mediated RNA delivery should be feasible. Moreover, RNAs that interfere with gene circuits at multiple anchor points will allow for enhanced, highly specific and even personalized combinatorial gene therapies. Kinetic modelling of LNP delivery and expression is a prerequisite for a reliable system-level prediction of gene expression response and will be a guiding tool for future precision engineering of therapeutic options.

Credit authorship contribution statement

Judith A. Müller: Conceptualization, Formal analysis, Writing – original draft, Writing – review & editing. **Nathalie Schäffler:** Visualization, Writing – original draft. **Thomas Kellerer:** Software, Writing – original draft. **Gerlinde Schwake:** Methodology, Supervision, Validation. **Thomas S. Ligon:** Software, Writing – original draft. **Joachim O. Rädler:** Conceptualization, Funding acquisition, Supervision, Writing – original draft, Writing – review & editing.

Declaration of competing interest

The authors declare that they have no known competing financial interests or personal relationships that could have appeared to influence the work reported in this paper.

Data availability

Data will be made available on request.

Acknowledgments

This work was funded by the Deutsche Forschungsgemeinschaft (DFG, German Research Foundation) – Project-ID 201269156 – SFB

1032-B01 as well as by the Federal Ministry of Education and Research (BMBF) and the Free State of Bavaria under the Excellence Strategy of the Federal Government and the Länder through the ONE MUNICH Project Munich Multiscale Biofabrication. Support by a grant from the Bayerische Forschungsstiftung is gratefully acknowledged. T.K. acknowledges funding through BMBF, Germany Projekt FKZ13N16300.

References

[1] H. Yin, R.L. Kanasty, A.A. Eltoukhy, A.J. Vegas, J.R. Dorkin, D.G. Anderson, Non-viral vectors for gene-based therapy, Nat Rev Genet 15 (2014) 541–555, https://doi.org/10.1038/nrg3763.
[2] P.R. Cullis, M.J. Hope, Lipid Nanoparticle Systems for Enabling Gene Therapies, Mol. Ther. 25 (2017) 1467–1475, https://doi.org/10.1016/j.ymthe.2017.03.013.
[3] A.N. Kuhn, T. Beißert, P. Simon, B. Vallazza, J. Buck, B.P. Davies, O. Tureci, U. Sahin, mRNA as a Versatile Tool for Exogenous Protein Expression, 12 (2012). Doi: 10.2174/156652312802762536.
[4] E. Kon, N. Ad-El, I. Hazan-Halevy, L. Stotsky-Oterin, D. Peer, Targeting cancer with mRNA–lipid nanoparticles: key considerations and future prospects, Nat Rev Clin Oncol (2023), https://doi.org/10.1038/s41571-023-00811-9.
[5] S. Kreiter, M. Diken, A. Selmi, Ö. Türeci, U. Sahin, Tumor vaccination using messenger RNA: prospects of a future therapy, Curr. Opin. Immunol. 23 (2011) 399–406, https://doi.org/10.1016/j.coi.2011.03.007.
[6] J.G. Rurik, I. Tombácz, A. Yadegari, P.O.M. Fernández, S.V. Shewale, L. Li, T. Kimura, O.Y. Soliman, T.E. Papp, Y.K. Tam, B.L. Mui, S.M. Albelda, E. Puré, C.H. June, H. Aghajanian, D. Weissman, H. Parhiz, J.A. Epstein, CAR T cells produced in vivo to treat cardiac injury, (2022).
[7] J.D. Finn, A.R. Smith, M.C. Patel, L. Shaw, M.R. Youniss, J. Van Heteren, T. Dirstine, C. Ciullo, R. Lescarbeau, J. Seitzer, R.R. Shah, A. Shah, D. Ling, J. Growe, M. Pink, E. Rohde, K.M. Wood, W.E. Salomon, W.F. Harrington, C. Dombrowski, W.R. Strapps, Y. Chang, D.V. Morrissey, A Single Administration of CRISPR/Cas9 Lipid Nanoparticles Achieves Robust and Persistent In Vivo Genome Editing, Cell Rep. 22 (2018) 2227–2235, https://doi.org/10.1016/j.celrep.2018.02.014.
[8] S.C. Semple, A. Akinc, J. Chen, A.P. Sandhu, B.L. Mui, C.K. Cho, D.W.Y. Sah, D. Stebbing, E.J. Crosley, E. Yaworski, I.M. Hafez, J.R. Dorkin, J. Qin, K. Lam, K. G. Rajeev, K.F. Wong, L.B. Jeffs, L. Nechev, M.L. Eisenhardt, M. Jayaraman, M. Kazem, M.A. Maier, M. Srinivasulu, M.J. Weinstein, Q. Chen, R. Alvarez, S. A. Barros, S. De, S.K. Klimuk, T. Borland, V. Kosovrasti, W.L. Cantley, Y.K. Tam, M. Manoharan, M.A. Ciufolini, M.A. Tracy, A. De Fougerolles, I. MacLachlan, P. R. Cullis, T.D. Madden, M.J. Hope, Rational design of cationic lipids for siRNA delivery, Nat Biotechnol 28 (2010) 172–176, https://doi.org/10.1038/nbt.1602.
[9] X. Hou, T. Zaks, R. Langer, Y. Dong, Lipid nanoparticles for mRNA delivery, Nat Rev Mater 6 (2021) 1078–1094, https://doi.org/10.1038/s41578-021-00358-0.
[10] A. Akinc, A. Zumbuehl, M. Goldberg, E.S. Leshchiner, V. Busini, N. Hossain, S. A. Bacallado, D.N. Nguyen, J. Fuller, R. Alvarez, A. Borodovsky, T. Borland, R. Constien, A. De Fougerolles, J.R. Dorkin, K. Narayanannair Jayaprakash, M. Jayaraman, M. John, V. Koteliansky, M. Manoharan, L. Nechev, J. Qin, T. Racie, D. Raitcheva, K.G. Rajeev, D.W.Y. Sah, J. Soutschek, I. Toudjarska, H.-P. Vornlocher, T.S. Zimmermann, R. Langer, D.G. Anderson, A combinatorial library of lipid-like materials for delivery of RNAi therapeutics, Nat Biotechnol 26 (2008) 561–569, https://doi.org/10.1038/nbt1402.
[11] A.K.K. Leung, I.M. Hafez, S. Baoukina, N.M. Belliveau, I.V. Zhigaltsev, E. Afshinmanesh, D.P. Tieleman, C.L. Hansen, M.J. Hope, P.R. Cullis, Lipid Nanoparticles Containing siRNA Synthesized by Microfluidic Mixing Exhibit an Electron-Dense Nanostructured Core, J. Phys. Chem. C 116 (2012) 18440–18450, https://doi.org/10.1021/jp303267y.
[12] M. Yanez Arteta, T. Kjellman, S. Bartesaghi, S. Wallin, X. Wu, A.J. Kvist, A. Dabkowska, N. Székely, A. Radulescu, J. Bergenholtz, L. Lindfors, Successful reprogramming of cellular protein production through mRNA delivered by functionalized lipid nanoparticles, Proc. Natl. Acad. Sci. U.S.A. 115 (2018), https://doi.org/10.1073/pnas.1720542115.
[13] M.A. Maier, M. Jayaraman, S. Matsuda, J. Liu, S. Barros, W. Querbes, Y.K. Tam, S. M. Ansell, V. Kumar, J. Qin, X. Zhang, Q. Wang, S. Panesar, R. Hutabarat, M. Carioto, J. Hettinger, P. Kandasamy, D. Butler, K.G. Rajeev, B. Pang, K. Charisse, K. Fitzgerald, B.L. Mui, X. Du, P. Cullis, T.D. Madden, M.J. Hope, M. Manoharan, A. Akinc, Biodegradable Lipids Enabling Rapidly Eliminated Lipid Nanoparticles for Systemic Delivery of RNAi Therapeutics, Mol. Ther. 21 (2013) 1570–1578, https://doi.org/10.1038/mt.2013.124.
[14] D. Adams, A. Gonzalez-Duarte, W.D. O'Riordan, C.-C. Yang, M. Ueda, A. V. Kristen, I. Tournev, H.H. Schmidt, T. Coelho, J.L. Berk, K.-P. Lin, G. Vita, S. Attarian, V. Planté-Bordeneuve, M.M. Mezei, J.M. Campistol, J. Buades, T. H. Brannagan, B.J. Kim, J. Oh, Y. Parman, Y. Sekijima, P.N. Hawkins, S. D. Solomon, M. Polydefkis, P.J. Dyck, P.J. Gandhi, S. Goyal, J. Chen, A.L. Strahs, S.V. Nochur, M.T. Sweetser, P.P. Garg, A.K. Vaishnaw, J.A. Gollob, O.B. Suhr, Patisiran, an RNAi Therapeutic, for Hereditary Transthyretin Amyloidosis, N Engl J Med 379 (2018) 11–21, https://doi.org/10.1056/NEJMoa1716153.
[15] Y. Dong, D.J. Siegwart, D.G. Anderson, Strategies, design, and chemistry in siRNA delivery systems, Adv. Drug Deliv. Rev. 144 (2019) 133–147, https://doi.org/10.1016/j.addr.2019.05.004.
[16] N. Pardi, S. Tuyishime, H. Muramatsu, K. Kariko, B.L. Mui, Y.K. Tam, T. D. Madden, M.J. Hope, D. Weissman, Expression kinetics of nucleoside-modified mRNA delivered in lipid nanoparticles to mice by various routes, J. Control. Release 217 (2015) 345–351, https://doi.org/10.1016/j.jconrel.2015.08.007.
[17] A.-T. Dinh, C. Pangarkar, T. Theofanous, S. Mitragotri, Understanding Intracellular Transport Processes Pertinent to Synthetic Gene Delivery via Stochastic Simulations and Sensitivity Analyses, Biophys. J. 92 (2007) 831–846, https://doi.org/10.1529/biophysj.106.095521.
[18] C. Leonhardt, G. Schwake, T.R. Stögbauer, S. Rappl, J.-T. Kuhr, T.S. Ligon, J. O. Rädler, Single-cell mRNA transfection studies: Delivery, kinetics and statistics by numbers, Nanomed.: Nanotechnol. Biol. Med. 10 (2014) 679–688, https://doi.org/10.1016/j.nano.2013.11.008.
[19] C.M. Varga, K. Hong, D.A. Lauffenburger, Quantitative Analysis of Synthetic Gene Delivery Vector Design Properties, Mol. Ther. 4 (2001) 438–446, https://doi.org/10.1006/mthe.2001.0475.
[20] H. Kamiya, H. Akita, H. Harashima, Pharmacokinetic and pharmacodynamic considerations in gene therapy, Drug Discov. Today 8 (2003) 990–996, https://doi.org/10.1016/S1359-6446(03)02889-7.
[21] T.S. Ligon, C. Leonhardt, J.O. Rädler, Multi-Level Kinetic Model of mRNA Delivery via Transfection of Lipoplexes, PLoS One 9 (2014) e107148.
[22] X. Zhang, V. Goel, G.J. Robbie, Pharmacokinetics of Patisiran, the First Approved RNA Interference Therapy in Patients With Hereditary Transthyretin-Mediated Amyloidosis, J. Clin. Pharma 60 (2020) 573–585, https://doi.org/10.1002/jcph.1553.
[23] C. Lorenz, M. Fotin-Mleczek, G. Roth, C. Becker, T.C. Dam, W.P.R. Verdurmen, R. Brock, J. Probst, T. Schlake, Protein expression from exogenous mRNA: Uptake by receptor-mediated endocytosis and trafficking via the lysosomal pathway, RNA Biol. 8 (2011) 627–636, https://doi.org/10.4161/rna.8.4.15394.
[24] B. Snijder, L. Pelkmans, Origins of regulated cell-to-cell variability, Nat Rev Mol Cell Biol 12 (2011) 119–125, https://doi.org/10.1038/nrm3044.
[25] S.J. Altschuler, L.F. Wu, Cellular Heterogeneity: Do Differences Make a Difference? Cell 141 (2010) 559–563, https://doi.org/10.1016/j.cell.2010.04.033.
[26] A. Murschhauser, P.J.F. Röttgermann, D. Woschée, M.F. Ober, Y. Yan, K. A. Dawson, J.O. Rädler, A high-throughput microscopy method for single-cell analysis of event-time correlations in nanoparticle-induced cell death, Commun Biol 2 (2019) 35, https://doi.org/10.1038/s42003-019-0282-0.
[27] L. Zheng, S.R. Bandara, Z. Tan, C. Leal, Lipid Nanoparticle topology regulates endosomal escape and delivery of RNA to the cytoplasm, PNAS 120 (2023) 10, https://doi.org/10.1073/pnas.2301067120.
[28] J.C.W. Locke, M.B. Elowitz, Using movies to analyse gene circuit dynamics in single cells, Nat Rev Microbiol 7 (2009) 383–392, https://doi.org/10.1038/nrmicro2056.
[29] Y. Shav-Tal, R.H. Singer, X. Darzacq, Imaging gene expression in single living cells, Nat Rev Mol Cell Biol 5 (2004) 855–862, https://doi.org/10.1038/nrm1494.
[30] R.Y. Tsien, THE GREEN FLUORESCENT PROTEIN, Annu. Rev. Biochem. 67 (1998) 509–544, https://doi.org/10.1146/annurev.biochem.67.1.509.
[31] R. Heim, R.Y. Tsien, Engineering green fluorescent protein for improved brightness, longer wavelengths and fluorescence resonance energy transfer, Curr. Biol. 6 (1996) 178–182, https://doi.org/10.1016/S0960-9822(02)00450-5.
[32] B.C. Campbell, E.M. Nabel, M.H. Murdock, C. Lao-Peregrin, P. Tsoulfas, M. G. Blackmore, F.S. Lee, C. Liston, H. Morishita, G.A. Petsko, mGreenLantern: a bright monomeric fluorescent protein with rapid expression and cell filling properties for neuronal imaging, Proc. Natl. Acad. Sci. U.S.A. 117 (2020) 30710–30721, https://doi.org/10.1073/pnas.2000942117.
[33] T.W.J. Gadella, L. Van Weeren, J. Stouthamer, M.A. Hink, A.H.G. Wolters, B.N. G. Giepmans, S. Aumonier, J. Dupuy, A. Royant, mScarlet3: a brilliant and fast-maturing red fluorescent protein, Nat Methods 20 (2023) 541–545, https://doi.org/10.1038/s41592-023-01809-y.
[34] J.L. Kirschman, S. Bhosle, D. Vanover, E.L. Blanchard, K.H. Loomis, C. Zurla, K. Murray, B.C. Lam, P.J. Santangelo, Characterizing exogenous mRNA delivery, trafficking, cytoplasmic release and RNA–protein correlations at the level of single cells, Nucleic Acids Res. 45 (2017) e113–e, https://doi.org/10.1093/nar/gkx290.
[35] K. Rombouts, K. Braeckmans, K. Remaut, Fluorescent Labeling of Plasmid DNA and mRNA: Gains and Losses of Current Labeling Strategies, Bioconjugate Chem. 27 (2016) 280–297, https://doi.org/10.1021/acs.bioconjchem.5b00579.
[36] A. Reiser, D. Woschée, S.M. Kempe, J.O. Rädler, Live-cell Imaging of Single-Cell Arrays (LISCA) - a Versatile Technique to Quantify Cellular Kinetics, J vis Exp (2021), https://doi.org/10.3791/62025.
[37] R. Krzysztoń, D. Woschée, A. Reiser, G. Schwake, H.H. Strey, J.O. Rädler, Single-cell kinetics of siRNA-mediated mRNA degradation, Nanomedicine: Nanotechnology, Biology and Medicine 21 (2019) 102077, https://doi.org/10.1016/j.nano.2019.102077.
[38] J.A. Müller, G. Schwake, J.O. Rädler, Einzelzellmikroskopie im Hochdurchsatz auf Mikrostrukturen, BIOspektrum 28 (2022) 723–725, https://doi.org/10.1007/s12268-022-1857-8.
[39] S. Hou, C. Johnson, K. Welsher, Real-Time 3D Single Particle Tracking: Towards Active Feedback Single Molecule Spectroscopy in Live Cells, Molecules 24 (2019) 2826, https://doi.org/10.3390/molecules24152826.
[40] B. Brandenburg, X. Zhuang, Virus trafficking – learning from single-virus tracking, Nat Rev Microbiol 5 (2007) 197–208, https://doi.org/10.1038/nrmicro1615.
[41] S.-L. Liu, Z.-G. Wang, H.-Y. Xie, A.-A. Liu, D.C. Lamb, D.-W. Pang, Single-Virus Tracking: From Imaging Methodologies to Virological Applications, Chem. Rev. 120 (2020) 1936–1979, https://doi.org/10.1021/acs.chemrev.9b00692.

[42] S. Patel, N. Ashwanikumar, E. Robinson, Y. Xia, C. Mihai, J.P. Griffith, S. Hou, A. A. Esposito, T. Ketova, K. Welsher, J.L. Joyal, Ö. Almarsson, G. Sahay, Naturally-occurring cholesterol analogues in lipid nanoparticles induce polymorphic shape and enhance intracellular delivery of mRNA, Nat Commun 11 (2020) 983, https://doi.org/10.1038/s41467-020-14527-2.
[43] A.J. Rozo, M.H. Cox, A. Devitt, A.J. Rothnie, A.D. Goddard, Biophysical analysis of lipidic nanoparticles, Methods 180 (2020) 45–55, https://doi.org/10.1016/j.ymeth.2020.05.001.
[44] N. Ruthardt, D.C. Lamb, C. Bräuchle, Single-particle Tracking as a Quantitative Microscopy-based Approach to Unravel Cell Entry Mechanisms of Viruses and Pharmaceutical Nanoparticles, Mol. Ther. 19 (2011) 1199–1211, https://doi.org/10.1038/mt.2011.102.
[45] N. Korabel, A. Taloni, G. Pagnini, V. Allan, S. Fedotov, T.A. Waigh, Ensemble heterogeneity mimics ageing for endosomal dynamics within eukaryotic cells, Sci Rep 13 (2023) 8789, https://doi.org/10.1038/s41598-023-35903-0.
[46] S. Ben Djemaa, K. Hervé-Aubert, L. Lajoie, A. Falanga, S. Galdiero, S. Nedellec, M. Soucé, E. Munnier, I. Chourpa, S. David, E. Allard-Vannier, gH625 Cell-Penetrating Peptide Promotes the Endosomal Escape of Nanovectorized siRNA in a Triple-Negative Breast Cancer Cell Line, Biomacromolecules 20 (2019) 3076–3086, https://doi.org/10.1021/acs.biomac.9b00637.
[47] Z. Cheng, G. Teo, S. Krueger, T.M. Rock, H.W. Koh, H. Choi, C. Vogel, Differential dynamics of the mammalian mRNA and protein expression response to misfolding stress, Mol. Syst. Biol. 12 (2016) 855, https://doi.org/10.15252/msb.20156423.
[48] L. Shang, P. Gao, H. Wang, R. Popescu, D. Gerthsen, G.U. Nienhaus, Protein-based fluorescent nanoparticles for super-resolution STED imaging of live cells, Chem. Sci. 8 (2017) 2396–2400, https://doi.org/10.1039/C6SC04664A.
[49] T. Andrian, R. Riera, S. Pujals, L. Albertazzi, Nanoscopy for endosomal escape quantification, Nanoscale Adv. 3 (2021) 10–23, https://doi.org/10.1039/D0NA00454E.
[50] M.Y. Berezin, S. Achilefu, Fluorescence Lifetime Measurements and Biological Imaging, Chem. Rev. 110 (2010) 2641–2684, https://doi.org/10.1021/cr900343z.
[51] T. Kellerer, J. Janusch, C. Freymüller, A. Rühm, R. Sroka, T. Hellerer, Comprehensive Investigation of Parameters Influencing Fluorescence Lifetime Imaging Microscopy in Frequency- and Time-Domain Illustrated by Phasor Plot Analysis, IJMS 23 (2022) 15885, https://doi.org/10.3390/ijms232415885.
[52] J.J. Rennick, C.J. Nowell, C.W. Pouton, A.P.R. Johnston, Resolving subcellular pH with a quantitative fluorescent lifetime biosensor, Nat Commun 13 (2022) 6023, https://doi.org/10.1038/s41467-022-33348-z.
[53] R. Datta, T.M. Heaster, J.T. Sharick, A.A. Gillette, M.C. Skala, Fluorescence lifetime imaging microscopy: fundamentals and advances in instrumentation, analysis, and applications, J. Biomed. Opt. 25 (2020) 1, https://doi.org/10.1117/1.JBO.25.7.071203.
[54] T.h. Förster, Zwischenmolekulare Energiewanderung und Fluoreszenz, Ann. Phys. 437 (1948) 55–75, https://doi.org/10.1002/andp.19484370105.
[55] T. Chen, B. He, J. Tao, Y. He, H. Deng, X. Wang, Y. Zheng, Application of Förster Resonance Energy Transfer (FRET) technique to elucidate intracellular and In Vivo biofate of nanomedicines, Adv. Drug Deliv. Rev. 143 (2019) 177–205, https://doi.org/10.1016/j.addr.2019.04.009.
[56] L. Loura, FRET in membrane biophysics: an overview, Front. Physio. 2 (2011), https://doi.org/10.3389/fphys.2011.00082.
[57] M. Ferizi, C. Leonhardt, C. Meggle, M.K. Aneja, C. Rudolph, C. Plank, J.O. Rädler, Stability analysis of chemically modified mRNA using micropattern-based single-cell arrays, Lab Chip 15 (2015) 3561–3571, https://doi.org/10.1039/C5LC00749F.
[58] T. Frei, F. Cella, F. Tedeschi, J. Gutiérrez, G.-B. Stan, M. Khammash, V. Siciliano, Characterization and mitigation of gene expression burden in mammalian cells, Nat Commun 11 (2020) 4641, https://doi.org/10.1038/s41467-020-18392-x.
[59] G. Sahay, D.Y. Alakhova, A.V. Kabanov, Endocytosis of nanomedicines, J. Control. Release 145 (2010) 182–195, https://doi.org/10.1016/j.jconrel.2010.01.036.
[60] J. Gilleron, W. Querbes, A. Zeigerer, A. Borodovsky, G. Marsico, U. Schubert, K. Manygoats, S. Seifert, C. Andree, M. Stöter, H. Epstein-Barash, L. Zhang, V. Koteliansky, K. Fitzgerald, E. Fava, M. Bickle, Y. Kalaidzidis, A. Akinc, M. Maier, M. Zerial, Image-based analysis of lipid nanoparticle–mediated siRNA delivery, intracellular trafficking and endosomal escape, Nat Biotechnol 31 (2013) 638–646, https://doi.org/10.1038/nbt.2612.
[61] D. Manzanares, V. Ceña, Endocytosis: The Nanoparticle and Submicron Nanocompounds Gateway into the Cell, Pharmaceutics 12 (2020) 371, https://doi.org/10.3390/pharmaceutics12040371.
[62] J.J. Rennick, A.P.R. Johnston, R.G. Parton, Key principles and methods for studying the endocytosis of biological and nanoparticle therapeutics, Nat. Nanotechnol. 16 (2021) 266–276, https://doi.org/10.1038/s41565-021-00858-8.
[63] J. Rejman, A. Bragonzi, M. Conese, Role of clathrin- and caveolae-mediated endocytosis in gene transfer mediated by lipo- and polyplexes, Mol. Ther. 12 (2005) 468–474, https://doi.org/10.1016/j.ymthe.2005.03.038.
[64] K. Von Gersdorff, N.N. Sanders, R. Vandenbroucke, S.C. De Smedt, E. Wagner, M. Ogris, The Internalization Route Resulting in Successful Gene Expression Depends on both Cell Line and Polyethylenimine Polyplex Type, Mol. Ther. 14 (2006) 745–753, https://doi.org/10.1016/j.ymthe.2006.07.006.
[65] S. Behzadi, V. Serpooshan, W. Tao, M.A. Hamaly, M.Y. Alkawareek, E.C. Dreaden, D. Brown, A.M. Alkilany, O.C. Farokhzad, M. Mahmoudi, Cellular uptake of nanoparticles: journey inside the cell, Chem. Soc. Rev. 46 (2017) 4218–4244, https://doi.org/10.1039/C6CS00636A.
[66] A. Akinc, W. Querbes, S. De, J. Qin, M. Frank-Kamenetsky, K.N. Jayaprakash, M. Jayaraman, K.G. Rajeev, W.L. Cantley, J.R. Dorkin, J.S. Butler, L. Qin, T. Racie, A. Sprague, E. Fava, A. Zeigerer, M.J. Hope, M. Zerial, D.W. Sah, K. Fitzgerald, M.A. Tracy, M. Manoharan, V. Koteliansky, A.D. Fougerolles, M. A. Maier, Targeted Delivery of RNAi Therapeutics With Endogenous and Exogenous Ligand-Based Mechanisms, Mol. Ther. 18 (2010) 1357–1364, https://doi.org/10.1038/mt.2010.85.
[67] K. Liu, R. Nilsson, E. Lázaro-Ibáñez, H. Duàn, T. Miliotis, M. Strimfors, M. Lerche, A.R. Salgado Ribeiro, J. Ulander, D. Lindén, A. Salvati, A. Sabirsh, Multiomics analysis of naturally efficacious lipid nanoparticle coronas reveals high-density lipoprotein is necessary for their function, Nat Commun 14 (2023) 4007, https://doi.org/10.1038/s41467-023-39768-9.
[68] N. Aliakbarinodehi, A. Gallud, M. Mapar, E. Wesén, S. Heydari, Y. Jing, G. Emilsson, K. Liu, A. Sabirsh, V.P. Zhdanov, L. Lindfors, E.K. Esbjörner, F. Höök, Interaction Kinetics of Individual mRNA-Containing Lipid Nanoparticles with an Endosomal Membrane Mimic: Dependence on pH, Protein Corona Formation, and Lipoprotein Depletion, ACS Nano 16 (2022) 20163–20173, https://doi.org/10.1021/acsnano.2c04829.
[69] L. Miao, J. Lin, Y. Huang, L. Li, D. Delcassian, Y. Ge, Y. Shi, D.G. Anderson, Synergistic lipid compositions for albumin receptor mediated delivery of mRNA to the liver, Nat Commun 11 (2020) 2424, https://doi.org/10.1038/s41467-020-16248-y.
[70] V. Francia, R.M. Schiffelers, P.R. Cullis, D. Witzigmann, The Biomolecular Corona of Lipid Nanoparticles for Gene Therapy, Bioconjugate Chem. 31 (2020) 2046–2059, https://doi.org/10.1021/acs.bioconjchem.0c00366.
[71] D. Zhu, H. Yan, Z. Zhou, J. Tang, X. Liu, R. Hartmann, W.J. Parak, N. Feliu, Y. Shen, Detailed investigation on how the protein corona modulates the physicochemical properties and gene delivery of polyethylenimine (PEI) polyplexes, Biomater. Sci. 6 (2018) 1800–1817, https://doi.org/10.1039/C8BM00128F.
[72] E. Álvarez-Benedicto, Z. Tian, S. Chatterjee, D. Orlando, M. Kim, E.D. Guerrero, X. Wang, D.J. Siegwart, Spleen SORT LNP Generated in situ CAR T Cells Extend Survival in a Mouse Model of Lymphoreplete B Cell Lymphoma, Angew Chem Int Ed 62 (2023) e202310395.
[73] I. Tombácz, D. Laczkó, H. Shahnawaz, H. Muramatsu, A. Natesan, A. Yadegari, T. E. Papp, M.-G. Alameh, V. Shuvaev, B.L. Mui, Y.K. Tam, V. Muzykantov, N. Pardi, D. Weissman, H. Parhiz, Highly efficient CD4+ T cell targeting and genetic recombination using engineered CD4+ cell-homing mRNA-LNPs, Mol. Ther. 29 (2021) 3293–3304, https://doi.org/10.1016/j.ymthe.2021.06.004.
[74] H. Parhiz, V.V. Shuvaev, N. Pardi, M. Khoshnejad, R.Y. Kiseleva, J.S. Brenner, T. Uhler, S. Tuyishime, B.L. Mui, Y.K. Tam, T.D. Madden, M.J. Hope, D. Weissman, V.R. Muzykantov, PECAM-1 directed re-targeting of exogenous mRNA providing two orders of magnitude enhancement of vascular delivery and expression in lungs independent of apolipoprotein E-mediated uptake, J. Control. Release 291 (2018) 106–115, https://doi.org/10.1016/j.jconrel.2018.10.015.
[75] A. Gallud, M.J. Munson, K. Liu, A. Idström, H.M.G. Barriga, S.R. Tabaei, N. Aliakbarinodehi, M. Ojansivu, Q. Lubart, J.J. Doutch, M.N. Holme, L. Evenäs, L. Lindfors, M.M. Stevens, A. Collén, A. Sabirsh, F. Höök, E.K. Esbjörner, Time evolution of PEG-shedding and serum protein coronation determines the cell uptake kinetics and delivery of lipid nanoparticle formulated mRNA, Biophysics (2021), https://doi.org/10.1101/2021.08.20.457104.
[76] J.E. Dahlman, K.J. Kauffman, Y. Xing, T.E. Shaw, F.F. Mir, C.C. Dlott, R. Langer, D.G. Anderson, E.T. Wang, Barcoded nanoparticles for high throughput in vivo discovery of targeted therapeutics, Proc. Natl. Acad. Sci. U.S.A. 114 (2017) 2060–2065, https://doi.org/10.1073/pnas.1620874114.
[77] M.J. Munson, G. O'Driscoll, A.M. Silva, E. Lázaro-Ibáñez, A. Gallud, J.T. Wilson, A. Collén, E.K. Esbjörner, A. Sabirsh, A high-throughput Galectin-9 imaging assay for quantifying nanoparticle uptake, endosomal escape and functional RNA delivery, Commun Biol 4 (2021) 211, https://doi.org/10.1038/s42003-021-01728-8.
[78] D.S. Dimitrov, Virus entry: molecular mechanisms and biomedical applications, Nat Rev Microbiol 2 (2004) 109–122, https://doi.org/10.1038/nrmicro817.
[79] P. Paramasivam, C. Franke, M. Stöter, A. Höijer, S. Bartesaghi, A. Sabirsh, L. Lindfors, M.Y. Arteta, A. Dahlén, A. Bak, S. Andersson, Y. Kalaidzidis, M. Bickle, M. Zerial, Endosomal escape of delivered mRNA from endosomal recycling tubules visualized at the nanoscale, J. Cell Biol. 221 (2022) e202110137.
[80] S.E.A. Gratton, P.A. Ropp, P.D. Pohlhaus, J.C. Luft, V.J. Madden, M.E. Napier, J. M. DeSimone, The effect of particle design on cellular internalization pathways, Proc. Natl. Acad. Sci. U.S.A. 105 (2008) 11613–11618, https://doi.org/10.1073/pnas.0801763105.
[81] J. Rejman, V. Oberle, I.S. Zuhorn, D. Hoekstra, Size-dependent internalization of particles via the pathways of clathrin- and caveolae-mediated endocytosis, Biochem. J 377 (2004) 159–169, https://doi.org/10.1042/bj20031253.
[82] H. Yuan, J. Li, G. Bao, S. Zhang, Variable Nanoparticle-Cell Adhesion Strength Regulates Cellular Uptake, Phys. Rev. Lett. 105 (2010) 138101, https://doi.org/10.1103/PhysRevLett.105.138101.
[83] S.K. Lai, K. Hida, C. Chen, J. Hanes, Characterization of the intracellular dynamics of a non-degradative pathway accessed by polymer nanoparticles, J. Control. Release 125 (2008) 107–111, https://doi.org/10.1016/j.jconrel.2007.10.015.
[84] K.J. Hassett, J. Higgins, A. Woods, B. Levy, Y. Xia, C.J. Hsiao, E. Acosta, Ö. Almarsson, M.J. Moore, L.A. Brito, Impact of lipid nanoparticle size on mRNA vaccine immunogenicity, J. Control. Release 335 (2021) 237–246, https://doi.org/10.1016/j.jconrel.2021.05.021.

[85] S. Cao, X. Liu, X. Li, C. Lin, W. Zhang, C.H. Tan, S. Liang, B. Luo, X. Xu, P.E. Saw, Shape Matters: Comprehensive Analysis of Star-Shaped Lipid Nanoparticles, Front. Pharmacol. 11 (2020) 539, https://doi.org/10.3389/fphar.2020.00539.

[86] A. Wittrup, A. Ai, X. Liu, P. Hamar, R. Trifonova, K. Charisse, M. Manoharan, T. Kirchhausen, J. Lieberman, Visualizing lipid-formulated siRNA release from endosomes and target gene knockdown, Nat Biotechnol 33 (2015) 870–876, https://doi.org/10.1038/nbt.3298.

[87] M.P. Dobay, A. Schmidt, E. Mendoza, T. Bein, J.O. Rädler, Cell Type Determines the Light-Induced Endosomal Escape Kinetics of Multifunctional Mesoporous Silica Nanoparticles, Nano Lett. 13 (2013) 1047–1052, https://doi.org/10.1021/nl304273u.

[88] E.J. Sayers, S.E. Peel, A. Schantz, R.M. England, M. Beano, S.M. Bates, A.S. Desai, S. Puri, M.B. Ashford, A.T. Jones, Endocytic Profiling of Cancer Cell Models Reveals Critical Factors Influencing LNP-Mediated mRNA Delivery and Protein Expression, Mol. Ther. 27 (2019) 1950–1962, https://doi.org/10.1016/j.ymthe.2019.07.018.

[89] S. Patel, N. Ashwanikumar, E. Robinson, A. DuRoss, C. Sun, K.E. Murphy-Benenato, C. Mihai, Ö. Almarsson, G. Sahay, Boosting Intracellular Delivery of Lipid Nanoparticle-Encapsulated mRNA, Nano Lett. 17 (2017) 5711–5718, https://doi.org/10.1021/acs.nanolett.7b02664.

[90] A. Parodi, C. Corbo, A. Cevenini, R. Molinaro, R. Palomba, L. Pandolfi, M. Agostini, F. Salvatore, E. Tasciotti, Enabling cytoplasmic delivery and organelle targeting by surface modification of nanocarriers, Nanomedicine 10 (2015) 1923–1940, https://doi.org/10.2217/nnm.15.39.

[91] I.M.S. Degors, C. Wang, Z.U. Rehman, I.S. Zuhorn, Carriers Break Barriers in Drug Delivery: Endocytosis and Endosomal Escape of Gene Delivery Vectors, Acc. Chem. Res. 52 (2019) 1750–1760, https://doi.org/10.1021/acs.accounts.9b00177.

[92] K.V. Kilchrist, S.C. Dimobi, M.A. Jackson, B.C. Evans, T.A. Werfel, E.A. Dailing, S. K. Bedingfield, I.B. Kelly, C.L. Duvall, Gal8 Visualization of Endosome Disruption Predicts Carrier-Mediated Biologic Drug Intracellular Bioavailability, ACS Nano (2019), https://doi.org/10.1021/acsnano.8b05482 acsnano.8b05482.

[93] M. Maugeri, M. Nawaz, A. Papadimitriou, A. Angerfors, A. Camponeschi, M. Na, M. Hölttä, P. Skantze, S. Johansson, M. Sundqvist, J. Lindquist, T. Kjellman, I.-L. Mårtensson, T. Jin, P. Sunnerhagen, S. Östman, L. Lindfors, H. Valadi, Linkage between endosomal escape of LNP-mRNA and loading into EVs for transport to other cells, Nat Commun 10 (2019) 4333, https://doi.org/10.1038/s41467-019-12275-6.

[94] S. Sabnis, E.S. Kumarasinghe, T. Salerno, C. Mihai, T. Ketova, J.J. Senn, A. Lynn, A. Bulychev, I. McFadyen, J. Chan, Ö. Almarsson, M.G. Stanton, K.E. Benenato, A Novel Amino Lipid Series for mRNA Delivery: Improved Endosomal Escape and Sustained Pharmacology and Safety in Non-human Primates, Mol. Ther. 26 (2018) 1509–1519, https://doi.org/10.1016/j.ymthe.2018.03.010.

[95] H. Zhang, J. Bussmann, F.H. Huhnke, J. Devoldere, A. Minnaert, W. Jiskoot, F. Serwane, J. Spatz, M. Röding, S.C. De Smedt, K. Braeckmans, K. Remaut, Together is Better: mRNA Co-Encapsulation in Lipoplexes is Required to Obtain Ratiometric Co-Delivery and Protein Expression on the Single Cell Level, Adv. Sci. 9 (2022) 2102072, https://doi.org/10.1002/advs.202102072.

[96] M. Schlich, R. Palomba, G. Costabile, S. Mizrahy, M. Pannuzzo, D. Peer, P. Decuzzi, Cytosolic delivery of nucleic acids: The case of ionizable lipid nanoparticles, Bioeng Transl Med 6 (2021), https://doi.org/10.1002/btm2.10213.

[97] J.O. Rädler, I. Koltover, T. Salditt, C.R. Safinya, Structure of DNA-Cationic Liposome Complexes: DNA Intercalation in Multilamellar Membranes in Distinct Interhelical Packing Regimes, Science 275 (1997) 810–814, https://doi.org/10.1126/science.275.5301.810.

[98] I. Koltover, T. Salditt, J.O. Rädler, C.R. Safinya, An Inverted Hexagonal Phase of Cationic Liposome-DNA Complexes Related to DNA Release and Delivery, Science 281 (1998) 78–81, https://doi.org/10.1126/science.281.5373.78.

[99] H.M.G. Barriga, O. Ces, R.V. Law, J.M. Seddon, N.J. Brooks, Engineering Swollen Cubosomes Using Cholesterol and Anionic Lipids, Langmuir 35 (2019) 16521–16527, https://doi.org/10.1021/acs.langmuir.9b02336.

[100] Z. Li, J. Carter, L. Santos, C. Webster, C.F. Van Der Walle, P. Li, S.E. Rogers, J. R. Lu, Acidification-Induced Structure Evolution of Lipid Nanoparticles Correlates with Their *In Vitro* Gene Transfections, ACS Nano 17 (2023) 979–990, https://doi.org/10.1021/acsnano.2c06213.

[101] H. Yu, A. Angelova, B. Angelov, B. Dyett, L. Matthews, Y. Zhang, M. El Mohamad, X. Cai, S. Valimehr, C.J. Drummond, J. Zhai, Real-Time pH-Dependent Self-Assembly of Ionisable Lipids from COVID-19 Vaccines and In Situ Nucleic Acid Complexation, Angew Chem Int Ed 62 (2023) e202304977.

[102] J. Philipp, A. Dabkowska, A. Reiser, K. Frank, R. Krzyszton, C. Brummer, B. Nickel, C.E. Blanchet, A. Sudarsan, M. Ibrahim, S. Johansson, P. Skantze, U. Skantze, S. Östman, M. Johansson, N. Henderson, K. Elvevold, B. Smedsrød, N. Schwierz, L. Lindfors, J.O. Rädler, pH-dependent structural transitions in cationic ionizable lipid mesophases are critical for lipid nanoparticle function, PNAS (2023).

[103] M.R. Hunter, L. Cui, B.T. Porebski, S. Pereira, S. Sonzini, U. Odunze, P. Iyer, O. Engkvist, R.L. Lloyd, S. Peel, A. Sabirsh, D. Ross-Thriepland, A.T. Jones, A. S. Desai, Understanding Intracellular Biology to Improve mRNA Delivery by Lipid Nanoparticles, Small, Methods (2023) 2201695, https://doi.org/10.1002/smtd.202201695.

[104] B. Li, X. Luo, B. Deng, J. Wang, D.W. McComb, Y. Shi, K.M.L. Gaensler, X. Tan, A. L. Dunn, B.A. Kerlin, Y. Dong, An Orthogonal Array Optimization of Lipid-like Nanoparticles for mRNA Delivery in Vivo, Nano Lett. 15 (2015) 8099–8107, https://doi.org/10.1021/acs.nanolett.5b03528.

[105] J. Zhang, R. Xue, W.-Y. Ong, P. Chen, Roles of Cholesterol in Vesicle Fusion and Motion, Biophys. J. 97 (2009) 1371–1380, https://doi.org/10.1016/j.bpj.2009.06.025.

[106] C.M. Bailey-Hytholt, G. Ulinski, J. Dugas, M. Haines, M. Lazebnik, P. Piepenhagen, I.E. Zarraga, A. Bandekar, Intracellular trafficking kinetics of nucleic acid escape from lipid nanoparticles via fluorescence imaging, CPB 24 (2023), https://doi.org/10.2174/1389201024666230403094238.

[107] J. Nguyen, F.C. Szoka, Nucleic Acid Delivery: The Missing Pieces of the Puzzle? Acc. Chem. Res. 45 (2012) 1153–1162, https://doi.org/10.1021/ar3000162.

[108] L.M.P. Vermeulen, T. Brans, S.K. Samal, P. Dubruel, J. Demeester, S.C. De Smedt, K. Remaut, K. Braeckmans, Endosomal Size and Membrane Leakiness Influence Proton Sponge-Based Rupture of Endosomal Vesicles, ACS Nano 12 (2018) 2332–2345, https://doi.org/10.1021/acsnano.7b07583.

[109] C. Peetla, S. Jin, J. Weimer, A. Elegbede, V. Labhasetwar, Biomechanics and Thermodynamics of Nanoparticle Interactions with Plasma and Endosomal Membrane Lipids in Cellular Uptake and Endosomal Escape, Langmuir 30 (2014) 7522–7532, https://doi.org/10.1021/la5015219.

[110] A. Reiser, D. Woschée, N. Mehrotra, R. Krzyszton, H.H. Strey, J.O. Rädler, Correlation of mRNA delivery timing and protein expression in lipid-based transfection, Integr. Biol. 11 (2019) 362–371, https://doi.org/10.1093/intbio/zyz030.

[111] R.L. Ball, K.A. Hajj, J. Vizelman, P. Bajaj, K.A. Whitehead, Lipid Nanoparticle Formulations for Enhanced Co-delivery of siRNA and mRNA, Nano Lett. 18 (2018) 3814–3822, https://doi.org/10.1021/acs.nanolett.8b01101.

[112] A.G. Hamilton, K.L. Swingle, R.A. Joseph, D. Mai, N. Gong, M.M. Billingsley, M. Alameh, D. Weissman, N.C. Sheppard, C.H. June, M.J. Mitchell, Ionizable Lipid Nanoparticles with Integrated Immune Checkpoint Inhibition for mRNA CAR T Cell Engineering, Adv Healthcare Materials (2023) 2301515, https://doi.org/10.1002/adhm.202301515.

[113] Y. Zhu, R. Shen, I. Vuong, R.A. Reynolds, M.J. Shears, Z.-C. Yao, Y. Hu, W.J. Cho, J. Kong, S.K. Reddy, S.C. Murphy, H.-Q. Mao, Multi-step screening of DNA/lipid nanoparticles and co-delivery with siRNA to enhance and prolong gene expression, Nat Commun 13 (2022) 4282, https://doi.org/10.1038/s41467-022-31993-y.

[114] C.L. Xu, M.Z.C. Ruan, V.B. Mahajan, S.H. Tsang, Viral Delivery Systems for CRISPR, Viruses 11 (2019) 28, https://doi.org/10.3390/v11010028.

[115] W.L. Chew, M. Tabebordbar, J.K.W. Cheng, P. Mali, E.Y. Wu, A.H.M. Ng, K. Zhu, A.J. Wagers, G.M. Church, A multifunctional AAV–CRISPR–Cas9 and its host response, Nat Methods 13 (2016) 868–874, https://doi.org/10.1038/nmeth.3993.

[116] G. Ronzitti, D.-A. Gross, F. Mingozzi, Human Immune Responses to Adeno-Associated Virus (AAV) Vectors, Front. Immunol. 11 (2020) 670, https://doi.org/10.3389/fimmu.2020.00670.

[117] T. Wei, Q. Cheng, Y.-L. Min, E.N. Olson, D.J. Siegwart, Systemic nanoparticle delivery of CRISPR-Cas9 ribonucleoproteins for effective tissue specific genome editing, Nat Commun 11 (2020) 3232, https://doi.org/10.1038/s41467-020-17029-3.

[118] J.B. Miller, S. Zhang, P. Kos, H. Xiong, K. Zhou, S.S. Perelman, H. Zhu, D.J. Siegwart, Non-viral CRISPR/Cas gene editing in vitro and in vivo enabled by synthetic nanoparticle co-delivery of Cas9 mRNA and sgRNA, (2018).

[119] J.P. Han, M. Kim, B.S. Choi, J.H. Lee, G.S. Lee, M. Jeong, Y. Lee, E.-A. Kim, H.-K. Oh, N. Go, H. Lee, K.J. Lee, U.G. Kim, J.Y. Lee, S. Kim, J. Chang, H. Lee, D. W. Song, S.C. Yeom, In vivo delivery of CRISPR-Cas9 using lipid nanoparticles enables antithrombin gene editing for sustainable hemophilia A and B therapy, Sci. Adv. 8 (2022) eabj6901, https://doi.org/10.1126/sciadv.abj6901.

[120] D. Rosenblum, A. Gutkin, R. Kedmi, S. Ramishetti, N. Veiga, A.M. Jacobi, M. S. Schubert, D. Friedmann-Morvinski, Z.R. Cohen, M.A. Behlke, J. Lieberman, D. Peer, CRISPR-Cas9 genome editing using targeted lipid nanoparticles for cancer therapy, Sci. Adv. 6 (2020) eabc9450, https://doi.org/10.1126/sciadv.abc9450.

[121] K. Lee, M. Conboy, H.M. Park, F. Jiang, H.J. Kim, M.A. Dewitt, V.A. Mackley, K. Chang, A. Rao, C. Skinner, T. Shobha, M. Mehdipour, H. Liu, W. Huang, F. Lan, N.L. Bray, S. Li, J.E. Corn, K. Kataoka, J.A. Doudna, I. Conboy, N. Murthy, Nanoparticle delivery of Cas9 ribonucleoprotein and donor DNA in vivo induces homology-directed DNA repair, Nat Biomed Eng 1 (2017) 889–901, https://doi.org/10.1038/s41551-017-0137-2.

[122] G. Schwake, S. Youssef, J.-T. Kuhr, S. Gude, M.P. David, E. Mendoza, E. Frey, J. O. RÃ¤dler, Predictive modeling of non-viral gene transfer, Biotechnol. Bioeng. (2010), https://doi.org/10.1002/bit.22604.

[123] J.R. Melamed, K.A. Hajj, N. Chaudhary, D. Strelkova, M.L. Arral, N. Pardi, M.-G. Alameh, J.B. Miller, L. Farbiak, D.J. Siegwart, D. Weissman, K.A. Whitehead, Lipid nanoparticle chemistry determines how nucleoside base modifications alter mRNA delivery, J. Control. Release 341 (2022) 206–214, https://doi.org/10.1016/j.jconrel.2021.11.022.

[124] C.A. Lino, J.C. Harper, J.P. Carney, J.A. Timlin, Delivering CRISPR: a review of the challenges and approaches, Drug Deliv. 25 (2018) 1234–1257, https://doi.org/10.1080/10717544.2018.1474964.

[125] L. Duan, K. Ouyang, X. Xu, L. Xu, C. Wen, X. Zhou, Z. Qin, Z. Xu, W. Sun, Y. Liang, Nanoparticle Delivery of CRISPR/Cas9 for Genome Editing, Front. Genet. 12 (2021) 673286, https://doi.org/10.3389/fgene.2021.673286.

[126] F.J. Khan, G. Yuen, J. Luo, Multiplexed CRISPR/Cas9 gene knockout with simple crRNA:tracrRNA co-transfection, Cell Biosci 9 (2019) 41, https://doi.org/10.1186/s13578-019-0304-0.

[127] L.L. Lesueur, L.M. Mir, F.M. André, Overcoming the Specific Toxicity of Large Plasmids Electrotransfer in Primary Cells In Vitro, Mol. Ther. Nucleic Acids 5 (2016) e291.

[128] U. Sahin, K. Karikó, Ö. Türeci, mRNA-based therapeutics — developing a new class of drugs, Nat Rev Drug Discov 13 (2014) 759–780, https://doi.org/10.1038/nrd4278.

[129] K.J. Hassett, K.E. Benenato, E. Jacquinet, A. Lee, A. Woods, O. Yuzhakov, S. Himansu, J. Deterling, B.M. Geilich, T. Ketova, C. Mihai, A. Lynn, I. McFadyen, M.J. Moore, J.J. Senn, M.G. Stanton, Ö. Almarsson, G. Ciaramella, L.A. Brito, Optimization of Lipid Nanoparticles for Intramuscular Administration of mRNA Vaccines, Mol. Ther. Nucleic Acids 15 (2019) 1–11, https://doi.org/10.1016/j.omtn.2019.01.013.

[130] C.-Y. Wu, C.-W. Cheng, C.-C. Kung, K.-S. Liao, J.-T. Jan, C. Ma, C.-H. Wong, Glycosite-deleted mRNA of SARS-CoV-2 spike protein as a broad-spectrum vaccine, Proc. Natl. Acad. Sci. U.S.A. 119 (2022), https://doi.org/10.1073/pnas.2119995119 e2119995119.

[131] P.C.N. Rensen, L.A.J.M. Sliedregt, M. Ferns, E. Kieviet, S.M.W. Van Rossenberg, S. H. Van Leeuwen, T.J.C. Van Berkel, E.A.L. Biessen, Determination of the Upper Size Limit for Uptake and Processing of Ligands by the Asialoglycoprotein Receptor on Hepatocytesin Vitro and in Vivo, J. Biol. Chem. 276 (2001) 37577–37584, https://doi.org/10.1074/jbc.M101786200.

Chapter 3

Microscopy

„What we observe is not nature itself, but nature exposed to our method of questioning.“

Werner Heisenberg

Fluorescence microscopy has long been a cornerstone in biological research, valued for its ability to produce clear, image-based insights [78]. However, the data we extract — and the conclusions we draw — are deeply influenced by the methods and tools at our disposal. Expanding fluorescence microscopy to address the specific challenges of vector-based gene therapy has proven to be a promising strategy, offering both refined techniques and new perspectives [79].

In this chapter, we outline the principles of **T**wo-**P**hoton **E**xcited **F**luorescence **M**icroscopy, the core technique employed in this work [80, 81, 82, 83]. We discuss the theoretical basis of fluorescence generation and highlight how TPEFM can be adapted to track rapidly moving particles with precision. This is demonstrated by the integration of TPEFM with an acoustofluidic trap, enabling detailed motion studies of particles and biological constructs such as Adenocarcinomic human alveolar basal epithelial cells (A549) [84] and **R**ed **B**lood **C**ells (RBC) under osmotic stress. The here presented analysis tools are the fundamentals for the newly developed tracking microscopy technique in **Chapter 6**.

Heisenberg's insight serves as a reminder that every method of observation reveals only a part of the whole, shaped by the lens through which we view it. By modifying the widely used TPEFM, we are able to shift our "lens" to explore the dynamics of biological particles with greater precision. Our ability to adapt and refine this technique, integrating it with complementary methods such as acoustofluidic trapping, enables us to address complex research questions in new and innovative ways. Thus, the observations we make, shaped by our evolving methods, provide deeper insights into the behavior of particles under various conditions, offering a more complete view of the biological systems we study.

3.1 Fluorescence Microscopy

Since its inception, microscopy has undergone remarkable advancements, demonstrating the principle of emergence as interdisciplinary thinking combines physics with biology to gain deeper insights into cellular processes. One notable milestone was the introduction of the fluorescence microscope between 1911 and 1913 by Otto Heimstaedt and Heinrich Lehmann, which marked a significant turning point in microscopy [78, 85]. The invention of the laser by Theodor Maiman in 1960 further pushes fluorescence-based microscopy into new territories, making it widely accessible [86].

Today, microscopy allows us to resolve structures well below the diffraction limit established by Ernst Abbe in 1873 [87], thanks to techniques like super-resolution microscopy [2]. Advancements have also made it possible to apply microscopy in clinical settings, such as for intraoperative cancer detection [88, 89].

The principle behind fluorescence microscopy is the absorption of a photon by a molecule, which under certain conditions leads to radiative emission in the form of a fluorescence photon. For this absorption process to occur, specific conditions must be met: the energy of the photon must match the energy gap between the ground state and the first excited state of the molecule, and the cross-section of the molecule must be large enough to facilitate absorption [90]. In **S**ingle-**P**hoton (1P) absorption, these requirements leading to fluorescence across the entire Gaussian caustic of the laser excitation [83]. This principle is used in most wide-field microscopy techniques, were the focus plane is recorded with a camera. This technique remains one of the most commonly employed methods in fluorescence microscopy. However, because fluorescence is generated at every point within the sample, it suffers from a loss of optical resolution caused by out-of-focus blur originating from different Z-planes [91].

The development of CLSM by Marvin Minsky in 1955 [92] enhanced resolution by reducing the detection volume, also known as the confocal volume [93]. While wide-field microscopy detects the entire sample with a camera, CLSM uses the confocal volume that must be scanned across the sample to generate an image, which results in slower frame rates. Nevertheless, the ability to produce resolution-limited images and optical sectioning justifies the trade-off in detection speed [91]. However, because CLSM still excites the entire sample with the laser, photobleaching remains a concern [91, 94]. This challenge led, in the early 1990s, to the development of a fundamental fluorescence technique classified under nonlinear microscopy [81, 95]: TPEFM [80, 81, 82]. With this technique certain advantages can be used for real-time live cell imaging and will be discussed in the following subsection.

3.1.1 Two-Photon Excited Fluorescence Microscopy (TPEFM)

The primary goal of this work was to perform long-term live-cell imaging experiments while having the flexibility to use different fluorophores as sensors for microenvironmental sensing [96]. This is why TPEFM was the technique of choice. It works with nearly every commonly available fluorophore as long as its two-photon cross-section is large enough, and it offers optical sectioning, live-cell imaging, and an easy-to-modify setup [83, 97]. This

made it possible to develop two new microscopy techniques for fast lifetime detection (see **Chapter 5**) and single particle tracking (refer to **Chapter 6**). The underlying process of TPEFM is the simultaneous absorption of two photons [97], resulting in a small excitation volume that is intrinsically confocal [80], reducing photodamage compared to CLSM and wide-field microscopy [98]. To achieve **T**wo-**P**hoton (2P) absorption, the photon density must be high, which is accomplished using ultrashort pulsed lasers and objectives with a high numerical aperture [80]. The excitation wavelengths typically fall in the **N**ear-**I**nfrared **R**ange (NIR), which allows for greater penetration depth in biological tissue due to the low absorption coefficient in this wavelength region, also known as optical window [99]. All of the named benefits of the TPEFM are schematically shown in **Figure 3.1**.

Due to the nonlinear process, the intensity is proportional to the square of the excitation power [100, 95]. This, together with sensitive photodetectors, allows for the use of a resonant galvo-scanner for image acquisition, where only eight laser pulses are required to detect enough fluorescence photons to create a good **S**ignal to **N**oise **R**atio (SNR) and thus an image contrast. This enables imaging of moving samples at video-rate ($\geq$ 25 fps).

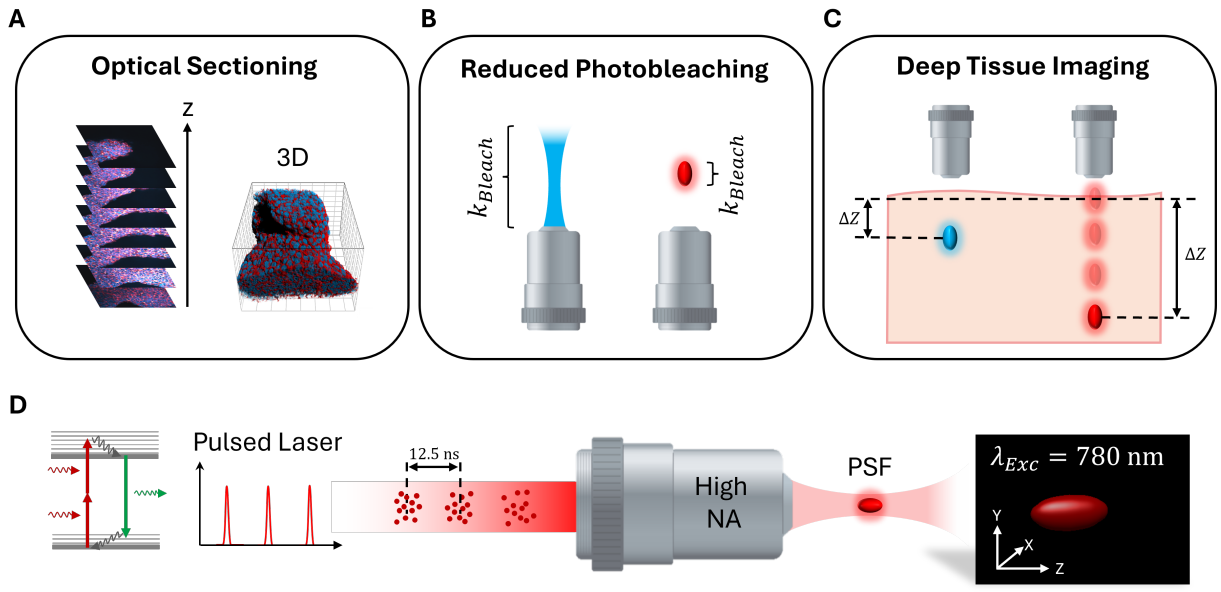

Figure 3.1: The Advantages of TPEFM: With TPEFM the 3D illustration is possible because of the optical sectioning **(A)**. Due to the intrinsical confocallity the photobleaching is reduced compared to other techniques like shown in **(B)**. By using wavelengths in the NIR the penetration depth in biological tissue is much higher than for wavelengths in the visible range like it is used in CLSM or wide-field microscopy (**C**). The requirements for a 2P process is the use of ultrashort pulsed laser and objectives with high numerical apertures as shown in **(D)**.

This capability opens up a wide range of analysis methods for fast-moving particles, including feedback-based tracking methods (see **Chapter 6**). For instance, by recording images at a high frame rate, 3D reconstructions (**Figure 3.1 - A**) of the sample or fast-moving processes can be captured and analyzed (**B**). These images can then be used to

extract various changes over time. We demonstrated this on an acoustofluidic microchannel capable of trapping cells or particles in a **S**pherical **M**icro**c**hamber (SMC) [101]. With this trap, the movement of particles, measured by **M**ean **S**quared **D**isplacement (MSD), as well as morphological changes over time, were analyzed like illustrated in **Figure 3.2 - C** [102, 103]. The setup used here is based on a modified Nikon Ti2 microscope equipped with various 3D-printed components and mechanical mounts, making it suitable for most nonlinear imaging techniques, such as **S**econd **H**armonic **G**eneration (SHG) [104], **T**hird **H**armonic **G**eneration (THG) [105], **S**um-**F**requency **G**eneration (SFG) [106], FLIM [107, 108], or **C**oherent **A**nti-Stokes **R**aman **S**cattering (CARS) [109, 110]. The setup consists of four spectrally separated detection channels and a resonant galvo-scanner, enabling video-rate time-lapse measurements (see **Appendix C**).

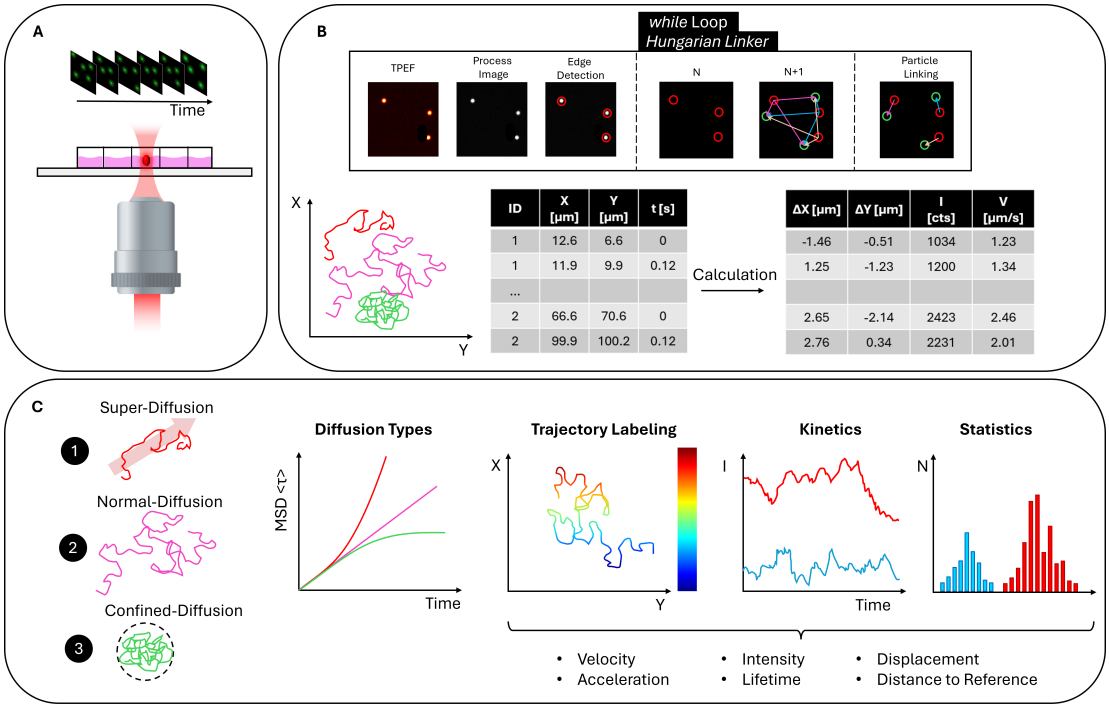

Figure 3.2: Analyzing Methods for Two-Photon Time-Lapse Datasets: Imaging moving particles with a TPEFM produces a series of high-resolution frames over time (**A**). These images are subsequently processed as illustrated in (**B**): the raw data from the TPEFM are analyzed using techniques such as Hough-Transformation to detect shapes, including circles. A Hungarian algorithm is then applied to link particles between consecutive frames (e.g. image N and image N+1), predicting their trajectories. This information is used to extract various parameters, such as position, intensity, speed, and lifetime. These parameters enable the calculation of diffusion types and the visualization of results in diverse representation plots (**C**). Furthermore, all calculations can be extended to three-dimensional datasets.

3.2 Two-Photon microscopy and analysis for diffusing particles

Authors	**Thomas Kellerer**, Bettina Sailer, Patrick Byers, Rune Barnkob, Oliver Hayden and Thomas Hellerer
Title	*Two-photon microscopy of acoustofluidic trapping for highly sensitive cell analysis*
Journal	Lab on a Chip (IF: 6.1 - 2024)
DOI	`https://doi.org/10.1039/d4lc00144c`

We utilized an acoustofluidic trap to develop advanced analysis tools capable of detecting single-particle movements and temporal changes, which were later applied to proof of principle measurements of LNP. This approach allowed us to extract substantial data from live-cell timelapse experiments, as demonstrated in **Figure 3.2**. By optimizing our setup, we achieved imaging at frame rates of up to 31 fps with a resolution of 515 x 512 pixels.

Advanced image processing techniques, such as the Hough transformation, enabled the detection of spherical particles by determining their diameters and center positions [111, 112]. These positions were subsequently linked across frames using a Hungarian algorithm, generating trajectories for individual particles [113]. The imaging properties—including pixel size and frame rate—facilitated a detailed analysis of particle trajectories in terms of speed, displacement, brightness, size, and other parameters. These measurements were used to calculate the MSD, verifying the type of motion exhibited by the particles. In the case of the acoustofluidic trap a confined diffusion due to the acoustic radiation force were clearly observed.

This framework served as the foundation for the XY-Tracking of our expanded technique, SEMPA-Track, which enables also three-dimensional tracking of LNP. In addition to foundational experiments, which characterized the SMC and demonstrated the advantages of TPEFM, we investigated osmotic shock effects on A549 cells and RBC. While LNP were observed to swell due to the proton sponge effect [45], we further explored osmotic processes and highlighted their rapid and significant impact on biological samples. The video-rate imaging capability's are shown on 1 µm small fluorescent beads that undergo an acoustic streaming effect

The publication "*Two-photon microscopy of acoustofluidic trapping for highly sensitive cell analysis*" [19] represents the advantages and capabilities of the TPEFM. The presented algorithms and data representations are further used for the new SPT method called SEMPA-Track (**Chapter 6**).

3.2.1 Contribution

This publication represents a shared first authorship between Thomas Kellerer and Bettina Sailer. Mrs. Sailer developed the acoustofluidic trap, while Thomas Kellerer was responsible for the experimental design, optical setup, and integration of the acoustofluidic chip with the two-photon microscope. This was done with various 3D-prints and custom made mechanic mounts. He also handled the cell culture and sample preparation, ensuring optimal experimental conditions.

Thomas Kellerer extracted results, such as MSD traces and osmosis experiments, from raw data through various digital image processing steps. The algorithms and calculations for these analyses were developed in MATLAB, utilizing additional packages from ImageJ. He further analyzed the diffusion behavior and interpreted the biological implications of size changes under osmotic stress.

Additionally, Thomas Kellerer designed the experimental workflow, including the synchronization of all required electronic and optical components, to enable precise characterization measurements in 2D and 3D. The manuscript was collaboratively written by Thomas Kellerer, Thomas Hellerer, and Bettina Sailer.

Thomas Kellerer also leaded and managed the project between the Munich university of applied sciences and the TranslaTUM.

Lab on a Chip

PAPER

View Article Online
View Journal | View Issue

Cite this: *Lab Chip*, 2024, **24**, 3456

Two-photon microscopy of acoustofluidic trapping for highly sensitive cell analysis

Thomas Kellerer, †[a] Bettina Sailer,†[b] Patrick Byers,[a] Rune Barnkob,[c] Oliver Hayden[b] and Thomas Hellerer *[a]

Received 14th February 2024,
Accepted 7th May 2024

DOI: 10.1039/d4lc00144c

rsc.li/loc

We combine two-photon-excited fluorescence microscopy and acoustofluidic trapping in a spherical microchamber to *in vitro* study cells and cell clusters three-dimensionally close to *in vivo* conditions. The two-photon microscopy provides the in-depth 3D analysis of the spherical microchamber dimensions as well as the positions of trapped samples therein with high spatial precision and high temporal resolution enabling even tracking of the fast moving particles. Furthermore, optical sectioning allows to gather information of individual cells in trapped cell clusters inside the chamber. We demonstrate real-time monitoring of osmosis in A549 lung cells and red blood cells as one possible biomedical application. The observed osmosis reduced the cell membrane diameter by approximately 4 μm in the A549 cells and by approximately 2 μm in the red blood cells. Our approach provides an important optical tool for future investigations of cell functions and cell–cell interactions avoiding wall-contact inside an acoustofluidic device.

1 Introduction

Many patients suffer from acute chronic inflammation, which can lead to cancer, autoimmunity, or cardiovascular diseases.[1] Understanding the influence of the immune system on different etiologies is important for future personalization of therapies. However, as discussed by Chattopadhyay *et al.*,[2] most cell functional analysis methods are performed on a single-cell level or in 2D with a limited spatiotemporal resolution for the 3D. Today, we have many ways for preclinical research, but only some standardizable cell function methods are available for clinical routine diagnostics.[3] Amongst other reasons, most cell function methods require a large amount of patient samples for, *e.g.*, fluorescence flow cytometry, which is rarely the case.[4,5] In particular, the complex interactions of cells, such as the tumor microenvironment, are a significant challenge for standardized diagnostic measurements and the development of personalized therapies. The only functional analysis method in 3D accepted by regulatory authorities is animal testing for pharma studies with limited translational value.[6] Most recently, organoid or tumoroid analysis in 3D using non-standardizable Matrigel as a preferred matrix has been of general interest. Still, all these methods require a time-to-result over even weeks, which is inappropriate for clinical diagnostics. Rapid time-to-result methods are very important as in case of acute inflammation, it can lead to sepsis in the worst case. In the case of chronic inflammation, a long time-to-result can lead to tissue destruction which causes the previously mentioned diseases.[7]

A promising field for an *in vitro* cell analysis method that works under near *in vivo* conditions is the combination of microfluidics and acoustics, often referred to as acoustofluidics. This combination of techniques offers touch-free cell manipulation in 3D, fast time-to-result, and a high potential for standardization with a minimum amount of cells. The field of microfluidics allows the investigation of cell suspensions in small volumes and within a very short time.[8] The acoustic part of the technology permits the purely mechanical manipulation of cells and particles in an acoustic pressure field induced by ultrasonic piezo-actuation of microfluidic systems. The theoretical and practical working principle of using acoustofluidics for particle analysis has been published for over a decade. However, previous works in acoustofluidics have been focused on particle separation and sorting of cells in mainly rectangular or semi-rectangular cross-sectional microfluidic channels.[9,10] Less work investigated acoustics for cell aggregation with a high degree of control in a microfluidic flow chamber. Previous work used chambers similar to petri dishes.[11,12] The presented acoustofluidics method is an *in vitro* cell analysis prototype

[a] *Multiphoton Imaging Lab, Munich University of Applied Sciences, 80335 Munich, Germany. E-mail: thomas.hellerer@hm.edu*
[b] *Heinz-Nixdorf-Chair of Biomedical Electronics, School of Computation, Information and Technology, Technical University of Munich, TranslaTUM, 81675 Munich, Germany*
[c] *Microfluidics Solutions, 00154 Rome, Italy*
† These authors contributed equally to this work.

working close to *in vivo* perfusion conditions using an acoustic trap in a spherical microchamber (SMC). The SMC is a tool for fast cell function diagnostics and is not limited to fluorescence microscopy, but is also suitable for label-free microscopy such as brightfield or phase contrast microscopy. The particles and cells in the SMC are pushed into the cavity center due to the acoustic radiation force. The second effect generated in the pressure field is acoustic streaming, which acts on suspended particles and cells *via* the viscous drag force. Sailer *et al.* have already introduced the fundamental verification of the SMC in trapping particles/cells and a detailed overview of the platform.[13,14] The SMC allows efficient focusing, trapping, and cell testing over any time range from seconds to weeks with complete spatiotemporal control for even a few cells to small aggregates (10–100 cells) without any wall contact for improved analysis of cell functions and cell–cell interaction. The visual sample analysis is generally performed using bright-field or confocal microscopy.[10,15–17] Furthermore, Santos *et al.*[18] presented an acoustofluidic device in combination with Raman spectroscopy. However, the Raman method worked only well for particles with a diameter larger than 15 μm in their case because smaller particles were liable to microstreaming effects. On the other hand, it can be expected that the Raman signal will vanish for very small particles as the effect has orders of magnitudes lower cross sections compared to fluorescence.[19] Therefore, the visualization with label-free Raman is challenging for high temporal resolution of complex cell–cell interactions.

A promising method to study the acoustofluidic chamber in its entirety is two-photon-excited fluorescence microscopy (TPEFM).[20–22] The advantage of TPEFM is the infrared-based excitation that allows for deep penetration depths in biological samples and chamber dimensions due to the wavelength-dependent absorption and scattering coefficients.[23] Since the excitation volume is severely limited by the two-photon absorption cross-section,[24] the technique exhibits an intrinsic confocality, which allows optical sectioning of the sample.[20] Today's rapid technical development provides very precise and sensitive actuators and detectors, enabling the imaging of various processes by video rate and allowing very low fluorescent structures to be detected sufficiently well. The two-photon fluorescence excitation is suitable for analyzing bioaffinity assays with high sensitivity and dynamic range.[25] Here, TPEFM was employed to resolve biological structures at the diffraction-limit in 3D, to track particles diffusing inside the acoustic trap, and to determine spatial dimensions of the SMC, cell membranes and of cell nuclei. The TPEFM method thus delivers all required spatial as well as temporal information over an extended time span of an acoustofluidic device to assess the setup for clinical utilization.

This article presents the combination of two-photon-excited fluorescence microscopy with acoustic trapping in a spherical microchamber to verify the acoustofluidic functionalities. Its capability to analyze cell functions and cell–cell interactions is demonstrated by studying osmosis on red blood cells (RBC) and lung cells (A549) as one possible biological example.

2 Results

2.1 Why TPEFM

While several fluorescence-based microscopy techniques are capable of achieving 3D images with high spatial and temporal resolution, TPEFM stands out in comparison to others such as confocal laser scanning microscopy (CLSM)[26] and single plane illumination microscopy (SPIM).[27,28]

CLSM has traditionally been considered the gold standard for fluorescence-based experiments requiring 3D information or high resolution. By incorporating a point detector in place of a camera and utilizing dual pinhole apertures – one in the detection and one in the illumination paths, along with a galvo–galvo scanner system – this microscopy type allows the recording of 3D images through restricted detection areas enabled by the pinholes.[29] However, there are substantial reasons TPEFM is preferred for observing biological processes in acoustofluidic devices.

Multiphoton microscopy inherently provides optical sectioning since signal generation is confined exclusively to the objective's focal area, which occupies a volume of less than one femtoliter (1 μm^3).[21,30] Within this region, the density of the excitation light is high enough to initiate the nonlinear signal generation process, thereby effectively eliminating signals from out-of-focus areas without the necessity for pinholes.[21,29,31,32] This results in the creation of an intrinsic confocal volume. Importantly, regions outside the high photon density focus are spared from potential damage since multiphoton excitation does not occur, contrasting with confocal microscopy, where the entire laser path can introduce phototoxic effects.[29] In addition to preserving the sample, two-photon imaging reduces the likelihood of photo-bleaching, which is particularly advantageous for prolonged imaging sessions. Furthermore, using longer wavelengths, which fall within the tissue optical window of the near-infrared spectrum, leads to improved tissue penetration depth.[23]

SPIM stands out for its high speed volumetric scans and low phototoxic effects, ideal for live imaging and dynamic studies. It employs a light sheet that excites a sample in a single plane, captured by an objective placed orthogonal to the excitation, and a fast camera system. With this geometry and technique, fast processes like forming the trapped particles inside the SMC can be observed. However, the integration of SPIM with acoustofluidic technology presents particular challenges due to the specific geometrical arrangement required for excitation and detection. While single-objective light sheet setups[33] have been developed to address such hurdles, they typically involve more complex systems with multiple galvanometric scanners and objectives, adding to the experimental complexity compared to TPEFM setups. Furthermore, conventional SPIM techniques use single-photon excitation, which can suffer from blurred images in samples that scatter light or are thick. Optical

clearing may be required to improve image quality, further complicating the experimental process. Yet, the field has seen promising progress with new SPIM techniques that employ two-photon excitation, simple setups reducing scattering issues for imaging. In this way, the potential for detailed biological investigations can be extended. Typically, acoustofluidic traps are used with microscopy methods such as brightfield or phase contrast microscopy. Although these techniques allow for rapid imaging of cluster formation, they often fall short of providing adequate resolution.

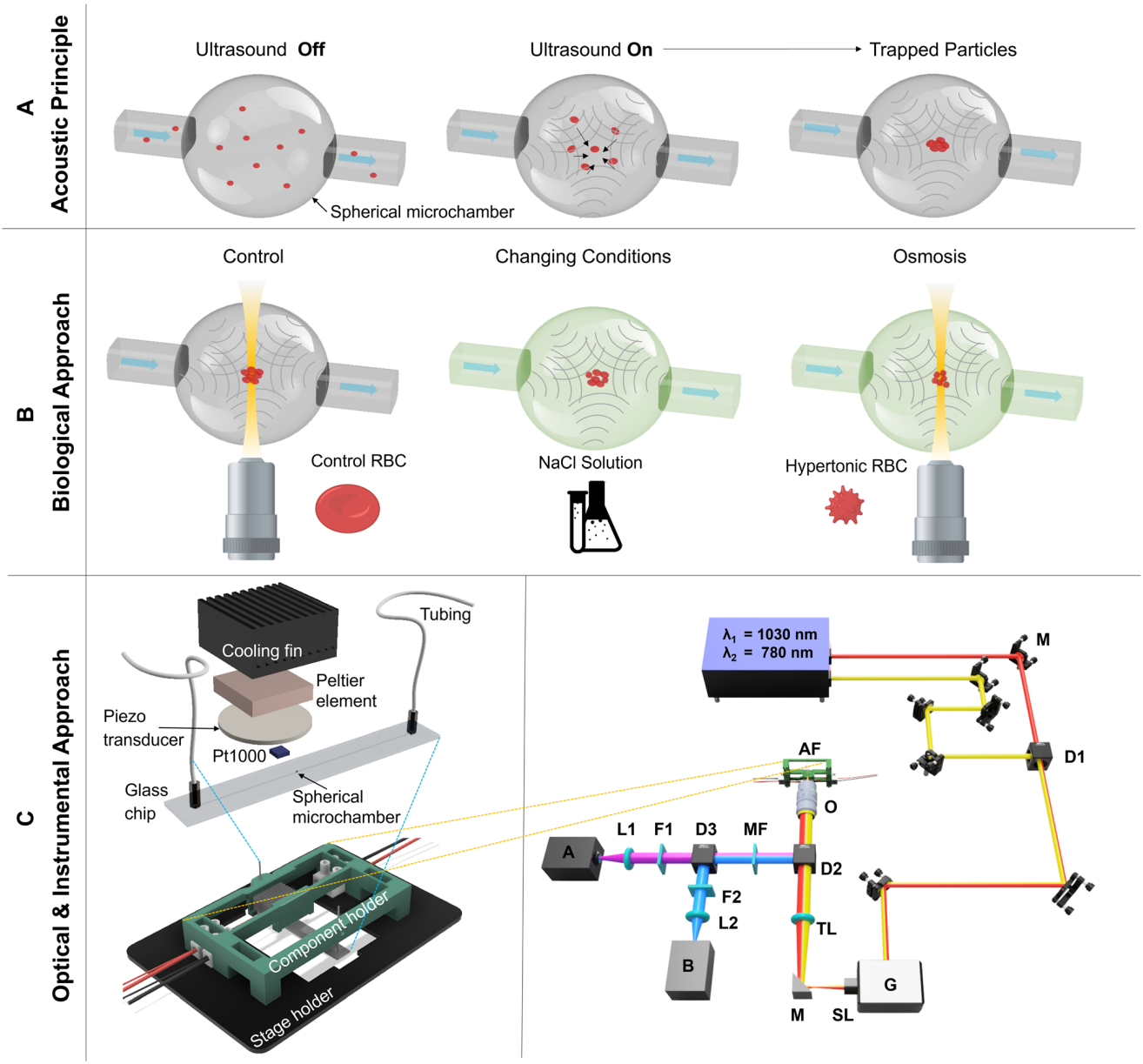

Fig. 1 Concept and working principle of acoustofluidic platform technology and two-photon-excited fluorescence microscopy. A) The schematic shows the working principle for acoustophoretic trapping of particles in a spherical microchamber (SMC). The particles are homogeneously distributed in the SMC before the onset of the ultrasound. Directly after inducing an acoustic pressure field in the SMC (ultrasound on), the particles (acoustically hard material) start to migrate to areas of low pressure p = 0 due to the acoustic radiation force. In the presented SMC, the particles are moved into the center of the spherical cavity. B) Schematic of the biological approach using osmosis on red blood cells (RBC) in the SMC with visual analysis under the two-photon-excited fluorescence microscopy. C) The drawing of the acoustofluidic platform technology is shown on the left side, which includes the stage holder for the microscope and the component holder for the acoustic components. The acoustofluidic prototype consists of a glass chip with tubings, a piezo transducer for the acoustic actuation, and a PT1000 temperature sensor, Peltier element, and a cooling fin for the temperature control. A detailed schematic of the two-photon-excited fluorescence microscopy is shown on the right side. The laser-scanning approach is accomplished with a resonant-galvo scanner **G** working with 8 kHz and a laser source offering two wavelengths at λ_1 = 1030 nm and λ_2 = 780 nm. With two photomultiplier tubes (PMT) **A** and **B** as well as different filters **F** and dichroic mirrors **D** the generated fluorescence is separated from the excitation and detected. The acoustofluidic setup **AF** is mounted with different 3D printed parts above the used microscopy objective **O**.

2.2 Merging of techniques

For the first time to our knowledge, an acoustofluidic trap is imaged with multiphoton microscopy enabling the application of profound analysis to the workings of the trap and demonstrating its suitability for studying cell functions and cell–cell interactions. The main advantage of our approach is the 3D-sectioning capability of the microscopy technique in conjunction with its high spatial and temporal resolution. Quantitative analyses of trajectories as well as of small changes in size of living cells, namely red blood cells (RBC) and human lung cells (A549), after osmotic shock, are carried out. The concept and working principle of the acoustofluidic platform technology in combination with two-photon-excited fluorescence microscopy are visualized in Fig. 1.

For the merging of the acoustofluidic trap with the multiphoton microscope, the former was adapted with 3D-printing parts to fit into the home-built optical setup based on a commercial microscope stand which is equipped with a resonant-galvo scanner and a piezo-driven objective for laser-scanning the sample in two lateral and one axial directions. A detailed description of the setup, as shown in Fig. 1 – C (right side), is given in section 5.1.

2.2.1 Optical sectioning allows 3D-reconstruction of the SMC. As mentioned in the foregone sections one of the main advantages of the TPEFM is the optical section potential.

To illustrate these capabilities, the SMC was filled with a few 10 μm-sized trapped particles suspended in fluorescein-dextran solution. Subsequently, a *z*-stack of multiphoton *xy*-images was acquired to reconstruct this ensemble in 3D shown in Fig. 2. The solution and particles were recorded with different detection channels, spectrally separated by a dichroic mirror and appropriate bandpass filters (see 5.1). Quantitative analysis reveals the spatial dimensions of the SMC to be $x = (547 \pm 9)$ μm, $y = (540 \pm 9)$ μm, and $z = (586 \pm 9)$ μm as compared to the manufacturer's specified size of 550 μm in all dimensions. The position of one trapped particle closest to the SMC center is determined to $x = (257 \pm 3)$ μm, $y = (279 \pm 3)$ μm, and $z = (318 \pm 3)$ μm

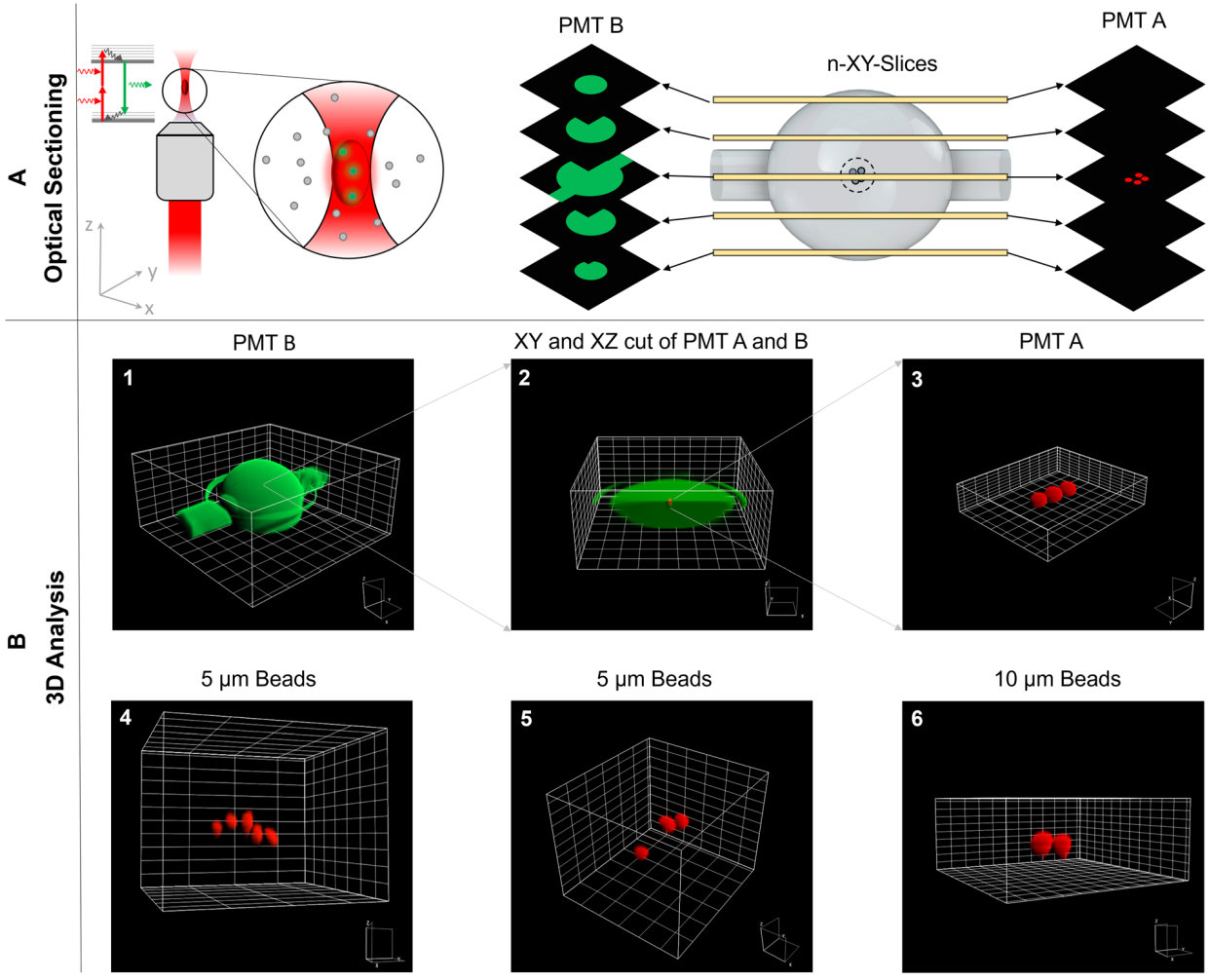

Fig. 2 Three-dimensional particle analysis *via* the TPEFM. The schematic of the laser beam in the TPEFM and the optical sectioning in the SMC along the *z*-direction are presented in A). The detailed 3D analysis of the SMC by optically cutting through the cavity is demonstrated in B) 1–3. In images 4–6 3D images of beads with two different sizes were presented.

which is only slightly off-center by 6.42%, 4.78%, and 7.86% in the *x*-, *y*-, and *z*-direction, respectively.

It was not clear from the outset that the refraction occurring at the glass-solution interface of the SMC would not interfere with aberration-free high resolution imaging. However, the quantitative analysis suggests that minor aberrations do not alter the SMC's and individual particles' round shapes nor influence the magnification factor since the imaged shapes and sizes are determined correctly. Only a visible circumference surrounds the SMC in the vertical center plane, which is undoubtedly classified as a measurement artifact. Furthermore, the area in which imaging takes place is always the central zone. Consequently, the incoming wavefronts pass through this central sector of the SMC, a region where the spherically symmetrical shape leads to negligible refraction effects on the wavefronts. This minimal refraction preserves the accuracy of the imaging process. In cases where an attempt is made to image the entire SMC, aberrations can occur that affect the absolute measurement accuracy. To address these issues and increase

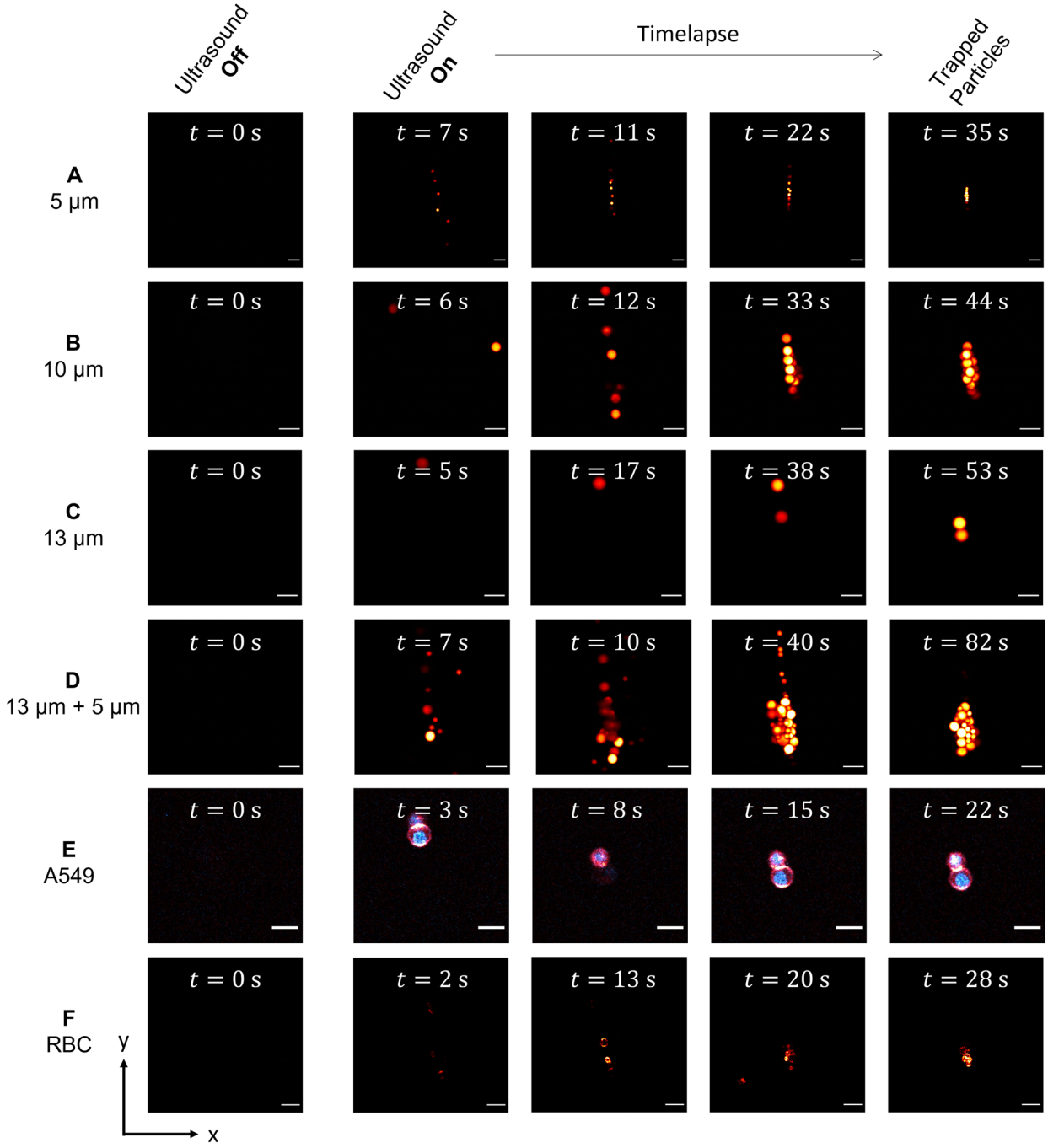

Fig. 3 Acoustic particle trapping under the two-photon-excited fluorescence microscope. From A–D different particle sizes ranging from A) 5 μm, B) 10 μm, C) 13 μm and a mixture of D) 13 μm and 5 μm are displayed, in E) the time series of A549 cells and in F) of RBC cells are shown. Scale bar: 20 μm.

measurement accuracy, additional investigations, including further empirical measurements or advanced optical simulations, should be performed.

2.2.2 Observation of transient acoustofluidic trapping. The imaging technique's high temporal resolution allows the observation of the suspended particle motion after turning on the piezo actuators to set up an acoustic field inside the SMC. The acoustic resonance in the SMC is built almost instantaneously, whereafter the suspended particles are subject to the acoustic radiation force migrating them to the trap's center. Fig. 3 shows examples of acoustophoretic movement of different-sized microparticles and cell types. For multiphoton imaging, a time series of only center *xy*-planes is acquired starting with the switch-on of the piezo actuators. The frame rate of the 1024 × 1024 pixel sized images was 16 fps. At the beginning the particles are out-of-focus and, therefore, not visible. Then, step by step, the particles move to the center and into the focal plane of the microscope, where they accumulate homogeneously (see columns 3 and 4). The time it takes to form the trapped clusters depends on size, density, and shape of the particles/cells in the center of the SMC ($z \approx 290$ μm). Therefore, the time scale is different for all rows shown in Fig. 3. The universal applicability of the trap is highlighted by covering a wide range of particle sizes from 5 μm to 13 μm (row A–C) and even mixed ensembles (5 μm together with 13 μm shown in row D). Human lung cells (A549) and red blood cells (RBC) were also included as biological samples (rows E and F). For all measurements the modulated piezo frequency was set to f_{110} = 1.75–1.85 MHz with a modulation frequency of 14 Hz and a peak-to-peak amplitude of U_{pp} = 14.6 V_{pp} resulting in a successful trapping that could be maintained over several hours. During the experiment, the number of trapped particles was increased to reach a few hundred: whereas, for small numbers, a perfectly round conglomerate was formed, a more elliptically shape is noticeable for higher numbers of particles and is discussed in detail in section 3.1.

2.2.3 Diffusive motion of trapped particles. The synergetic advantage of multiphoton microscopy's high spatial and high temporal resolution is highlighted by tracking trapped particles followed by a quantitative analysis of their motion in a homogeneous fluid. To derive the mean square displacement

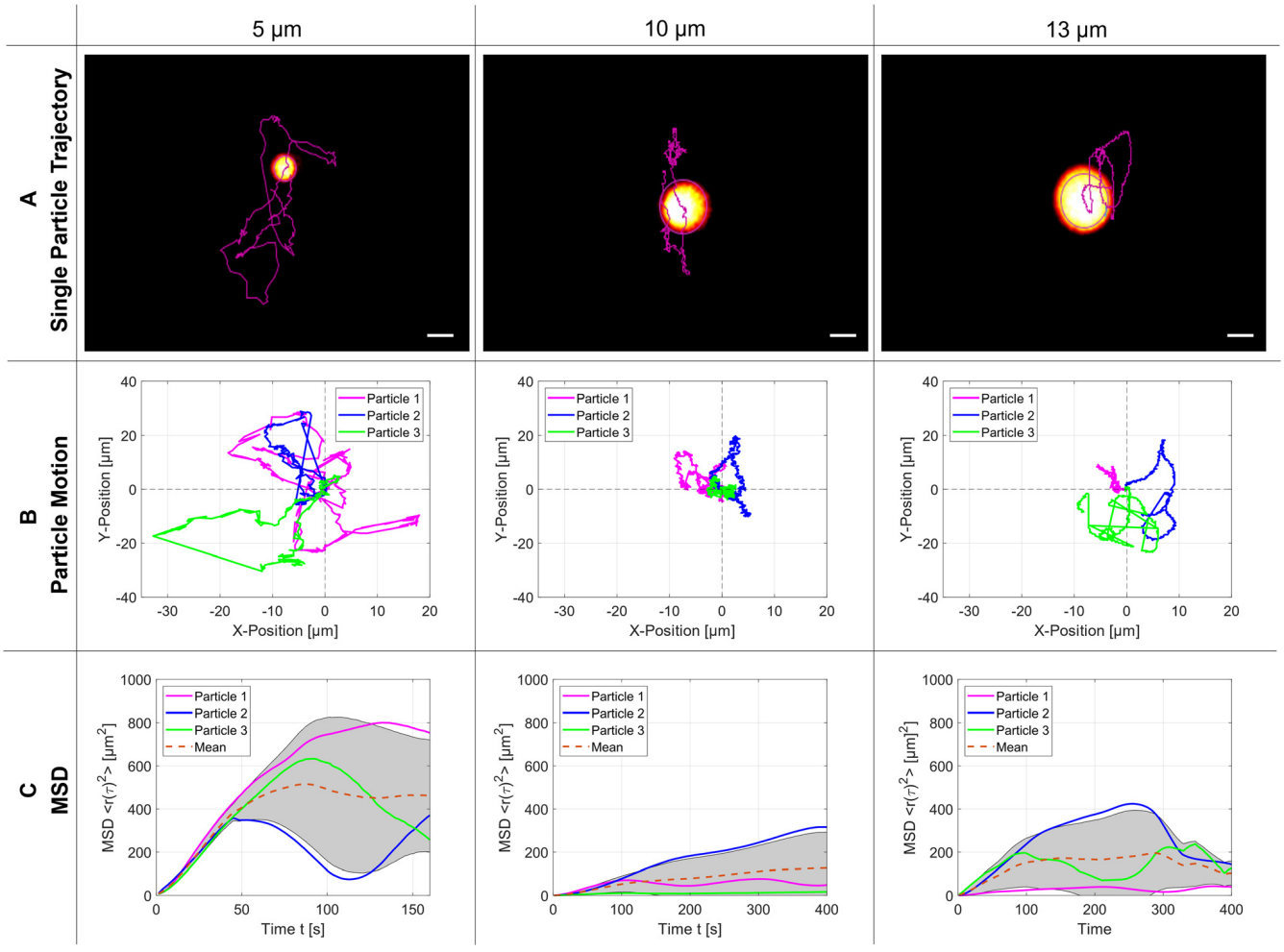

Fig. 4 Motion of trapped particles. A) Particle trajectory for a single PS microparticle of diameter 5 μm, 10 μm, and 13 μm – scale bar: 5 μm. Three repetitions of the particle trajectories for each diameter are presented in B). In C), we demonstrate the calculated mean square displacement of the particles over time, respectively.

of the hindered diffusion of trapped particles, we recorded three trajectories of polystyrene (PS) particles for the particle diameters 5 μm, 10 μm, and 13 μm, see Fig. 4. Panel (A) shows the trajectory of a single trapped particle superimposed with the last image from a 120 s long time series at 130 ms intervals (FPS = 7.7). In most cases the particle displacements between consecutive images are much smaller than the particle sizes, only possible due to the high optical resolution of approximately 261 nm (NA = 1.49 and λ = 780 nm) for multiphoton excitation with high numerical aperture objectives. In panel (B), the trajectories of three particles for each size are overlayed to visualize the random Brownian motion, which is a possible perturbation on the trapped particles in an acoustofluidic system.[34] Qiu *et al.* could prove numerically that the smaller the particle size the larger the Brownian motion due to the larger diffusion coefficient.[34]

Without statistical proof it can be directly seen that 5 μm particles occupy more space inside the SMC than the two bigger particles, which is a clear indication that the trapping force changes significantly with the particle size. From atomic force microscopy it is well-known that a more detailed analysis of the hindered Brownian motion could determine the strength of the trapping force but would be beyond the scope of this article.[35] In panel (C), the calculated mean square displacement (MSD) is plotted over time: at the beginning it grows linearly. Still, it can later only reach a bound set by the finite size of the acoustic trap, which is significantly smaller than the dimensions of the SMC. The mean value for the plateaus of the MSD is reached at 500 μm^2, 130 μm^2, and 170 μm^2 for the particle sizes of 5 μm, 10 μm and 13 μm, respectively. The acoustic parameters for every particle size are the modulated resonance frequency range f_{110} = 1.75–1.85 MHz and the peak-to-peak amplified amplitude U_{pp} = 14.6 V_{pp}.

2.2.4 Visualization of acoustic streaming. As described in the previous section, we observed that the acoustic radiation force, responsible for the trapping, decreases for decreasing particle size. As the particle size is reduced below a critical value, the acoustic radiation force is no longer strong enough to keep the particles trapped, and their motion will be dominated by the viscous drag from the acoustic streaming arising from viscous attenuation of the acoustic waves. To visualize the streaming, smaller particles of 1 μm diameter were introduced into the SMC during acoustic excitation. Like above-described investigations, a time series of *xy*-images was recorded, but this time at three axial positions: at the center, halfway to the top, and close to the top of the SMC. The results are shown in Fig. 5. For better understanding, a sketch of the acoustic streaming effect is placed to the left indicating where the three optical sections were taken.[16] The three measured images to the right are overlays of 20 consecutive raw images for better visualization of the paths taken by the particles. At the center (1 in magenta) the movement is circular around the center of the trap. Halfway to the top (2 in green) this changes into loops, whereas close to the top (3 in blue) no distinct collective motion is visible.

2.3 Application to biology

2.3.1 A549 cells. The SMC is designed to trap living cells in a nurturing fluid, avoiding contact with any surface, to study cell–cell interactions inside an organoid-like cell cluster. Therefore, monitoring biological samples showing that trapped cells are reacting to environmental stimuli is of high interest. For this purpose, we studied osmosis on RBCs and A549 lung cells with images taken at just the center plane of the SMC. This simplifies the image analysis and is only possible because single cells are automatically brought to focus by the acoustic trap. For the osmotic shock experiments, cells were suspended in a sodium chloride solution (*ca.* 1100 mOsm) before filled into the microchamber for optical inspection. Afterwards this procedure was repeated with control cells suspended in phosphate-buffered saline (*ca.* 271 mOsm). The subsequent image analysis extracts the diameter of the cell membrane in two directions – the major and minor axis – together with the diameter of the cell nucleus. Table 1 shows the average values and differences between control A549 cells and their counterparts under osmotic shock. A more detailed illustration of the osmotic effect in A549 lung cells is presented in Fig. 6.

The distributions of 73 membrane and 42 nucleus diameters are presented in the histograms in columns B and C, respectively. The vertical dashed lines indicate the mean values of the Gaussian distributions. The membrane diameters change significantly by 4 μm for both major and

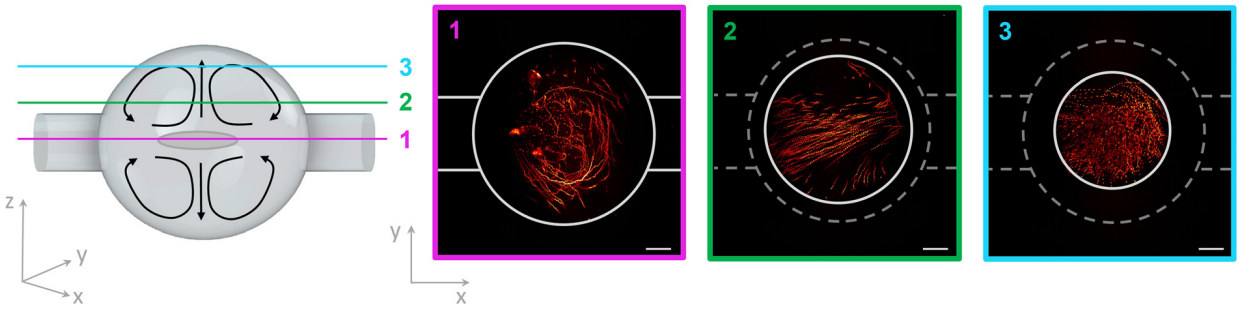

Fig. 5 Acoustic streaming in the spherical microchamber. A sketch of the spherical microchamber with acoustic streaming is shown on the left side. The recorded layers 1–3 in *xy*-direction are marked in different colours. On the right side, the acoustic streaming of 1 μm microparticles is demonstrated for each layer in the SMC. Scale bar: 100 μm.

Table 1 Results for A549 cells and RBC, before and after the osmotic shock

		Membrane aspect ratio	Membrane major axis [μm]	Membrane minor axis [μm]
A549 membrane	Control	0.96 ± 0.05	17.45 ± 1.44	16.71 ± 1.35
	Osmotic shock	0.92 ± 0.08	13.66 ± 1.93	12.54 ± 1.98
	Difference	0.04 ± 0.09	3.79 ± 2.41	4.17 ± 2.40
	Percentage	4.17%	21.72%	24.96%
		Nucleus aspect ratio	Nucleus major axis [μm]	Nucleus minor axis [μm]
A549 nucleus	Control	0.87 ± 0.13	11.19 ± 1.48	9.65 ± 1.18
	Osmotic shock	0.88 ± 0.10	9.87 ± 1.66	8.56 ± 1.18
	Difference	−0.01 ± 0.16	1.32 ± 2.22	1.09 ± 1.67
	Percentage	−0.44%	11.80%	11.30%
		Aspect ratio	Major axis [μm]	Minor axis [μm]
RBC	Control	0.91 ± 0.07	7.59 ± 1.04	6.87 ± 0.85
	Osmotic shock	0.91 ± 0.07	5.71 ± 0.63	5.19 ± 0.57
	Difference	0.0 ± 0.1	1.88 ± 1.22	1.68 ± 1.02
	Percentage	0.00%	24.77%	24.45%

minor axes and decrease from about 17 μm to 13 μm whereas the nucleus diameters stay nearly the same at around 10 μm with only a small change of about 1 μm. The exact numbers are given in Table 1. The aspect ratio for the control group implies a nearly round shape for the membrane that decreases slightly for cells after osmotic shock. Although the aspect ratio for the nucleus is still lower than for the membranes, it does not change after stimulus. The side-to-side comparison of an intensity profile of a typical control cell and a cell after osmotic shock is plotted in the last row of Fig. 6 on the left side and the above-mentioned diameter differences are illustrated with a bar graph to the right.

2.3.2 Red blood cells. The osmotic shock experiment was also performed with RBCs. Therefore, 40 cells were exposed to a high osmolarity of 500 mOsm. The major and minor axes of these cells were subsequently extracted by our analysis. For comparison, a total number of 64 control cells were trapped in phosphate buffered saline (PBS) at *ca.* 271 mOsmol. Since RBCs are not spherical but flattened, strict attention was paid to measure only those cells with their flat side aligned along the image plane as seen in Fig. 7 in the first row in A and B. The results of the aspect ratio and the major and minor axis of the control group and the cells after osmotic shock are listed in Table 1.

The size distribution of the RBCs in the control group was around 7 μm with an aspect ratio of 0.91. In literature, the average size of a red blood cell is 7.5 μm in which our measurements are in good agreement.[36] After osmotic shock, the diameters decreased significantly by 1.8 μm without changing the aspect ratio. The exact numbers are listed in Table 1 and visualized in the bar graph of Fig. 7 – comparison – B.

3 Discussion

3.1 3D analysis of acoustofluidic device

The TPEFM method enables the optical sectioning of trapped particles inside an SMC to reconstruct them in all three spatial dimensions, as seen in Fig. 2. The recorded image stacks allow for quantitative analysis of particle or living cell positions, sizes, shapes and some aspects of how well the acoustic trap is functioning. In our experiment, for example, the trap was not formed in perfect spherical shape but somewhat elongated along the *x*-axis. This could be attributed partly to the chamber's shape, which strongly influences the standing wave pattern of the acoustic trap. On the other hand, although great care was taken, we could not rule out completely that there was still a very small flow between the inlet and outlet of the chamber. In short, the 3D image analysis has the potential for in-depth investigation of cell clusters for biomedical research applications using this acoustofluidic device.

3.2 Two-dimensional acoustic trapping of microparticles and human cells

As mentioned in the introduction, the acoustic particle trapping in a spherical microchamber is performed in the so-called mode (1, 1, 0), which leads to the accumulation of the particles in the center of the SMC.[13,14] The evolving accumulation, which takes place after turning on the piezo actuators, is monitored as shown in the time series in Fig. 3A–F for different particle sizes as well as for labeled RBCs and A549 cells. Additionally, the TPEFM method delivers high resolution diffraction-limited images at video rate to classify different cell types and visualize compartments like membranes and nuclei.

3.3 Mean squared displacement

The next experiment shows that the TPEFM method is capable of visualizing the particles themselves and delivering quantitative data about their dynamic motion. After the trap is established, the motion of the PS microparticles is governed by hindered diffusion. The imaging time series for the different-sized particles (5 μm, 10 μm, and 13 μm) reveal the exact positions of the individual particles over time. They

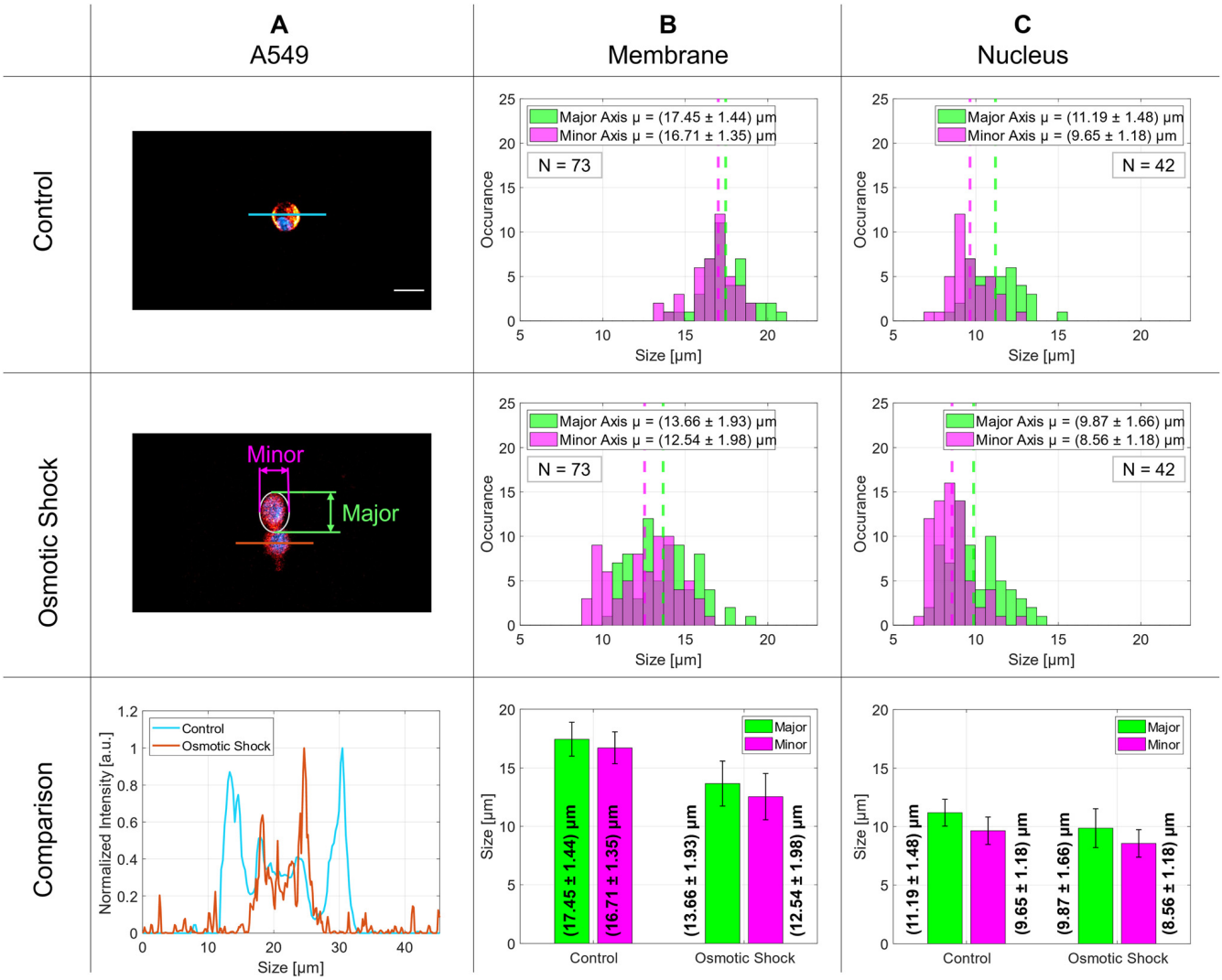

Fig. 6 Demonstration of the osmotic shock in A549 lung cells. Column A displays representative microscopy images with a control cell in the first row and a cell post-osmotic shock in the second row. The third row provides a comparative analysis of intensity profiles derived from images in rows one and two. Column B illustrates the size distribution of the control group (first row) and cells after osmotic shock (second row), with a bar graph in the third row depicting mean values for the major (green) and minor (magenta) axes. The results for the nucleus are shown in C. Scale bar 20 μm.

are subsequently linked together by self-written code to produce a track of each, which can be further analyzed by determining the mean-square displacement of their diffusion. As shown in Fig. 4(C), the MSDs change with particle size, because the acoustic radiation force depends on the particle size ($F_{\mathrm{rad}} \propto a^3$) and differences in mass density and compressibility in relation to the suspending fluid.[37] Therefore, the smaller the particle size with equal compressibility and density, the larger and faster their motion in the acoustic pressure field. Furthermore, the MSD increases linearly during the first few seconds due to the Brownian motion and reaches a plateau afterwards.[38] This leads to the conclusion that an external force or confined barrier results from the acoustic trap responsible for the hindered diffusion. Careful inspection of the trajectories in Fig. 4(B) uncovered that the movement in the *y*-direction is more pronounced than in the *x*-direction due to the above-mentioned reasons (SMC roundness, backflow, *etc.*). For these experiments, the flow of the liquid was stopped. Consequently, the particles were subject only to Brownian motion and acoustic forces. Given that we consider the cavity to be perfectly round, we can approximate the diffusion as isotropic across all three spatial directions. However, for a more precise analysis, the diffusion must be considered as anisotropic due to inaccuracies within the chamber as well as a residual mass flow resulting from the remaining liquid flow.

3.4 Acoustic streaming

Another effect in an acoustofluidic pressure field is the so-called acoustic streaming, which generates a steady flow or circulation of the fluid due to the viscous attenuation of the acoustic waves. The trapped cells in the SMC are surrounded by a nutrient medium and analytes. The circulation of the

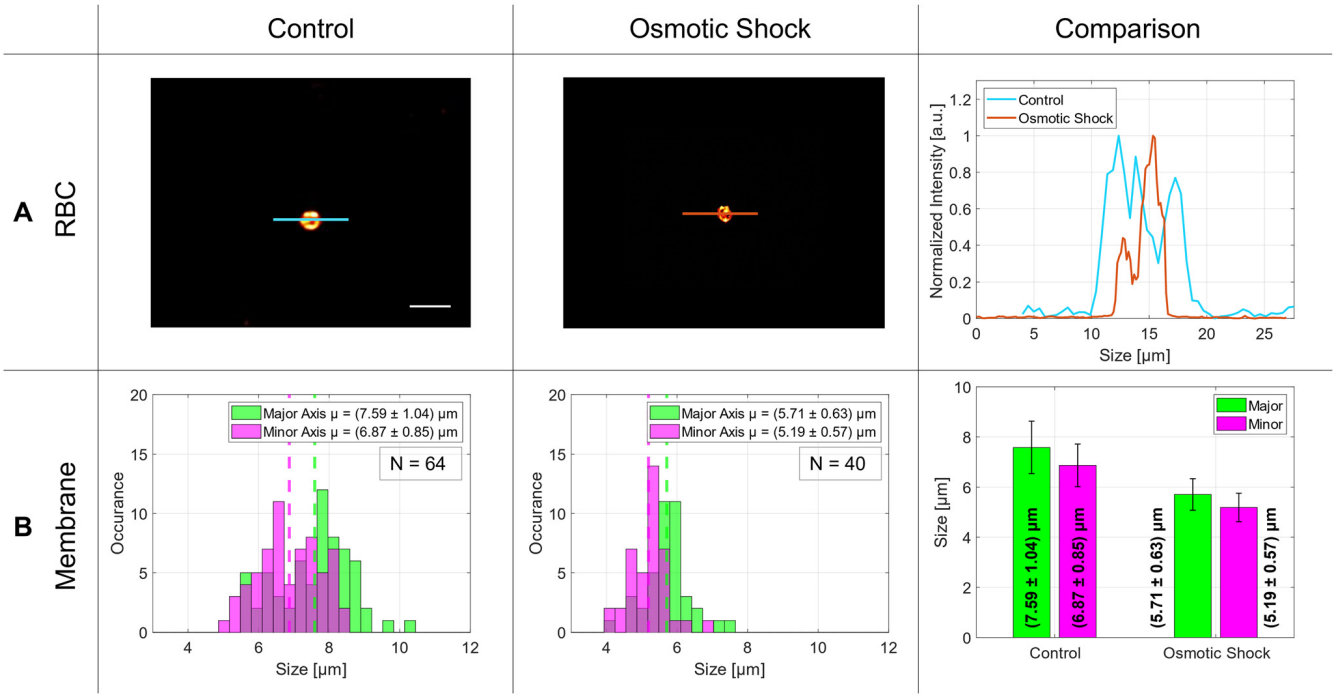

Fig. 7 Statistical analysis of the osmotic shock in RBCs. Row A showcases two-photon microscopy images of control cells in the first column and cells subjected to osmotic shock displayed in the second column. The intensity line profile of both cells are shown in the third column. In row B, histograms demonstrate the size distributions of cells, accompanied by a bar graph in the far-right column, which highlights fluctuations in their mean values. Scale bar: 10 µm.

fluid caused by the streaming effect guarantees the mixing of the fluid medium and results in a homogeneous distribution of the nutrition and the analytes. This condition is very crucial for cell viability over the experimental period. The interaction between the sound waves and the fluid is well described in Bach *et al.*[39] The acoustic streaming is dominant over the acoustic radiation force for fluid molecules and particles smaller than 1.4 µm.[40] Wiklund *et al.* simulated the acoustic streaming patterns in a circular chamber. This we demonstrated experimentally as shown in Fig. 5.[16] The 1 µm-sized particles move in so-called vortices inside the SMC, optically sectioned with our TPEFM method at three different layers inside the chamber to make the streaming trajectories thoroughly visible.

3.5 Osmotic shock as biological application

The last experiment shows the applicability of the acoustofluidic trap in combination with the TPEFM method for biological applications such as the investigation of the osmotic effect on living cells. In this scenario, many advantages of our setup come into play, mainly the possibility (i) to make long-term observations (ii) under near *in vivo* conditions and (iii) to analyze the sample in 3D (iv) with high spatial and temporal resolution. We chose to study osmosis because it is part of many physiological processes and, therefore, a relevant topic for life science research. One of the major problems is that the osmotic active particles are only measured within samples bound to a surface – usually the glass surface of a cover slip. In contrast to this common procedure, the SMC enables us to investigate the osmotic effect on samples that are kept in the center of a chamber filled with fluid, preventing them from touching any surface. In this experiment we compared the diameter of trapped RBCs and A549 cells suspended in a phosphate-buffered saline solution (isotonic), and sodium chloride (hypertonic). The osmotic pressure of the isotonic solution equals the pressure inside the RBCs/A549 cells, so they do not undergo any chemical or physical transformations. However, the hypertonic medium has more effective osmotic pressure than the intracellular fluid. This results in a so-called net movement of the intracellular fluid through the semi-permeable cell membrane into the hypertonic medium. This leads to the visible shrinking of the cells that are reducing their volume by the fluid moving out.[41,42]

3.6 A549 cells

The osmotic response was examined for A549 cells suspended in a medium as shown in the results section in Fig. 6 and Table 1. The use of the SMC makes it easy to analyze the size of the living cells in real-time and to increase their number arbitrarily to improve the statistical analysis. In the analysis of the cellular components, we observed a notable reduction in the dimensions of the membrane's axes after changing the isotonic medium into a hypertonic medium. Specifically, the major axis diminished from an initial size of 17.45 µm by (3.79 ± 2.41) µm, signifying an

average contraction of 21.72%. Similarly, the minor axis exhibited a reduction from the initial length of 16.71 μm by (4.17 ± 2.40) μm, relating to an average decrease of 24.96%. Furthermore, the nuclear dimensions also displayed a decrease. The major axis of the nucleus, starting at 11.19 μm, shrank by 11.80%, corresponding to a change of (1.32 ± 2.22) μm. The minor axis of the nucleus, starting at a size of 9.65 μm, decreased by 11.30%, with an absolute change of (1.09 ± 1.67) μm. The membrane diameter decreases significantly under osmotic shock whereas the nucleus diameter shows a much smaller effect. This compares well with what is reported in literature for A549 cells.[43] The elevated standard deviations observed in the nucleus measurements can be attributed to the inherent variability in nuclear morphology; the cell nucleus cannot be assumed to be perfectly spherical. Depending on the cell type and its physiological state, the nuclear shape may undergo significant transformations, resulting in irregular configurations.[44]

3.7 Red blood cells

The same experiment was repeated with living red blood cells. As can be seen in Fig. 7 and in Table 1, the RBC reduces its average diameter by (1.88 ± 1.21) μm in the major axis and by (1.68 ± 1.02) μm in the minor axis. The absolute diameter of the major axis was 7.6 μm on average and diminished to 5.7 μm under osmotic shock. In literature, the osmotic response was measured with the help of optical tweezers avoiding the interaction with a surface as well. There, the RBCs changed their size from around 9.8 μm to 8.0 μm.[45] Similar results were obtained by Gautam *et al.*, where they observed a diameter change from 8.0 μm to 6.4 μm using another measurement method.[46] This shows that our results fit well with the former ones. In summary, the application of our new device to biological problems seems to work very well and demonstrates that the A549 cells, as well as the RBCs, are studied under healthy conditions, and our analysis method works well for this kind of investigation.

4 Conclusion

This article presents two- and three-dimensional acoustic particle trapping experiments under a two-photon-excited fluorescence microscope. The TPEFM allows for sensitive verification of particle position and motion in the acoustic trap and chamber dimensions in 3D by optical sectioning. Likewise, the acoustic streaming effects on small particles in the SMC were demonstrated for multiple cavity layers. As a biological example of combining the acoustofluidic platform technology with the TPEFM method, we performed the osmosis on RBCs and lung cells (A549). This biological approach is a potential biomedical *in vitro* research application working close to *in vivo* conditions for sensitive analysis of cell functions and cell–cell interactions.

To fully harness the wide range of benefits offered by the TPEFM technique, future efforts will focus on applying this framework to spheroids or larger biological aggregates over extended time scales. Following successful integration with these samples, the technique may be further refined and potentially serve as a viable alternative to animal testing.

5 Methods

5.1 Two-photon microscopy setup

For diffraction-limited 3D images of the SMC and its function, a homebuilt TPEFM setup was used (Fig. 1 – C-right). As an excitation source, an ultrashort laser pulse system with two wavelengths λ_1 = 1030 nm and λ_2 = 780 nm (FemtoFiber Dichro Design, TOPTICA Photonics AG) was employed. Both lasers provide a maximal power of 100 mW with 80 fs pulses at a repetition rate of 80 MHz. The two beams were overlayed with the help of different mirrors (see Fig. 1 labeled as **M**) and a dichroic mirror **D1** (F38-825, AHF Analysentechnik). After the beams were superimposed, they reached a resonant-galvo scanner system **G** (Multiphoton Essential Kit, Thorlabs) for laser scanning. The systems runs at 8 kHz and delivers 31 frames per second with an image size of (1024 × 1024) pixels. With a telecentric system consisting of the scan lens **SL** and tube lens **TL**, the beams were coupled into a 20× Nikon water immersion objective **O** (CFI Apo MRD77200, Nikon) with a NA of 0.95 and a working distance of 0.9–0.99 mm. The point spread function was measured with 200 nm fluorescent nanobeads (F8806, ThermoFisher) and resulted to a lateral resolution of 443 nm and an axial resolution of 1.13 μm inside the SMC. With the help of a 3D printed stage adapter, the acoustofluidic setup (**AF**) was mounted on a *xyz*-stage (TI2-S-SE-E, Nikon). The fluorescence was collected with the same objective lens in epi-direction. A dichroic mirror **D2** (FF825-sDi01, Laser2000) separates the excitation light from the fluorescence light, and with two InGaAsP photomultiplier tubes (Multiphoton Essential Kit, Thorlabs) labeled as **A** and **B** it is quantified in a non-descanned configuration. Another dichroic mirror **D3** in the detection path separates the light with individual filters into a red **F1** (AT 600 LP, AHF Analysentechnik) for PMT A and blue **F2** (F76-594, AHF Analysentechnik) spectral emission range for PMT B. With two lenses, **L1** and **L2**, the fluorescence photons are focused on the detection area of the PMTs. Two multiphoton filters **MF** (F39-745, AHF Analysentechnik) block out scattered excitation light to improve the signal-to-noise ratio. To obtain 3D datasets, the microscope stage was synchronized with the scanner system and the detectors. The experiment as a whole was controlled by a self-written NIS-program.

5.2 Acoustofluidic platform

The acoustofluidic platform consists of a microfluidic chip, an acoustic drive unit with an automated temperature control, and a microfluidic control unit for automated injection of microparticles/cells and media as seen in Fig. 1 (C left part). The microfluidic glass chip (70 × 10 × 0.6) mm^3 consists of a wet-etched 500 μm diameter

spherical microchamber (SMC, nearly perfect sphere with 15–20% deviation) with straight inlet and outlet channels with cross-section 150 μm × 150 μm. The chips were fabricated by IMT Masken und Teilungen AG (Switzerland). The fabrication includes the etching process of two hemispherical chambers and the bonding to a microfluidic chip. The channel inlet and outlet are connected with tubing attached and sealed *via* super- and silicone glue. The tubing was connected to a pressure-based flow control through a valve system for achieving automated microfluidic control. A 2 MHz piezo transducer was fixed to the glass chip using super glue to generate the acoustic pressure field in the SMC. To trap the particles in the mode (1, 1, 0), the piezo transducer was excited with frequency modulated frequency f_{110} from 1.75 to 1.85 MHz with a modulation rate of 14.6 Hz and an amplitude U_{pp} = 14.6 V_{pp}. The mode shape (1, 1, 0) results from the calculation of the Helmholtz wave equation $\nabla^2 p + k^2 p = 0$ (ref. 8) with pressure p and wave number k in spherical coordinates (r, θ, ϕ) which is given by the pressure field $p(r, \theta, \phi) = R(r)\Theta(\theta)\Phi(\phi)$, where r describes the radial and θ and ϕ the angular parts of the equation. The detailed calculation of the mode shapes in a spherical cavity can be seen in Russell.[47] The resulting notation (n, l, m) describes the number of nodal surfaces in a spherical cavity. For trapping particles in the center of the SMC, we need the lowest degenerate pair of modes which results in (1, 1, 0). The temperature control consists of a temperature sensor, a Peltier element Pt1000 (M222, Heraeus Nexensos), and an aluminum cooling fin. As seen in Fig. 1-C, all components are implemented in a self-designed and 3D printed holder plugged into a 3D printed stage holder. The stage holder can be easily modified for every type of microscope.

5.3 Microparticles and fluorescent dye

5.3.1 Microparticles. For the calibration and verification of the platform technology with the TPEFM, we used polystyrene (PS) and melamine resin (MF) particles from microParticles GmbH (red-fluorescent (PS-FluoRed): ex/em 530 nm/607 nm and orange-fluorescent (MF-FluoOrange): ex/em 560 nm/584 nm). The selected PS particles of diameter (4.99 ± 0.16) μm and (9.89 ± 0.10) μm are references for red and white blood cells. Therefore, an excitation wavelength of 1030 nm was chosen, and the signal was detected with PMT A. For trapping of particles with different excitation parameters and sizes, we added MF particles of diameter (13.35 ± 0.19) μm. The fluorescence signal was gathered with PMT B, and the excitation was done with the 780 nm laser. We used PS particles of diameter (1.14 ± 0.03) μm to verify the acoustic streaming in the SMC. The particle suspension consists of 12 μL buffer (demineralized water), 3 μL glycerol (Alfa Aesar, 99+%, A16205) to achieve the mass density equal to the particles, and 0.01% Tween20 (Sigma Aldrich, 1 μL Tween20/15 ml sample; P1379-25ML).

5.3.2 Fluorescent dye. To measure the complete volume of the acoustofluidic device, a fluorescent solution was created and filled into the device. Therefore, a solution of 2.5 mg fluoresceinisothiocyanat-carboxymethyl-dextran (FITC-Dextran, average molecular weight 150 000 Da, Sigma-Aldrich) in 5 mL PBS was mixed and vortexed. The 780 nm laser was used for the excitation, and the fluorescence signal was detected with PMT B.

5.4 Cell lines and medium

5.4.1 A549 lung cells. A549 cells were cultured in Dulbecco's modified Eagle medium (DMEM) (BS.FG 0445, Bio&SELL GmbH) supplemented with 1% penicillin–streptomycin (BS.A 2213, Bio&SELL GmbH), 10% fetal calf serum (F7524-500 mL Sigma-Aldrich Chemie) and 1% GlutaMAX (35 050 038, Life Technologies GmbH) under humidified conditions at 37 °C and 5% CO_2. After reaching the desired confluency, the cells were detached from the surface using 0.5% trypsin–EDTA solution (BS.L 2163, Bio&SELL GmbH) and either used for experiments or seeded in a ratio of 1 : 6 in T175 cell culture flasks (83.3912.002, Sarstedt AG und Co.).

5.4.2 Red blood cells. For the application to biology, we tested the platform with human whole blood (donation by an anonymous healthy donor at the University Hospital Klinikum München rechts der Isar, Germany). The cell suspension consists of 2 mL phosphate-buffered saline (BS.L 1825, Bio&SELL GmbH) and 0.5 μL whole blood and is contained in a 2 mL tube (Eppendorf). The experiments were carried out immediately after receipt of the blood samples.

5.4.3 Osmotic shock. To induce an osmotic shock onto the RBC and A549 cells, a 5 M solution of sodium chloride was fabricated. Therefore, 29.22 g of the sodium chloride salt (P029.1, Carl Roth GmbH + Co. KG) was diluted in 100 mL PBS. The osmolarity of the phosphate-buffered saline (BS.L 1825, Bio&SELL GmbH) and the sodium chloride solution used in the osmotic experiments was carried out with an osmomat (Gonotec, Osmomat 3000). To obtain a statistically significant measurement value, each experiment was repeated five times. The initial solution of 50 μL PBS volume resulted in an osmolarity of (271.40 ± 1.36) mOsmol. Afterwards the NaCl solution was added to the PBS in sequence until we received a stagnation of the osmolarity at a value of (495.60 ± 0.49) mOsmol. Additionally, the same measurement was performed with the mixture of PBS and desalinated water. The samples were prepared with a 2 mL tube (Eppendorf) to mix 0.5 μL of RBC cells with 750 μL PBS and 250 μL of the sodium chloride solution. For the A549 cells the mixture contained 1750 μL DMEM including the cells and 150 μL sodium chloride. The osmolarity for the RBC is therefore around 500 mOsmol and for the A549 cell of around 1100 mOsmol. After a 5 min incubation time the sample was loaded into the acoustofluidic setup.

5.5 Immunostaining

5.5.1 Cell membrane staining. For two photon microscopy the cell membrane was stained with a

fluorescence tension reporter called Flipper-TR (Spirochrome SC02, Tebubio GmbH). Starting from a 1 mM stock solution, a staining solution was prepared containing 1 μL Flipper-TR dye and 1 mL of DMEM medium (1 : 1000 dilution) including the desired cell type. After a 30-minute-incubation-time at 37 °C and 5% CO_2 the cells were ready for the nucleus stain or the imaging procedure. The excitation maximum wavelength of the Flipper-TR is at 480 nm, therefore the 1030 nm laser was used for the excitation and PMT A for detection.

5.5.2 Nucleus stain. For the A549 cells also the nucleus was stained. Therefore, a 1 : 2000 dilution of a 1 mM stock solution of Hoechst (62249, Thermo Fisher Scientific Inc.) and the cell medium was prepared. Like the cell membrane stain, the solution was given 30 min time to incubate at 37 °C and 5% CO_2. The fluorescence signal was observed with PMT B after excitation with a wavelength of 780 nm.

5.6 Image analysis

5.6.1 2D and 3D image analysis. 2D image analyses were carried out with self-written Matlab (R2020a, MathWorks, USA) code in combination with the open-source software Fiji.[48] For 3D measurements and representations, the Huygens software (Scientific Volume Imaging) was used.

5.6.2 MSD analysis. MSD analysis enables the investigation of particle motion and provides information on diffusion rates, movement patterns (random or directed), interactions (particle–particle and with the medium) and the influence of external forces. It is a versatile tool that provides insights into the dynamics and physical properties of systems – from cellular environments to material structures.

To calculate a displacement trajectory of the trapped objects, a self-written Matlab code based on the Fiji plugin TrackMate was used.[49] From the obtained position and experiment information the pathwise mean square displacements were calculated according to eqn (1):

$$\mathrm{MSD}(\tau) = \frac{1}{N-j+1} \cdot \sum_{\tau=1}^{j} |X((\tau+j)\Delta) - X((\tau)\Delta)| \qquad (1)$$

5.6.3 Osmosis analysis. For size determination of the cells in normal conditions and under an osmotic force an edge detection together with an elliptical fit was used to extract the minor and major axis of the nucleus (only for A549 cells) and the cell membrane.

5.6.4 Acoustic streaming analysis. In order to display the acoustic streaming in different chamber positions, the recorded image sequence was superimposed over 500 single images.

Institutional Review Board statement

This study (620/21 S-KK) was approved by Ethikkommission an der Technischen Hochschule München, approved on 26 October 2021.

Author contributions

T. K., B. S., T. H. and O. H. conceived the experiments, T. K. and B. S. conducted the experiments, T. K., B. S., P. B., T. H., R. B. analysed the results. All authors reviewed the manuscript.

Conflicts of interest

There are no conflicts to declare.

Acknowledgements

This work was supported by the Bavarian Academic Forum (Bay-WISS) – Joint Academic Partnership 'Health' and was funded by the Bavarian State Ministry of Science and the Arts and by LaKoF Bayern – State Conference of Women's and Equal Opportunity Representatives at Bavarian Universities. This work was financially supported by the Munich University of Applied Sciences HM and the German Research Foundation (DFG) through the "Open Access Publication Costs (NE 1911/2-1)" program. Furthermore, we want to thank Dr. Stefanie Kiderlen and Dr. Lukas Krainer who supported our preliminary work with their demo TPEFM device. We are grateful to Franka Schulz, who performed the results for the osmolarity measurements.

References

1 D. Furman, J. Campisi, E. Verdin, P. Carrera-Bastos, S. Targ, C. Franceschi, L. Ferrucci, D. W. Gilroy, A. Fasano and G. W. Miller, *et al.*, *Nat. Med.*, 2019, **25**, 1822–1832.
2 P. K. Chattopadhyay, T. M. Gierahn, M. Roederer and J. C. Love, *Nat. Immunol.*, 2014, **15**, 128–135.
3 J. Rodrigues, M. A. Heinrich, L. M. Teixeira and J. Prakash, *Trends Cancer*, 2021, **7**, 249–264.
4 K. M. McKinnon, *Curr. Protoc. Immunol.*, 2018, **120**, DOI: 10.1002/cpim.40.
5 A. Adan, G. Alizada, Y. Kiraz, Y. Baran and A. Nalbant, *Crit. Rev. Biotechnol.*, 2017, **37**, 163–176.
6 M. B. Bracken, *J. R. Soc. Med.*, 2009, **102**, 120–122.
7 A. E. Sorour, J. Lönn, S. S. Nakka, T. Nayeri and F. Nayeri, *Cytokine*, 2015, **71**, 8–15.
8 H. Bruus, *Theoretical Microfluidics*, Oxford University Press, vol. 18, 2008.
9 P. Augustsson, R. Barnkob, S. T. Wereley, H. Bruus and T. Laurell, *Lab Chip*, 2011, **11**, 4152–4164.
10 M. Wu, C. Chen, Z. Wang, H. Bachman, Y. Ouyang, P.-H. Huang, Y. Sadovsky and T. J. Huang, *Lab Chip*, 2019, **19**, 1174–1182.
11 B. Kang, J. Shin, H.-J. Park, C. Rhyou, D. Kang, S.-J. Lee, Y.-s. Yoon, S.-W. Cho and H. Lee, *Nat. Commun.*, 2018, **9**, 5402.
12 Z. Ao, Z. Wu, H. Cai, L. Hu, X. Li, C. Kaurich, J. Chang, M. Gu, L. Cheng and X. Lu, *et al.*, *Adv. Sci.*, 2022, **9**, 2201478.
13 B. Sailer, R. Barnkob and O. Hayden, Acoustofludics 2020, Virtual Conference, 2020, Abstract No. 0077.
14 B. Sailer, R. Barnkob and O. Hayden, MicroTAS 2020, Virtual Conference, 2020, Abstract No. 3029.

15 K. Olofsson, V. Carannante, M. Ohlin, T. Frisk, K. Kushiro, M. Takai, A. Lundqvist, B. Önfelt and M. Wiklund, *Lab Chip*, 2018, **18**, 2466–2476.
16 M. Wiklund, H. Brismar and B. Önfelt, *Lab Chip*, 2012, **12**, 3221–3234.
17 J. Novotny, A. Lenshof and T. Laurell, *Electrophoresis*, 2022, **43**, 804–818.
18 H. D. Santos, A. E. Silva, G. C. Silva, E. B. Lima, A. S. Marques, M. S. Alexandre-Moreira, A. C. Queiroz, C. Jacinto, J. Henrique Lopes and U. Rocha, *et al.*, *Adv. Eng. Mater.*, 2021, **23**, 2100552.
19 V. Charwat, K. Schütze, W. Holnthoner, A. Lavrentieva, R. Gangnus, P. Hofbauer, C. Hoffmann, B. Angres and C. Kasper, *J. Biotechnol.*, 2015, **205**, 70–81.
20 W. Denk, J. H. Strickler and W. W. Webb, *Science*, 1990, **248**, 73–76.
21 W. R. Zipfel, R. M. Williams and W. W. Webb, *Nat. Biotechnol.*, 2003, **21**, 1369–1377.
22 P. T. So, C. Y. Dong, B. R. Masters and K. M. Berland, *Annu. Rev. Biomed. Eng.*, 2000, **2**, 399–429.
23 R. R. Anderson and J. A. Parrish, *J. Invest. Dermatol.*, 1981, **77**, 13–19.
24 M. Göppert-Mayer, *Ann. Phys.*, 1931, **401**, 273–294.
25 P. Hänninen, A. Soini, N. Meltola, J. Soini, J. Soukka and E. Soini, *Nat. Biotechnol.*, 2000, **18**, 548–550.
26 A. D. Elliott, *Curr. Protoc. Cytom.*, 2020, **92**, e68.
27 C. Gomez-Cruz, S. Laguna, A. Bachiller-Pulido, C. Quilez, M. Cañadas-Ortega, I. Albert-Smet, J. Ripoll and A. Muñoz-Barrutia, *Biosensors*, 2022, **12**, 1110.
28 J. Huisken and D. Y. Stainier, *Development*, 2009, **136**, 1963.
29 P. Luu, S. E. Fraser and F. Schneider, *Commun. Biol.*, 2024, **7**, 364.
30 M. Rubart, *Circ. Res.*, 2004, **95**, 1154–1166.
31 K. W. Dunn and P. A. Young, *Nephron Exp. Nephrol.*, 2006, **103**, e33–e40.
32 J. Jonkman, C. M. Brown, G. D. Wright, K. I. Anderson and A. J. North, *Nat. Protoc.*, 2020, **15**, 1585–1611.
33 B. Yang, M. Lange, A. Millett-Sikking, X. Zhao, J. Bragantini, S. VijayKumar, M. Kamb, R. Gómez-Sjöberg, A. C. Solak and W. Wang, *et al.*, *Nat. Methods*, 2022, **19**, 461–469.
34 W. Qiu, H. Bruus and P. Augustsson, *Phys. Rev. E*, 2020, **102**, 013108.
35 T. Li and M. G. Raizen, *Ann. Phys.*, 2013, **525**, 281–295.
36 M. Diez-Silva, M. Dao, J. Han, C.-T. Lim and S. Suresh, *MRS Bull.*, 2010, **35**, 382–388.
37 H. Bruus, *Lab Chip*, 2012, **12**, 1014–1021.
38 M. J. Saxton, *Biophys. J.*, 2007, **92**, 1178–1191.
39 J. S. Bach and H. Bruus, *Phys. Rev. E*, 2019, **100**, 023104.
40 R. Barnkob, P. Augustsson, T. Laurell and H. Bruus, *Phys. Rev. E: Stat., Nonlinear, Soft Matter Phys.*, 2012, **86**, 056307.
41 M. Rasouli, *Clin. Biochem.*, 2016, **49**, 936–941.
42 L. K. Goodhead and F. M. MacMillan, *Adv. Physiol. Educ.*, 2017, **41**, 298–305.
43 P. D'Angelo, G. Tarabella, A. Romeo, A. Giodice, S. Marasso, M. Cocuzza, F. Ravanetti, A. Cacchioli, P. G. Petronini and S. Iannotta, *MRS Commun.*, 2017, **7**, 229–235.
44 A. Sneider, J. Hah, D. Wirtz and D.-H. Kim, *Cell Adhes. Migr.*, 2019, **13**, 50–62.
45 Y. Liang, G. Liang, Y. Xiang, J. Lamstein, R. Gautam, A. Bezryadina and Z. Chen, *Phys. Rev. Appl.*, 2019, **12**, 064060.
46 R. Gautam, Y. Xiang, J. Lamstein, Y. Liang, A. Bezryadina, G. Liang, T. Hansson, B. Wetzel, D. Preece and A. White, *et al.*, *Light: Sci. Appl.*, 2019, **8**, 31.
47 D. A. Russell, *Am. J. Phys.*, 2010, **78**, 549–554.
48 J. Schindelin, I. Arganda-Carreras, E. Frise, V. Kaynig, M. Longair, T. Pietzsch, S. Preibisch, C. Rueden, S. Saalfeld and B. Schmid, *et al.*, *Nat. Methods*, 2012, **9**, 676–682.
49 J.-Y. Tinevez, N. Perry, J. Schindelin, G. M. Hoopes, G. D. Reynolds, E. Laplantine, S. Y. Bednarek, S. L. Shorte and K. W. Eliceiri, *Methods*, 2017, **115**, 80–90.

Chapter 4

Fluorescence Lifetime Imaging Microscopy

„The small is as important as the great, for the smallest detail reveals the laws of the universe.“

Fyodor Dostoevsky

In the previous **Chapter (3)**, we explored the capabilities of two-photon fluorescence microscopy for imaging and analyzing moving particles, extracting not only morphologic parameters but also detailed diffusion information. However, a deeper understanding emerges when we go beyond merely counting fluorescence photons and instead examine their arrival times [114]. This additional dimension, known as fluorescence lifetime τ, offers insights into subtle changes that might remain hidden when relying solely on intensity, such as shifts in polarity or pH levels in the surrounding environment [20, 115]. Fluorescence lifetime reflects the delicate interplay between the fluorophore and its environment, as any alteration—whether in the molecular structure of the fluorophore or in its surroundings—affects its photophysical properties, and consequently, its lifetime. This makes fluorophores versatile sensors for detecting specific environmental changes [116, 117, 118, 119]. Depending on the fluorophore, these changes may manifest as significant shifts of several nanoseconds or as more subtle changes [20]. By leveraging fluorescence lifetime in our investigation of the endosomal pathway and release mechanisms, we aim to uncover the intricate dynamics of pH shifts within endosomes, providing a more nuanced view of these processes. In this section, we will examine why fluorescence lifetime changes occur, the techniques available for measuring this critical parameter, and the limitations of these approaches. As Dostoevsky's words remind us, the smallest details—such as the subtle variations in fluorescence lifetime—can reveal profound truths about the underlying mechanisms of complex systems.

4.1 Photophysical Properties of Fluorophores

The fluorescence lifetime (τ) is a fundamental photophysical parameter that describes how long a molecule remains in its excited state before returning to the ground state, typically via photon emission (typical 0.1 - 10 ns) [120]. In 1916, Albert Einstein introduced three key interactions between photons and matter (**Figure** 4.1): absorption described by the coefficient B_{12}, stimulated emission with the coefficient B_{21}, and the spontaneous emission referred to the A_{21} coefficient [121].

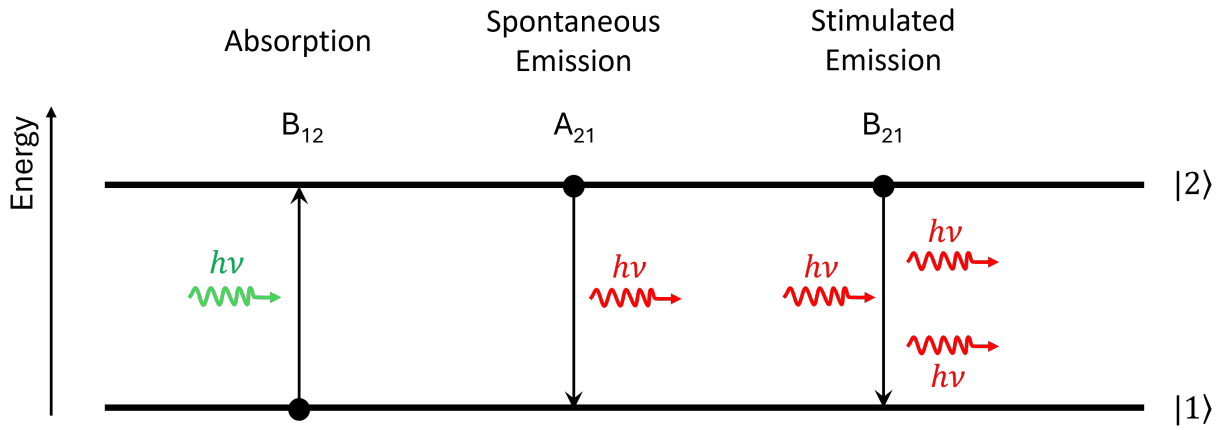

Figure 4.1: The three Einstein Coefficients: Here the three Einstein coefficients are displayed. With the absorption of a photon B_{12}, the spontaneous emission A_{21} which is the fundamental of the fluorescence process and the stimulated emission B_{21}.

The spontaneous emission, characterized by the Einstein coefficient A_{21}, corresponds to the inverse fluorescence lifetime for purely radiative transitions and is, in this idealized case, a material constant. However, in real systems, the observed fluorescence lifetime is not fixed but depends on a complex interplay of molecular properties and external factors [115]. At the molecular level, the fluorescence lifetime is governed by the ratio between radiative (k_R) and non-radiative (k_{NR}) decay pathways as seen in **Equation 4.1**.

$$k = k_{NR} + k_R \tag{4.1}$$

This relationship can be expressed for τ like in **Equation 4.2**:

$$\tau = \frac{1}{k} = \frac{1}{k_{NR} + k_R} \tag{4.2}$$

This equation shows that an increase in non-radiative decay rates (k_{NR}) leads to a decrease in the observed lifetime τ, assuming the radiative decay rate (k_R) remains constant.

Both decay pathways k_R and k_{NR} are strongly influenced by the molecule's electronic-structure and its interaction with the surrounding environment, making FLIM a powerful technique for sensing changes in molecular environments and properties. A critical parameter governing radiative decay is the transition dipole moment ($\vec{M}$). This parameter is categorized in the electronic-dipole, the magnetic-dipol, the electric quadrupole and the higher multipole transition moments, where we will only focus on the first because it has the strongest effect on the lifetime parameter [121]. This quantity describes the interaction of the molecule's electronic structure with the electromagnetic field of light. Mathematically, it is defined as **Equation 4.3**:

$$\vec{M} = \langle \psi_{S_1} | \vec{\mu} | \psi_{S_0} \rangle \tag{4.3}$$

Here ψ_{S_0} and ψ_{S_1} are the electronic wavefunctions of the ground $|S_0\rangle$ and excited states $|S_1\rangle$, while $\vec{\mu}$ is the position operator. The transition dipole moment quantifies the likelihood of photon absorption or emission, reflecting the strength of the coupling between the molecule and the electromagnetic field. Larger values of $\vec{M}$ correspond to higher probabilities of radiative transitions, directly influencing the radiative decay rate (k_R). Building upon the concept of the transition dipole moment, the oscillator strength (f) provides a dimensionless measure of the probability of an electronic transition [121]. It is proportional to the square of the transition dipole moment ($\vec{M}^2$) and the energy gap ΔE between the electronic states (**Equation 4.4**).

$$f \propto |\vec{M}|^2 \Delta E \tag{4.4}$$

A high oscillator strength f corresponds to efficient radiative transitions and, consequently, shorter fluorescence lifetimes. Conversely, weak or forbidden transitions (e.g., due to molecular symmetry) are associated with low oscillator strengths, leading to dominance of non-radiative decay pathways and longer lifetimes known as **I**nter**s**ytem **C**rossing (ISC) [122, 123]. Quantum mechanical properties, such as molecular symmetry, heavily influence both the transition dipole moment and the oscillator strength. For instance, transitions to triplet states are symmetry-forbidden and have negligible oscillator strengths, resulting in extremely low k_R values and extended radiative transitions also known as phosphorescence [124]. Also the energy gap itself has a big influence. For small energy gaps the vibronical transition pathways are more likely and promotes **I**nternal **C**onversion (IC), a non-radiative transition between electronic states of the same multiplicity. Smaller energy gaps resulting therefore to smaller lifetimes and *vice versa* [125]. With the Jabłoński diagram the different transitions for a molecule can be visualized easily, see **Figure 4.2** [126]. The characteristic relaxation times for transitions between $|S_1\rangle$ and $|S_0\rangle$ levels are summarized in **Table 4.1** [127]. The fact that the electron always relaxes from the first excited state is called the Kasha Rule, named after Michael Kasha [128].

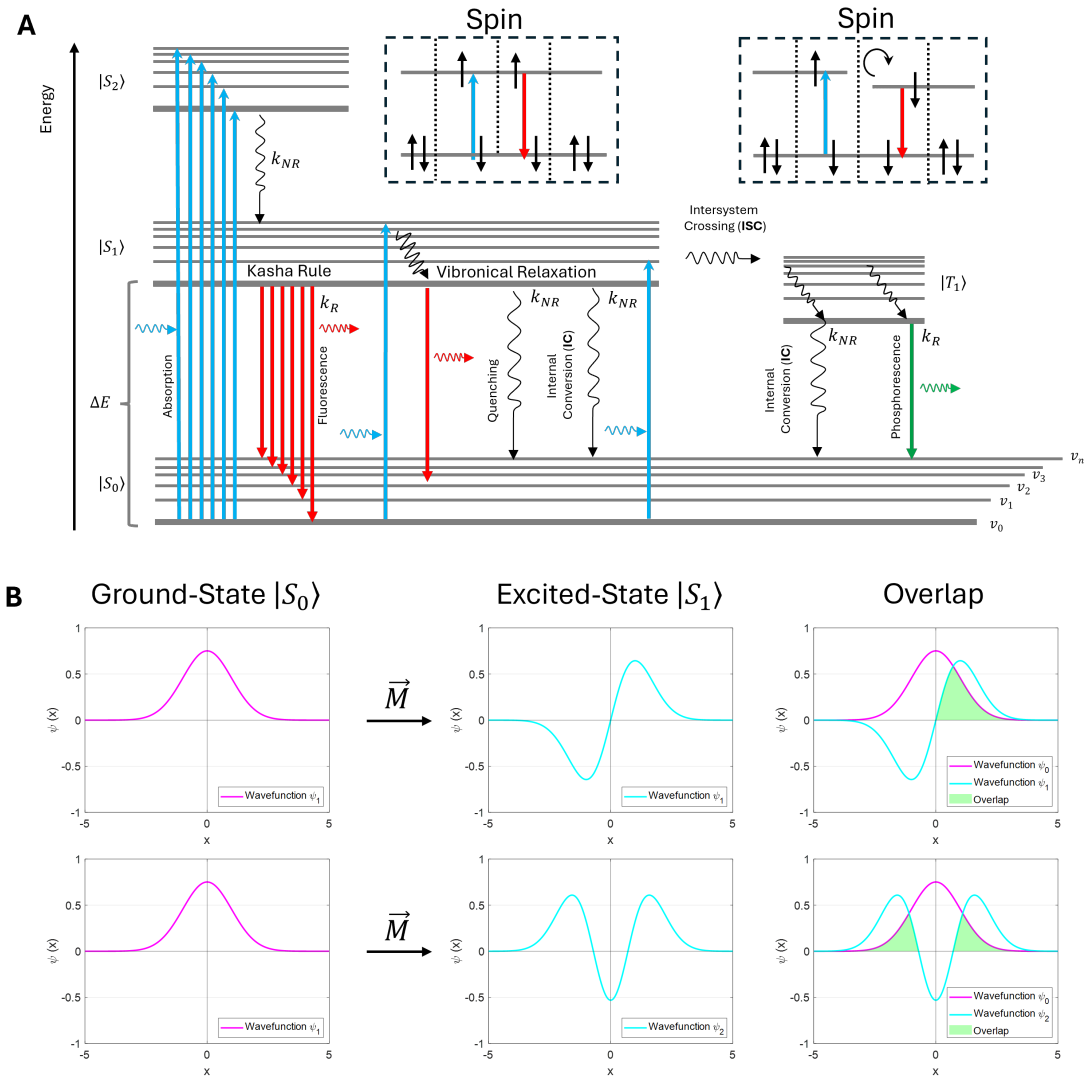

Figure 4.2: A Detailed Jabłoński Diagram: (**A**) illustrates a detailed Jabłoński diagram. When a molecule absorbs light, it can transition to various vibrational states (ν_n) within an electronic excited state, depending on the overlap between the wavefunctions of the ground and excited states, as well as the dipole moment $\vec{M}$ and the oscillator strength, as exemplified in (**B**). This concept is part of the Franck-Condon principle and also describes the symmetry between absorption and emission spectra [120]. Non-radiative transitions due to vibrational relaxation then occur, bringing the molecule to the lowest vibrational level of the first excited electronic state, a process known as Kashas rule. From this state, the molecule can undergo radiative transitions such as fluorescence or non-radiative processes such as quenching or IC. If a spin flip occurs, an ISC can transition the molecule to a triplet state. From this triplet state, the molecule can return to the ground state either through non-radiative transitions or via phosphorescence. Due to the spin flip requirement, phosphorescence is less probable and occurs over a longer timescale.

Additionally, the orientation of the transition dipole moment relative to the electric field polarization of light affects the transition probability. Maximum absorption or emission occurs when the electric field is aligned with the dipole moment, while the probability is minimized if they are orthogonal [129].

For rotating or tumbling fluorophores, this orientation dependence introduces an important spectroscopic concept: the magic angle, approximately 54.7° [129]. At this angle, fluorescence anisotropy becomes independent of rotational motion, which is critical for measurements such as time-resolved fluorescence spectroscopy and fluorescence anisotropy experiments [130].

Using this photophysical knowledge a variety of fluorophores with adjustable lifetime can be synthesised [131]. This is realized by combination of changes in the transition dipole moment or the oscillation strength and mechanical alterations. An example is the Flipper-TR fluororphore [119]. It consists of two stiff planar aromatic sections connected with flexible molecules. An applied force (e.g. osmosis, membrane tension, etc.) alters the stiff sections of the fluorophore which results in changed transition dipole moments. This causes a variation of the oscillation strength finally modifying the lifetime. By tweaking the molecular structure, the membrane tension can be adapted in order to linearize the lifetime change. This makes the Flipper-TR to a perfect sensor [132, 133].

Table 4.1: Transition times of a two-level system.

Transition	Absorption	Vibrational Relaxation	Internal Conversion	Fluorescence	Phosphorescence
Time [s]	10^{-15}	$10^{-14} - 10^{-11}$	$10^{-14} - 10^{-11}$	$10^{-9} - 10^{-7}$	$10^{-3} - 10^{2}$

4.2 Microenvironmental Properties

Fluorescent lifetime not only depends on the photophysical parameters described in **Chapter 4.1**. Also, the direct surrounding can change these properties and hence the lifetime of the fluorophores. In this context the focus is set to the following microenvironmental properties:

1. Solvent Polarity
2. Temperature
3. pH-Value
4. Quenching

Understanding their influence additional information can be extracted from lifetime or other spectroscopic methods like the fluorescence anisotropy or FCS [134, 135, 136].

Please note, that due to the large amount of fluorophores no general statement about the lifetime and its environment can be made. Nevertheless, in the following sub-chapters the most common characteristics of the microenvironmental properties are described.

Solvent Polarity

Polarity describes the distribution of electrical charge within a molecule or solvent. The polarity of the environment can significantly influence the electronic states of a fluorophore due to interactions between the solvent dipoles and the transition dipole moment of the molecule. Polar solvents have a permanent dipole moment, while nonpolar solvents do not. When a fluorophore absorbs light and transits to its excited state, its electronic charge distribution often shifts, resulting in a change in its dipole moment. In polar solvents, the surrounding molecules realign their dipoles to stabilize the new charge distribution of the excited state. This realignment is energetically favorable, as the electrostatic interactions between the solvent and the molecule lower the energy of the excited state. This process is referred to as stabilization and often extends the lifetime of the excited state [137, 115, 138].

Additionally, this stabilization involves a relaxation of the solvent environment to accommodate the new dipole configuration of the excited molecule. This solvent relaxation leads to a Stokes shift in the emission spectrum, as the energy expended in stabilizing the excited state is no longer available for photon emission, resulting in a red-shifted fluorescence signal [139] (**Figure 4.3**). This can be calculated with the Lippert-Mataga **Equation 4.5** and can help to estimate the effects of different solvents [140]:

$$\Delta\vec{\nu} = \frac{2\Delta f}{4\pi\epsilon_0 hca^3} \cdot (\vec{\mu}_{S_1} - \vec{\mu}_{S_0})^2 + const. \tag{4.5}$$

The spectra- or stokes shift $\Delta\vec{\nu}$ is thereby calculated in wavenumbers by using Δf as a solubility parameter, the dielectric constant ϵ, the Planck constant h, the speed of light c and the Onsager cavity radius a in which the chromophore resides, together with the dipole moments for the ground- ($\vec{\mu}_{S_0}$) and excited state ($\vec{\mu}_{S_1}$) [141].

Temperature

Higher temperatures are resulting in stronger molecular vibrations that in turn enhances non-radiative transition paths like IC. Thus, the lifetime of the sample can be changed strongly. Dependent on the structure of the fluorophore this parameter may have a stronger [117, 118] or weaker effect [20]. This can be estimated by the degrees of freedom of the molecule [115]. The dependency on the detected lifetime τ_{Det} and the real lifetime τ, determined by the rotational movement of the molecule can be described with the Stokes-Einstein-Debye relationship [142].

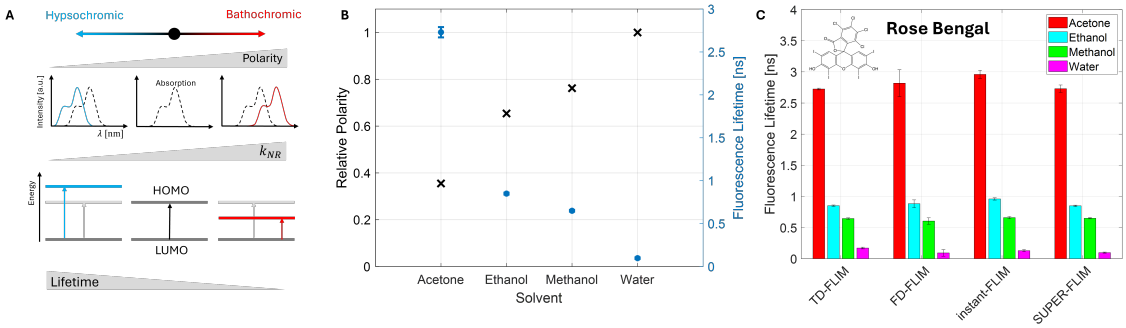

Figure 4.3: Microenvironmental Sensing Illustrated through Polarity: A shows the influence of polarity on the photophysical properties of fluorophores. As polarity increases, a bathochromic (red) shift in the emission spectrum occurs, leading to more non-radiative decay pathways (k_{NR}) and a corresponding decrease in fluorescence lifetime. This shift is due to the stabilization of the **H**ighest **O**ccupied **M**olecular **O**rbital (HOMO) and **L**owest **U**noccupied **M**olecular **O**rbital (LUMO) states caused by solvatochromic effects. For Rose Bengal dissolved in four different solvents, we demonstrate that an increase in solvent polarity results in a decrease in fluorescence lifetime **B**. The displayed lifetime values were obtained using the SUPER-FLIM technique. This polarity-sensitive lifetime shift was also used to benchmark our method **C** against TD-FLIM, FD-FLIM, and Instant FLIM, which we also used to measure these solvents.

$$\tau_{Det} = \frac{1}{\frac{1}{\tau} + \frac{k_B T}{4\pi r^3 \eta}} \tag{4.6}$$

Including the Boltzmann constant k_B, the Temperature T, the radius r and the viscosity η.

pH-Value

The pH-dependent changes in fluorescence lifetime are influenced by several factors, all of which involve alterations in the molecular configuration [115]. For instance, protonation (accumulation of protons) or deprotonation of specific functional groups in the molecule can modify its transition dipole moment, leading to variations in the fluorescence lifetime. Additionally, the stability of the excited state can be affected by the presence of protons: in acidic conditions (low pH), protonation can stabilize the excited state, resulting in a longer lifetime. In contrast, in basic conditions (high pH), the absence of protons can destabilize the excited state, shortening the fluorescence lifetime. A more complex scenario involves quenching effects due to protonation, which can increase the rate of non-radiative decay processes, further reducing the lifetime.

Quenching

Quenching processes play a significant role in changes to fluorescence lifetime under various conditions. The two main types of quenching are dynamic quenching and static quenching [143]. Dynamic quenching occurs due to collisional interactions between the fluorophore and quencher molecules, such as oxygen. Hereby the energy is transferred to the quencher molecule that converts it into thermal energy resulting in more non radiative transitions and thus shorter lifetimes. In contrast, static quenching results in the formation of non-fluorescent complexes, where the fluorescence intensity decreases, but the lifetime remains unchanged [120]. Both types of quenching can be described using the Stern-Volmer **Equation 4.7** [144, 145].

$$\frac{F_0}{F} = \frac{\tau_0}{\tau} = 1 + K_{SV} \cdot |Q| \tag{4.7}$$

With the fluorescence intensity F_0 and lifetime τ_0 without the quencher and F, τ with the quencher. The parameter K_{SV} is the Stern-Volmer coefficient and $|Q|$ the quenching-concentration.

Another important quenching mechanism, especially in biophysical applications, is **F**örster **R**esonance **E**nergy **T**ransfer (FRET) [146]. In this process, energy is transferred non-radiatively between two spatially close molecules, known as the donor and acceptor. The donor molecule transfers energy to the acceptor molecule through a resonance interaction, causing a decrease in the donor's fluorescence lifetime. The efficiency of this energy transfer depends on the spectral overlap between the donor and acceptor, as well as their distance and relative orientation.

While the fluorophore concentration does not directly determine fluorescence lifetime, it is important to consider that high concentrations can still lead to lifetime changes as part of quenching phenomena [20]. Based on the Einstein coefficient even one molecule results in the correct lifetime if the observation time is long enough. However, at higher concentrations, excited molecules are more likely to undergo collisions, which increases the rate of non-radiative transitions and shortens the fluorescence lifetime. Additionally, a small Stokes shift can lead to greater overlap between the absorption and emission spectra, facilitating a process known as reabsorption [147]. In this case the lifetime is prolonged.

4.3 Fluorescence Lifetime Imaging Microscopy Techniques

The vast amount of information that can be derived from fluorescence lifetime as a single parameter led to the development of methods for its measurement as early as 1988 [148]. Since then, the precision and usability of these methods have drastically improved, diverging into two main categories: TD-FLIM and FD-FLIM [107, 108]. Each technique has distinct advantages and disadvantages, which were carefully evaluated at the beginning of this work to determine the most suitable approach for measuring the pH value within endosomes. In the publication *"Comprehensive Investigation of Parameters Influencing*

Fluorescence Lifetime Imaging Microscopy in Frequency- and Time-Domain Illustrated by Phasor Plot Analysis." we explored the working principles, analysis methods, advantages, disadvantages, and fundamental differences of these techniques in detail [20]. Importantly, we employed the phasor plot as a visualization tool, which allows for direct comparison between the two methods despite their differing analysis principles [149, 150]. This data representation is also commonly used for segmentation that is more and more combined with **A**rtificial **I**ntelligence (AI) [151, 152]. The use of this approach is nowadays also used for other techniques like hyperspectral imaging and thus shows its importance in the microscopy community [153, 154].

4.3.1 Time-Domain FLIM

The most widely used FLIM method is TD-FLIM [155, 108]. It can be conceptually likened to a stopwatch. Here, short laser pulses serve as the excitation source, and point-source detectors capable of single-photon detection are used for measurement. When the excitation pulse interacts with the sample, the "stopwatch" starts, and it stops when the first photon is detected. The time interval is recorded and added to a histogram, a process repeated until sufficient statistics are gathered. This is done by devices called TCSPC [156, 157]. Since fluorescence decay is a statistical process following an exponential distribution, data collection continues until a reliable histogram is obtained. The fluorescence lifetime is then determined by fitting an exponential decay curve, with the $\frac{1}{e}$ value representing the lifetime. For samples with multiple fluorophores, multi-exponential fitting may be required, which can make the analysis process complex and time-consuming, especially for imaging applications. Also here the advantages of AI and machine learning make great progress [158]

In imaging, additional challenges arise due to the need for **L**aser-**S**canning **M**icorsocpy (LSM) or **S**ample-**S**canning **M**icorsocpy (SSM), as a separate decay profile must be recorded for each pixel. This makes TD-FLIM relatively slow. However, TD-FLIM's compatibility with confocal microscopy and TPEFM provides advantages such as high spatial resolution, optical sectioning, and deep tissue penetration in the case of TPEFM [20, 108].

4.3.2 Frequency-Domain FLIM

FD-FLIM can be compared to a forced oscillation system. In this technique, the sample is excited with an intensity-modulated **c**ontinuous **w**ave (cw) laser. The fluorescence emitted by the sample is also modulated at the same frequency but exhibits both a phase shift and a reduction in amplitude relative to the excitation. These shifts depend on the fluorescence lifetime: longer lifetimes produce larger phase shifts and lower amplitude modulations, whereas shorter lifetimes result in smaller phase shifts and higher modulations [20, 108]. To measure these properties, specialized detectors such as multichannel plates, dual-tap sensors, or systems capable of homo- or heterodyne detection are used [159, 160, 161]. These detectors extract the phase and amplitude information, which can then be converted

into fluorescence lifetime values. The wide-field setup enabled by camera-based detection provides a significant speed advantage for FD-FLIM compared to TD-FLIM.

However, FD-FLIM differs fundamentally from TD-FLIM in its analysis. While TD-FLIM directly measures the exponential decay profile, FD-FLIM calculates phase- and amplitude-lifetimes, which can be confusing for more complex samples. For single fluorophores, these values match, but for multi-component systems, discrepancies can arise, complicating data interpretation [162]. To address this, a relatively new visualization tool, the phasor plot, has been developed [149, 150].

4.4 The Phasor Plot Approach

The phasor plot bridges the gap between TD-FLIM and FD-FLIM by providing a unified visualization of the fluorescence lifetime data [149, 150]. Using Fourier transformation, both the exponential decay profile from TD-FLIM and the phase- and amplitude-lifetimes from FD-FLIM can be transformed into the same representation [20].

Each pixel in the image is represented as a vector in a polar coordinate system, characterized by an angle and magnitude, or as a point in Cartesian coordinates with G (cosine component) and S (sine component) values. By calculating these parameters for each pixel, a distribution of points, or a phasor plot, is generated. This plot provides a direct visualization of lifetime distributions.

A semi-circle, adjusted to the excitation frequency, serves as a reference on the phasor plot. Points lying on the semi-circle correspond to mono-exponential decays, while points inside the semi-circle indicate multi-exponential decays. For multi-exponential decays, the distribution's position and spread allow estimation of lifetime components and their relative contributions [163]. Additionally, the broadness of the distribution provides insight into measurement precision. The phasor plot is highly advantageous for comparing different FLIM techniques and enables advanced applications such as lifetime-based image segmentation also based on machine learning and AI [152, 164]. This approach facilitates intuitive interpretation of complex fluorescence lifetime data, yielding powerful results in both basic and applied research [153, 165].

4.5 Comprehensive Investigation of Parameters Influencing FLIM

Authors	**Thomas Kellerer**, Janko Janusch, Christian Freymüller, Adrian Rühm, Ronald Sroka and Thomas Hellerer
Title	*Comprehensive Investigation of Parameters Influencing Fluorescence Lifetime Imaging Microscopy in Frequency- and Time-Domain Illustrated by Phasor Plot Analysis.*
Journal	Internation Journal of Molecular Sciences (IF: 4.9 - 2023)
DOI	`https://doi.org/10.3390/ijms232415885`

As we have seen, numerous factors can influence the measured fluorescence lifetime. A key challenge arises from the fact that the observed lifetime reflects the sum of radiative (k_R) and non-radiative (k_{NR}) decay rates. This interdependence often complicates the interpretation of results and can lead to discrepancies in reported values across different studies. Variations in experimental conditions, such as pH, solvent, sample concentration, and temperature, can further contribute to these inconsistencies. Therefore, it is essential to carefully control and document all relevant parameters to ensure reproducibility and comparability between experiments.

In addition to environmental and sample-related factors, the question if the measurement technique itself can affect the observed lifetimes was often formulated. For example, if the choice between 1P and 2P excitation can yield different lifetime values due to differences in excitation mechanisms and associated photophysical processes. To address these issues systematically, we conducted a comprehensive measurement campaign to investigate how various setup- and sample-dependent parameters influence fluorescence lifetimes. Using a single experimental setup, we compared the two most common FLIM techniques, TD-FLIM and FD-FLIM, across a range of fluorophores under controlled conditions.

The results, along with a detailed explanation of the TD-FLIM and FD-FLIM techniques and their application to phasor plot analysis, are presented in the publication *"Comprehensive Investigation of Parameters Influencing Fluorescence Lifetime Imaging Microscopy in Frequency- and Time-Domain Illustrated by Phasor Plot Analysis."* [20]. We showed that the technique is not affecting the fluorescence lifetime drastically but the microenvironmental properties often do. To use FLIM for the detection of pH-changes of endosomes we tested a wide range of fluorophores and tested which molecule is most suitable for this purpose. The sample of choice was herby Fluorescein showing a strong lifetime change for pH-changes.

4.5.1 Contribution

This paper was conceptualized and structured by Thomas Kellerer, who also designed and implemented the optical setup and conducted the initial measurements. To obtain statistical data, additional measurements were performed by Janko Janusch as part of his bachelor thesis, which was supervised by Thomas Kellerer. Christian Freymüller contributed by preparing the samples and providing the fluorophores used in the experiments.

Thomas Kellerer was responsible for the evaluation and interpretation of the data, as well as the development of software tools, including the implementation of the phasor plot calculations. He also took the lead in drafting the manuscript. Thomas Hellerer supervised the project and contributed to the manuscript writing, while all co-authors reviewed and provided feedback on the final manuscript.

International Journal of
Molecular Sciences

MDPI

Article

Comprehensive Investigation of Parameters Influencing Fluorescence Lifetime Imaging Microscopy in Frequency- and Time-Domain Illustrated by Phasor Plot Analysis

Thomas Kellerer [1,2], Janko Janusch [1,3,4], Christian Freymüller [3,4], Adrian Rühm [3,4], Ronald Sroka [3,4] and Thomas Hellerer [1,*]

[1] Multiphoton Imaging Lab, Munich University of Applied Sciences, 80335 Munich, Germany
[2] Faculty of Physics, Soft Condensed Matter, Ludwig-Maximilians-University, 80539 Munich, Germany
[3] Laser-Forschungslabor, LIFE Center, Department of Urology, University Hospital, Ludwig-Maximilians-University, 82152 Planegg, Germany
[4] Department of Urology, University Hospital, Ludwig-Maximilians-University, 81377 Munich, Germany
* Correspondence: hellerer@hm.edu

Abstract: Having access to fluorescence lifetime, researchers can reveal in-depth details about the microenvironment as well as the physico-chemical state of the molecule under investigation. However, the high number of influencing factors might be an explanation for the strongly deviating values of fluorescent lifetimes for the same fluorophore reported in the literature. This could be the reason for the impression that inconsistent results are obtained depending on which detection and excitation scheme is used. To clarify this controversy, the two most common techniques for measuring fluorescence lifetimes in the time-domain and in the frequency-domain were implemented in one single microscopy setup and applied to a variety of fluorophores under different environmental conditions such as pH-value, temperature, solvent polarity, etc., along with distinct state forms that depend, for example, on the concentration. From a vast amount of measurement results, both setup- and sample-dependent parameters were extracted and represented using a single display form, the phasor-plot. The measurements showed consistent results between the two techniques and revealed which of the tested parameters has the strongest influence on the fluorescence lifetime. In addition, quantitative guidance as to which technique is most suitable for which research task and how to perform the experiment properly to obtain consistent fluorescence lifetimes is discussed.

Keywords: fluorescence lifetime imaging microscopy; FLIM; fluorescence microscopy; two-photon microscopy; phasor-plot; image analysis; time-domain; frequency-domain; bioimaging

Citation: Kellerer, T.; Janusch, J.; Freymüller, C.; Rühm, A.; Sroka, R.; Hellerer, T. Comprehensive Investigation of Parameters Influencing Fluorescence Lifetime Imaging Microscopy in Frequency- and Time-Domain Illustrated by Phasor Plot Analysis. *Int. J. Mol. Sci.* **2022**, *23*, 15885. https://doi.org/10.3390/ijms232415885

Academic Editors: Antonino Mazzaglia, Angela Scala and Enrico Caruso

Received: 16 November 2022
Accepted: 9 December 2022
Published: 14 December 2022

1. Introduction

Modern microscopy excels at uncovering the morphology of living samples [1]. Today, advanced techniques, such as stimulated Raman scattering (SRS) [2], fluorescence correlation spectroscopy (FCS) [3,4] and fluorescence lifetime imaging microscopy (FLIM) [5], give additional access to photo-physical, chemical and biological information, to mention just three types [6]. Furthermore, this information can be quantified, e.g., by measuring the local concentration of a molecular species in an area as small as one femtoliter [7]. Unfortunately, the majority of microscopy methods rely on signal intensities, which are dependent on the experimental setup, such as the excitation/detection efficiencies, or susceptible to unwanted phenomena, such as photo-bleaching of the markers used [8]. Therefore, only relative changes are commonly quantified. FLIM is an exception here because the measured lifetime is not dependent on the kind of excitation, e.g., via one-photon (1P) or two-photon (2P) absorption or on matching the laser wavelength to the excitation profile of the sample. Furthermore, different kinds of detection, e.g., single photon counting with a point-detector or a camera-based widefield approach, deliver the same results. This paper refers to this desirable feature as the FLIM-advantage. Why then is the lifetime of a specific fluorophore

not the same under all circumstances? Consulting the literature, one finds differing values that lead to the impression that FLIM may not be a reliable method. As a benchmark, two examples are represented: the reported lifetime of rhodamine B ranges from 1.74 to 3.13 ns [9–12], or the lifetime of rose bengal ranges from 0.095 to 2.4 ns [13–16]. Despite these huge differences, there is no evidence that the authors of the published data made any mistake in their measurements or conclusions. Therefore, the aim of this paper is to clarify how these discrepancies arise and what circumstances lead to differing lifetime values. On the other hand, it will be shown that time domain (TD) and frequency domain (FD) FLIM lead to the same results although they employ the different setup parameters mentioned above. Unfortunately, they are not directly comparable because the corresponding data analysis is different. Therefore, the data of both methods are transformed to retrieve a so-called phasor plot, which makes the comparison an easy task. The reason for the superficial discrepancy in lifetimes is due to certain parameters that influence the sample directly, such as concentration, pH-value, solvent polarity, and temperature, etc. This fact will be demonstrated in our comprehensive investigation. On the other hand, if these parameters are under the control of the researcher, they can use this to their advantage and utilize the fluorophore as the smallest possible reporter inside a living cell.

2. Results

All parameters that were studied in this rigorous investigation fall within two categories—setup-dependent and sample-dependent. The former determines the accuracy and range in which the lifetime can be obtained. The latter includes all parameters related to the microenvironment and the photo-physical properties of the fluorophore that affect its lifetime.

2.1. Setup Dependent Parameters

Starting with the different measurement setups, interdependent advantages and disadvantages of each were worked out. While the TD setup stands out with its diffraction-limited resolution, deep tissue penetration and optical sectioning possibilities, the needed detection time must be long enough to gather sufficient photon statistics. If a high resolution is not needed, the fast image acquisition of the FD setups provides the greatest advantage.

2.1.1. Wavelength

An often-formulated question is whether the kind of absorption process, e.g., 1P- or 2P-absorption, or the excitation wavelength, affect the fluorescence lifetime [12]. Therefore, the setups chosen in this series differ in the way the excitation takes place. For the TD setup, two ultrashort pulsed lasers with center wavelengths at 780 and 1034 nm were utilized, whereas the FD setup employed two wavelengths at 405 and 445 nm. To compare the lifetimes resulting from two-photon (TD FLIM) and one-photon (FD FLIM) absorption, a single dye with suitable spectral properties was used (Figure 1A). Rose bengal dissolved in ethanol at a concentration of 10^{-2} M met this requirement. The lifetimes determined using all four wavelengths, as well as one-photon and two-photon absorption, gave consistent results of around 0.85 ns (Figure 1B). A *p*-value test yielded a result of 0.046, which met the requirement for the measurement to be considered statistically significant. To also show the mono-exponential behavior within the FD, a *p*-value between the phase and demodulation lifetime was determined (Table 1). The mono-exponential behavior in the TD was verified by the residuals of the single exponential fit.

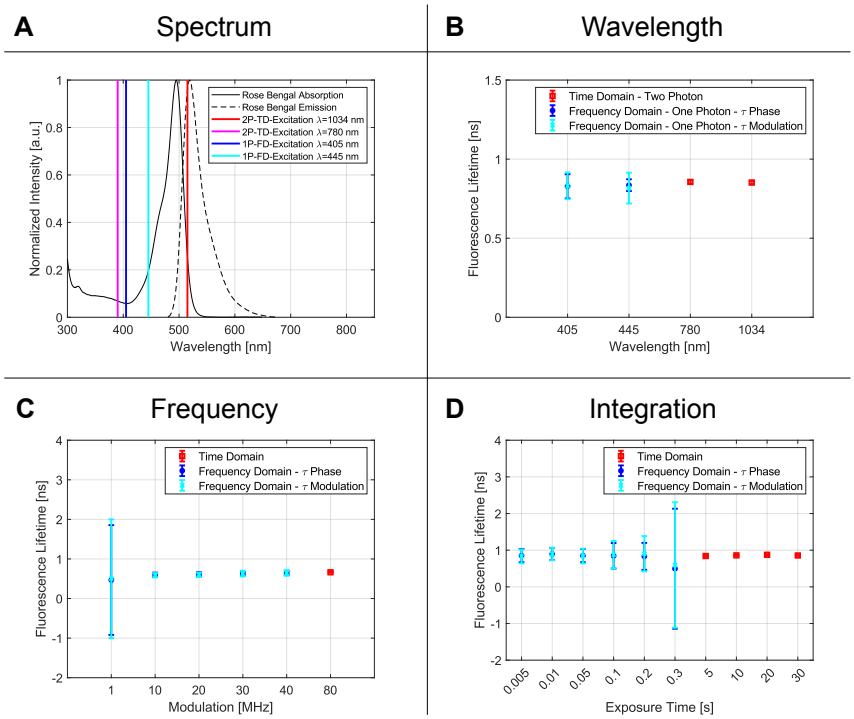

Figure 1. In (**A**), the absorption and emission spectrum of rose bengal and the individual excitation wavelengths are shown. The blue (405 nm) and cyan line (445 nm) represent the FD Wavelengths. For TD FLIM, the two-photon excitation wavelengths are shown in pink (two-photon excitation at 390 nm) and red (two-photon excitation at 515 nm). Although the laser lines are only slightly within the absorption spectrum, a sufficiently high fluorescence can be generated. In (**B**), the obtained fluorescence lifetimes for the wavelength dependency measurements were presented. In blue (phase lifetime) and cyan (demodulation lifetime), the results for the FD are shown, and in red the results for the TD are shown. In section (**C**), the influence of the repetition rate (TD) and the modulation frequency (FD) are shown. For the FD, the tangential relationship leads to inaccurate results for small modulation frequencies for lifetimes in the range of 1–10 ns. As the last parameter, the time constant for the different measurement methods is illustrated in (**D**). For the FD FLIM, high exposure times lead to pixel saturation and therefore creates bigger standard deviations. For the TD, the correlation is inverse. For longer integration times, a smaller error bar is detected due to the larger number of photons that form the decay statistic.

2.1.2. Modulation Frequency

The modulation frequency, with which the sample is excited, plays an important role; hence, it defines in which range the fluorescence lifetime can be detected. For the TD, the limiting factor is the repetition rate of the laser source. All photons detected during an excitation cycle can be accurately assigned to a specific excitation-pulse and thus counted for the statistics. If the time between pulses increases (i.e., the repetition rate decreases), longer lifetimes can be measured and vice versa.

Because of the tangent function in Equation (17), it can be derived that a smaller modulation frequency must be selected for longer lifetimes. If this criterion is not met, the measurement results are more scattered. The reason for this could be explained easily by the phase lifetime. While the frequency increases, the working line becomes steeper due to the stretched tangent function. The phase determination is, therefore, less accurate and results in scattered lifetimes with bigger errors, as can be seen in Figure 1C and Table 1.

Table 1. Single and overall *p*-values for each frequency for the phase- and demodulation-lifetime of the FD technique, when measuring rose bengal.

	Modulation Frequency					
	1 MHz	**10 MHz**	**20 MHz**	**30 MHz**	**40 MHz**	**Overall *p*-Value**
τ_P [ns]	0.468	0.599	0.613	0.628	0.645	0.048
σ_P [ns]	1.387	0.056	0.053	0.04	0.052	
τ_M [ns]	0.501	0.589	0.602	0.631	0.645	0.046
σ_M [ns]	1.499	0.055	0.055	0.072	0.071	
Single *p*-Values	0.063	0.034	0.021	0.027	0	

For statistical evaluation, the *p*-value analysis for all phase- and demodulation-lifetimes was performed. The overall *p*-value (Table 1, last column) is the statistical proof that, for the different frequencies, the same lifetime is detected, while the single *p*-value (Table 1 bottom row) represents the consistent results between the phase- and demodulation-lifetimes. Due to the obviously too-large standard deviation for the frequency of 1 MHz, the corresponding raw data were left out for the calculation. This resulted in an overall *p*-value of 0.048 for the phase lifetime and 0.046 for the demodulation lifetime in a frequency range of 10 to 40 MHz. For the TD, a fluorescence lifetime of 0.633 ns was obtained for a frequency of 80 MHz. This value coincides with those from the FD.

The experimental results imply that the lifetime is not dependent on the modulation frequency as long as the repetition rate of the pulsed laser in TD or the modulation frequency of the laser in FD are adequately chosen.

2.1.3. Integration Time

The time period for how long the fluorescence signal is collected is given by the exposure time of the camera, whereas in TD, it is the time interval over which the laser focus remains at each sample point to gather sufficient events for building the histogram. For short integration times down to 0.3 s, only FD measurements are presented, whereas for longer times, TD measurements only up to 30 s are shown. Here, the expectation would be that the longer the integration time, the more accurate the determination of the lifetime due to increased statistics. This is confirmed for TD but not in the same manner for FD, as can be clearly seen in Figure 1D, with increasing error bars for FD measurements. Here, a saturation effect caused by the limited dynamic range of the camera plays an important role, which will be discussed later in detail.

Again, the *p*-value is used to make statistical statements. Here, the raw data at 300 ms exposure time in the FD were not taken into account due to the high standard deviation caused by pixel saturation. For the other measurements, the overall *p*-value was 0.010 (phase lifetime) and 0.038 (modulation lifetime). The *p*-value of the TD analysis was 0.024 and thus statistically significant. The comparison of the FD measurement series and their individual lifetime components (single *p*-values) can be seen in Table 2.

On the one hand, the longer the integration time in TD, the more events are collected, resulting in more accurate lifetimes due to better statistics. On the other hand, for the camera-based lifetime measurement, the exposure time can not be extended to arbitrary values because pixel saturation counteracts the improvement in accuracy due to the limited dynamic range of 14 bit in our case. If the exposure time is too long, the saturation distorts the measurement and causes larger error bars. To circumvent the saturation effect, several camera images with shorter integration times should be accumulated to improve the accuracy more effectively.

Table 2. Single and overall *p*-values for each exposure time for the phase- and demodulation-lifetime of the FD setup, as well as the exposure time of the TD setup for measurements on rose bengal.

	Integration Time (TD)						
	5 s	**10 s**	**20 s**	**30 s**			**Overall *p*-Value**
τ [ns]	0.842	0.859	0.875	0.856			0.024
σ [ns]	0.020	0.015	0.013	0.011			
	Exposure Time (FD)						
	5 ms	**10 ms**	**50 ms**	**100 ms**	**200 ms**	**300 ms**	**Overall *p*-Value**
τ_P [ns]	0.852	0.897	0.852	0.847	0.832	0.495	0.010
σ_P [ns]	0.181	0.166	0.180	0.348	0.368	1.636	
τ_M [ns]	0.832	0.895	0.842	0.877	0.904	0.595	0.038
σ_M [ns]	0.190	0.169	0.200	0.377	0.480	1.712	
Single *p*-Values	0.001	0.001	0.020	0.042	0.049	0.053	

2.2. Sample Dependent Parameter

Because the setup-dependent parameters have shown consistent results for TD and FD, the parameters regarding the fluorophore itself and its microenvironment were investigated with the following setup parameters fixed: FD excitation of 405 nm and 40 MHz, while for TD, the excitation wavelength was set to 780 nm (2P excitation at 390 nm) and 80 MHz. The values for the exposure or integration time are set individually depending on the fluorescence intensity. For all coming figures, only the phase lifetime is presented because up to this point, the consistency of phase- and demodulation-lifetimes is convincingly demonstrated. In addition to the *p*-values for the fluorophore-dependent parameters, *t*-tests were carried out to check if linear correlations are statistically significant [17].

2.2.1. Concentration

Although fluorescence is an intra-molecule relaxation process, some research groups were able to experimentally demonstrate a dependency on the molecular concentration, which suggests an inter-molecular influence. From moderate to high concentrations, an increase in the lifetime [12] was noticeable, while for even higher concentrations, drastic lifetime reductions occurred [6]. Inter-molecular interactions may cause these effects, which are, for example, re-absorption, self-quenching or other energy transfer mechanisms. The spectral overlap between the absorption and emission spectrum determines how strongly these mechanisms have an impact on the measured lifetime.

For the investigation of these effects, two dyes were chosen, which were measured in a concentration range starting from 10^{-1} M down to 10^{-5} M in the TD and the FD. The first used dye is lucifer yellow dissolved in ethanol, which has a small spectral overlap of its excitation and emission spectra. Fluorescein (dissolved in water) is used as the counterpart, which has a very large spectral overlap and should show a strong lifetime change in concentration-dependent measurements (Figure 2A).

As can be derived from Table 3, the series of measurements for lucifer yellow exhibits an approximately constant lifetime of around (10.289 ± 0.371) ns for the FD over the concentration range of 10^{-5} to 10^{-4} M. The TD shows an increase from 8.837 to 11.476 ns presumably due to a re-absorption process. For high concentrations beginning from 10^{-3} M, a slight decrease in TD and FD lifetime measurements can be detected that may result from energy transfer mechanisms. For a concentration of 10^{-1} M, the FD-results showed an average lifetime of 9.685 ns. The small effects of re-absorption and energy transfer for lucifer yellow can be seen in its spectrum in Figure 2B. Within the limits of the measurement accuracy, an agreement of the TD with the FD method could be shown. Furthermore, the *p*-values (Table 3) imply congruous experimental data. The phasor plot illustrates the consistent lifetime, which is characterized by the point cloud along the semicircle (Figure 2).

Table 3. TD and FD fluorescence lifetimes and *p*-values obtained for the concentration series for lucifer yellow and fluorescein.

Lucifer Yellow					
Concentration	**0.00001 M**	**0.0001 M**	**0.001 M**	**0.01 M**	**0.1 M**
τ_{TD} [ns]	8.837	11.476	11.087	10.265	9.907
σ_{TD} [ns]	1.027	0.565	0.221	0.053	0.049
τ_{FD} [ns]	10.532	10.646	10.294	10.288	9.685
σ_{FD} [ns]	1.020	0.647	0.506	0.267	0.298
Single *p*-Value	0.052	0.499	0.045	0.042	0.049
Fluorescein					
Concentration	**0.00001 M**	**0.0001 M**	**0.001 M**	**0.01 M**	**0.1 M**
τ_{TD} [ns]	4.015	4.049	4.212	3.176	0.209
σ_{TD} [ns]	0.064	0.025	0.018	0.028	0.002
τ_{FD} [ns]	3.356	3.623	4.336	3.520	0.380
σ_{FD} [ns]	0.203	0.115	0.075	0.045	0.106
Single *p*-Value	0.062	0.051	0.034	0.021	0.039

The second investigated fluorophore is fluorescein, whose spectral overlap between the absorption and emission spectra is large compared to lucifer yellow, as can be seen in Figure 2B. The TD-derived lifetimes show an increase in concentrations of 10^{-5} M to 10^{-3} M, mainly through the re-absorption process (Table 3). If the concentration is increased further (up to 10^{-1} M), a strong reduction in the lifetime to a value of 0.209 ns can be detected caused by self-quenching effects [18]. Compared to FD, the rise of the lifetime for concentrations of 10^{-5} M to 10^{-3} M is larger and possible due to the different absorption processes. The self-quenching caused a reduction to a value of 0.380 ns for 10^{-1} M, which is illustrated in Figure 2B.

The visual representation of the lifetimes by the phasor plot illustrates the self-quenching effect, which is characterized by an elongated point cloud distribution along the universal circle. By comparing the phasor plot of the TD and the FD, a slightly different distribution can be observed, which is also obvious by looking at the *p*-values in Table 3.

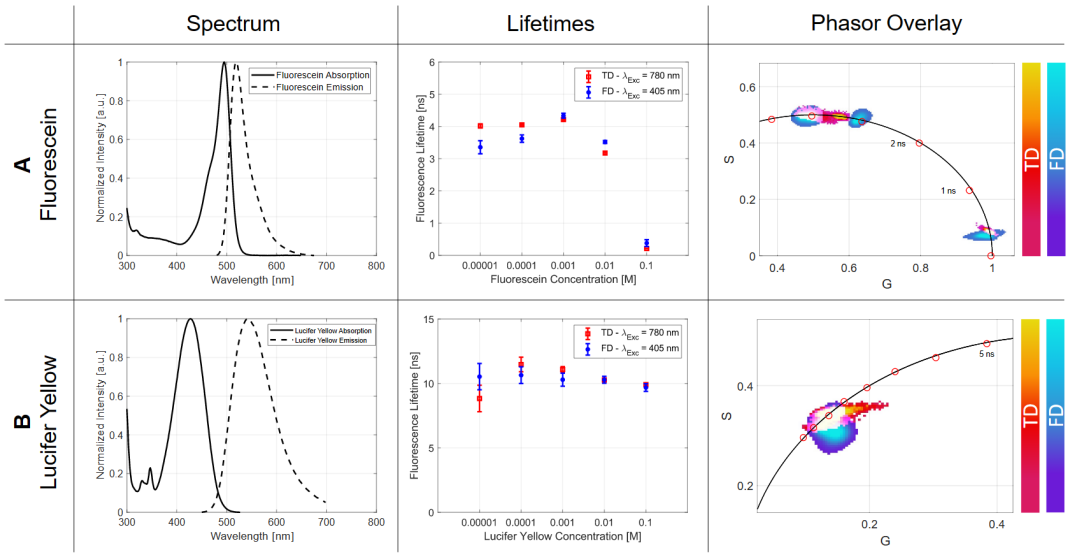

Figure 2. In this figure, the spectral properties of the two fluorophores used, fluorescein and lucifer yellow, are shown in (**A**) to check if the concentration could lead to an influencing parameter while measuring lifetime values, the spectral overlap must be observed. Fluorescein shows a relatively big spectral overlap compared to lucifer yellow. With the graphs in (**B**), the lifetimes of the TD are shown in red and the ones of the FD are in blue. For fluorescein, the lifetime change for high concentrations can be seen clearly, whereas the results of lucifer yellow stay nearly the same. The last column presents this relation in the phasor plot for the TD, as well as for the FD data.

2.2.2. Solvent Polarity

The fluorescence lifetime of a fluorophore changes based on the surrounding medium due to induced conformational changes [19]. For a variety of applications, these media must be chosen accordingly.

The extent of the solvent influence was measured by using both FLIM setups on rose bengal. Figure 3A visualizes the results for the fluorescence lifetimes in relation to the used media. The main influencing factor of the solvent is its polarity, therefore, a direct correlation can be seen (Figure 3B). An increase in the polarity results in a reduction in the lifetime and vice versa.

The graphical presentation (Figure 3C) of the lifetimes measured by TD as well as FD shows consistent results within the standard deviation. The lifetimes with the respective *p*-values for each solvent are given in Table 4.

Table 4. Calculated *p*-values, detected lifetimes and relative polarity values for different solvents.

Figure Declaration	Solvent	Relative Polarity	τ_{TD} [ns]	σ_{TD} [ns]	τ_{FD} [ns]	σ_{FD} [ns]	Single *p*-Value
a	Water	1	0.127	0.014	0.093	0.052	0.050
b	Methanol	0.762	0.645	0.012	0.605	0.052	0.045
c	Ethanol	0.654	0.852	0.011	0.883	0.062	0.039
d	Aceton	0.355	2.725	0.014	2.819	0.214	0.021

The phasor plot shows the individual point clouds of the different measurements for the corresponding media. Due to the linear relationship between the lifetime and the polarity change in the solvent, it can be stated that the polarity increases along the semicircle.

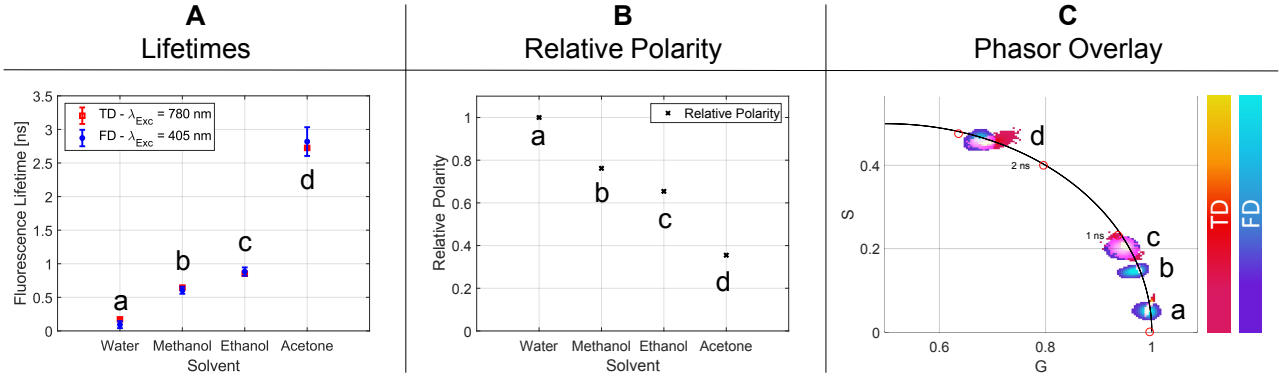

Figure 3. In section (**A**), the relative polarity of each individual solvent is illustrated. Compared to the obtained lifetimes in (**B**), an indirectly proportional behavior to the polarity is noticeable. Section (**C**) represents the overlayed phasor plots of the TD and FD data.

2.2.3. Temperature

Although there are well-known temperature influences on the fluorescence lifetime, which are treated later in the discussion section, this investigation uses fluorescein as an example to show the opposite. Measuring fluorescein (10^{-3} M in ethanol), the lifetime curve for different temperatures in the range of 21–42 °C is shown in Figure 4A and all individual lifetimes in Table 5. Using linear regression, a slope of 0.0021 ns/°C in the TD and a slope of 0.0015 ns/°C for the FD technique can be obtained. For most FLIM setups, accuracy in the two- to three-digit picosecond range is possible. The fluorescence lifetime change resulting from the temperature variation for fluorescein can thus be neglected. Furthermore, the standard deviation of each measurement showed no strong variation.

A *t*-test was used to check the consistency of the slopes determined and their intercept for TD and FD. A significance value of $T_{Slope} = 0.00313$ was determined for the slope and $T_{Axis} = 0.00689$ for the axis intercept. Both values are thus below the significance level of 0.05 and are consistent.

The phasor plot analysis illustrates the mono-exponential behavior of the temperature dependency measurement due to the point cloud on the semicircle (Figure 4A). Since the

values change only by a few picoseconds per measurement, all measurements together result in a uniform distribution.

Table 5. P-values and obtained lifetimes for the temperature series of fluorescein.

	Fluorescein								
Temperature [°C]	**23**	**25**	**27**	**29**	**31**	**33**	**35**	**37**	**39**
τ_{TD} [ns]	3.857	3.813	3.830	3.769	3.789	3.783	3.781	3.796	3.763
σ_{TD} [ns]	0.110	0.107	0.113	0.112	0.115	0.112	0.111	0.111	0.0122
τ_{FD} [ns]	3.859	3.833	3.834	3.832	3.828	3.823	3.815	3.816	3.816
σ_{FD} [ns]	0.110	0.110	0.120	0.130	0.130	0.120	0.110	0.120	0.120
Single *p*-Values	0.016	0.038	0.018	0.041	0.038	0.038	0.034	0.021	0.040

2.2.4. pH-Value

The pH-value of a fluorophore solution is of central importance during a fluorescence lifetime measurement. Based on the chemical composition of the dye, different spectral property changes can be obtained related to the pH-value. Therefore, a pH series of a 10^{-4} M concentration of fluorescein in water was measured in the TD and FD. The adjusted pH-values cover a range from 3 to 12. The detected lifetimes show a plateau for strongly acidic and alkaline pH-ranges, whereas the transition between them shows an approximately linear dependence. The resulting sigmoid function showed an overall lifetime change of ca. 1.5 ns for the adjusted pH range (Figure 4B and Table 6). The linear section from pH 6 to 9 was fitted and a *t*-test was performed. The slope of the TD was (0.336 ± 0.022) ns and for the FD (0.348 ± 0.028) ns. The *t*-test for the slope has a value of $T_{Slope} = 0.039$ and for the axis intercept $T_{Axis} = 0.021$.

Table 6. Measured lifetimes for the pH-series in the TD and FD for fluorescein.

	Fluorescein								
pH-Value	**3**	**4.5**	**7.5**	**7.8**	**8**	**8.2**	**9.3**	**11.2**	**12**
τ_{TD} [ns]	3.107	3.330	3.944	3.945	4.144	4.154	4.345	4.424	4.514
σ_{TD} [ns]	0.084	0.084	0.076	0.053	0.038	0.038	0.038	0.039	0.042
pH-Value	**3**	**4.5**	**6.5**	**7**	**7.5**	**8**	**8.5**	**10.5**	**12**
τ_{FD} [ns]	3.104	3.303	3.565	3.832	3.885	3.985	4.327	4.445	4.615
σ_{FD} [ns]	0.108	0.127	0.146	0.189	0.134	0.162	0.226	0.168	0.155

Furthermore, for the pH dependence, comparable results within the respective standard deviations could be retrieved for TD and FD. With the aid of the phasor plot, the lifetime change can be easily tracked and, with the appropriate calibration, also mapped to the corresponding pH level of the microenvironment (Figure 4B).

2.2.5. Quencher

Similar to the fluorescence lifetime dependency on the microenvironment (solvent polarity, temperature, pH), there are also other possibilities to intentionally quench a dye and thus obtain a shortening of the lifetime. For example, this can be utilized to mimic pathologically relevant coenzymes such as nicotinamide adenine dinucleotide (NADH) or flavin adenine dinucleotide (FAD) in optical phantoms used for clinical studies [20]. Here, coumarin 1 and coumarin 6 have similar spectra to the coenzymes but different lifetimes. To fix this issue and to fine-tune the desired lifetime of the phantom, quenching materials such as 4-hydroxy TEMPO are applied.

For the demonstration of the artificial quenching effect, this system is used as well. The starting solution was a coumarin 1 and a coumarin 6 mixture in ethanol with a concentration of $2 \cdot 10^{-4}$ M. The initial measurements showed a consistent lifetime for coumarin 1 of $\tau_{TD} = (3.239 \pm 0.017)$ ns in TD and $\tau_{FD} = (3.268 \pm 0.097)$ ns in FD (Figure 5A), and for coumarin 6 of $\tau_{TD} = (2.663 \pm 0.013)$ ns and $\tau_{FD} = (2.615 \pm 0.118)$ ns, respectively

(Figure 5B). Shortened lifetimes could be produced by adding different concentrations of 4-hydroxy TEMPO, which are shown in Figure 5.

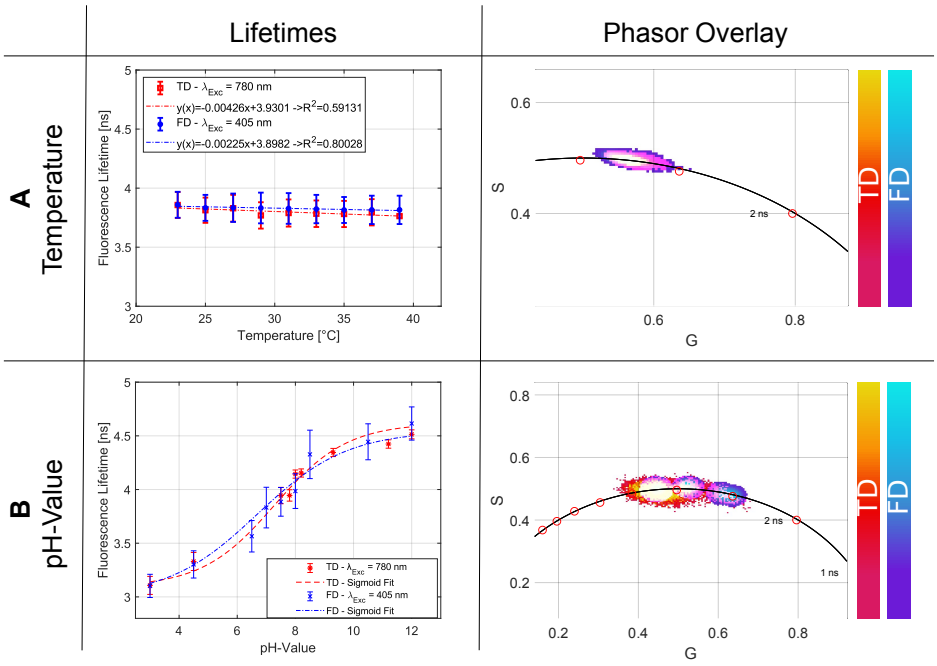

Figure 4. (**A**) shows the obtained results for the temperature dependency between 22–39 °C and the slope of the fitted linear regression for fluorescein in ethanol. The overall lifetimes for the TD and FD are also represented in the phasor plot where a single point cloud indicates no significant lifetime change. In (**B**) the pH dependency for values between 3 and 12 are shown, which follow a sigmoid function.

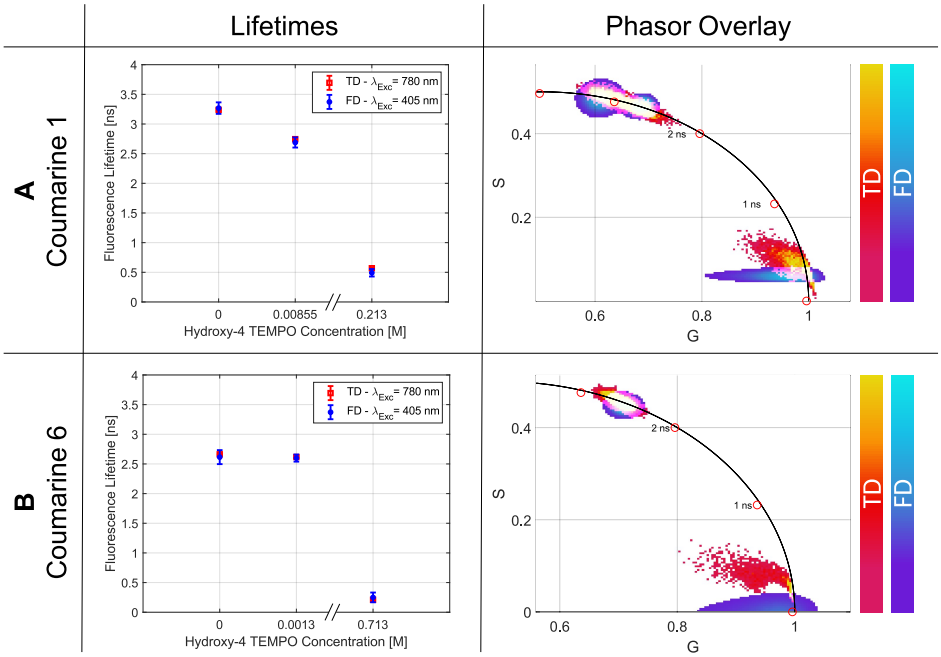

Figure 5. Results of the fluorescence lifetimes and phasor plot for the quenching series of coumarine 1 are illustrated in (**A**,**B**) for coumarine 6. With the help of 4-hydroxy TEMPO, it is possible to decrease the fluorescence lifetime to a specific value.

The phasor plot illustrates the shortening of the lifetime. The obtained values together with the *p*-values are listed in Table 7.

Table 7. Results for the quenching experiments for coumarine 1 and coumarine 6.

	Coumarine 1			Coumarine 6		
4-hydroxy TEMPO	**0 M**	**0.00855 M**	**0.234 M**	**0 M**	**0.0013 M**	**0.713 M**
τ_{TD} [ns]	3.239	2.745	0.569	2.663	2.617	0.209
σ_{TD} [ns]	0.017	0.016	0.011	0.013	0.014	0.002
τ_{FD} [ns]	3.268	2.689	0.492	2.615	2.599	0.25
σ_{FD} [ns]	0.097	0.086	0.063	0.118	0.060	0.082
Single *p*-Value	0.031	0.041	0.050	0.022	0.044	0.061

3. Discussion

By comparing TD- with FD-FLIM data of various fluorophores in different microenvironmental conditions and measured with different excitation and detection schemes, a statistical proof could be given that both techniques deliver equal lifetime values and become visible when using the phasor plot evaluation.

3.1. Setup Dependent Parameter

Specifically, experiments were performed by changing system parameters such as one- and two-photon excitation at various wavelengths, detection of many photons with a camera or single photons with a point detector, and using different modulation frequencies and exposure times (FD-FLIM) or repetition rates and acquisition times (TD-FLIM), respectively. All results retrieved with either technique were consistent, as demonstrated by statistical analysis. This remarkable outcome is based on the FLIM-advantage, which is extensively discussed in Section 4.1 of this manuscript.

3.1.1. Wavelength

The results showed that the lifetime data are independent with respect to the wavelength and to the kind of absorption process (1P- or 2P-excitation). The Einstein model for a two-level system gives an accurate explanation for both observations. Here, the fluorescence intensity resembles the population in the excited state, whereas the lifetime corresponds to the inverse radiative transition rate described by the so-called Einstein coefficient [21]. In this picture, the absorption process leading to the population in the excited state depends not only on the transition rate but also on the intensity of the excitation light source and how well it matches the photo-physical properties of the molecule. This is worth considering because, for excitation with two photons, one would expect to double the wavelength of the laser to reach the same excitation state as with one photon. However, it was demonstrated already in 1995 by Watt W. Webb and Chris Xu that 2P absorption spectra are most likely blue shifted to the 1P spectra because the cross sections of excited singlet states are not the same for 1P and 2P excitation [22]. This leads to different excitation probabilities for the various wavelengths and, thus, different fluorescence intensities. Interestingly, the radiative transition to the ground state seems to always start from the same excited singlet state. Therefore, the transition rate responsible for the lifetime is not affected by the kind of excitation process giving rise to the FLIM-advantage (see Section 4.1).

3.1.2. Modulation Frequency

For both techniques, the modulation frequency defines the range in which the fluorescence lifetime can be measured. While the FD laser can be modulated internally, the TD laser is limited by its repetition rate. Therefore, only the FD-FLIM setup was tested for different modulation frequencies showing a consistent lifetime in the range of 10–40 MHz. While the modulation frequency decreases, a slightly larger standard deviation can be noticed that results from the tangent function in Equation (10).

3.1.3. Integration Time

For different integration times in both techniques, an overall consistent lifetime for rose bengal in ethanol could be achieved (Figure 1D and Table 2). Whereas the TD-FLIM setup benefits from a longer integration time and statistics, the FD-FLIM setup suffers from overexposure and pixel saturation. This context can also be seen in the standard deviations listed in Table 2.

3.2. Sample Dependent Parameter

More interestingly are the sample-dependent parameters because they are responsible for differing lifetimes if comparing experiments performed under circumstances that are not always openly reported. One important goal of this extensive investigation was to demonstrate as many influencing parameters as possible to raise awareness among FLIM microscopists for taking full control over their experiment.

3.2.1. Concentration

The fact that the fluorescence lifetime is subject to a statistically independent process leads to the assumption that the concentration of a dye has no influence on this parameter. Even the fluorescence of only a small number of fluorophores is sufficient to record a decay curve if the integration/exposure time is set accordingly long.

Here, several effects cause variations in lifetime, as can be seen in Table 3 and Figure 2. For example, the apparently longer lifetimes can be explained by the effect of re-absorption: one molecule relaxes back to the ground state emitting a photon that is subsequently re-absorbed by another molecule lifting it to the excited state [23]. In contrast to the true lifetime τ, which is not affected, the detected lifetime τ_{Det} is prolonged because many photons may reach the detector only after this secondary step. Parameters that influence this process are the quantum yield Φ, as well as the concentration-dependent spectral overlap $J(\lambda,C)$ of the fluorophore (Equation (1)).

$$\tau_{Det} = \frac{\tau}{1 - J(\lambda, C) \cdot \Phi} \tag{1}$$

The difference in the 1P- to 2P-absorption spectra, absorption cross section and, further, the quantum yield suggest different τ_{Det} for 1P- and 2P-absorptions. This translates in this experiment to FD for 1P- and to TD for 2P-absorption.

Further, energy transfer mechanisms such as the self-quench effect or the Förster Resonance Energy Transfer (FRET) are responsible for the lifetime decrease in highly concentrated samples [6,24]. Here, a more efficient energy transfer occurs, where, for example, an excited molecule partially transfers its energy to a molecule in the ground state. This leads to the fact that only very fast transitions can undergo the radiative relaxation path of emission, which leads to a shortened detectable lifetime [25]. Again, the probability of these effects is based on several spectral and geometrical properties of the sample. The most important factor is the spectral overlap $J(\lambda, C)$ between the absorption $E(\lambda)$ and the emission $F(\lambda)$ spectrum (Equation (2)). This context determines whether a concentration-dependent lifetime change can be detected experimentally or not. The higher the overlap, the larger the possible self-quench effect.

$$J(\lambda, C) = \int E(\lambda) \cdot F(\lambda) \cdot \lambda^4 \, d\lambda \tag{2}$$

Fortunately, consistent lifetimes are most likely for the widely used working dilutions of around 10^{-6} M. However, for time-resolved measurements with high or changing concentrations, these effects have to be kept in mind.

3.2.2. Solvent Polarity

In Section 2.2.2, the fluorescent lifetimes of rose bengal were related to the solvent used. The graphic representation in Figure 3A showed that the increasing lifetime could

be correlated to a decrease in the solvent polarity (Figure 3B). The decisive parameter for this behavior will probably be the so-called solvatochromism [26]. It describes the spectral changes of a fluorophore while interacting with solvent molecules. A decreasing solvent polarity is understood as a negative solvatochromism, which is expressed by a higher energy difference between the ground and excited state. This change causes a hypsochromic shift, thus the blue shift of the absorption spectrum. The contrary case is a bathochromic shift and, therefore, has a lower energy difference. In addition to these spectral properties, parameters such as dipole moment, dielectric constant, refractive index and others are also changed, which are related to the observed fluorescence lifetime [27,28]. Again, time-resolved microscopy can be used to determine the environment more precisely and, in this case, to make statements about the polarity of a solvent [29].

3.2.3. Temperature

When changing the temperature, the non-radiative rate k_{NR}, also known as the quenching rate, is affected. With the help of the Stokes–Einstein–Debye relationship, the quenching rate can be expressed with a dependence on the temperature and the viscosity [6,30]. Looking at Equation (3), it is obvious that an increase in the temperature T is related to a decrease in the detected fluorescence lifetime τ_{Det}:

$$\tau_{Det} = \frac{1}{\frac{1}{\tau} + \frac{k_B T}{4\pi r^3 \eta}} \quad (3)$$

In Equation (3), next to the Boltzmann constant k_B, the radius r and the viscosity η are also included. How strongly the temperature affects the detected lifetime τ_{Det} depends on the structure of the fluorophore. While some of them only show a small change, such as fluorescein in this case, other specially designed dyes show a strong and well-defined lifetime change that is used as temperature sensors [31,32].

3.2.4. pH-Value

The pH-induced fluorescence lifetime change was also demonstrated by the group of Seungrag Lee, showing its importance in cancer research in modern days [33]. A chemical restructuring due to the additional uptake of H^+ ions with increasing pH-value results in altered photo-physical properties. In addition to this, there are also specially designed dyes that use the FRET mechanism to detect pH level changes by time-resolved methods [34].

3.2.5. Quencher

With quenching reagents such as 4-hydroxy TEMPO, it is possible to actively shorten the fluorescence lifetime due to a quenching process. The two most common quenching mechanisms are the following: The first one is the so-called static quenching process. In this situation, the quenching molecule, together with the fluorophore, creates a non-fluorescent complex. The outcome is a reduced concentration of fluorescent molecules leading to a weaker intensity. The radiative transition rate remains the same, and therefore, no fluorescence lifetime change can be noticed [35]. The second mechanism is the dynamic quenching effect. In this situation, a collision between the quenching molecule and the excited fluorophore takes place. Due to this collision, the fluorophore converts to the ground state without emitting a photon and therefore shortening the fluorescence lifetime [35]. The concentration of the quencher determines the extent to which the lifetime is shortened. This makes it possible to set almost any time constant desired. For different tasks, it is therefore possible to mimic defined biological components, for example, NADH and FAD by coumarine 1 and coumarine 6 [20]. With the help of the Stern-Volmer representation, it is possible to distinguish wherever a dynamic or static quenching process takes place [35]. For the sake of completeness, it has to be mentioned that next to the two above-mentioned quenching mechanisms, the FRET process [36] and proton/electron transfer reactions could possibly create a shortened lifetime as well [37].

3.3. Technique Comparison

Nevertheless, there are some differences between both techniques that are necessary to mention here. First, the image acquisition is either serial in TD or parallel in FD. In TD, the laser is focused and scanned over the sample. This takes more time than imaging the entire field of view at once with a camera, such as in FD. Therefore, the FD approach is faster compared to TD. On the other hand, two-photon excitation is only possible with focused light because of the high intensities needed for the nonlinear optical process to occur. The associated longer wavelengths lie in the near infrared, which is related to an optical window for biological tissue [38]. This enables deeper optical penetration depths by the excitation laser light in highly scattering media. Another advantage of two-photon over one-photon excitation is the optical sectioning capability, i.e., the sample can be virtually sliced like in confocal microscopy [7,39]. In conclusion, the TD technique plays out its potential the most in multiphoton microscopy, where an expensive ultrashort pulsed laser is required. On the other hand, if acquisition speed is of utmost importance, the FD technique clearly wins the race.

In addition to the acquisition, the data post processing and representation is complementary. While for the TD, no prior knowledge of the detected lifetime is needed, for the FD, more accurate values can be achieved if the modulation frequency of the excitation light is adjusted accordingly. Further, the extraction of the lifetime in the TD is complicated by the fact that dependent on the sample system, a mono- or multi-exponential fit has to be calculated. However, the interpretation is relatively easy, while for each exponential fit, a single lifetime and amplitude are calculated. In the FD, the raw data result in two lifetime components that are difficult to understand and illustrate in a concordant form.

With the help of the phasor plot, a graphical representation can be created that overcomes the above-mentioned problems. While the fit algorithm in the TD is omitted, the two components in the FD are compressed to a single vector. The phasor plot also helps to understand the lifetime distribution in an intuitive way. By comparing these graphs in biological contexts, changes in fluorophore ratios, quenching effects or other events can be easily observed and interpreted [40,41].

4. Materials and Methods

4.1. Theoretical Background

In order to understand the FLIM-advantage, the underlying quantum process is described briefly. The excitation photon elevates the sample molecules to an excited electronic state where they remain for a stochastic time period before they return to the electronic ground state either by radiative relaxation (k_R) under emission of one photon per molecule or by non-radiative relaxation (k_{NR}) through one or more so-called dark channels. The overall decay rate k is given by Equation (4):

$$k = k_R + k_{NR} \tag{4}$$

Using this definition, the decay of the population N of the excited state is governed by the following differential equation:

$$\frac{dN}{dt} = -k \cdot N \tag{5}$$

The solution to this is a single-exponential function:

$$N(t) = N_0 \cdot \exp(-k \cdot t) \tag{6}$$

The initial population N_0 is dependent on the excitation and, therefore, susceptible to the kind of excitation (1P or 2P) and the efficiency thereof, which is, besides other influences, defined by the excitation wavelength. The signal intensity corresponds to the number of emitted photons and is thus the negative rate described in Equation (5), that is $k \cdot N(t)$. The product reflects not only the decay rate k but also the amount of excited molecules

N—the better the excitation, the stronger the signal. However, if bleaching occurs, the initial population N_0 diminishes, and the signal drops accordingly.

On the other hand, FLIM only determines the decay rate k defined in Equation (4) and does not share this flaw of intensity measurements. However, it should be noted here that, though FLIM detects photons associated with the radiative channel k_R, it also reflects the non-radiative channels k_{NR} and, therefore, the overall rate k. Therefore, one must distinguish the detected lifetime $\tau_{Det} = \frac{1}{k}$ from the so-called true lifetime $\tau = \frac{1}{k_R}$. This is the reason for the differing lifetimes reported in the literature: experiments performed under different circumstances incorporate different dark channels that lead to the above-mentioned discrepancies in τ_{Det}. What makes it even more complicated is the fact that for a variety of experimental scenarios, Equation (6) may be written as a series of exponential functions accounting for several fluorescent components present in the sample. For convenience, this series shall be written in terms of the signal intensity $I(t)$ instead of the population $N(t)$:

$$I(t) = \sum_{n=1}^{N} I_n \cdot \exp\left(-\frac{t}{\tau_n}\right) \tag{7}$$

4.1.1. Time-Domain (TD)

In TD-FLIM, a time-correlated single photon counting (TCSPC) device measures the stochastic time period between excitation and emission of the fluorescent molecule, which determines the arrival time of each measured photon. Although advanced versions such as rapidFLIM [42] increased the detection rate considerably, the latter is still limited because the detection of single photons is a prerequisite of this technique. For data analysis, sufficient events are required for making the subsequent histogram of the arrival times statistically significant. Furthermore, the origin of each photon is localized by scanning the sample point-wise in a serial fashion. Therefore, statistics based on single-photon detection combined with serial point-scanning of the sample make the acquisition time long compared to frequency domain FLIM.

In this experiment, all samples were made with dye solutions containing neither structures nor different components to increase the validity of the results. Therefore, the measured histograms were fitted with a single-exponential reconvolution fit (Equation (8)), where the instrument response function (IRF) is convolved ($\otimes$) with the intensity decay curve including a background B.

$$FIT(t) = IRF \otimes I_0 \cdot \exp\left(-\frac{t}{\tau}\right) + B \tag{8}$$

The samples were scanned over a range of 200 times 200 pixels to average over the many molecules of the solutions. As expected, the recorded lifetimes of all pixels showed a statistically normal distribution. For calculating the expectation value and the standard deviation of the measurements, a Gaussian fit function was used.

4.1.2. Frequency Domain (FD)

In FD-FLIM, consecutive widefield images are taken in a rapid sequence with a camera to extract the lifetime for each pixel in parallel. Using specially developed sensors, these sequences can be recorded very fast and efficiently in a homodyne or heterodyne fashion [11]. Compared to conventional image sensors, each pixel of this sensor has two charge collection sites, including a switch that enables fast recording of two consecutive images. The switch is synchronized to the modulation of the excitation laser so that each image corresponds to half a period of the modulation. Please see [43,44] for a detailed description.

The excitation $E(t)$ of the sample is performed using a sinusoidal modulated light source and can be expressed as follows:

$$E(t) = A_{Exc} + B_{Exc} \cdot \sin(2\pi \cdot f_{Mod} \cdot t + \phi_{Exc}) \tag{9}$$

The parameter A_{Exc} describes the offset, B_{Exc} the amplitude and ϕ_{Exc} the phase of the excitation. With previous knowledge of the lifetime range τ to be measured, one can choose the optimal modulation frequency f_{Mod} in the experiment according to Equation (10):

$$f_{Mod} = \frac{1}{2\pi \cdot \tau} \tag{10}$$

In analogy to a forced oscillation, the generated fluorescence $F(t)$ is delayed, as well as demodulated (Equation (11)):

$$F(t) = C_{Em} + D_{Em} \cdot \sin(2\pi \cdot f_{Mod} \cdot t + \phi_{Em}) \tag{11}$$

The modulation depths M of the excitation $E(t)$, as well as of the fluorescence emission $F(t)$, are defined in Equations (12) and (13):

$$M_{Exc} = \frac{B_{Exc}}{A_{Exc}} \tag{12}$$

$$M_{Em} = \frac{D_{Em}}{C_{Em}} \tag{13}$$

The transfer function between excitation $E(t)$ and fluorescence $F(t)$ shows a demodulation (Equation (14)) and a phase shift (Equation (15)), which are directly related to the photo-physical properties of the sample.

$$M = \frac{M_{Em}}{M_{Exc}} \tag{14}$$

$$\phi = \phi_{Em} - \phi_{Exc} \tag{15}$$

Finally, with definitions made in Equations (14) and (15), two lifetimes τ_M and τ_P can be derived in the FD approach:

$$\tau_M = \frac{\sqrt{1 - M^2}}{2\pi \cdot f_{Mod} \cdot M} \tag{16}$$

$$\tau_P = \frac{\tan(\phi)}{2\pi \cdot f_{Mod}} \tag{17}$$

For single-exponential systems, both lifetimes τ_M and τ_P are the same. However, if the sample contains several fluorescent components with lifetimes lying in the range between τ_1 and τ_2, the demodulation lifetime τ_M differs from the phase lifetime τ_P [45]. Here, no direct assignment to the individual lifetimes of the components can be made. In this case, the single lifetime τ in Equation (10) should be substituted with the expression $\sqrt{\tau_1 \cdot \tau_2}$ for choosing the best possible modulation frequency when performing the experiment.

The FD camera (pco.FLIM, pco AG, Germany) used in the experiments detects the two components τ_M and τ_P with a homodyne detection scheme [43,46]. In contrast to TD-FLIM, an intensity-modulated diode laser was used for widefield illumination that excited the samples via one-photon absorption. Analogous to the TD evaluation, all detected pixel lifetimes are collected in a histogram and evaluated using a normal distribution fit (Figure 6B).

4.1.3. Phasor Plot Approach

Assuming that the emitted fluorescence of a fluorophore has a linear time-invariant behavior, it is possible to measure the lifetime in the TD as well as in the FD [46] without loss of information. For both approaches, however, the lifetime is not measured directly but has to be extracted from the data by subsequent analysis. Especially in the TD, this often leads to erroneous results depending on the selected fit function. Using the FD technique instead, the statistical fit is omitted, but the fact that two lifetimes are calculated complicates the interpretation of the results if the sample contains not just one but several components.

The strength of the phasor plot lies in the consistent representation of lifetimes measured with either technique. Furthermore, the fit algorithm needed in TD becomes obsolete, and the ambiguity present in FD is avoided [47,48]. For this expedient representation, the respective pixel information is transformed into a vector with a defined magnitude and angle. Because the pixel information differs in FD- and TD-FLIM, the two vector components G and S are calculated in different ways. In the FD, the transformation is based on the demodulation $M_{x,y}$ and the phase shift $\phi_{x,y}$ for each pixel (x, y):

$$G_{FD}(x, y) = M_{x,y} \cdot \cos(\phi_{x,y}) \tag{18}$$

$$S_{FD}(x, y) = M_{x,y} \cdot \sin(\phi_{x,y}) \tag{19}$$

For data collected in the TD, the decay curve $I(t)$ for each pixel (x, y) must be Fourier-transformed and normalized, as described by Equations (20) and (21):

$$G_{TD}(x, y) = \frac{\int_0^T I_{x,y}(t) \cdot \cos(2\pi \cdot f_{Rep} \cdot t) \cdot dt}{\int_0^T I_{x,y}(t) \cdot dt} \tag{20}$$

$$S_{TD}(x, y) = \frac{\int_0^T I_{x,y}(t) \cdot \sin(2\pi \cdot f_{Rep} \cdot t) \cdot dt}{\int_0^T I_{x,y}(t) \cdot dt} \tag{21}$$

The tips of the vectors, when plotted, are located within a semicircle, also called the universal circle. This graphical representation allows a quick and detailed overview of the lifetime distribution. If the vector point ends on the universal circle, it represents a single-exponential lifetime. However, if the vector points are inside the circle, this indicates that multiple fluorescent components have been detected (Figure 6C). Using this plot, it is possible to graphically represent the correspondence of TD to FD data. When plotting the vectors of all pixels in a single phasor plot, one can check the accuracy of the measurement by comparing the sizes and densities of the respective clouds. With this representation, further analysis methods such as image segmentation can be used, where only a defined portion of the phasor plot is reproduced in the intensity image [49]. This eliminates the need for shape-based segmentations for some applications and could be a way to label images for artificial-intelligence-based algorithms [50]. Furthermore, an innovative approach to metabolic imaging could be achieved with the help of the phasor plot [51]. For example, in the field of bacteria research, different metabolic states induced by their environment could be differentiated by applying segmentation to the phasor plot representation [52].

For comparing the obtained results of lifetime data and their different influence factors, a self-made Matlab (R2020a, MathWorks, USA) program calculates the phasor plot from the raw data detected either by the TCSPC device or the FD camera. The phasor plot depiction is then represented according to an additive color overlay. For the FD- and TD-results, a separate color map was created, which generates a corresponding blended color when superimposed (here pink to white).

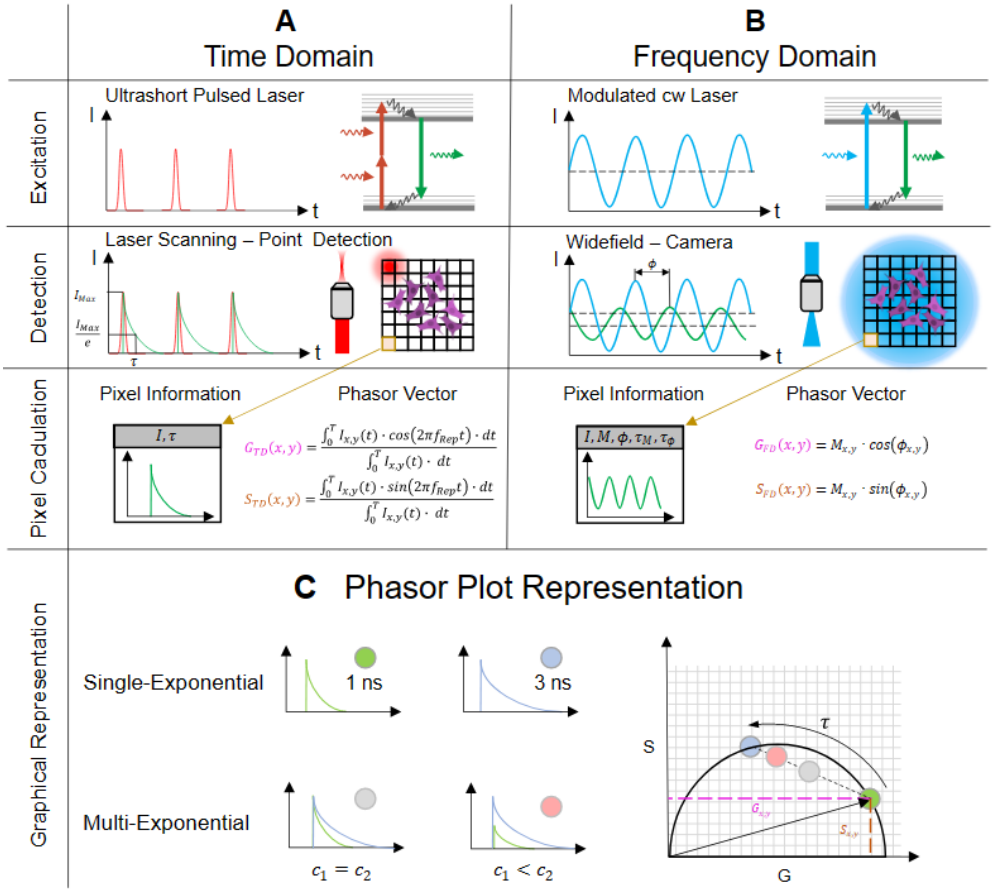

Figure 6. This figure shows both methods of obtaining the fluorescence lifetime in the (**A**) time-domain as well as in the frequency-domain (**B**). In the time-domain (**A**), a TCSPC device acts as a stopwatch and registers the time differences between the excitation (top row) and the arrival of the emitted fluorescence photon detected by a single photon detector (middle row). In the frequency-domain (**B**), the lifetime information is calculated by comparing the phase and amplitude between the modulated excitation (top row) and the modulated fluorescence of the sample (middle row). The obtained values in TD- and FD-FLIM (bottom row) are correlated by the Fourier transformation. (**C**) shows a way to represent both measurement results in a single plot, the so-called phasor plot. Each lifetime of a pixel is represented by a vector with the components G and S. Single exponential decays are located on the semicircle while multi-exponential decays are located within the semicircle. The position of the point cloud along the connection line between the two dyes indicates the concentration ratio c between them.

4.2. Experimental Setup

In order to obtain fluorescence lifetime data of different fluorophores, a custom-built two-photon excited fluorescence microscope (TPEFM) was used. The optical setup is built around a Nikon Eclipse Ti2 body, which was modified with various 3D-printed parts to make it suitable for a broad variety of multiphoton microscopy techniques as well as for the combination of TD- and FD-FLIM (Figure 7).

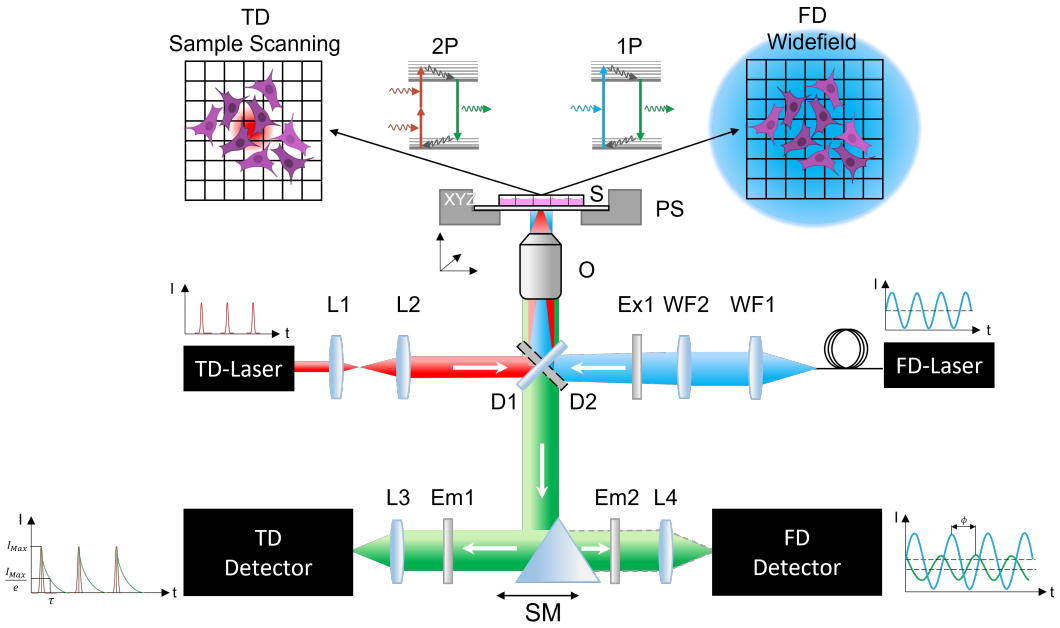

Figure 7. Schematic drawing of the optical setup. The excitation beam path for the TD setup is indicated in red. The fluorescence (green) for each pixel is detected with a single photon detector by switching the selection mirror **SM** to the right position. The widefield excitation beam path for the FD setup is shown in blue. Because one-photon excitation is used in FD and two-photon excitation is used in TD, the dichroic mirror **D1** differs from **D2**, thus excluding a simultaneous measurement. Instead, individual filter cubes, one containing the excitation filter **Ex1** and dichroic mirror **D1** and the other containing **D2**, are placed in the beam path depending on the measurement. L: lens, WF: widefield lens, Ex: excitation filter, D: dichroic mirror, S: sample, PS: piezo stage, Em: emission filter, SM: selection mirror, 1P: one-photon excitation, 2P: two-photon excitation, O: objective lens.

4.2.1. Time-Domain Experiment

Optical Setup: For the TD measurements, a sample scanning approach was realized (Figure 7). An ultrashort pulsed fiber laser (FemtoFiber Dichro Design, TOPTICA Photonics AG, Gräfelfing, Germany)—referred to as **TD Laser**—emitting pulses of 95 fs duration at two wavelengths of $\lambda_1 = 780$ nm and $\lambda_2 = 1034$ nm was used for excitation. Both pulse trains with a repetition rate of 80 MHz have a maximum laser power of 100 mW each. Next, a Kepler-telescope consisting of two lenses **L1** ($f_1 = 20$ mm) and **L2** ($f_2 = 100$ mm) with a 5× magnification was integrated. It was used to overfill the back aperture of the objective, thus focusing the light to the diffraction limit. The beam enters the microscope body through the rear input port and is reflected by a dichroic mirror **D1** (F38-749, AHF Analysentechnik, Tübingen, Germany) towards the objective. This optical component is located in a filter cube. The water immersion objective (CFI Apo MRD77200, Nikon, Japan) has a 20× magnification and a numerical aperture of 0.95. A piezo stage **PS** (Nano-LPS, Mad City Labs, Madison, WI, USA) moves the sample **S** along a defined path while the laser focus stays fixed. The generated fluorescence is then collected through the same objective and passes the dichroic mirror. A selection mirror **SM** reflects the fluorescence light either to the **TD Detector** or the **FD Camera**. For TD measurements, the fluorescence is filtered by a bandpass filter **Em1** (F39-653, AHF Analysentechnik, Germany) at (550 ± 25) nm before a lens **L3** ($f = 7.5$ mm) focuses it onto a single photon detector (MPD-APD 50, Micro Photon Devices Srl, Bolzano, Italy).

Electronic Signal Path: A TCSPC card (Multiharp 150, PicoQuant, Berlin, Germany) was used to detect the laser reference signal, as well as the signal of the single photon detector to measure the time difference between them. Care was taken that each detected photon was assigned correctly to the corresponding excitation laser pulse, which is recorded

by a photodiode. For this purpose, the photodiode signal is fed into an electronic pulse delay device (Picosecond Delayer, Micro Photon Devices Srl, Italy). This can shift the electrical signal with picosecond accuracy to compensate for time delays caused by the optical and electronic setup when recording the signals. The frame- and line-trigger required for image acquisition are generated by the control unit of the piezo stage.

Control Software: Two control programs were used for image acquisition. The Symphotime software (SymPhoTime64 Version: v2.6.5544, PicoQuant, Germany) manages data acquisition and raw data fitting. A self-made program (LabView Version: 17.0, National Instruments, Austin, TX, USA) is used to control the piezostage for sample scanning and generates the required line-start, line-end and frame trigger signals.

4.2.2. Frequency-Domain Setup

Optical Setup: For lifetime detection in the FD, a widefield approach is required (Figure 7). Thus, the moving piezostage **PS** with which the sample is moved in the TD was omitted. Two separate laser diodes (LuxX Series, Omicron, Germany) were used, offering an internal modulation capability to generate sinusoidal radiation at wavelengths of 405 and 445 nm with 100 mW laser power for each **FD Laser**. A liquid light guide directs the light to a widefield coupling located at the rear of the microscope containing appropriate lenses to collimate (**WF1**) and to focus (**WF2**) the emerging light into the back focal plane of the objective. A clean-up filter **Ex1** (405 nm: F49-406; 445 nm: F39-448, AHF Analysentechnik, Germany) in the beam path blocks all other wavelength components but the laser wavelength itself. To image the sample, the TD Objective **O** was reused. The laser light was separated by a dichroic mirror **D2** (405 nm: F48-425; 445 nm: F38-470, AHF Analysentechnik, Germany). For the elimination of any laser radiation or ambient light, an appropriate fluorescence filter **Em2** (405 nm: F47-424; 445 nm: F76-460, AHF Analysentechnik, Germany) was used. The selection mirror **SM** was aligned in order to focus the fluorescence signal via a lens **L4** onto an FD FLIM camera (pco.FLIM, pco AG, Kelheim, Germany).

Signal Path: The signal path includes two BNC cables between the camera and the laser. These cables were used to synchronize the homodyne detection method within the camera and the modulation signal of the laser. The data transfer between the control computer and the pco.FLIM camera was done via a USB 3.0 interface.

Control Software: The NIS Elements software (V5.0, Nikon, Japan) serves as control software. In addition to all control parameters for the lifetime detection, it is also used for analyzing the raw data. For calibration, a reference measurement with a sample of known lifetime (Starna Green, Starna Scientific Limited, Ilford, UK) has to be performed at the start of each measurement campaign.

4.3. Sample Preparation

To cover a wide range of dyes, a sample selection was made on the basis of spectral data to be measurable both with the TD and the FD systems. Among common fluorophores, those were selected with regard to their chemical properties to react, for example, strongly to a pH change such as fluorescein [53]. All sample fluorophores are listed in Table 8. For microscopic examination, a volume of 30 µL was placed in a sterile ibidi μ-Slide VI0.4 (80606, ibidi GmbH, Gräfelfing, Germany) and subsequently measured.

Table 8. Sample fluorophores with the respective concentration.

Number	Fluorophore	Distributor	Article No.	Molar Weight (g/mol)	Concentration (M)
1	Rose Bengal	Sigma Aldrich	330000	1017.64	10^{-1}, 10^{-2}, 10^{-3}, 10^{-4}
2	Lucifer Yellow	Sigma Aldrich	LO144	521.57	10^{-1}, 10^{-2}, 10^{-3}, 10^{-4}, $8{\cdot}10^{-5}$
3	Fluorescein	Sigma Aldrich	46955	332.31	10^{-1}, 10^{-2}, 10^{-3}, 10^{-4}
4	Coumarin 1	Sigma Aldrich	D87759	231.29	10^{-1}, 10^{-2}, 10^{-3}, 10^{-4}
5	Coumarin 6	Sigma Aldrich	546283	350.43	10^{-1}, 10^{-2}, 10^{-3}, 10^{-4}

Concentration: All sample fluorophores here were in salt form. Using the substance-specific property of the molar weight M and the desired amount of salt for a specific concentration c, the final volume V was calculated according to Equation (22). For concentration series, a stock solution of V = 1.5 µL with a concentration of $c = 0.1$ mol/L was produced that was afterward diluted to the desired concentration value.

$$m_{Fluorophore} = V \cdot c \cdot M \tag{22}$$

Solvent Polarity: To investigate whether the polarity has an influence on the fluorescence lifetime, the dyes were dissolved in different solvents (Table 9).

Table 9. Solvent used for the different types of fluorophores.

Solvent	**Distributor**	**Article No.**	**Fluorophores**
Water	Merck	1.15333	1, 2, 3
Methanol	Merck	1.06002	1, 2, 3, 4, 5
Ethanol	Merck	1.0098	1, 2
Aceton	Sigma Aldrich	270725-1L	1, 2

Microenvironment: As variable environmental parameters, the pH level and the temperature of the solvent were varied. The pH level adjustments were carried out on a dye solution of 20 ml that was diluted with HCl or NaOH, respectively, to achieve pH-values in the range between 3 and 12. The exact pH-value was checked with a pH-meter (CyberScan ph 100, Eutech InstrumentsPte Lte, Singapore) measuring device before and after each lifetime measurement.

A stage top incubation system (10720, ibidi GmbH, Germany) was used for controlled temperature changes. The temperature range to be covered was between 21 and 42 °C. For temperature verification, a chamber of the µ-Slide filled with the fluorophore solution under investigation was equipped with a temperature probe. For each measurement, a 10 min settling period was ensured to avoid possible temperature fluctuation during the measurement.

Quencher: Quencher experiments were made with 4-hydroxy TEMPO (176141, Sigma Aldrich Chemie GmbH, Darmstadt, Germany) in combination with coumarine 1 and coumarine 6 in two different concentrations. For coumarine 1, quencher concentration of 0.00855 and 0.234 M were used and for coumarine 6, quencher concentrations of 0.0013 and 0.713 M.

4.4. Statistics

To meet statistical standards, both TD and FD experiments were repeated seven times for each measurement. To confirm the reproducibility of the series, a p-value was calculated [54]. Therefore, a binomial distribution of τ and its error was assumed. If the p-value lies under a threshold of 0.05, it is statistically proven that the lifetimes that are obtained under different conditions are consistent. These conditions may be the application of a specific setup such as TD and FD or changing specific parameters such as temperature, pH level and so forth. For the graphical presentation of the measurement results, the mean values and their averaged standard deviation are displayed next to the phasor plot.

5. Conclusions

In this work, several experimental parameters are demonstrated to have an influence on the lifetime of specific fluorophores. This sensitivity can be used to the advantage of the experimenter: monitoring the lifetime will reveal how much a parameter changes during the measurement. On the other hand, having these findings in mind, one has to be careful to have control over all influencing parameters to make the results comparable and consistent with other measurements [55]. Therefore, it would be beneficial in future publications to also name the solvent polarity, the temperature and the pH-value next to

the fluorophore. If a large spectral overlap between the absorption and emission spectrum of the fluorophore exists, its concentration should also be mentioned.

The statistical analysis of all measurements proved without exception that the results of the TD setup are consistent with the ones obtained with the FD setup. Therefore, it can be concluded that both setups produce reliable data if all influencing parameters are under the control of the experimenter. Both techniques have the advantage in common of not relying on the way the fluorophore is excited. Therefore, their independence from the excitation laser wavelength or from the number of photons absorbed to transfer the fluorophore to its excited state was demonstrated.

While the discussion section explains which fundamental process lies behind each influencing parameter, it is possible to use this information and create fluorophores that function as biological sensors. For example, fluorescein is used in clinical studies to image the pH-value and infer cancer in breast tissue [33]. Further, special dyes were developed that can monitor the intracellular viscosity through the fluorescence lifetime [56]. Other fluorophores give the possibility to detect intracellular temperature changes [31]. Each experiment can thus benefit from selecting the right dye for the particular parameter that has to be determined.

Author Contributions: T.H. supervised the project. T.K. and J.J. made the experimental work along with the evaluation, validation and interpretation. C.F. helped with the sample preparation. T.K., J.J. and T.H. wrote the manuscript. T.H., R.S., A.R., J.J., T.K. and C.F. made reviews of the manuscript. All authors have read and agreed to the published version of the manuscript.

Funding: This research was funded by the BMBF project "OMOXI" (FKZ 13N14507), the FFG Bridge project "LITEScope" and the Bavarian Academic Forum (BayWISS)—Doctoral Consortium "Health Research".

Institutional Review Board Statement: Not applicable.

Informed Consent Statement: Not applicable.

Data Availability Statement: The data presented in this study are available in the article.

Acknowledgments: The authors would like to thank Lukas Krainer and Stefanie Kiderlen of the company Prospective Instruments and all their members for the possibility of using their fluorescent lifetime devices and their outstanding cooperation.

Conflicts of Interest: The authors declare no conflict of interest.

References

1. Ettinger, A.; Wittmann, T. Fluorescence live cell imaging. *Methods Cell Biol.* **2014**, *123*, 77–94. [PubMed]
2. Freudiger, C.W.; Min, W.; Saar, B.G.; Lu, S.; Holtom, G.R.; He, C.; Tsai, J.C.; Kang, J.X.; Xie, X.S. Label-free biomedical imaging with high sensitivity by stimulated Raman scattering microscopy. *Science* **2008**, *322*, 1857–1861. [CrossRef] [PubMed]
3. Ries, J.; Schwille, P. Fluorescence correlation spectroscopy. *BioEssays* **2012**, *34*, 361–368. [CrossRef] [PubMed]
4. Elson, E.L.; Magde, D. Fluorescence correlation spectroscopy. I. Conceptual basis and theory. *Biopolym. Orig. Res. Biomol.* **1974**, *13*, 1–27. [CrossRef]
5. Gratton, E.; Breusegem, S.; Sutin, J.D.B.; Ruan, Q.; Barry, N.P. Fluorescence lifetime imaging for the two-photon microscope: Time-domain and frequency-domain methods. *J. Biomed. Opt.* **2003**, *8*, 381–390. [CrossRef]
6. Berezin, M.Y.; Achilefu, S. Fluorescence lifetime measurements and biological imaging. *Chem. Rev.* **2010**, *110*, 2641–2684. [CrossRef]
7. Rubart, M. Two-photon microscopy of cells and tissue. *Circ. Res.* **2004**, *95*, 1154–1166. [CrossRef]
8. Icha, J.; Weber, M.; Waters, J.C.; Norden, C. Phototoxicity in live fluorescence microscopy, and how to avoid it. *BioEssays* **2017**, *39*, 1700003. [CrossRef]
9. Boens, N.; Qin, W.; Basarić, N.; Hofkens, J.; Ameloot, M.; Pouget, J.; Lefevre, J.P.; Valeur, B.; Gratton, E.; VandeVen, M.; et al. Fluorescence lifetime standards for time and frequency domain fluorescence spectroscopy. *Anal. Chem.* **2007**, *79*, 2137–2149. [CrossRef]
10. Casey, K.G.; Quitevis, E.L. Effect of solvent polarity on nonradiative processes in xanthene dyes: Rhodamine B in normal alcohols. *J. Phys. Chem.* **1988**, *92*, 6590–6594. [CrossRef]
11. Gadella Jr, T.W.; Jovin, T.M.; Clegg, R.M. Fluorescence lifetime imaging microscopy (FLIM): Spatial resolution of microstructures on the nanosecond time scale. *Biophys. Chem.* **1993**, *48*, 221–239. [CrossRef]

12. Kristoffersen, A.S.; Erga, S.R.; Hamre, B.; Frette, Ø. Testing fluorescence lifetime standards using two-photon excitation and time-domain instrumentation: Rhodamine B, coumarin 6 and lucifer yellow. *J. Fluoresc.* **2014**, *24*, 1015–1024. [CrossRef] [PubMed]
13. Fleming, G.; Knight, A.; Morris, J.; Morrison, R.; Robinson, G. Picosecond fluorescence studies of xanthene dyes. *J. Am. Chem. Soc.* **1977**, *99*, 4306–4311. [CrossRef]
14. Periasamy, A.; Wodnicki, P.; Wang, X.F.; Kwon, S.; Gordon, G.W.; Herman, B. Time-resolved fluorescence lifetime imaging microscopy using a picosecond pulsed tunable dye laser system. *Rev. Sci. Instruments* **1996**, *67*, 3722–3731. [CrossRef]
15. Krishnan, R.V.; Masuda, A.; Centonze, V.F.E.; Herman, B.A. Quantitative imaging of protein–protein interactions by multiphoton fluorescence lifetime imaging microscopy using a streak camera. *J. Biomed. Opt.* **2003**, *8*, 362–367. [CrossRef]
16. Lakowicz, J. *Principles of Fluorescence Spectroscopy*, 2nd ed.; Plenum: New York, NY, USA, 1999.
17. Andrade, J.; Estévez-Pérez, M. Statistical comparison of the slopes of two regression lines: A tutorial. *Anal. Chim. Acta* **2014**, *838*, 1–12. [CrossRef]
18. Glasgow, B.J. Fluorescence lifetime imaging microscopy reveals quenching of fluorescein within corneal epithelium. *Exp. Eye Res.* **2016**, *147*, 12–19. [CrossRef]
19. Love, L.C.; Upton, L.M.; Ritter, A.W. Solvent effects on fluorescence spectra decay times and quantum yields of atabrine and its homologs. *Anal. Chem.* **1978**, *50*, 2059–2064. [CrossRef]
20. Freymüller, C.; Kalinina, S.; Rück, A.; Sroka, R.; Rühm, A. Quenched coumarin derivatives as fluorescence lifetime phantoms for NADH and FAD. *J. Biophoton.* **2021**, *14*, e202100024. [CrossRef]
21. Hilborn, R.C. Einstein coefficients, cross sections, f values, dipole moments, and all that. *Am. J. Phys.* **1982**, *50*, 982–986. [CrossRef]
22. Xu, C.; Webb, W.W. Measurement of two-photon excitation cross sections of molecular fluorophores with data from 690 to 1050 nm. *JOSA B* **1996**, *13*, 481–491. [CrossRef]
23. Shibasaki, Y.; Suenobu, T.; Nakagawa, T.; Katoh, R. Effect of reabsorption of fluorescence on transient absorption measurements. *Spectrochim. Acta Part A Mol. Biomol. Spectrosc.* **2019**, *220*, 117127. [CrossRef] [PubMed]
24. Ishikawa-Ankerhold, H.C.; Ankerhold, R.; Drummen, G.P. Advanced fluorescence microscopy techniques—Frap, Flip, Flap, Fret and flim. *Molecules* **2012**, *17*, 4047–4132. [CrossRef] [PubMed]
25. Wallrabe, H.; Periasamy, A. Imaging protein molecules using FRET and FLIM microscopy. *Curr. Opin. Biotechnol.* **2005**, *16*, 19–27. [CrossRef] [PubMed]
26. Loving, G.S.; Sainlos, M.; Imperiali, B. Monitoring protein interactions and dynamics with solvatochromic fluorophores. *Trends Biotechnol.* **2010**, *28*, 73–83. [CrossRef]
27. Berezin, M.Y.; Lee, H.; Akers, W.; Achilefu, S. Near infrared dyes as lifetime solvatochromic probes for micropolarity measurements of biological systems. *Biophys. J.* **2007**, *93*, 2892–2899. [CrossRef] [PubMed]
28. Spange, S.; Reuter, A.; Vilsmeier, E. On the determination of polarity parameters of silica by means of solvatochromic probe dyes. *Colloid Polym. Sci.* **1996**, *274*, 59–69. [CrossRef]
29. Xiao, H.; Li, P.; Tang, B. Recent progresses in fluorescent probes for detection of polarity. *Coord. Chem. Rev.* **2021**, *427*, 213582. [CrossRef]
30. Jue, T. *Fundamental Concepts in Biophysics*; Springer: Cham, Switzerland, 2009; Volume 1.
31. Okabe, K.; Inada, N.; Gota, C.; Harada, Y.; Funatsu, T.; Uchiyama, S. Intracellular temperature mapping with a fluorescent polymeric thermometer and fluorescence lifetime imaging microscopy. *Nat. Commun.* **2012**, *3*, 705. [CrossRef]
32. Zhang, H.; Huang, H.; He, S.; Zeng, H.; Pralle, A. Monodisperse magnetofluorescent nanoplatforms for local heating and temperature sensing. *Nanoscale* **2014**, *6*, 13463–13469. [CrossRef]
33. Lee, J.; Kim, B.; Park, B.; Won, Y.; Kim, S.Y.; Lee, S. Real-time cancer diagnosis of breast cancer using fluorescence lifetime endoscopy based on the pH. *Sci. Rep.* **2021**, *11*, 16864. [CrossRef] [PubMed]
34. Burgstaller, S.; Bischof, H.; Gensch, T.; Stryeck, S.; Gottschalk, B.; Ramadani-Muja, J.; Eroglu, E.; Rost, R.; Balfanz, S.; Baumann, A.; et al. pH-Lemon, a fluorescent protein-based pH reporter for acidic compartments. *ACS Sensors* **2019**, *4*, 883–891. [CrossRef] [PubMed]
35. Albrecht, C. *Joseph R. Lakowicz: Principles of Fluorescence Spectroscopy*; Springer: Cham, Switzerland, 2008.
36. Förster, T. Zwischenmolekulare energiewanderung und fluoreszenz. *Ann. Der. Phys.* **1948**, *437*, 55–75. [CrossRef]
37. Doose, S.; Neuweiler, H.; Sauer, M. Fluorescence quenching by photoinduced electron transfer: A reporter for conformational dynamics of macromolecules. *ChemPhysChem* **2009**, *10*, 1389–1398. [CrossRef] [PubMed]
38. Anderson, R.R.; Parrish, J.A. The optics of human skin. *J. Investig. Dermatol.* **1981**, *77*, 13–19. [CrossRef]
39. Conchello, J.A.; Lichtman, J.W. Optical sectioning microscopy. *Nat. Methods* **2005**, *2*, 920–931. [CrossRef] [PubMed]
40. Lou, J.; Scipioni, L.; Wright, B.K.; Bartolec, T.K.; Zhang, J.; Masamsetti, V.P.; Gaus, K.; Gratton, E.; Cesare, A.J.; Hinde, E. Phasor histone FLIM-FRET microscopy quantifies spatiotemporal rearrangement of chromatin architecture during the DNA damage response. *Proc. Natl. Acad. Sci. USA* **2019**, *116*, 7323–7332. [CrossRef]
41. Ranjit, S.; Datta, R.; Dvornikov, A.; Gratton, E. Multicomponent analysis of phasor plot in a single pixel to calculate changes of metabolic trajectory in biological systems. *J. Phys. Chem. A* **2019**, *123*, 9865–9873. [CrossRef]
42. Orthaus-Mueller, S.; Kraemer, B.; Dowler, R.; Devaux, A.; Tannert, A.; Roehlicke, T.; Wahl, M.; Rahn, H.J.; Erdmann, R. RapidFLIM: The new and innovative method for ultra fast flim imaging. *PicoQuant Appl. Note* **2017**, *2017*, 1–8.
43. Chen, H.; Holst, G.; Gratton, E. Modulated CMOS camera for fluorescence lifetime microscopy. *Microsc. Res. Tech.* **2015**, *78*, 1075–1081. [CrossRef]

44. Esposito, A.; Oggier, T.; Gerritsen, H.; Lustenberger, F.; Wouters, F. All-solid-state lock-in imaging for wide-field fluorescence lifetime sensing. *Opt. Express* **2005**, *13*, 9812–9821. [CrossRef] [PubMed]
45. Verveer, P.J.; Squire, A.; Bastiaens, P.I. Global analysis of fluorescence lifetime imaging microscopy data. *Biophys. J.* **2000**, *78*, 2127–2137. [CrossRef] [PubMed]
46. Franke, R.; Holst, G.A. Frequency-domain fluorescence lifetime imaging system (pco. flim) based on a in-pixel dual tap control CMOS image sensor. *Imaging Manip. Anal. Biomol. Cells Tissues* **2015**, *9328*, 241–259.
47. Ranjit, S.; Malacrida, L.; Jameson, D.M.; Gratton, E. Fit-free analyss of fluorescence lifetime imaging data using the phasor approach. *Nat. Protoc.* **2018**, *13*, 1979–2004. [CrossRef]
48. Sun, Y.; Liao, S.C. *The Ultimate Phasor Plot and Beyond*; ISS Inc.: San Antonio, TX, USA, 2014.
49. Zhang, Y.; Hato, T.; Dagher, P.C.; Nichols, E.L.; Smith, C.J.; Dunn, K.W.; Howard, S.S. Automatic segmentation of intravital fluorescence microscopy images by K-means clustering of FLIM phasors. *Opt. Lett.* **2019**, *44*, 3928–3931. [CrossRef]
50. Mannam, V.; Zhang, Y.; Yuan, X.; Ravasio, C.; Howard, S.S. Machine learning for faster and smarter fluorescence lifetime imaging microscopy. *J. Phys. Photon.* **2020**, *2*, 042005. [CrossRef]
51. Datta, R.; Heylman, C.; George, S.C.; Gratton, E. Label-free imaging of metabolism and oxidative stress in human induced pluripotent stem cell-derived cardiomyocytes. *Biomed. Opt. Express* **2016**, *7*, 1690–1701. [CrossRef]
52. Bhattacharjee, A.; Datta, R.; Gratton, E.; Hochbaum, A.I. Metabolic fingerprinting of bacteria by fluorescence lifetime imaging microscopy. *Sci. Rep.* **2017**, *7*, 3743. [CrossRef]
53. Martin, M.M.; Lindqvist, L. The pH dependence of fluorescein fluorescence. *J. Lumin.* **1975**, *10*, 381–390. [CrossRef]
54. Krzywinski, M.; Altman, N. Significance, *p* values and *t*-tests. *Nat. Methods* **2013**, *10*, 1041–1042. [CrossRef]
55. Montero Llopis, P.; Senft, R.A.; Ross-Elliott, T.J.; Stephansky, R.; Keeley, D.P.; Koshar, P.; Marqués, G.; Gao, Y.S.; Carlson, B.R.; Pengo, T.; et al. Best practices and tools for reporting reproducible fluorescence microscopy methods. *Nat. Methods* **2021**, *18*, 1463–1476. [CrossRef] [PubMed]
56. Peng, X.; Yang, Z.; Wang, J.; Fan, J.; He, Y.; Song, F.; Wang, B.; Sun, S.; Qu, J.; Qi, J.; et al. Fluorescence ratiometry and fluorescence lifetime imaging: Using a single molecular sensor for dual mode imaging of cellular viscosity. *J. Am. Chem. Soc.* **2011**, *133*, 6626–6635. [CrossRef] [PubMed]

Chapter 5

Speed-Up Fluorescence Lifetime Imaging Microscopy

„Everything we hear is an opinion, not a fact. Everything we see is a perspective, not the truth.“

Mark Aurel

FLIM provides a unique perspective on biological sample systems, offering deeper insights into processes that are otherwise invisible through conventional methods [107]. For LNP research, FLIM can reveal pH-value shifts caused by proton pumps acidifying endosomes [166]. By employing pH-sensitive fluorophores such as SNARF [167], pHrodo [167, 168], Fluorescein [169, 20], or using FRET-based sensors [170], these microenvironmental changes can be quantified. However, the dynamic movement of LNPs and their subdiffractional size makes it challenging to measure lifetimes with sufficient accuracy to produce reproducible and meaningful datasets.

As discussed in **Chapter 4** and the accompanying publication [20] comparing established FLIM techniques, LNPs present unique challenges: their rapid movement exceeds the temporal resolution of TD-FLIM, while their small size complicates FD-FLIM measurements. These limitations prompted the development of alternative approaches to fluorescence lifetime measurements. By combining aspects of two advanced techniques— instant FLIM [171] and phase-resolved FLIM [172] — we developed a novel method that leverages the strengths of both. Using a lock-in amplifier [15], we achieved unprecedented speed, making FLIM compatible with resonant image scanning at a line frequency of 8 kHz, enabling a frame rate of 7.6 fps and generating 1024 x 1024 images in just 128 ms. Possible is this with the use of a digital lock-in amplifier that is able to stream fluorescence intensity-, lifetime- and phasor data with a suitable mathematical framework. This innovation surpasses the fastest commercial FLIM system called rapidFLIM [173] by a factor of 32 and is thus the fastest FLIM technique at the moment. A comparison of the performance of different lifetime techniques is given in **Appendix A.1**.

In this section, we present an overview of established FLIM techniques that already combined TD-FLIM and FD-FLIM and introduce our **S**peed-**U**p **P**has**E** **R**esolved **F**luorescence **L**ifetime **I**maging **M**icroscopy (SUPER-FLIM) method, showcasing its performance in the publication: *"Speed-Up Phase Resolved Fluorescence Lifetime Imaging (SUPER-FLIM) for Real-Time microenvironmental Sensing"*. This work illustrates how a shift in perspective—challenging established methods and embracing unconventional solutions—can transform limitations into innovative breakthroughs, reminding us that what we observe often depends on the lens through which we choose to see.

5.1 Combinations of TD- and FD-FLIM

With rapid advancements in detectors, lasers, and microscopy equipment, the precision and speed of FLIM techniques have steadily increased [174, 175]. This progress is exemplified by a TD-FLIM method known as rapidFLIM, which achieves frame rates of 3–5 frames per second for 300 × 300 pixels, corresponding to pixel dwell times of approximately 4 µs [173]. Such performance enables the study of biological systems in highly diffusive environments or systems undergoing rapid transitions, making FLIM measurements feasible in dynamic and challenging conditions.

However, despite these advancements, TD-FLIM remains slower in acquisition speed compared to FD-FLIM techniques, which are inherently faster due to their camera based nature. To address this limitation, some research groups are exploring hybrid approaches that combine the strengths of TD-FLIM and FD-FLIM [171, 172]. These efforts aim to leverage the high spatial resolution and accuracy of TD-FLIM with the speed advantages of FD-FLIM, creating a methodology that offers the best of both worlds. A comparison of the performance parameters of different as well as here not mentioned FLIM technologies can be found in the **Appendix A.1**.

5.1.1 instant FLIM

One significant technique that contributed to the development of our approach is instant FLIM, introduced by Yide Zhang *et al.* [171]. This FLIM method employs an ultrashort laser pulse to excite the sample via two-photon absorption, with fluorescence collected using a point detector. Instead of recording single photons, the complete fluorescence signal is routed into a miniaturized electronic circuit. Within this circuit, the signal is split into four paths, each subjected to a distinct phase shift. These signals are then multiplied by the laser signal, which is collected with a laser diode. Afterward, the signals are filtered to isolate the **D**irect **C**urrent (DC) component, which is subsequently recorded using a **D**ata **Aq**uisition (DAQ) card.

This process enables the extraction of phase and amplitude shifts between the laser pulse (simplified as a Dirac pulse) and the fluorescence response (represented as an exponential decay). Essentially, the technique integrates the excitation principles of TD-FLIM with the detection methodology of FD-FLIM. By employing a lock-in detection approach, this

method achieves both resolution-limited and super-resolution FLIM imaging at high frame rates, with pixel dwell times as short as 1 µs—comparable to those attained in FD-FLIM.

Despite its cost-effectiveness, the electronic circuits in this method are prone to day-to-day variability, requiring frequent recalibration. Additionally, the setup demands multiple analog inputs and outputs, which constrain the data transfer rates of standard DAQ cards. However, another group has implemented a similar lock-in detection scheme for fluorescence lifetime measurement, which offers improved stability, smaller error margins, and higher data transfer rates, potentially overcoming some of these limitations [172].

5.1.2 Phase Resolved FLIM

The group led by Kawata recorded FLIM data using an ultrashort laser pulse in conjunction with a lock-in amplifier [172]. Similar to the method developed by Yide Zhang [171], Kawata's group employed the excitation scheme of TD-FLIM combined with the detection approach of FD-FLIM, extracting both phase and amplitude modulations. To measure fluorescence lifetimes, the signal was mixed with four phase-shifted laser reference signals. By applying a reference curve to correct for amplitude-dependent lock-in signals, the lifetime information could be accurately extracted. This method enabled the group to determine lifetimes in a spectroscopic setup within approximately 90 s.

These techniques laid the groundwork for our novel approach, termed **S**peed-**U**p **P**has**E** **R**esolved **F**luorescence **L**ifetime **I**maging **M**icroscopy (SUPER-FLIM). We aimed to refine this technique to achieve faster detection, more precise lifetime measurements, and simplified data processing.

5.2 Speed-Up Phase Resolved Fluorescence Lifetime Imaging

Authors	**Thomas Kellerer**, Lukas Moser, Judith A. Müller, Joachim O. Rädler, and Thomas Hellerer
Title	*Speed-Up Phase Resolved Fluorescence Lifetime Imaging Microscopy (SUPER-FLIM) for Real-Time Microenvironmental Sensing*
Journal	Nature Communication Engineering Under review
DOI	—

We present an ultra-fast fluorescence lifetime imaging (FLIM) technique, SUPER-FLIM, enabling 3D live-imaging at unprecedented speeds. Traditional lifetime methods, such as rapidFLIM, achieve pixel dwell times of 4 µs using TCSPC [173]. Our method, leveraging digital lock-in detection combined with laser-scanning excitation, achieves a 30-fold improvement with acquisition times of only 102 ns, compatible with resonant galvo-scanners.

SUPER-FLIM uniquely supports high-resolution 3D imaging due to its scanning-based architecture, overcoming limitations of camera-based FD-FLIM but keeping its detection speed. Using this technique, we visualized endosomal acidification in live cells. This was made possible by changing the lipid composition of the DSPC lipid of the LNP by adding a lipid that contains carboxyfluorescein on its headgroup. Since the headgroup is in direct contact with the endosomal environment we can sense it with the lifetime parameter. A static measurment over a timespan of one hour revealed a lifetime reduction of 700 ps that revealed a pH-shift from physiological pH at 7.4 to a value of 4.0 according to our reference curve.

We also extended the technique and developed applications extending beyond imaging. For example, rapid lifetime acquisition enables **m**ulti-**l**ifetime-**FCS** (ml-FCS), sorting individual fluorescence bursts based on lifetime. This innovation enhances applications like **F**luorescence **L**ifetime **C**orrelation **S**pectroscopy (FLCS) [176, 177, 178], overcoming traditional FCS resolution constraints [179], and facilitates single-detector cross-correlation studies by leveraging decay differences when multiple fluorophores diffuse through the focus [180].

Our streamlined setup simplifies lifetime acquisition through novel mathematical models and software packages. Unlike previous techniques [171, 172], SUPER-FLIM is compatible with one-photon excitation using pulsed laser diodes or amplitude-modulated cw-lasers, eliminating reliance on ultrashort-pulsed lasers. For the first time, resonant galvanometer scanning achieves single frame lifetime images, unlocking rapid pixel dwell times (102 ns) and broadening the technique's utility across diverse microscopy and spectroscopy applications.

Detailed characterization of SUPER-FLIM is presented in the publication *"Speed-Up*

Phase-Resolved Fluorescence Lifetime Imaging (SUPER-FLIM) for Real-Time microenvironmental Sensing". A comprehensive statistical analysis compared our technique to existing methods, demonstrating its superior precision under identical sample conditions. Supplementary materials (**Appendix A.1**) provide insights into key system parameters, such as the lock-in amplifier's time constant, image averaging, and **P**hoto**m**ultiplier **T**ube (PMT) gain, further validating our approach.

5.2.1 Contribution

The technique, including its conceptualization, design, and implementation, was developed by Thomas Kellerer, who also created the optical and electronic setup. In addition, he was responsible for the sample preparation and carried out the experimental work. The mathematical framework and characterization measurements were conducted in collaboration with Thomas Hellerer and Lukas Moser as part of his project study. Thomas Kellerer also recreated the instant FLIM technique together with Lukas Moser.

For the biological experiments, Judith Müller, Gerlinde Schwake, and Daria Maksutova prepared the cells and LNP. The manuscript was primarily written by Thomas Kellerer and Thomas Hellerer. Furthermore, Thomas Kellerer developed the open-source software accompanying this technique, making it accessible for integration into almost any microscopy setup.

This work was part of a VDI-funded project, which Thomas Kellerer also managed, supervising all aspects of the project from the initial design to the final execution (SEMPA-Track FKZ: 13N16300).

Speed-Up Phase Resolved Fluorescence Lifetime Imaging (SUPER-FLIM) for Real-Time Microenvironmental Sensing

Thomas Kellerer[1,2], Lukas Moser[1], Judith A. Müller[2], Joachim O. Rädler[2], and Thomas Hellerer[1,*]

[1]Multiphoton Imaging Lab, Munich University of Applied Sciences, 80335 Munich, Germany
[2]Faculty of Physics and Center for NanoScience, Ludwig Maximilians-University, 80539 Munich, Germany
[*]Hellerer@hm.edu

ABSTRACT

Imaging cell biological processes while simultaneously sensing the microenvironment at high spatial and temporal resolution is a key goal in modern live-cell microscopy. However, adding parameters such as fluorescence lifetime compromises acquisition speed. To address this challenge, we introduce **S**peed-**U**p **P**has**E** **R**esolved **F**luorescence **L**ifetime **I**maging **M**icroscopy (SUPER-FLIM), an ultra-fast fluorescence lifetime imaging method that enables 3D live-imaging at unprecedented speed. Our approach combines digital lock-in detection with laser scanning excitation, allowing the simultaneous capture of fluorescence intensity, lifetime, and phasor data in real-time. With an acquisition time of 100 ns, SUPER-FLIM is ten times faster than state of the art FLIM techniques and is, for the first time, integrated with resonant galvo-scanners. SUPER-FLIM is a major step forward in live imaging as it provides high spatial resolution in 3D that cannot be achieved with camera-based frequency domain FLIM. As a proof of concept, we demonstrate its utility in observing lipid-nanoparticle acidification within living cells. Beyond imaging, SUPER-FLIM's rapid lifetime acquisition unlocks new applications, including multi-lifetime fluorescence correlation spectroscopy (ml-FCS), a novel FCS mode that sorts and correlates fluorescence bursts from diffusing particles based on lifetime characteristics. The technique is compatible with virtually any modulated light source and can be easily integrated into any laser scanning microscope using our open-source software.

Keywords: Fluorescence Lifetime Imaging Microscopy, Fluorescence Correlation Spectroscopy, Two-Photon Excitation, Resonant Galvo Scanner, Lipid Nanoparticles, Endosomes

1 Introduction

Fluorescence lifetime imaging microscopy (FLIM) has undergone many improvements since its first introduction in 1988[1]. From the very beginning, since 1989, not only time-correlated single photon counting (TCSPC) but also phase-resolved detection was used to determine the fluorescence lifetime[2]. Later, this technological division led to the terms time-domain(TD)- and frequency-domain(FD)-FLIM as depicted in **Figure 1 - A and B**. Despite the continued progress made in both fields, some of their key features have remained to this day: FD-FLIM excels at fast acquisition times, while TD-FLIM in combination with confocal detection or multiphoton excitation enables optical sections and thus extends the high spatial resolution to the third dimension[3–5] (**Figure 1 - a and b**). The reason for FD-FLIM being faster in acquisition is that it detects the integrated signal from many fluorophores whereas TD-FLIM detects the arrival times of single photons from individual fluorophores.
It is therefore crucial for 3D imaging to speed-up the acquisition in TD-FLIM to overcome its major disadvantage. A few successful attempts have been made and named digital frequency domain (DFD)[6], spectro-temporal laser imaging by diffracted excitation (SLIDE)[7] and rapidFLIM[8] among others. The reported pixel dwell times for recording an image are 40 µs, 23 µs and 4 µs, respectively. These values are close to those commonly used in laser-scanning fluorescence microscopy, and therefore, the techniques took full advantage of optical sectioning without slowing down the imaging speed.
However, live-imaging with resonant galvo-scanners requires significantly shorter pixel dwell times: for example, fast scanning of one axis/line divided into 1024 pixels with a resonance frequency of 8 kHz results in pixel dwell times of 122.3 ns. This is a factor of 33 to 328 times shorter than the reported values mentioned above. Here we present FLIM in combination with a resonant galvo-scanner, which for the first time to our knowledge fulfills the requirements while being able to obtain reliable lifetime data from a single frame. This is possible thanks to a hybrid approach: the excitation is similar to TD-FLIM while the detection is similar to FD-FLIM (**Figure 1 - C**). Other groups have pursued such an approach before: Zhang and co-workers

introduced instant FLIM[9] and Kawata and co-workers used a lock-in amplifier for phase-resolved detection[10]. While the former was interested in rapid imaging, the latter carried out spectroscopy with a reported acquisition time of 90 s. Our approach is very similar to Kawata's, as the hardware consists also of a lock-in amplifier, but because of our record-breaking short acquisition time of 102 ns, we call it speed-up phase-resolved(SUPER)-FLIM. Yet another difference between the two previous approaches and our own is the extraction of the fluorescence lifetime from the recorded signals, which we will compare in the subsection 2.2.

The overview depicted **Figure 1 - A and B** shows at the top that TD- and FD-FLIM also differ in excitation: sub 100 ps pulsed diode lasers or ultrafast solid-state lasers are used for TD-FLIM, while radio frequency modulated diode lasers are generally used for FD-FLIM. The detection of FD-FLIM is based on camera devices for extreme parallelization: it takes only 1 ms to record the fluorescence lifetimes for all sensor pixels, typically 1 million pixels[11]. This goes hand in hand with wide-field illumination, which in turn is only possible with single-photon (1P) excitation. On the other hand, TD-FLIM uses a more sensitive single-pixel detector and is usually combined with confocal microscopy or two-photon (2P) excitation for optical sectioning, which involves raster scanning of a focused laser beam across the sample. The higher detection sensitivity leads to pixel dwell times down to 4 µs as mentioned above, but it would take at least 4 s to capture an entire image of 1 million pixels. As shown in **Figure 1 - C**, we employ laser-scanning of a femtosecond laser for 2P excitation to take advantage of optical sectioning. However, in contrast to existing TD-FLIM techniques, we capture images containing 1 million pixels in only 128 ms which is 30 times faster. On the other hand, SUPER-FLIM does not rely on sophisticated laser sources emitting sub 100 ps pulses as required for TD-FLIM: we show that it is compatible also with 3 MHz modulated continuous-wave diode lasers used for 1P excitation that are cheaper and typically used in FD-FLIM.
Other microscopy techniques that go beyond imaging will also benefit from SUPER-FLIM. In these scenarios, the parallelization of camera-based detection does not come into play, as only a single or very few pixels are evaluated in the experiment. We show three examples: **1)** environmental sensing in living cells, **2)** measuring diffusion times with fluorescence correlation spectroscopy (FCS)[12,13] combined with lifetime information and **3)** live tracking of diffusing particles. These applications require short acquisition times and profit from higher information content by simultaneous monitoring the fluorescence lifetime[4]. Our examples contain the detection of **1)** pH-changes[14] in dye solutions and **2)** as particle separation in FCS experiments based on the lifetime.
For **3)** we have chosen a biological application and focused on a platform technology that has not only helped to contain the spread of the coronavirus, but will also be used to combat other widespread diseases such as cancer in the near future[15,16]. In this context, we monitored the cellular pathway of lipid nanoparticles (LNP) delivering messenger ribonucleic acid (mRNA) into living cells[17,18]. Initially, the ∼80 nm sized LNPs diffuse freely in cell culture medium until they attach to the cell membrane. Upon contact, some LNPs are taken up by the cell through endocytosis, forming membrane-bound vesicles known as endosomes. These endosomes then migrate within the cytoplasm. Over time, proton pumps begin to acidify the endosomal interior, triggering changes in the lipid layers of the nanoparticles. This acidification can destabilize the LNP structure, promoting the release of mRNA from the endosome into the cytosol where it can be translated[18]. The entire pathway is illustrated in a simplified form in **Figure 7 - a**. One key focus of ongoing research is the mechanism of endosomal release or escape. There are two hypotheses, the core of which is a changing pH value. Both will be explained in detail in the result section 2.8. For monitoring the cellular pathway, we have combined a fast tracking method with the ability of SUPER-FLIM to sense the environment, e.g. the pH value inside the living cell.

2 Results

2.1 Centerpiece of Speed-Up Phase Resolved Fluorescence Lifetime Imaging (SUPER-FLIM)

The key component of SUPER-FLIM is a lock-in amplifier, which is an effective tool for detecting noisy or weak signals. It requires two modulated inputs, e.g. in addition to the signal, a reference that is synchronized with it. In a first step, both inputs are mixed, which results in a frequency spectrum containing the sum and difference of their frequencies. As the latter are the same, the difference at zero frequency is reflected in the direct current (DC) component of the mixed output and extracted by applying a low-pass filter. In a second parallel step, the same procedure is repeated but with a 90° phase-shifted version of the reference. The output from the first step is the G-component and the output from the second step is the S-component of the phasor plot used for displaying FLIM data[19,20]. Dividing S by G results in the tangent of the phase lag φ (**Figure 1 - C**). For a detailed mathematical description of the lock-in amplifier please see the supplementary file (**S1**). The most important parameters that influence the accuracy and acquisition speed are the filter order and the time constant (TC) of the low-pass filter used. The shortest TC time we used was set to 102 ns to match the pixel dwell time for resonant galvo-scanning of 122.3 ns. SUPER-FLIM converts the detected phase lag into a fluorescence lifetime as in FD-FLIM which is explained briefly in the following.

In FD-FLIM, the excitation of molecules is modulated with frequency ω and, as a direct consequence, their emitted fluorescence as well. The detected signal can therefore be characterized by the modulation M and phase lag φ which results

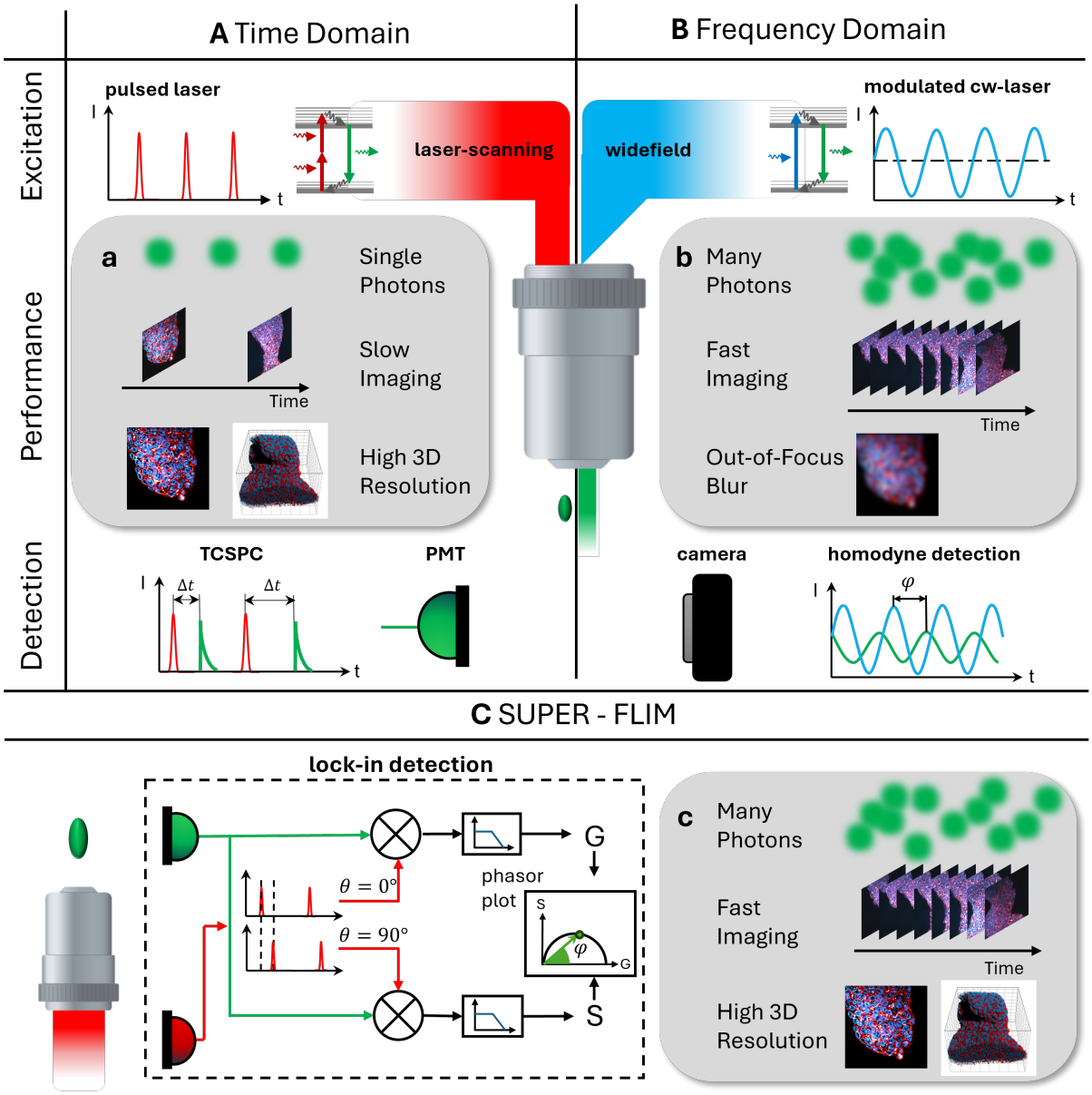

Figure 1. Comparison of TD- and FD-FLIM and Working Schematic of SUPER-FLIM. Section **A** describes the working mechanism of the TD-FLIM. Usually in a laser scanning setup a pulsed laser excitation is exciting the sample pixel wise. The fluorescence is detected by a point source detector and a TCSPC device records single photons. In **a** the the working scheme is shown, that single photons were detected, the imaging speed is moderate but capable of optical sectioning, deep tissue imaging and high resolution. In **B** the working mechanism of the FD-FLIM is illustrated where modulated cw-Laser are used and the fluorescence is collected with cameras in a widefield approach. In **b** we see that in FD-FLIM all photons are collected resulting in a higher frame rate but lower resolution with no optical sectioning capabilitys. On the bottom in **C** the SUPER-FLIM technique is shown. Here we are using the same optical setup like in TD-FLIM but using a lock-in detection to extract the phase information imitating the FD-FLIM detection. In **c** we see the combined advantages of **a** and **b**. In SUPER-FLIM we are using all photons and increase the frame rate further. The resolution is the same like in TD-FLIM enabeling optical sectioning and deep tissue imaging.

in two lifetimes for one sample: the modulation-lifetime τ_M and the phase-lifetime τ_φ. Both lifetimes coincide if the sample consists of a single class of fluorophores corresponding to a single-exponential decay in TD-FLIM. For a detailed description of both lifetimes and their difference please refer to[21]. Since we are only dealing with the phase-lifetime τ_φ here, we omit the index φ and simply refer to it as lifetime τ, for which **Equation 1** holds:

$$\omega\tau = \tan(\varphi) \tag{1}$$

As there is no direct access to the phase lag φ, the signal is compared to a reference $\cos(\omega t + \theta)$ oscillating with the same frequency ω but a known phase θ: signal and reference are mixed and integrated over one period $T = \frac{2\pi}{\omega}$. The integral value is maximized if the phase shift between both is zero and thus the signal phase φ equals the known phase θ. However, optical and electrical paths in the setup may differ for reference and signal and must be factored out before the lifetime can be correctly derived. Therefore, the setup needs to be calibrated either with second harmonic generation (SHG)[22,23] - a signal with virtually no delay - or with a known fluorescence lifetime of a standard sample[24,25]. More detailed explanations of the calibration procedure are presented in the supplementary material (**S3**). For the mathematical description we must treat the time evolution of the signal as the convolution of the modulated excitation with the fluorescent decay of the molecule under study. This is simplified to the exponential decay itself $\hat{a}e^{-\frac{t}{\tau}}$, if ultrashort laser pulses excite all molecules at once during each period corresponding to repetitive Dirac pulses. By calculating the integral, we obtain the expression given in **Equation 2** which is measured as voltage V in the experiment. The detailed derivation including double partial integration can be found in the supplementary document (**S2**).

$$V = \int_0^T \hat{a}e^{-\frac{t}{\tau}} \cdot \cos(\omega t + \theta)dt = \frac{\hat{a}\tau}{\omega^2\tau^2 + 1} \cdot \left(e^{-\frac{T}{\tau}}\omega\tau \cdot \sin(\theta) - e^{-\frac{T}{\tau}}\cos(\theta) - \omega\tau \cdot \sin(\theta) + \cos(\theta)\right) \tag{2}$$

The integral value V depends not only on the phase shift θ which is directly related to the phase lag φ but unfortunately also on the detected signal strength $\hat{a}$. Fortunately, the latter is simply a prefactor and can be eliminated by forming a quotient from integrals with different phase shifts θ.

2.2 Comparison with Similar FLIM Techniques

In the following, we present two existing approaches based on the above considerations and on excitation with ultrashort laser pulses: one called instant FLIM introduced by Yide Zhang *et al.*[9] and another called Phase Resolved FLIM introduced by the group of Yoshimasa Kawata[10]. Thereafter, we will present our approach called SUPER-FLIM for easy comparison. The phase shifts θ used in the three methods amount to 0°, 45°, 90°, 180° and 270°. For convenience of the reader, the expressions for the integrals V are summarized in **Table 1** by inserting these θ values into **Equation 2**.

Table 1. Equation for different phase shifts.

Phase shift θ	Multiple of $\frac{\pi}{4}$	Expression
0°	0	$V_0 = \frac{\hat{a}\tau}{\omega^2\tau^2+1}\left(e^{-\frac{2\pi}{\omega\tau}} - 1\right) \cdot (-1)$
45°	1	$V_1 = \frac{\hat{a}\tau}{\omega^2\tau^2+1}\left(e^{-\frac{2\pi}{\omega\tau}} - 1\right) \cdot \left(\frac{\omega\tau-1}{\sqrt{2}}\right)$
90°	2	$V_2 = \frac{\hat{a}\tau}{\omega^2\tau^2+1}\left(e^{-\frac{2\pi}{\omega\tau}} - 1\right) \cdot (+\omega\tau)$
180°	4	$V_4 = \frac{\hat{a}\tau}{\omega^2\tau^2+1}\left(e^{-\frac{2\pi}{\omega\tau}} - 1\right) \cdot (+1)$
270°	6	$V_6 = \frac{\hat{a}\tau}{\omega^2\tau^2+1}\left(e^{-\frac{2\pi}{\omega\tau}} - 1\right) \cdot (-\omega\tau)$

instant FLIM

In instant FLIM, four phase shifts of 0°, 90°, 180° and 270° are used[9]. We refer to the quotient defined by Zhang and given in **Equation 3** as α:

$$\alpha := \frac{V_0 - V_4}{V_2 - V_6} = -\frac{1}{\omega\tau} \Longleftrightarrow \omega\tau = -\frac{1}{\alpha} \tag{3}$$

On the right of this equation, we resolved the quotient α for the product $\omega\tau$, which equals the tangent of the phase lag φ (see **Equation 1**). As can be seen, the quotient α is the negative inverse of the tangent. Plotting the graph of $\tau(\alpha)$ has a hyperbolic shape as can be seen in **Figure 2 - b** for different values $\frac{\omega}{2\pi} = 40\,\text{MHz}$, 80 MHz and 120 MHz (dashed blue, solid black and dashed orange line).

Phase Resolved FLIM

In Phase Resolved FLIM, three phase shifts of 0°, 45°, and 90° are used[10]. We refer to the quotient defined by Kawata and given in **Equation 4** as β:

$$\beta := \frac{V_0 - V_1}{V_0 - V_2} = \frac{\omega\tau + \sqrt{2} - 1}{\sqrt{2}\omega\tau + \sqrt{2}} \Longleftrightarrow \omega\tau = -\frac{\beta + \frac{1}{\sqrt{2}} - 1}{\beta - \frac{1}{\sqrt{2}}} \tag{4}$$

Plotting the graph of $\tau(\beta)$ has likewise a hyperbolic shape as can be seen in **Figure 2 - c** for different values $\frac{\omega}{2\pi} = 40\,\text{MHz}$, 80 MHz and 120 MHz.

SUPER-FLIM

In SUPER-FLIM, only two phase shifts of 0° and 90° are used. We refer to our quotient given in **Equation 5** as γ:

$$\gamma := \frac{V_2}{V_0} = -\omega\tau \Longleftrightarrow \omega\tau = -\gamma \tag{5}$$

In SUPER-FLIM, the quotient γ is the negative tangent of the phase lag φ. Plotting the graph of $\tau(\gamma)$ has a linear shape with the inverse of ω as slope (**Figure 2 - d** showing graphs for different values $\frac{\omega}{2\pi} = 40\,\text{MHz}$, 80 MHz and 120 MHz). Because SUPER-FLIM uses only two phase shifts, which are inherent to lock-in detection, only one demodulation channel of the lock-in amplifier is required in contrast to the other methods. This increases the data transfer rate of the device significantly and makes further calculations easier.

Important Difference in Lifetime Mappings

For comparison of the presented methods, three simulated lifetimes of 1.0 ns, 4.0 ns and 7.0 ns were evaluated covering a wide range of commonly used fluorophores. The accuracies of the methods differ as can be clearly seen by inspecting the error bars of the corresponding data points in **Figure 2-b, c, d**. These are simulated with a set of 10.000 lifetime instances, assumed to follow a normal distribution with a standard deviation of $\sigma = 0.2$ ns as depicted in **Figure 2 - a**. Due to the hyperbolic shapes for instant FLIM and Phase Resolved FLIM there is a tipping point at which the accuracy of the lifetime changes from low to high sensitivity to fluctuations of the quotients α and β. For instant FLIM, this tipping point is around $\tau \approx 3$ ns with slight dependence on ω. For Phase Resolved FLIM, the tipping point is not as pronounced as for instant FLIM and lies at longer lifetimes around $\tau \approx 4$ ns. In contrast, SUPER-FLIM does not share this tipping behavior due to its linear dependence making the errors uniform for the full range of lifetimes.

It is therefore better suitable for measurements where the sample's lifetime is unknown or when the dependence of τ on an environmental parameter (e.g. the pH-Value) needs to be measured over a wide range with the same relative precision.

2.3 Validation of SUPER-FLIM

To experimentally validate our technique, we measured seven fluorescence lifetimes ranging from about 100 ps to about 4 ns. The samples were selected to cover a wide range of lifetimes, emission spectra, quantum yields and other photophysical properties. For a robust statistical analysis, we varied several sample and device parameters. Four different dyes in 1 mM solutions were examined: Rhodamine 6G, Rhodamine B, Fluorescein and Rose Bengal (RB). The latter was dissolved in dH_2O, methanol, ethanol and acetone to cover different solution polarities. For 2P-excitation, we used 100 fs-laser pulses with 80 MHz repetition rate and 1030 nm or 780 nm wavelength. All measurements were performed with eight different TC values of the lock-in amplifier as this strongly influences the accuracy of the result. Each measurement took 10 s and was repeated ten times. For the sake of clarity, **Figure 2** shows only some exemplary data for Rhodamine B in the midsection "Experiment". Further data, not shown here, can be found in the supplementary materials (**S4.II** and **S5**).

Figure 2- e displays the trace of the quotient γ with zoom-in to 1 s; **(f)** shows the corresponding lifetime with zoom-in to 1 s. **(g)** depicts the histogram built from all lifetimes of the trace, each measured with a TC value of 10 µs. The phasor plot of all data points is visualized in **(h)**. The measured lifetimes for all samples are plotted against γ in **(i)** making the linear dependence visible and are compared to literature values in the bar graph **(g)** (see **S5** for references used).

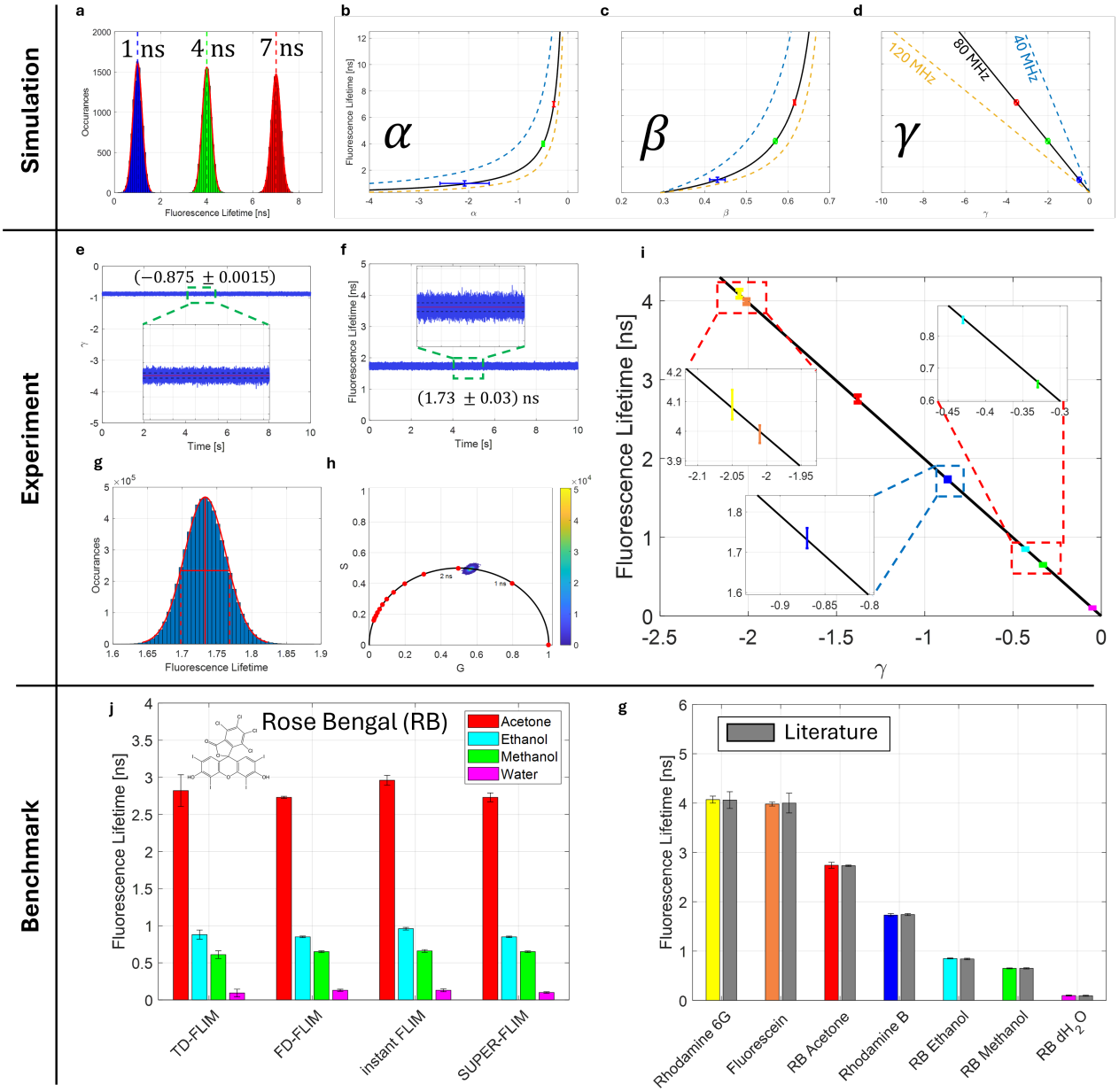

Figure 2. Intensity References for Lifetime Extraction: Due to the intensity dependency in the lock-in amplifier signal, we investigated three approaches to evaluate lifetimes that remain unaffected by varying intensity levels. To illustrate this, we simulated three lifetime distributions centered at 1 ns, 4 ns, and 7 ns with $\sigma = 0.2$, as shown in **(a)**. These distributions were used to calculate lifetime values, including error bars, across different approaches. The results are displayed for Instant FLIM in **(b)**, for phase-resolved FLIM in **(c)**, and for our approach in **(d)**. We also showed the course for different frequencs. The black solid line presents 80 MHz, the dashed blue line 40 MHz and the orange dashed line for 120 MHz. An experimental result for a 1 mM Rhodamine B solution the γ curve is represented in **e** with a zoomed inset. In **f** the lifetime distribution with the appropriated histogram in **g** is shown. From the lock-in values the phasor plot can be calculated (**h**). A statistical representation along with insets of the seven investigated samples is represented in **i** on the γ trace and in **g** as bar graph with the literature values. As benchmark between the most common FLIM techniques we measured the polarity dependend lifetime of Rose Bengal and displayed it in a bar graph in **j**.

2.4 Compatibility of SUPER-FLIM

The main part of the Results section focuses on the exceptional high acquisition speed of SUPER-FLIM. However, since many research groups have no access to resonant galvo-scanners, diode laser lasers with sub 100 ps pulses or ultrafast lasers for

2P-excitation, we wanted to demonstrate the compatibility of SUPER-FLIM with common light sources and conventional laser-scanners (see supplementary information **S10**). Thanks to this versatility, SUPER-FLIM can be easily integrated into a variety of microscope setups, making it even more attractive for users with restricted budget. To illustrate this, we have repeated the measurements presented in the above subsection 2.3, but with a different excitation scheme as diode lasers are common light sources in most commercially available laser-scanning microscopes. For 1P-excitation, a function generator modulated the 561 nm cw-diode laser at 3 MHz with two waveforms, sinusoidal and rectangular.

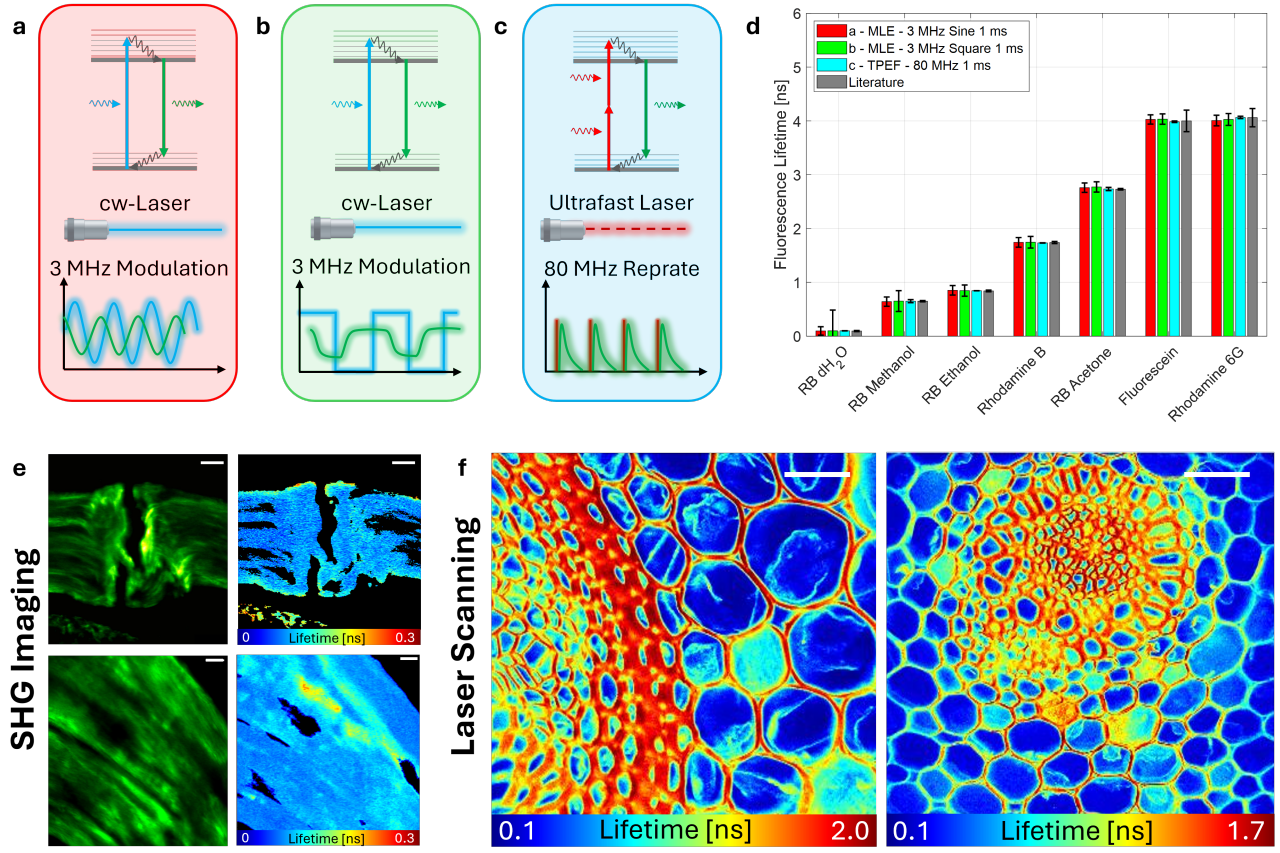

Figure 3. SUPER-FLIM with Various Excitation Sources: SUPER-FLIM is capable of measuring fluorescence lifetime using different excitation methods, including one-photon excitation with various modulation types (**a** sinusoidal and **b** squared waveforms). In **c**, two-photon excitation with a pulsed laser source is demonstrated. The results for seven different fluorophores, each tested across excitation forms and compared to literature values, are summarized in **d**. In **e**, two SHG images of collagen I fibers are shown, with lifetimes centered around 100 ps. In **f**, two lifetime images of a *Convallaria majalis* were acquired using a standard galvo-galvo scanner with a longer TC time of 1 µs. Scale bars: **e** - top 20 µm, botton 10 µm, **f** - 100 µm.

The fluorophore solutions were measured ten times for ten seconds each using two different time constants (TC) of 10 µs and 1 ms. The bar graph of Figure 3 displays the results for 1 ms TC alongside the results from Chapter 2.3 and some literature values. The statistics for Fluorescein illustrate our general findings: the relative error is highest for sinusoidal modulation, followed by square wave modulation and finally ultrafast laser pulses. Although it is only 0.95% in this case, the error is 1.37 times lower for quadratic modulation and 18.5 times lower for ultrafast laser pulses. This finding can also be attributed to the large difference in the modulation frequencies of 3 MHz (square wave, sine wave) and 80 MHz (ultrafast laser pulses). The complete statistical analysis together with the lock-in amplifier signals can be found in the supplementary **S5** and **S7**.
We decided to test conventional laser-scanning microscopy with an application where the signal is inherently weak, such as label-free tissue imaging. Using a conventional non-resonant scanner, we imaged 1024x1024 pixels with a 1 µs pixel dwell time resulting in a frame rate of 0.95 fps. Our first example is imaging mouse cartilage tissue with collagen-rich structures of type I with second harmonic generation (SHG)[26]. Intensity images of the SHG signal are displayed on the left of **Figure 3 - e** while the corresponding SUPER-FLIM images are on the right. Because SHG is a wave-mixing process, the measured lifetime is close to 0 ns and therefore used for calibration of our FLIM setup as described earlier in section 2.1. Our second example

consists of two autofluorescent cross-sections of *Convallaria majalis*, a standard sample used in lifetime imaging (**Figure 3 - f**). The imaging parameters were the same as in the first example.
These experiments are intended to demonstrate the flexibility of SUPER-FLIM in dealing with a wide range of lifetimes, different excitation schemes and scanning devices. Even no scanning was executed when measuring structureless dye solutions. The open source software packages for SUPER-FLIM further makes the implementation straight forward (see Supplementary file **S10**).

2.5 Environmental Sensing

The main advantage of FLIM is its ability to detect changes in the sample's microenvironment that go unnoticed in intensity images. For example, a decrease in intensity could be attributed to a decrease in concentration, an energy transfer to surrounding molecules or internal photochemical reactions leading to photobleaching, among many other possibilities. On the other hand, fluorescence lifetime can rule out some of these causes and is therefore more specific. To illustrate this, we carried out an experiment in which the solvent of the dye solution was exchanged in order to demonstrate its well-known stabilization effect on the ground and excited electronic states[27].Our measurements clearly demonstrate the polarity dependence, also known as solvatochronism. These results obtained with SUPER-FLIM can be easily added to our previous results obtained with instant FLIM and established TD- and FD-FLIM techniques[5]. The extended comparison is summarized in the bar chart in Figure **Figure 2 - j** where all data were measured with a single setup on the same samples. For example, Rose Bengal has a fluorescence lifetime of $\tau_{RBWater} = (0.098 \pm 0.087)$ ns in strongly polar water, while the lifetime in less polar solutions such as acetone is extended to $\tau_{RBAcetone}(2.73 \pm 0.062)$ ns - a 27-fold increase. This comparison illustrates the sensitivity of FLIM to the microenvironmental conditions and shows its clear advantage in detecting changes in solvent polarity, which is not possible with only intensity recordings.

2.6 Resonant Laser-Scanning

The main advantage of SUPER-FLIM is the exceptionally fast acquisition combined with a high data transfer rate, which is made possible by the lock-in amplifier. This setup enables seamless integration with a resonant laser-scanning system operating at 8 kHz and achieving high-speed imaging of 1024x1024 pixels with a frame rate of 7.6 fps using a TC time of 102 ns. These parameters represent the fastest FLIM acquisition achieved to date, as far as we know (See supplementary **S10**).
To illustrate the high speed acquisition, we imaged a mixture of two types of beads, each approximately 6 µm in diameter but with distinct fluorescence lifetimes. Using the above parameters for imaging, we monitored the beads freely diffusing in water over a period of 60 seconds. As shown in **Figure 4 - a**, each of the five exemplary images of the time series clearly reveal two lifetimes differentiated by false color coding. The corresponding histograms below the images (**b**) indicate two distinct peaks at approximately 1.7 ns and 2.7 ns, closely matching values reported in literature[28]. Another measurement, but with the same parameters, was conducted with a biological sample: HuH7 cells were labeled with a cell tracker dye (**c**) and monitored for 60 seconds. Over this brief period, observable changes in fluorescence lifetime were detected (**d**), highlighting the potential of high-speed FLIM acquisition to capture rapid biological dynamics.

Another application that benefits from fast acquisition is 3D imaging, where the acquisition of a z-stack containing several tens to hundreds images is required to reconstruct the full volume of the sample. This is demonstrated in **Figure 5 - a**, where we imaged a cell spheroid labeled with Höchst (targeting the nucleus) and Atto 488 Phalloidin (staining actin filaments). Distinct lifetimes were successfully measured for both fluorophores, with measured values aligning closely with established literature values: $\tau_{Meas} = (1.40 \pm 0.26)$ ns for the nucleus, compared to $\tau_{Lit} = (1.33 \pm 0.01)$ ns[29], and $\tau_{Meas} = (4.11 \pm 0.61)$ ns for actin filaments, closely matching $\tau_{Lit} = 4.1$ ns[30]. The histograms shown in (**Figure 5 -f**) are built from data of a single frame without the need for averaging or accumulation.
The full media/videos for the here presented results can be found in the supplementary section **S12**.

2.7 Multi-Lifetime Fluorescence Correlation Spectroscopy

Applications that benefit from fast lifetime acquisition go beyond pure imaging and include, for example, fluorescence lifetime correlation spectroscopy (FLCS)[31]. The underlying principle of fluorescence correlation spectroscopy (FCS) is the measurement of diffusion-related parameters — such as hydrodynamic radii, solution viscosity, or diffusion coefficients — by detecting the intensity fluctuations during the diffusion of a fluorophore through a small, static excitation volume, typical for confocal or two-photon microscopy setups (**Figure 6**). The autocorrelation function (ACF) of the detected time trace reveals the mean diffusion time of the particle through the focal volume, from which the above listed parameters can be calculated. Particles of similar size can only be distinguished if their diffusion time differs by more than a factor of 1.6[32] (**Figure 6 -g** and see also supplementary material **S6**). Here, the additional lifetime information can help to overcome this limit. To demonstrate this, two labeled bead samples with nearly identical diameters — around 200 nm — and similar excitation spectra were measured in a

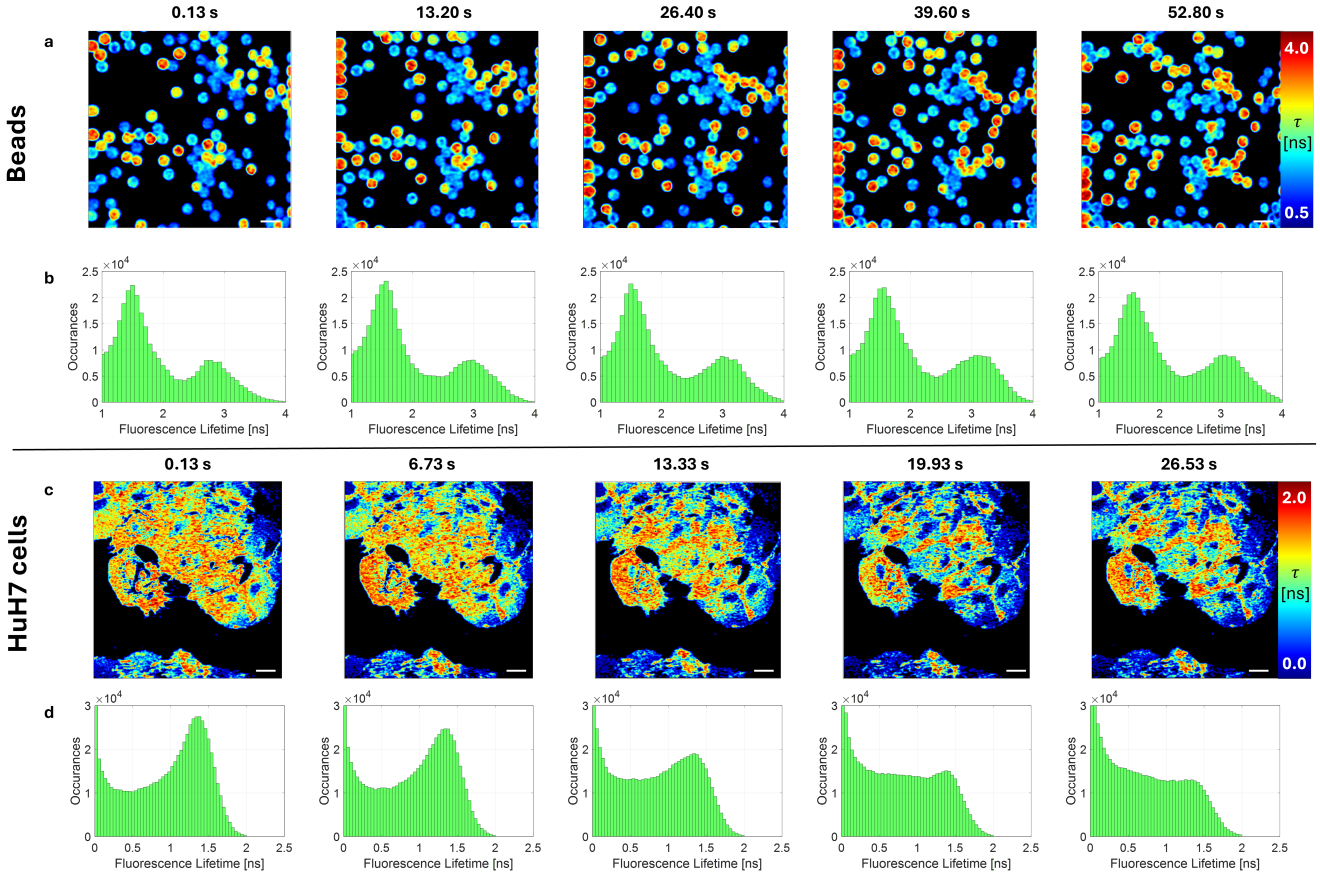

Figure 4. Fast Time Series Cabability of SUPER-FLIM To enable rapid imaging, a resonant galvo scanner was used, achieving a frame rate of 7.6 fps at 1024x1024 pixels with a TC time of 102 ns. This setup was used to image two bead types freely diffusing in water **(a)**. By examining the lifetime histograms in **(b)**, two distinct peaks are visible, corresponding to literature-reported lifetime values. The same measurement was performed for HuH7 cells, with lifetime images shown for five different time points in **(c)** and the corresponding lifetime histogram in **(d)**. Scale bars: 10 µm.

mixed solution (**Figure 6 - a**). In standard FCS setups, the intensity signal of the mixed sample cannot be differentiated (**Figure 6 -f**); however, using our technique, we were able to distinguish the two bead types by their lifetime signal (**Figure 6 -g**).

The calculated lifetime was therefore filtered and separated using a threshold window, after which the lifetime values within the users specifications (mean lifetime and given deviation) for both species were binarized and multiplied with the intensity trace (**Figure 6 -c** and **e**). Each trace was then used to calculate a separate ACF and fitted with a model for 2D-free diffusion (**Figure 6 -g**). In our experiment, we successfully separated two distinct lifetimes, with species one having $\tau_1 \approx 2$ ns and species two $\tau_2 \approx 3.0$ ns. The separated ACF functions resulted in mean diameters of $d_1 = 183.7$ nm and $d_2 = 225.6$ nm, compared to an average diameter from the overall ACF fit of $\langle d \rangle = 204.7$ nm. Therefore, we were able to clearly separate the two species despite their almost identical spectral and morphological characteristics.

This demonstrates the potential of combining SUPER-FLIM with other fluorescence-based techniques. Comparison with conventional FCS setups and further analysis are shown in the supplementary section **S6**.

2.8 Tracking of Lipid Nanoparticles

Building on our prior experiments, which demonstrated the remarkable speed and adaptability of our fluorescence lifetime imaging technique, we now extend its application to address specific biological questions involving lipid nanoparticles. These experiments illustrate the technique's practical potential, particularly in high-resolution imaging and optical sectioning using two-photon microscopy.

LNPs, which are widely used for the transport of mRNA in COVID-19 vaccines and are being investigated for therapies against cancer and other diseases, enter the target cells via endocytosis. Once within the endosome, proton pumps gradually acidify the compartment, theoretically leading to LNP disruption or fusion with the endosome and subsequent mRNA release — an essential yet inefficient process, with only approximately 2% (for siRNA) of LNPs successfully delivering their cargo into

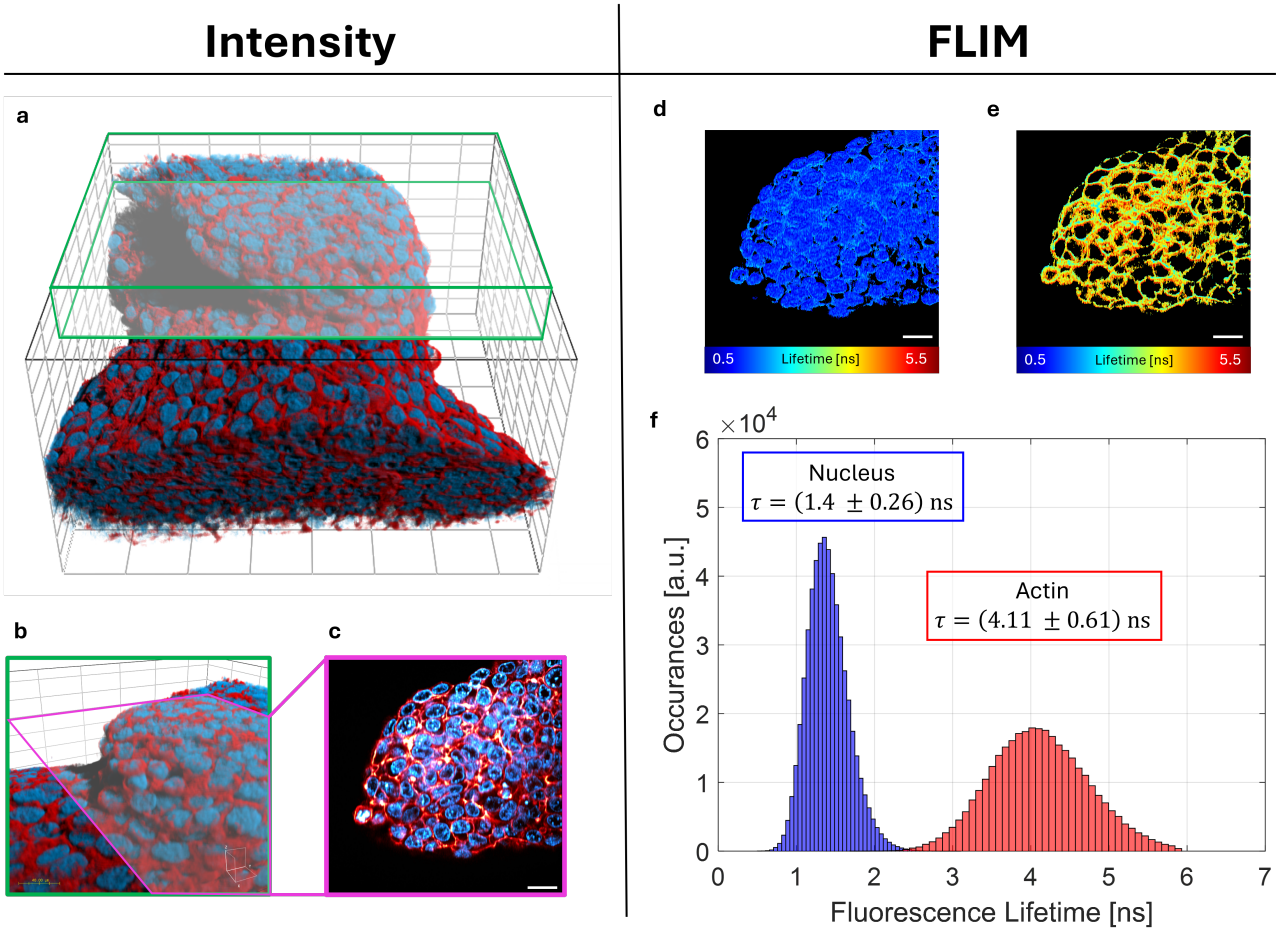

Figure 5. Imaging Capability of SUPER-FLIM: First, the optical sectioning ability of 2P excitation is demonstrated on a cell spheroid in **(a)** as a 3D rendering, in **(b)** as a detailed section, and in **(c)** as a single 2P image. For this single image, lifetime images are shown separately for the nuclear stain in **(d)** and the actin stain in **(e)**. The lifetime histogram of this image section is displayed in **(f)**, showing lifetimes in good agreement with reported literature values. Scale bars: 20 µm

the cytosol[33]. The mechanisms and kinetics of LNP disruption, as well as the acidification timing in the endosome, remain poorly understood[34]. One hypothesis involves the activation of proton pumps, which can trigger a phenomenon known as the "proton sponge effect," where osmotic pressure causes the lipid shells of the LNP to rupture[35,36]. Alternatively, the decrease in pH within the endosome may induce structural changes in the lipids, facilitating the fusion of the LNP with the endosome and resulting in the release of the mRNA[35]. Both of these hypotheses share a common factor: the pH-level plays a crucial role in the process of endosomal release and is therefore a significant topic of research[37,38].

To investigate these processes, we aimed to answer two key questions using our fluorescence lifetime technique. First, we assessed whether LNP swelling or structural disruption occurs in response to decreasing pH, as postulated by the proton sponge effect. By correlating fluorescence lifetime measurements with pH-values, we generated a reference curve for precise pH assessment within the sample. Second, we examined the timeline of endosomal acidification by tracking fluorescence lifetime changes in a pH-sensitive reporter fluorophore attached to the LNP exterior throughout the transfection period.

2.8.1 pH stability of Lipid Nanoparticles

While the proton sponge effect is expected to occur shortly before the endosomal release of mRNA, its statistical occurrence remains low due to the before mentioned 2% efficiency. To investigate this phenomenon, we developed a simplified model in which LNPs are anchored to a surface via a neutravidin-biotin bond and immersed in a Fluorescein solution. Fluorescein serves as the reporter molecule, exhibiting changes in its fluorescence absorption/emission spectra and, notably, its lifetime in response to pH variations due to a chemical restructuring of its molecular structure.

By systematically adjusting the pH of the solution, we monitored the LNPs' responses to determine whether the lipid shell's disruption — triggered by the proton sponge effect — leads to mRNA release. Our technique enables rapid and continuous

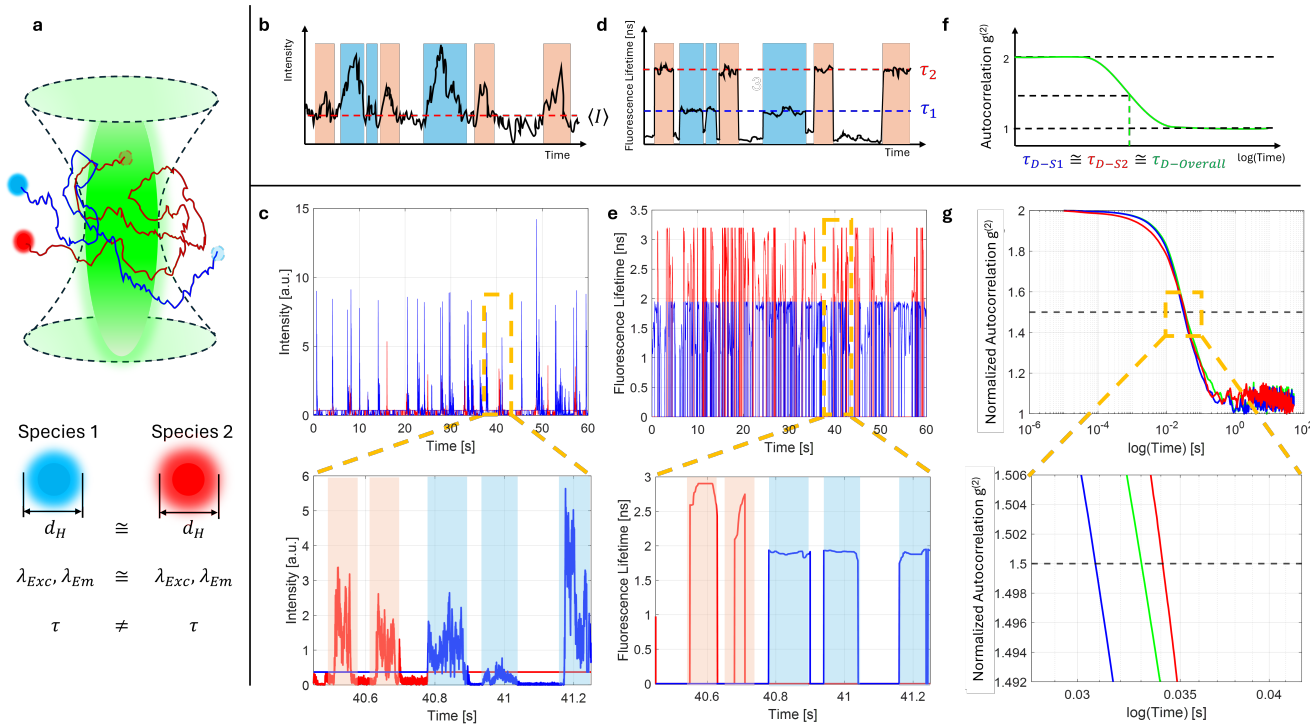

Figure 6. Using SUPER-FLIM for dual color Fluorescence Correlation Spectroscopy (FCS) Measurements: **(a)**For FCS experiments used two types of fluorescent nanoparticles with an average diameter of 200 nm and similar excitation and emission spectra. These particles were mixed in solution, and the FCS signal was recorded. A schematic illustration is shown in **(b)**, with the experimental signal in **(c)** with an inset shown below. Based on fluorescence lifetime differences, the two nanoparticle types can be distinguished, as illustrated schematically in **(d)** and demonstrated experimentally in **(e)**. Using this filtering approach, the intensity signal from **(c)** can be separated to calculate individual autocorrelation functions **(f)**, yielding three distinct ACFs with corresponding 3D free-diffusion fits **g**.

imaging of these changes in a small sample volume, providing insights into LNP evolution over time.

To correlate Fluorescein's fluorescence lifetime with pH values, we performed a pH titration and generated a reference curve depicting the measured lifetimes (see supplementary file **S9**). Using this calibration, we assessed the pH at the surface of the LNPs, finding that the particles remained stable down to the lowest pH-value of approximately 2.7 (see supplementary file **S8**). This finding indicates that mRNA release is unlikely to result from a straightforward disruption of the LNP shell, as previously hypothesized. Instead, it is more probable that mRNA release occurs via pH-induced membrane fusion between the LNP and the endosome.

2.8.2 Endosomal pH-Change

To investigate the timing of endosomal acidification, we employed fluorescence lifetime measurements by attaching a pH-sensitive reporter fluorophore to the exterior of lipid nanoparticles similar to recent publications where the LNP interior was measured in endosomes[39]. Specifically, we utilized a lipid conjugated with a Carboxyfluorescein molecule at its tail, which is well established as an effective pH probe due to its sensitivity to environmental pH changes. The expected outcome is a linear decrease in fluorescence lifetime as the surrounding environment becomes more acidic, reflecting the physicochemical changes associated with endosomal maturation and cargo release.

Initial characterization of the LNPs, with a mean diameter of (84.2 ± 3.6) nm, was performed via dynamic light scattering[40] (DLS) and (81.99 ± 6.26) nm with FCS (see supplementary **S10**).

We transfected HuH7 cells with the LNPs and initiated a time-lapse imaging sequence that spanned one hour. During post-processing, we extracted fluorescence lifetime distributions at five distinct time points: 0 min, 15 min, 30 min, 45 min, and 60 min. For each time point, we analyzed the fluorescence lifetimes of ten individual particles, with representative examples illustrated in **Figure 7 - c**.

At the initial time point (0 min), under physiological pH conditions (7.4), we observed a fluorescence lifetime of $\tau_{0min} = (1.89 \pm 0.22)$ ns. As the endosomal environment became progressively more acidic, we noted a significant decrease in the fluorescence lifetime, reaching $\tau_{60min} = (1.16 \pm 0.16)$ ns at approximately pH 4. This corresponds to a reduction

of nearly 700 ps over the hour-long observation period and the end of the endosome pathway by fusing with lysosomes (**Figure 7 - d**).

To correlate the fluorescence lifetime with pH-changes, we utilized a reference curve obtained from Fluorescein measurements, adjusted to account for the inherent differences between Fluorescein and Carboxyfluorescein. The latter exhibits a lower fluorescence lifetime due to the increased electronegativity introduced by the carboxyl-group, which enhances non-radiative relaxation pathways.

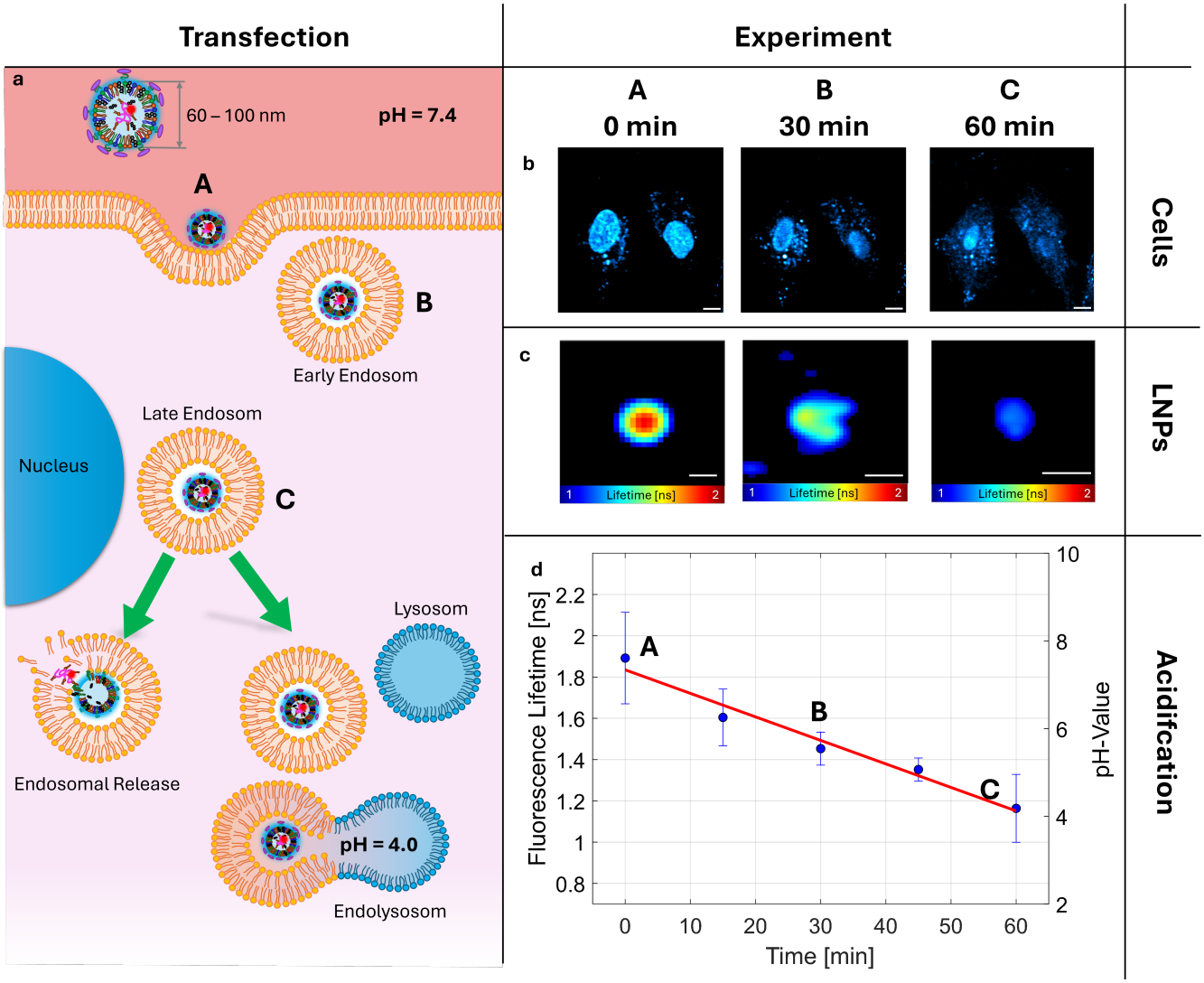

Figure 7. Endosomal pH-Change after mRNA LNP Transfection. In **a** a schematic of the LNP pathway is shown. Starting from the endocytosis to the different Endosome stages and two possibilys of the LNP. The first is the endosomal release and the second the fusion with lysosomes to the Endolysosome. During this process, the pH drops from the inital medium pH value of 7.4 to around 4.0. In **b** three intensity images of the transfection processes are shown, at 0 min, 30 min and 60 min. Below the intensity images, close ups of single LNP/Endosomes fluorescence lifetime images are presented (**c**). A statistical analysis of 10 particles for 0 min, 15 min, 30 min, 45 min and 60 min is displayed in **d**. Scale bar: **b** - 10 µm, **c-A** - 500 nm, **c-B,C** - 1 µm

The observed decrease in fluorescence lifetime is indicative of the ongoing endosomal acidification process, which is critical for effective cargo release. This acidification activates proton pumps within the endosomal membrane, leading to a decline in pH and subsequent structural changes in the lipid phases of the Endosome/LNPs. It triggers a change from an inverse micellar (L_{II}) to an inverse hexagonal (H_{II}) phase, causing membrane fusion that releases the nucleic cargo into the cytosol[18,35,41,42].

Our results suggest that rather than simply disrupting the lipid nanoparticles and endosomes, the low pH environment promotes a more complex interaction where the LNPs may fuse with the endosome, enabling the efficient release of their cargo. This process is crucial for enhancing the overall efficacy of mRNA delivery systems, particularly in therapeutic applications

such as COVID-19 vaccines and cancer treatments.

3 Discussion

The SUPER-FLIM technique represents a significant advancement in fluorescence lifetime imaging microscopy, achieving the high-speed acquisition and spatial resolution necessary for real-time imaging applications. By integrating characteristics from both TD- and FD-FLIM, SUPER-FLIM allows for accurate lifetime measurements with reduced error, making it particularly effective for applications that demand rapid data collection. This balance between speed and precision is essential for real-time microenvironmental sensing in dynamic biological processes, such as 3D single-particle tracking[43]. The combination between SUPER-FLIM and a new single particle tracking technique from our group is currently in review and showcase the advantages.

The technique's high temporal resolution, with pixel dwell times of only 122.3 ns, enables it to capture accurate lifetime data even for rapidly moving samples or those undergoing dynamic changes. It also enables to use resonant galvo-scanners without the need of averaging over multiple frames to generate a sufficient statistic. This ability to detect sensitive fluorescence lifetime variations linked to local factors like pH and polarity, SUPER-FLIM is a powerful tool for applications in cellular and molecular biology. For example, in studying lipid nanoparticle interactions and endosomal escape mechanisms, SUPER-FLIM's capability to observe real-time, pH-dependent lifetime shifts provides key insights into acidification and mRNA release processes, critical to the efficacy of gene therapy and vaccine delivery methods.

Our Multi-Lifetime Fluorescence Correlation Spectroscopy (ml-FCS) experiments further highlight SUPER-FLIM's compatibility with other fluorescence-based microscopy techniques. When combined with FCS, SUPER-FLIM adds lifetime information to intensity-based data, significantly enriching the dataset and expanding the analytical scope of traditional FCS. This integration demonstrates that SUPER-FLIM can be paired with other fluorescence techniques, such as the Förster Resonant Energy Transfer (FRET), to enhance the understanding of molecular interactions and diffusion dynamics in live cell environments[44].

Additionally, SUPER-FLIM's adaptability with various excitation sources, including one-photon and two-photon microscopy, makes it suitable for a range of imaging environments, from conventional fluorescence to advanced multiphoton microscopy setups. To adapt a microscope with a point detector for use with SUPER-FLIM, a lock-in amplifier is required. If the light source does not already contain a photodiode, one must be added. Once these components are in place, our open source software (description in supplementary file **S11**) can control a galvo-galvo scanner to create intensity images and incorporate the signals from the lock-in amplifier to detect FLIM images. These images can then be further analyzed with additional software packages also created by our group and open access.

Future developments should focus on optimizing SUPER-FLIM for imaging smaller particles and complex tissue structures to expand its *in vivo* applications. Integrating with complementary fluorescence techniques will further establish SUPER-FLIM as an all-encompassing tool for advanced biophysical analysis at the cellular level, enhancing its utility across a spectrum of biomedical research and diagnostic applications.

4 Material and Methods

4.1 *Convallaria majalis*

The *Convallaria majalis* sample was purchased at Boston Electronics.

4.2 Fluorophores

All dyes (**Table 2**) were in salt form and were dissolved in various solvents. To protect the dyes from evaporation and external influences, they were embedded in so-called single cavity slides (MS15C1, Thorlabs). For this, 60 µL of solution were pipetted into the cavity and then sealed with a high-precision coverslip (DH18, A. Hartenstein GmbH). Eukitt (03989, Sigma Aldrich) was used to affix and seal the coverslip onto the slide to prevent air infiltration and to preserve the sample. Below is a table containing all the dyes used:

Table 2. Sample fluorophores with the respective concentration.

Number	Fluorophore	Distributor	Article No.	Molar Weight [g/mol]	c [mM]
1	Rose Bengal	Sigma Aldrich	330 000	1017.64	1
2	Fluorescein	Sigma Aldrich	46955	332.31	1
3	Rhodamine B	Sigma Aldrich	83689	479.01	1
4	Rhodamine 6G	Sigma Aldrich	83697	479.01	1

All used solvents where listed in Table 3

Table 3. Solvent used for the different types of fluorophores.

Solvent	**Distributor**	**Article No.**	**Fluorophores**
Water	Merck	1.15333	1, 3, 4
Methanol	Merck	1.06002	1
Ethanol	Merck	1.0098	1
Aceton	Sigma Aldrich	270725-1L	1
NaOH	—	—	2

4.3 Fluorescent Nanobeads

The shown experiments used four different types of fluorescent beads. For the resonant imaging and tracking experiments, two fluorescent lifetime beads were used with a mean diameter of 6.5 µm and fluorescence lifetimes of 1.7 ns (110 00 006, PolyAn) and 2.7 ns (110 10 006, PolyAn). For the FLCS measurements, Dragon Green beads (FSDG002, Bangs Laboratories Inc.) with a diameter of 190–210 nm, an absorption peak at 480 nm, and an emission peak at 520 nm were used, along with PolyAn Red beads (204 02 175, PolyAn) with a diameter of 151–200 nm and absorption/emission peaks at 510/570 nm.

All samples were prepared by adding 5 µL of the bead suspension to 1 mL of distilled water and homogenized using a vortex mixer. Subsequently, 100 µL of this solution was carefully deposited into an ibidi 8-well μ-Slide (80606, ibidi). For the tracking and FLCS measurements, further dilution was applied as needed using distilled water.

4.4 pH-Samples

In order to correlate the measured lifetimes with a pH-value, a pH-calibration curve had to be established. For this purpose, a pH-meter (SevenDirect SD20, Mettler Toledo) was used. A 10 mL Fluorescein solution (1 mM in Water) was incrementally (5 µL) titrated with a 0.1 M solution of NaOH and HCl. After each addition, a waiting period of 30 s was bide to allow the pH-value to stabilize. This calibration curve was measured at a constant temperature of 20.6°, with continuous stirring.

4.5 Lipid Nanoparticles

ARCA Cy3 EGFP mRNA (APExBIO, R1008) was encapsulated in lipid nanoparticles with a molar ratio of DLin-MC3-DMA (Merck, AMBH93D5393F):DSPC (Avanti Polar Lipids, 850365):Cholesterol (Avanti Polar Lipids, 700100):DSPE-PEG2000 (Avanti Polar Lipids, 880128) of 50:10:38.5:1.5. Additionally 1% of 1,2-dioleoyl-sn-glycero-3-phosphoethanolamine-N-(carboxyfluorescein) (Avanti Polar Lipids, 810332) was added for fluorescence labeling of the outside of the LNP. Therefore, an aqueous phase was prepared with mRNA dissolved in RNAse free water (VWR, K978) with 100mM citrate buffer at pH 3. Additionally, the lipids were prepared in ethanol (Roth, 5054.3) to reach a final N/P ratio of 3. Microfludic mixing (NanoAssemblrTM SparkTM, Cytivia, Precision NanoSystems) was conducted at a flow ratio of 2:1 to reach a final mRNA concentration of 5 µg/mL. Following mixing, LNPs were incubated at room temperature for 20 min. Dialysis into water was performed with Slide-A-Lyzer™ MINI dialysis cups with a molecular cut-off of 3.5 kDa (Thermo Fisher, 69550).

4.6 Surface Binding

Four coupling of LNPs, the 20% of the PEG lipid was replaced by DSPE-PEG2000 Biotin (Avanti Polar Lipids, 880129P). 8-well µ-Slides were treated with oxygen plasma and coated with 10 mg/mL Neutravidin in PBS, followed by blocking with 2% (w/v) BSA (Thermo Fisher, A9418) to avoid unspecific binding. Chambers were filled with LNPs in solution and incubated for 1 hour at room temperature.

4.7 Cell Culture

The human liver carcinoma cell line HuH7 was maintained in Gibco™ RPMI (Roswell Park Memorial Institute) medium (ThermoFisher, 61870010) with supplements of 10% (v/v) fetal bovine serum (FBS, ThermoFisher, 10270106), 1 mM sodium pyruvate (Gibco™, ThermoFisher, 11360070), and 5 mM HEPES (Gibco™, ThermoFisher, 15630080). Cultures were incubated at 37°C in a humidified atmosphere containing 5% CO_2. Cell detachment was carried out using Accutase (Invitrogen, 00-4555-56) when cell confluence reached 70–90%. For experimental assays, cells were plated in growth medium in a 6-channel µ-slide (ibidi, 80607).

References

1. König, K. 1 brief history of fluorescence lifetime imaging. Multiphoton Microsc. Fluoresc. Lifetime Imaging 3–16 (2018).
2. Wang, X. F., Uchida, T. & Minami, S. A fluorescence lifetime distribution measurement system based on phase-resolved detection using an image dissector tube. Appl. Spectrosc. **43**, 840–845, DOI: https://doi.org/10.1366/0003702894202364 (1989).

3. Torrado, B., Pannunzio, B., Malacrida, L. & Digman, M. A. Fluorescence lifetime imaging microscopy. Nat. Rev. Methods Primers **4**, 80, DOI: https://doi.org/10.1038/s43586-024-00358-8 (2024).

4. Datta, R., Heaster, T. M., Sharick, J. T., Gillette, A. A. & Skala, M. C. Fluorescence lifetime imaging microscopy: fundamentals and advances in instrumentation, analysis, and applications. J. biomedical optics **25**, 071203–071203, DOI: https://doi.org/10.1117/1.JBO.25.7.071203 (2020).

5. Kellerer, T. et al. Comprehensive investigation of parameters influencing fluorescence lifetime imaging microscopy in frequency-and time-domain illustrated by phasor plot analysis. Int. J. Mol. Sci. **23**, 15885, DOI: https://doi.org/10.3390/ijms232415885 (2022).

6. Colyer, R. A., Lee, C. & Gratton, E. A novel fluorescence lifetime imaging system that optimizes photon efficiency. Microsc. research technique **71**, 201–213, DOI: https://doi.org/10.1002/jemt.20540 (2008).

7. Karpf, S. et al. Spectro-temporal encoded multiphoton microscopy and fluorescence lifetime imaging at kilohertz frame-rates. Nat. communications **11**, 2062, DOI: https://doi.org/10.1038/s41467-020-15618-w (2020).

8. Orthaus-Mueller, S. et al. rapidflim: the new and innovative method for ultra fast flim imaging. PicoQuant Appl. Note 1–8, DOI: https://doi.org/10.1117/12.2249757 (2016).

9. Zhang, Y. et al. Instant flim enables 4d in vivo lifetime imaging of intact and injured zebrafish and mouse brains. Optica **8**, 885–897, DOI: https://doi.org/10.1364/OPTICA.426870 (2021).

10. Halip, H., Yoshimura, Y., Inami, W. & Kawata, Y. Ultrashort laser based two-photon phase-resolved fluorescence lifetime measurement method. Methods Appl. Fluoresc. **8**, 025003, DOI: https://10.1088/2050-6120/ab71c2 (2020).

11. Chen, H., Holst, G. & Gratton, E. Modulated cmos camera for fluorescence lifetime microscopy. Microsc. research technique **78**, 1075–1081, DOI: https://doi.org/10.1002/jemt.22587 (2015).

12. Krichevsky, O. & Bonnet, G. Fluorescence correlation spectroscopy: the technique and its applications. Reports on Prog. Phys. **65**, 251, DOI: https://doi.org/10.1088/0034-4885/65/2/203 (2002).

13. Ries, J. & Schwille, P. Fluorescence correlation spectroscopy. BioEssays **34**, 361–368, DOI: https://doi.org/10.1002/bies.201100111 (2012).

14. Ogikubo, S. et al. Intracellular ph sensing using autofluorescence lifetime microscopy. The J. Phys. Chem. B **115**, 10385–10390, DOI: https://doi.org/10.1021/jp2058904 (2011).

15. Kon, E., Ad-El, N., Hazan-Halevy, I., Stotsky-Oterin, L. & Peer, D. Targeting cancer with mrna–lipid nanoparticles: key considerations and future prospects. Nat. Rev. Clin. Oncol. **20**, 739–754, DOI: https://doi.org/10.1038/s41571-023-00811-9 (2023).

16. Kreiter, S., Diken, M., Selmi, A., Türeci, Ö. & Sahin, U. Tumor vaccination using messenger rna: prospects of a future therapy. Curr. opinion immunology **23**, 399–406, DOI: https://doi.org/10.1016/j.coi.2011.03.007 (2011).

17. Cullis, P. R. & Hope, M. J. Lipid nanoparticle systems for enabling gene therapies. Mol. Ther. **25**, 1467–1475, DOI: https://doi.org/10.1016/j.ymthe.2017.03.013 (2017).

18. Hou, X., Zaks, T., Langer, R. & Dong, Y. Lipid nanoparticles for mrna delivery. Nat. Rev. Mater. **6**, 1078–1094, DOI: https://doi.org/10.1038/s41578-021-00358-0 (2021).

19. Digman, M. A., Caiolfa, V. R., Zamai, M. & Gratton, E. The phasor approach to fluorescence lifetime imaging analysis. Biophys. journal **94**, L14–L16, DOI: https://doi.org/10.1529/biophysj.107.120154 (2008).

20. Malacrida, L., Ranjit, S., Jameson, D. M. & Gratton, E. The phasor plot: a universal circle to advance fluorescence lifetime analysis and interpretation. Annu. Rev. Biophys. **50**, 575–593, DOI: https://doi.org/10.1146/annurev-biophys-062920-063631 (2021).

21. Esposito, A., Gerritsen, H. C. & Wouters, F. S. Fluorescence lifetime heterogeneity resolution in the frequency domain by lifetime moments analysis. Biophys. journal **89**, 4286–4299, DOI: https://doi.org/10.1529/biophysj.104.053397 (2005).

22. Mohler, W., Millard, A. C. & Campagnola, P. J. Second harmonic generation imaging of endogenous structural proteins. Methods **29**, 97–109, DOI: https://doi.org/10.1016/S1046-2023(02)00292-X (2003).

23. Ranjit, S. et al. Imaging fibrosis and separating collagens using second harmonic generation and phasor approach to fluorescence lifetime imaging. Sci. reports **5**, 13378, DOI: https://doi.org/10.1038/srep13378 (2015).

24. Boens, N. et al. Fluorescence lifetime standards for time and frequency domain fluorescence spectroscopy. Anal. chemistry **79**, 2137–2149, DOI: https://doi.org/10.1021/ac062160k (2007).

25. Kristoffersen, A. S., Erga, S. R., Hamre, B. & Frette, Ø. Testing fluorescence lifetime standards using two-photon excitation and time-domain instrumentation: rhodamine b, coumarin 6 and lucifer yellow. J. fluorescence **24**, 1015–1024, DOI: https://doi.org/10.1007/s10895-014-1368-1 (2014).

26. Mostaço-Guidolin, L., Rosin, N. L. & Hackett, T.-L. Imaging collagen in scar tissue: developments in second harmonic generation microscopy for biomedical applications. Int. journal molecular sciences **18**, 1772, DOI: https://doi.org/10.3390/ijms18081772 (2017).

27. Reichardt, C. Solvatochromic dyes as solvent polarity indicators. Chem. reviews **94**, 2319–2358, DOI: https://doi.org/10.1021/cr00032a005 (1994).

28. Lin, Y., Mos, P., Ardelean, A., Bruschini, C. & Charbon, E. Coupling a recurrent neural network to spad tcspc systems for real-time fluorescence lifetime imaging. Sci. Reports **14**, 3286, DOI: https://doi.org/10.1038/s41598-024-52966-9 (2024).

29. Scully, A. et al. Application of fluorescence lifetime imaging microscopy to the investigation of intracellular pdt mechanisms. Bioimaging **5**, 9–18, DOI: https://doi.org/10.1002/1361-6374(199703)5:1<9::AID-BIO2>3.0.CO;2-A (1997).

30. Thermo Fisher Scientific. Fluorescence quantum yields and lifetimes for alexa fluor dyes (2024). Accessed: 2024-11-02.

31. Kapusta, P., Wahl, M., Benda, A., Hof, M. & Enderlein, J. Fluorescence lifetime correlation spectroscopy. J. Fluoresc. **17**, 43–48, DOI: https://doi.org/10.1007/s10895-006-0145-1 (2007).

32. Meseth, U., Wohland, T., Rigler, R. & Vogel, H. Resolution of fluorescence correlation measurements. Biophys. journal **76**, 1619–1631, DOI: https://doi.org/10.1016/S0006-3495(99)77321-2 (1999).

33. Gilleron, J. et al. Image-based analysis of lipid nanoparticle–mediated sirna delivery, intracellular trafficking and endosomal escape. Nat. biotechnology **31**, 638–646, DOI: https://doi.org/10.1038/nbt.2612 (2013).

34. Müller, J. A. et al. Kinetics of rna-lnp delivery and protein expression. Eur. J. Pharm. Biopharm. **197**, 114222, DOI: https://doi.org/10.1016/j.ejpb.2024.114222 (2024).

35. Chatterjee, S., Kon, E., Sharma, P. & Peer, D. Endosomal escape: A bottleneck for lnp-mediated therapeutics. Proc. Natl. Acad. Sci. **121**, e2307800120, DOI: https://doi.org/10.1073/pnas.2307800120 (2024).

36. Behr, J.-P. The proton sponge: a trick to enter cells the viruses did not exploit. Chimia **51**, 34–34, DOI: https://doi.org/10.2533/chimia.1997.34 (1997).

37. Wittrup, A. et al. Visualizing lipid-formulated sirna release from endosomes and target gene knockdown. Nat. biotechnology **33**, 870–876, DOI: https://doi.org/10.1038/nbt.3298 (2015).

38. Patel, S. et al. Boosting intracellular delivery of lipid nanoparticle-encapsulated mrna. Nano letters **17**, 5711–5718, DOI: https://doi.org/10.1021/acs.nanolett.7b02664 (2017).

39. Zhao, B. et al. Determination of the interior ph of lipid nanoparticles using a ph-sensitive fluorescent dye-based dna probe. Biosens. Bioelectron. **251**, 116065, DOI: https://doi.org/10.1016/j.bios.2024.116065 (2024).

40. Stetefeld, J., McKenna, S. A. & Patel, T. R. Dynamic light scattering: a practical guide and applications in biomedical sciences. Biophys. reviews **8**, 409–427, DOI: https://doi.org/10.1007/s12551-016-0218-6 (2016).

41. Philipp, J. et al. ph-dependent structural transitions in cationic ionizable lipid mesophases are critical for lipid nanoparticle function. Proc. Natl. Acad. Sci. **120**, e2310491120, DOI: https://doi.org/10.1073/pnas.2310491120 (2023).

42. Semple, S. C. et al. Rational design of cationic lipids for sirna delivery. Nat. biotechnology **28**, 172–176, DOI: https://doi.org/10.1038/nbt.1602 (2010).

43. Kellerer, T. et al. An image based real-time 3d particle tracking fluorescence lifetime imaging microscope to follow lipid nanoparticles. In Microscopy Histopathology and Analytics, MM5A–6, DOI: https://doi.org/10.1364/MICROSCOPY.2024.MM5A.6 (Optica Publishing Group, 2024).

44. Jares-Erijman, E. A. & Jovin, T. M. Fret imaging. Nat. biotechnology **21**, 1387–1395, DOI: https://doi.org/10.1038/nbt896 (2003).

Acknowledgements

This research was funded by the BMBF project "SEMPA-Track" (FKZ 13N16300) and the Bavarian Academic Forum (BayWISS)—Doctoral Consortium "Health Research". We wanted to thank Heidi Potts from Zurich Instruments for her great support for the lock-in amplifier measurements. We also wanted to thank the CANTER lab form the Munich University of Applied Sciences that we could use their pH-meter. We also wanted to thank Dr. Gregor Posnjak for the help with the spectrum measurments and Carola Bartels for the surface binding protocol. Last but not least we wanted to thank Gerlinde Schwake and Daria Maksutova for helping with the sample preparation.

Author contributions statement

T.K. conceived, conducted the experiments, analysed the results and wrote the manuscript. L.M conducted the experiments, J.A.M, prepared the LNP samples. T.H. supervised the project and wrote the manuscript. J.O.R. supervised the project. All authors reviewed the manuscript.

Chapter 6

Single Particle Tracking

„You must have chaos within you to
give birth to a dancing star.“

Friedrich Nietzsche

Fluorescence microscopy is often driven by the pursuit of perfection, focusing on achieving the highest resolution, precise colocalization, and optimal performance [181]. However, sometimes innovation does not arise from strict adherence to established principles, but from embracing deviations that initially seem counterintuitive. This philosophy is at the heart of the development of the single-particle tracking technique presented here: **S**pectrally **E**ncoded **M**ultiphoton **PA**rticle-**Track**ing. By intentionally misaligning a telescope system in the optical beam path, a slight axial offset of the **P**oint **S**pread **F**unction (PSF) is introduced, creating a geometry that appears unconventional [182]. When combined with a second, conventionally aligned laser, this setup results in three distinct excitation regions: two separated volumes and their overlap (**Figure 6.2**). While this configuration disrupts axial colocalization, it enables the detection of axial movement of single particles through spectral separation of their fluorescence.

This approach draws inspiration from the concept of two-color two-photon microscopy [106, 183, 184, 185, 186], a technique traditionally dependent on the precise overlap of two PSFs to enable excitation processes such as 2P absorption [83], SHG [104], and SFG [106].

In this context, our approach exemplifies how apparent disorder—much like the "chaos" described by Nietzsche—can lead to transformative discoveries. By intentionally creating misalignments and embracing what seems like a chaotic arrangement, we have unlocked new possibilities for tracking and studying dynamic biological processes.

In the following section, we will review state-of-the-art 3D tracking microscopy systems, culminating in a discussion of our technique. As proof of principle the method is used to follow LNP on its erratic way on the outside- and the inside of a cell.

6.1 Single Particle Tracking Microscopy (SPT)

Single **P**article **T**racking microscopy refers to techniques capable of locking onto a single particle and following its iterative movement in all three dimensions. These approaches provide deeper insights into biological processes by revealing the dynamics of individual particles [16, 17]. A notable recent example is the study of motor proteins such as kinesin-1 using a tracking technique called **Min**imal photon **flux**es (MINFLUX) [187]. Although MINFLUX primarily operates in 2D and on single molecule level, it has uncovered the inchworm-like stepping mechanism of kinesin-1 along microtubules. This movement, characterized by alternating head binding and precise coordination, highlights the level of detail that can be uncovered when particle dynamics are tracked with high spatial and temporal resolution.

SPT techniques can be broadly categorized into passive and active tracking methods [16, 17]. Passive SPT involves the static observation of the particle under investigation, with its movement extracted during post-acquisition image processing. This method is effective for particles that remain within the **F**ield **o**f **V**iew (FOV), yielding valuable metrics such as diffusion coefficients and diffusion types (e.g. confined, directed, or free diffusion) [188, 189]. However, for particles exhibiting rapid movement or those quickly exiting the FOV, active SPT becomes essential (**Figure 6.1**). Active methods dynamically adjust the sample position or optical elements to keep the particle within the FOV, enabling continuous tracking.

Tracking LNPs presents additional challenges due to their small sizes, often below the optical resolution limit, and their high diffusion coefficients, which cause them to rapidly move out of the observable volume. While existing techniques have successfully been applied to LNPs, these methods often lack information at the single-particle level, particularly in the axial (Z) dimension [77, 12]. To address this, an active SPT method capable of robustly tracking LNPs in 3D were developed here. This is achieved by designing a feedback loop that decodes particle movement through changes in various parameters, most often intensity [190].

Active SPT techniques can be further divided into image-based and trajectory-based tracking approaches (**Figure 6.1**). Image-based techniques rely on capturing frames to continuously localize particles and their surrounding environment, whereas trajectory-based methods actively adjust the optical setup in real-time to follow the particle's movement, without focusing on its surroundings. Both approaches offer distinct advantages and limitations, depending on the experimental requirements. One of the most critical factors is detection speed. While detection speed in image-based techniques is limited by the frame rate ($\sim$ milliseconds) of the detection system (usually a camera), the detection speed in trajectory-based systems ($\sim$ mikroseconds) is more constrained by the optical and electronical elements responsible for relocating the laser or the sample.

In the following subsections, the state of the art in SPT techniques is described, highlighting their specific applications, advantages, and limitations. This discussion includes an overview of how these methods can be adapted and optimized for tracking LNPs, providing critical insights into their intracellular dynamics.

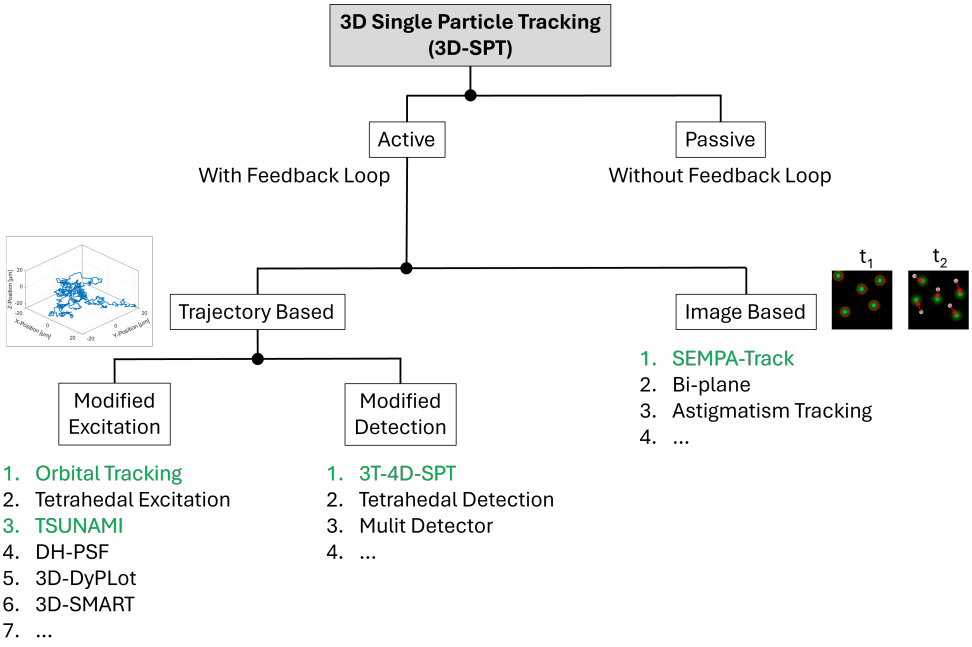

Figure 6.1: Classification of Different Tracking Mechanism: The figure categorizes 3D-SPT techniques, with a focus on active methods incorporating feedback loops. Examples of trajectory-based techniques using modified excitation are listed, with references provided in the same order [72, 191, 192, 193, 194, 195]. Techniques employing modified detection are also shown, with corresponding references available here [196, 197, 198]. Our SEMPA-Track approach is classified under image-based tracking methods, highlighting its place among various methodologies [199, 200]. The green marked methods represents techniques where next to the trajectory also the fluorescence lifetime is captured.

6.1.1 Trajectory-Based Feedback Tracking Techniques

In trajectory-based SPT techniques, the focus is on following the pathway of a single particle over an extended time period. The result is a 3D trajectory that represents the random walk of the particle, which can then be overlaid onto an overview image or used to extract information such as the diffusion coefficient by calculating the MSD. In this process, the fluorescence signal must be continuously monitored to detect the particle's movement, although signal fluctuations may occur due to photobleaching or other quenching mechanisms. To do so, the excitation or detection scheme is often modified.

Modified Excitation

To detect the displacement of a particle, the excitation is typically modified to follow a predefined pattern or pathway, which serves as a reference [72, 192, 193, 194, 201]. By extracting the fluorescence signal, previously hidden movement can be revealed, and the excitation position can be adjusted accordingly. One of the earliest and still frequently used

tracking techniques, serving as a template for newer methods, is orbital tracking which was first introduced by Jörg Enderlein in 2000 [202, 203]. In this approach, a focused laser is continuously moved in a circular pattern created by a galvo-galvo system. In the XY-plane, orthogonal to the optical axis, fluorescence is not detected if the particle is located inside the circle. However, when the particle moves randomly and reaches a position where the laser's circular motion intersects, a modulated fluorescence signal is detected. By comparing this signal with the reference and knowing the frequency and radius of the circular pattern, the direction of the movement can be detected. The circular pattern is then adjusted to bring the particle back to the center. For the third dimension (Z-axis), various approaches have been tested. One method involves rapidly changing the axial position with an **E**lectro **O**ptical **L**ens (EOL) [204], while others introduce a second laser [191, 205]. The detection approach remains the same: If a modulated signal is detected, the algorithm can calculate the particle's movement and initiate a feedback loop to track it.

Modified Detection

Another way to uncover the random movement of particles is the modification of the detection scheme [196, 197, 198]. In this approach, specially developed sensors, such as quadrant photodiodes or multiple detectors, are employed and strategically positioned in a specific arrangement [16, 17]. These detectors enable continuous monitoring of the particle's position with high temporal resolution by measuring the intensity variations across different regions of the detection area.

For instance, quadrant photodiodes are capable of detecting small displacements of a particle within the focal plane by analyzing the variation in light intensity that hits different quadrants of the diode [206]. This allows for real-time tracking of the particle's movement in two dimensions (2D), with the information used to update the particle's trajectory continuously. In the case of 3D tracking, additional detection elements, such as multiple cameras or split detectors, can be integrated to capture the particle's position along the third dimension [16, 17]. One of the key advantages of this method is the ability to track particles with high precision in real-time, even at high diffusion speeds, by adapting the detection system dynamically to follow the particle's movement. This type of active tracking is particularly useful in situations where particles undergo rapid motion or when maintaining the particle within the FOV is critical for accurate data collection. However, it is important to note that this approach requires careful calibration and alignment of the detectors to avoid distortions in the data caused by optical aberrations or misalignments.

6.1.2 Image-Based Feedback Tracking Techniques

In most real-world situations, the observed particles are surrounded by dense environments. In biological systems, particularly within cells, various cellular components can influence particle movement. Often, it is these interactions that we seek to reveal. To reliably confirm that the observed interactions, such as hindered diffusion (e.g., as discussed in the publication on acoustofluidic trapping [19] in **Chapter 3**) or altered diffusion speeds,

are the ones we aim to study, it is necessary to record images for sufficient proof. This is where image-based tracking methods come into play [199, 207]. While they generally lack the imaging speed and resolution of trajectory-based techniques, they provide higher information content, making them invaluable in such contexts.

The XY detection can be achieved using advanced image segmentation techniques that can identify particle movement direction in real-time as discussed in the following publication of this chapter. For axial detection, optical aberrations are commonly employed to distinguish the direction of particle diffusion [207]. One method involves applying astigmatism, which displaces the focal points in the axial direction for the X- and Y-axis. By incorporating a cylindrical lens, the direction of movement can be determined by analyzing the elongation of the PSF. Although this technique provides excellent tracking results, the optical aberrations negatively impact imaging quality. Another approach to detect Z-displacement is by separating the observation volume into two or more distinct observation planes [208]. The main problem about image-based tracking technologies is the frequent use of cameras as detector and pure wide-field approaches. Due to the out of focus blur [91] the axial resolution is limited and not suitable for enhanced tracking approaches.

6.1.3 Single Particle Tracking with Fluorescence Lifetime

To extract more data than just the trajectory, time-resolved devices such as TCSPC are used to determine the particle's position based on the photon arrival time. For example, in the technique called **T**racking **S**ingle particles **U**sing **N**onlinear **A**nd **M**ultiplexed **I**llumination (TSUNAMI) the excitation pattern is multiplied and spatially distributed to form a tetrahedral shape [209]. Each beam that shapes the PSF latter on, travels different optical distances, resulting in distinct excitation times. Using TCSPC, a gated detection system is implemented, where the photon arrival time reveals which PSF excites the particle, thereby determining its spatial position. Additionally, as photon arrival times are already recorded, the fluorescence lifetime can also be measured, providing further insights into the trajectory and properties of the particle. A recent approach published by Giuseppe Vicidomini's group utilized specific **A**valanche **P**hoto**d**iode (APD)s in an asynchronous readout mode [196]. This detector not only enables tracking but also allows the detection of fluorescence lifetime, adding a crucial dimension to the measurement. The already mentioned orbital tracking microscopy was also combined with TCSPC devices for lifetime measurement on FRET-pairs [191]. Till now, all SPT combinations with FLIM were done in the trajectory-based category and are therefore used in an spectroscopic way to the tracked particle [210].

In conclusion the active SPT methods were separated in two categories holding different advantages and limitations. While the trajectory-based group is fast and robust it misses the surrounding information. The image-based group consists of this information but to the cost of tracking speed and extended Z-tracking possibility's. In the following chapter we introduce the second developed technique, that combines image-based tracking with diffraction limited resolution and a fast tracking algorithm by modifying a TPEFM

system. Further, it is combined with SUPER-FLIM making it the first image-based SPT technique that not only measures the lifetime of the tracked particle but also the surrounding capable for lifetime based particle-discrimination

A detailed comparison of various up-to-date tracking technologies, including the one presented here, is provided in the supplementary information (**S7**) of the publication *"Spectrally Encoded Multiphoton Particle Tracking (SEMPA-Track): A Real-Time 4D-Single Particle Tracking Fluorescence Lifetime Imaging Microscope"*, which can also be found in the **Appendix B.1**.

6.2 Spectrally Encoded Multiphoton Particle Tracking (SEMPA-Track)

Authors	**Thomas Kellerer**, Tanja Grawert, Florian Schorre, Judith A. Müllerer, Joachim O. Rädler and Thomas Hellerer
Title	*Spectrally Encoded Multiphoton Particle Tracking (SEMPA-Track): A Real-Time 4D-Single Particle Tracking Fluorescence Lifetime Imaging Microscope*
Journal	Nature Communication Engineering Under review
DOI	—

In the specially designed SPT method to track LNPs in cells, we employed PSF engineering, a method werde the normally rugby shaped PSF is modified with phase plates or modern **S**patial **L**ight **M**odulator (SLM) [211]. A method using for example a double-helix shaped PSF showed astonishing results by the group of William Moerner [212]. For our method, the axial position of two laser spots is separated by introducing a small diverging angle in the backfocal aperture of the objective of one laser (**Figure 6.2**) and thus easier to implement without the need of phase-plates or an SLM. This setup creates three distinct laser volumes that utilize the fluorescent photons thrice: **i)** An image can be generated by detecting the amount of fluorescent photons; **ii)** The spectral information of the photons is used to detect the axial motion of the particles; and **iii)** the arrival time of the photons provides insights into the fluorescence lifetime, which reflects the microenvironment. By designing a suitable optical setup and integrating a tracking algorithm, it was possible to track LNPs ranging from 82 nm to large particles with diameters up to 6.5 µm. For particles around 170 nm, we were able to extend the observation time by a factor of 13, increasing the diffusion time from D=2.58 $\mu m^2 s^{-1}$ with a static observation time of 2.71 s to 34.59 s in a tracked observation. For slower diffusion coefficients achieved by adding glycerol to the solution, we were also able to track the same particles for up to 97.83 s at D=1.30 $\mu m^2 s^{-1}$.

This technique was used next to various characterization measurements to visualize endosomal pathways inside cells. Dual-labeled LNPs (mRNA: **Cy**anine**3** (Cy3), inside: Fluorescein) were used to transfect HuH7 cells. We demonstrated three distinct movement patterns, illustrating the strength of our real-time image-based SPT technique. First, we tracked the diffusion time of freely diffusing LNPs in the cell medium, which had a diffusion time of 1.94 $\mu m^2 s^{-1}$. Next, we observed an endosome inside the cell, carrying an LNP. This showed direct motion towards the cell nucleus and slower diffusion (0.11 $\mu m^2 s^{-1}$) due to the higher viscosity in the cytosol. Additionally, we tracked an LNP that was trapped at the cell membrane, exhibiting hindered diffusion with D=0.011 $\mu m^2 s^{-1}$ and a mean free path length of 0.6 µm. Lastly, we showed using basic XY-Tracking that the labeled mRNA

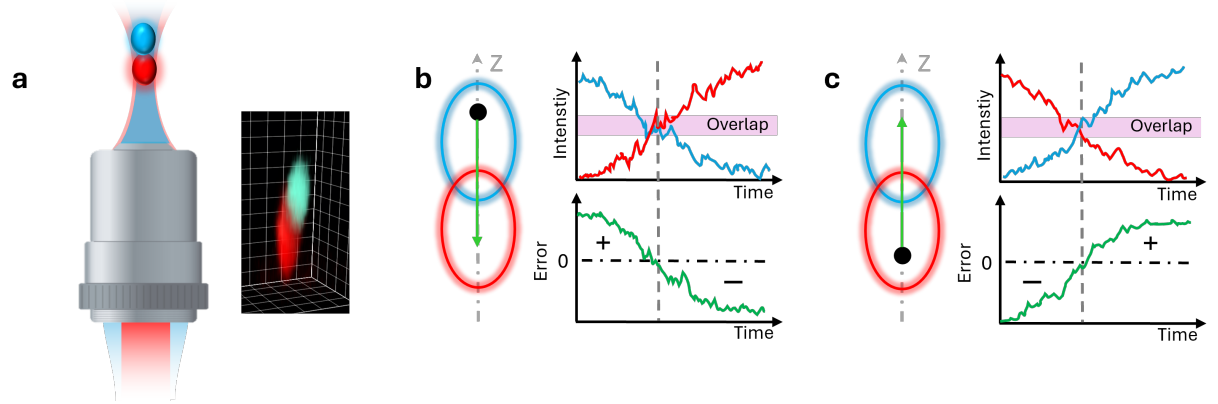

Figure 6.2: Schematic Representation of the SEMPA-Track Technology: The fundamental of this technique are the two shifted PSF along the optical axis (Z) as shown in **a**. The experimental validation was done with severel PSF scans. The feedback algorithm for a particle that is moving downwards is represented in **b**. Here the error signal changes its sign from positive to negative. The system changes the piezostag in a way, that the error signal increases until it reaches the overlap region where the difference signal is approximately zero. For a particle that is moving in the other direction the illustration in **c** displays the tracking signals.

diffuses near the nucleus with a diffusion constant of D=0.012 µm^2 s^{-1}, mostly representing the mRNA in the endoplasmic reticulum [38].

Furthermore, we demonstrated the potential integration of this technique with SUPER-FLIM (see **Chapter 5**) for combined experiments, significantly enhancing the amount of information that can be obtained. This capability offers substantial advantages, particularly in the context of modern tracking technologies. Many existing tracking methods are either unable to detect lifetime information or are limited to trajectory-based approaches. For trajectory-based tracking, lifetime extraction is achieved by accumulating signals over an extended period while maintaining the laser spot on a single particle. In contrast, image-based tracking methods face challenges with averaging due to the rapid changes in the FOV. With our ability to measure lifetimes within an astonishingly short pixel dwell time of 102 ns, we can capture lifetime data across a wide FOV within a single image. As a result, we are the first group to successfully combine real-time, image-based tracking microscopy with the simultaneous capability to measure lifetime values dynamically. This breakthrough enables unprecedented insights into particle behavior, opening new avenues for advanced imaging and tracking experiments.

6.2.1 Contribution

The technique, including its conceptualization, optical and electronic setup, sample preparation, and experimental execution, was developed and implemented by Thomas Kellerer. This work was part of a VDI-funded project, which Thomas Kellerer also managed, overseeing all aspects of the project from the initial design to the final execution (SEMPA-Track

FKZ:13N16300). The optical design and theoretical foundation for the axial offset were originally developed in the master's thesis of Florian Schorre, with PSF measurements performed by Tanja Grawert as part of her bachelor's thesis, both supervised by Thomas Kellerer. Judith Müller provided the cell and LNP samples. The manuscript was primarily written by Thomas Kellerer and Thomas Hellerer.

Spectrally Encoded Multiphoton Particle Tracking (SEMPA-Track): A Real-Time 4D-Single Particle Tracking Fluorescence Lifetime Imaging Microscope

Thomas Kellerer[1,2], Tanja Grawert[1], Florian Schorre[1], Judith A. Müller[2], Joachim O. Rädler[2], and Thomas Hellerer[1,*]

[1]Multiphoton Imaging Lab, Munich University of Applied Sciences, 80335 Munich, Germany
[2]Faculty of Physics and Center for NanoScience, Ludwig Maximilians-University, 80539 Munich, Germany
[*]hellerer@hm.edu

ABSTRACT

Image-based single particle tracking reveals specific movements or interactions of the particle under investigation with its surrounding. Existing methods often introduce optical aberrations, require multiple detectors, or rely on specific detection mechanisms to generate a feedback signal that keeps a particle in the field of view. These approaches are almost always camera-based, enabling rapid image acquisition but lacking fluorescence lifetime information and the high optical resolution associated with laser scanning microscopy. Using point spread function engineering, we modified the excitation geometry of two lasers by displacing their axial positions along the optical axis. These lasers were then scanned with a resonant galvo scanner in a two-photon laser scanning approach. The separated observation volumes enabled the extraction of the axial movement of the particle, while image information was used to detect XY-displacement. Both feedback values were fed into a piezoelectric stage to keep the observed particle in the field of view. By employing a digital lock-in amplifier for signal detection, the fluorescence could also be used to stream lifetime data by evaluating the phase shift in comparison to the two-photon excitation. We validated our tracking capabilities on lipid nanoparticles carrying messenger ribonucleic acid (mRNA) into HuH7 cells, analyzing diffusion coefficients and trajectories in intra- and extracellular environments. Subsequently, we combined the tracking approach with fluorescence lifetime measurements, adding an additional dimension to discriminate between different particles during tracking. We believe that this framework contributes to the advancement of real-time, image-based tracking technologies by integrating fluorescence lifetime data, thereby providing insights into the surrounding environment.

Keywords: Single-Particle Tracking, Fluorescence Lifetime Imaging Microsocpy, Two-Photon Excited Fluorescence Microscopy, Environmental Sensing, Lipid Nanoparticles, lock-in Amplifier, Transfection

Introduction

Regardless of the size scale, three-dimensional motion is an inherent aspect of biological processes. It ranges from the movement of cells at the millimeter scale[1] to the motion of motor proteins at the nanometer scale[2]. To gain insights into such complex dynamics, numerous techniques and approaches have been developed over the past decades[3–6]. Among them, microscopy stands out as a particularly intuitive method for capturing and analyzing motion. However, to effectively track dynamic movement of particles using microscopy, two fundamental prerequisites are required: high temporal and high spatial resolution. Achieving both simultaneously is a significant challenge, as these parameters are often optimized independently rather than concurrently[7]. Many research groups are working to overcome this obstacle by developing techniques that push both the spatial and temporal resolution beyond known limits[8–10].

While various techniques have been developed to track 2D movements of cells, cellular components, nanoparticles, and even proteins, yielding remarkable biological insights[11–14], the primary challenge remains in detecting motion in all three spatial dimensions. Most microscopy techniques capture movement in the XY-plane, while the Z-direction often remains elusive. This limitation arises because a microscopic image is essentially an intensity snapshot of a single plane (**Figure 1 - a**).

To address this, the field of single-particle tracking (SPT) microscopy has evolved[3,4]. Characterized by active and passive methods, its goal is to follow specific particles along their erratic paths. Passive SPT involves time-lapse recordings at different axial locations, with trajectories extracted during post-processing. In contrast, active SPT incorporates feedback algorithms to keep a particle constantly within the field of view. This approach has been extensively studied and is implemented by modifying either the detection- or excitation scheme. Most of these techniques focus solely on the particle's trajectory[15–20].

This so-called trajectory-based single-particle tracking approach has been widely used to address biological questions and has been combined with time-resolved measurements, such as fluorescence lifetime imaging microscopy (FLIM), to add an additional parameter to the trajectory[15,21–23]. However, in some cases, the spatial information provided by the particle's trajectory is insufficient, as jumps in the movement or anomalous diffusion often stem from the interaction of the target particle with its surrounding environment. To overcome this limitation, image-based tracking microscopy methods were developed, which additionally capture the surrounding[24,25]. However, this extra information typically comes at the cost of reduced tracking speed and the integration with FLIM techniques remains unfeasible to date. Nonetheless, understanding dynamic biological processes fundamentally requires studying the interaction between a structure and its microenvironment, as well as the changes within that environment.

An illustrative example of this is the delivery of messenger ribonucleic acid (mRNA) to cells using lipid nanoparticles (LNPs)[26,27]. Once internalized, these nanoparticles are trapped within an endosome and follow various paths over different timescales[28,29]. The movement of the LNPs within the endosome and the endosome's own motion play a crucial role in the process[30,31]. The targeted release of mRNA into the cytoplasm is highly inefficient (approximately 2% for siRNA)[32], making it a critical area of research. Studies on 3D virus tracking using orbital tracking combined with wide-field imaging[33] have provided valuable insights into the motion behavior of artificial virus particles. For LNP only one publication showed the three dimensional behavior in mucus like surroundings[34] but showed already great potential with the used trajectory-based SPT method[4,19]. However, to the best of our knowledge, image-based tracking algorithms including FLIM for such applications have not yet been reported.

The technique presented here called **S**pectrally **E**ncoded **M**ultiphoton **PA**rticle **Track**ing (SEMPA-Track) aims to simultaneously measure the real-time 3D motion of nanoparticles and capture the microenvironment of their surroundings (**Figure 1 - c**). This is achieved by utilizing fluorescence photons thrice: **i)**, to image the surroundings and track particles in the XY-plane based on signal intensity; **ii)**, to track particles along the Z-axis by spectrally discriminating the photons; and **iii)**, to extract the fluorescence lifetime by analyzing photon arrival times. To accomplish this, we modified the excitation geometry of a two-photon excited florescence microscope (TPEFM). By deliberately misaligning a telescope in the laser beam path, we created a slightly divergent beam at the objective lens's rear aperture, resulting in an axial offset of the point spread function (PSF) along the optical axis (Z-direction) (**Figure 1 - f**).

Using two lasers with different wavelengths, one of which experiences this axial offset, we generate three excitation zones: two separate volumes, one for each wavelength, and an overlap region in between. The particles under study are labeled with two dyes, each excited by a different laser and detected by spectrally separated channels. As the particle moves along the Z-axis, its direction of motion is determined by the calibrated difference in signals from the two detectors (**Figure 1 - d** and **e**). A piezoelectric stage, controlled in real-time by an algorithm, keeps the nanoparticle within the overlap region of the excitation zones.

By recording signals with a lock-in amplifier, we extract phase-shift information to determine the fluorescence lifetime. When excited with ultrashort pulsed lasers, the fluorescence signal is a convolution of the laser pulse (simplified as a Dirac pulse for $\tau < 100\,\mathrm{fs}$) with the exponential fluorescence decay. Measuring the phase shift between the reference laser signal and the fluorescence signal allows us to extract the lifetime within 102 ns, as previously described by our group[35,36]. This technique is ideally suited for applications where particle motion, as represented by trajectory information alone, is insufficient. Furthermore, emerging methods such as quantum sensing in biological contexts could benefit significantly from these advanced techniques[37]. Most importantly, this work demonstrates for the first time the ability to not only measure the lifetime of a tracked particle but also to capture its surrounding environment. For a more detailed state-of-the art comparison refer to supplementary file **S8**

Results

Axial PSF-Shift

The fundamental concept of our technique is based on the axial shift of the PSF of a focused laser beam, which corresponds to the optical aberration called defocus. To generate such an offset, various setups can be utilized (electro tunable lenses, acousto optical lenses, spatial light modulators, etc.), all of which make the laser beam divergent at the objective's rear aperture by introducing a slight wavefront curvature[38,39].

For our setup, we incorporated a Galilean type telescope into the optical system, featuring a movable diverging lens (DL). This simple optical device allows us to adjust the PSF shift, which is of crucial importance, as our basic theoretical simulations suggest and our experiments confirm (**Figure 1- h** and **Table 1**). In the search for a suitable arrangement and positioning of the telescope within the optical setup, Gaussian beam matrix analysis was performed using matrices T for translations over distances d in air and matrices L for thin lenses with focal lengths f. Thus, the entire optical path (**Figure 1 - g**) from the laser output to the focal point of the objective lens is described by the matrix product (**Equation 1**):

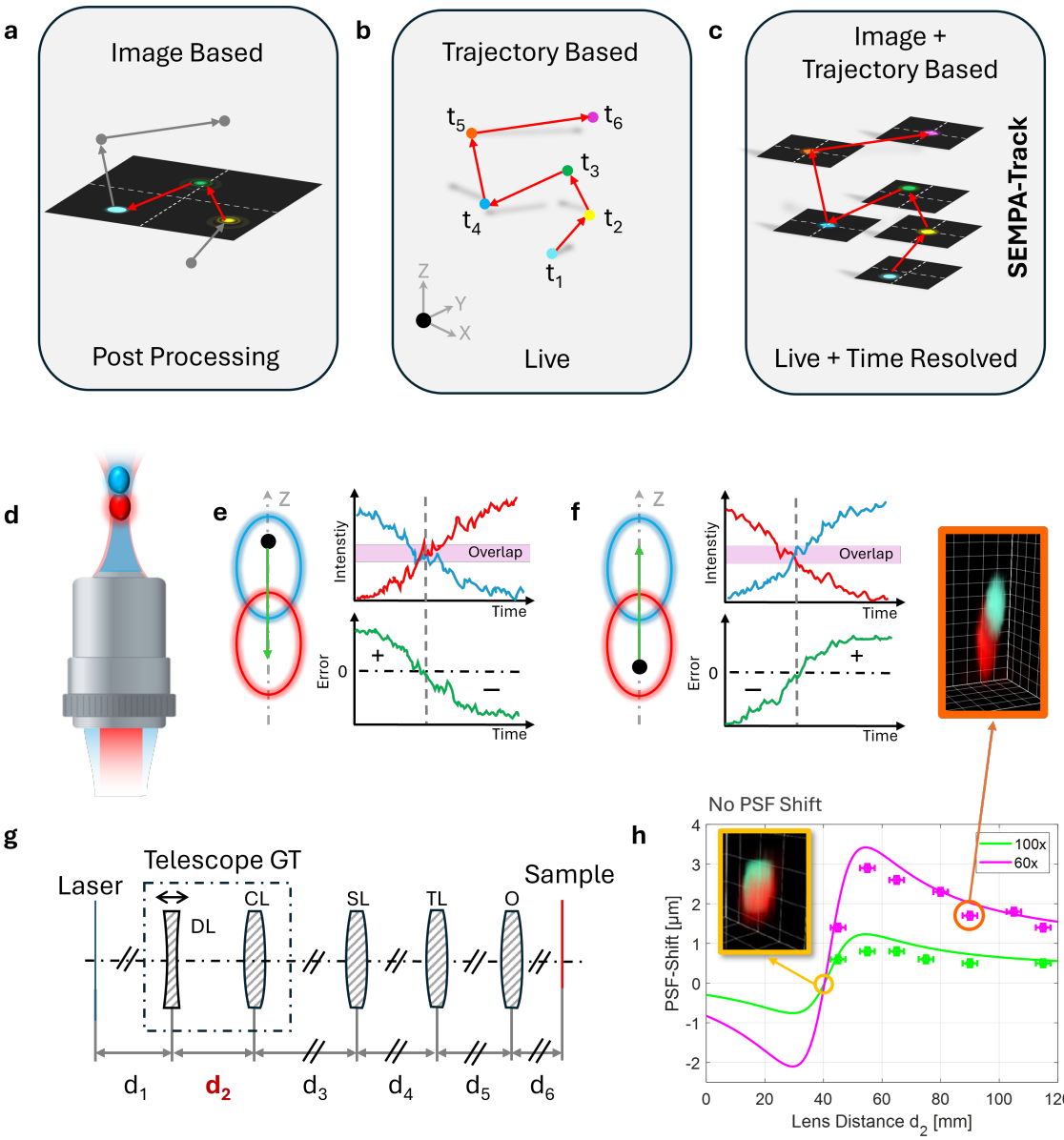

Figure 1. Different 3D tracking methods and principle of SEMPA-Track: The 3D tracking methods are separated into **a** image-based and **b** trajectory-based approaches. Our technique (**c**) combines both methods and also incorporates fluorescence lifetime information. The basic principle relies on the axial offset of two laser volumes, as shown in **d**. The working mechanism is illustrated in **e** and **f**. To create the PSF offset, a Galilean telescope (GT) is included in the optical path (**g**), enabling simulations **h** to predict axial displacement based on the configuration of the Galilean telescope. In this simulations also the experimental measured shifts are plotted. DL: diverging lens, CL: collimating lens, SL: scan lens, TL: tube lens, O: objective.

$$M = T_{d_6} \cdot L_O \cdot T_{d_5} \cdot L_{TL} \cdot T_{d_4} \cdot L_{SL} \cdot T_{d_3} \cdot L_{CL} \cdot T_{d_2} \cdot L_{DL} \cdot T_{d_1} \tag{1}$$

Applying the system matrix M to a Gaussian beam results in varying Z-positions of the final beam waist depending on the distance d_2 of the movable telescope lens as well as on the magnification of the objective lens (60x and 100x) which is linked to its focal length. Care was taken that for the overall length of the system was constant. If d_2 was changed also d_1 was adapted consequently. The resulting, relative PSF shift is visualized in **Figure 1 - h**. The other laser, which did not pass through the telescope, served as a reference.

To determine whether the simulations are comparable to our experimental setup, we measured the PSF by imaging 200 nm Crimson beads and collecting Z-stacks with 100 nm step size. As with the tracking experiments, we used two lasers with

different wavelengths: one laser beam is defocused, the second is not. The difference here is that we use a single dye that can be excited with both wavelengths. To distinguish the two separate excitation zones, only one laser was switched on at a time. Later, in the tracking experiments, we found that lens distances of d_2 =90 mm worked best for our objective lenses with 60x and 100x magnification, respectively. At this position the overlap as well as the separated excitation volume are equal in size. The resulting 1.7 µm axial shift for 60x magnification amounts nearly three times the 600 nm axial shift for 100x magnification because the elongation of the PSF along the Z-axis scales with the square of the magnification which is linked to the numerical aperture. All measured axial shifts are summarized in the following table and agree well with our simulations. Further evaluations and more detailed figures are displayed in the supplementary section **S2**.

Table 1. Results of the experimental gained PSF-shifts

	60x Objective					
d_2 [mm]	45 ± 5	55 ± 5	65 ± 5	80 ± 5	90 ± 5	115 ± 5
PSF-Shift [µm]	1.4 ± 0.2	2.9 ± 0.2	2.6 ± 0.2	2.3 ± 0.2	1.7 ± 0.2	1.4 ± 0.2
	100x Objective					
d_2 [mm]	45 ± 5	55 ± 5	65 ± 5	75 ± 5	90 ± 5	115 ± 5
PSF-Shift [µm]	0.2 ± 0.2	0.6 ± 0.2	0.8 ± 0.2	0.8 ± 0.2	0.6 ± 0.2	0.5 ± 0.2

Freely Diffusing Particles

To demonstrate SEMPA-track under real conditions, we tracked single nanoparticles, which are freely diffusing in solutions with different viscosities adjusted by the water:glycerol ratio. Two important diffusion parameters, the hydrodynamic diameter and the diffusion coefficient, were determined separately by Fluorescence Correlation Spectroscopy (FCS)[40]. From these measurements (see supplementary **S4** and **SM6**), we obtained $d = (169.88 \pm 18.10)$ nm as the mean hydrodynamic diameter and $D_{0\%} = (2.58 \pm 0.26)\ \mu\text{m}^2/\text{s}$ as the mean diffusion coefficient in pure distilled water. Adding 10% glycerol reduced the diffusion coefficient to $D_{10\%} = (2.10 \pm 1.07)\ \mu\text{m}^2/\text{s}$, and 25% glycerol lowered it further down to $D_{25\%} = (1.30 \pm 0.50)\ \mu\text{m}^2/\text{s}$. The results are summarized in **Table 2**.

Table 2. FCS Results for the Diffusion Coefficients.

Glycerol Fraction	0%	10%	25%
Viscosity η $[mPa \cdot s]$[41]	0.93	1.3	2.2
Diffusion Coefficient D $[\mu\,\text{m}^2/\text{s}]$	2.58 ± 0.26	2.10 ± 1.07	1.30 ± 0.50

Based on these independently calibrated parameters it is now possible to demonstrate one of the main advantages of trajectory-based tracking compared to image-based tracking. For the latter we imaged the particles while keeping the frame center of a time series fixed in space. Extracting the recorded 2D trajectories in a post-processing step, we measured the mean time to be 2.71 s, that a nanoparticle remained in the static observation frame. With the tracking switched on, the observation time of the tracked particle was extended to 34.59 s which is nearly 13 times longer. The frame rate of the time series was in both cases (tracking off/on) 7.6 fps with an image size of 1024x1024 pixels. The trajectory's along with separated images are shown in **Figure 2**. The observation time is limited mainly by the particle moving out of the image plane in the Z-direction. This is where the advantage of SEMPA-Track comes into play, because the error signal for tracking also contains the sign of the Z-direction (up or down), which accelerates the servo loop. The observation time increases for 10% (**b**) and 25% glycerol (**c**) mixtures to 75.67 s and 97.83 s, respectively (**Table 2**). **Figure 2 - a, b** and **c** shows exemplary 3D trajectories of 170 nm sized particles diffusing in solutions with 0%, 10% and 25% glycerol fractions (see supplementary video **SM6**). **Figure 2** shows five exemplary images of the tracking routine where two consecutive images are overlayed (image N in red and N+1 in cyan). XY-tracking moves the particle back to center as explained in subsection and supplementary **S6**.

mRNA loaded Lipid Nanoparticles

As biological application, we monitored the cellular pathway of lipid nanoparticles delivering mRNA into the cell. Initially, the 100 nm sized LNPs diffuse freely in cell culture medium until they attach to the cell membrane. Upon contact, some LNPs are taken up by the cell through endocytosis, forming membrane-bound vesicles known as endosomes. These endosomes then migrate within the cytoplasm. Over time, proton pumps begin to acidify the endosomal interior, triggering changes in the lipid layers of the nanoparticles. This acidification can destabilize the LNP structure, promoting the release of mRNA from the endosome into the cytosol where it can be translated[27]. This delivery process is illustrated in a simplified form in **Figure 3 - b**.

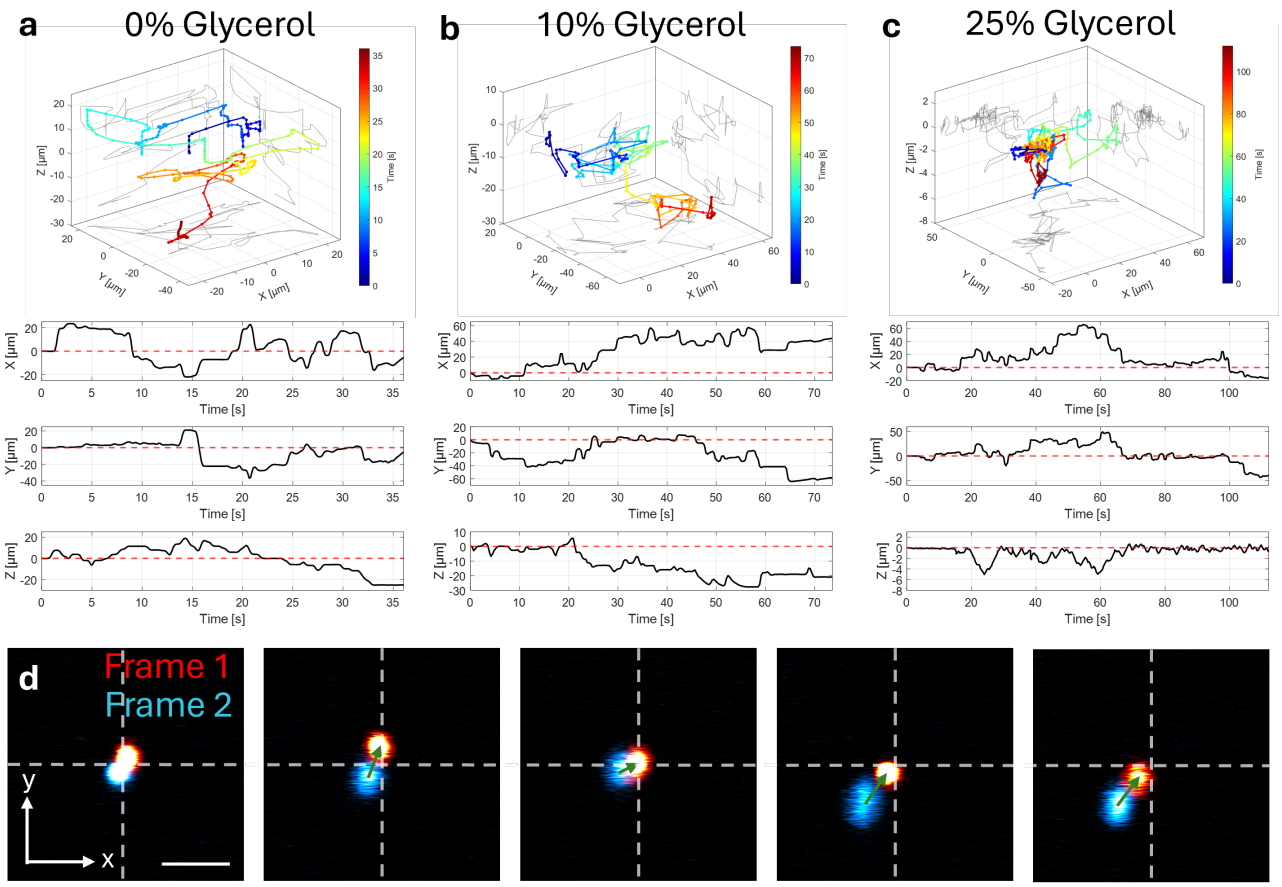

Figure 2. Trajectories of freely diffusion 170 nm **particles**. In **a** the trajectory of the piezoelectric stage is plotted with a color look up table representing the time. Underneath the respective position for the X-, Y- and Z-axis is displayed. In **a** the nanoparticles were diffusing in pure distilled water with a diffusion coefficient of 2.58 $\mu m^2 s^{-1}$. In **b.)** 10% glycerol was added resulted in a diffusion coefficient of 2.10 $\mu m^2 s^{-1}$. The measurements at a diffusion coefficient of 1.30 $\mu m^2 s^{-1}$ was created by adding 25% glycerol to the distilled water (**c**). Section **d** shows a small section of one track process. Here always two consecutive images are overlayed (Where N is red and N+1 is cyan). The green arrow represents re-centering.

In our experiment, HuH7 cells were seeded on a patterned slide[42] and transfected with Cy3-labeled mRNA encapsulated in LNPs together with Fluorescein solution as counterstain. The cell nuclei were stained with Höchst dye to localize the LNPs in relation to the cell. The fluorescence of the nuclei was detected with a third, spectrally separated channel. With the help of the patterned substrate, the living cells were firmly attached to the slide. In this way, LNPs taken up by the cell remained inside our observation frame, eliminating the need for XY-tracking. On the other hand, Z-tracking had to be carried out during the experiment because of the optical sectioning of our TPEFM. While the Z-position of the LNP were recorded with the tracking procedure, the XY-positions were subsequently extracted by post-processing the time series with the Fiji software[43].

The results of our experiment are visualized in **Figure 3** and the supplementary movies **SM1**-**SM3** (**S9 - S11**). We could divide the entire pathway into three steps. The first step (**A**), shown in **Figure 3 - A**, depicts the LNP diffusing outside the cell, with a measured diffusion coefficient D=1.95 $\mu m^2 s^{-1}$ (see supplementary movie **SM1** - **S9**). The latter was determined with the so-called mean squared displacement (MSD) analysis over a 60 s long tracking period. The rapid diffusion, along with the particle's distance from the cell nucleus, suggests that the LNP is freely diffusing in the surrounding cell culture medium.This finding is supported by the Einstein-Stokes-equation that results for a 100 nm a diffusion coefficient of 2.14 $\mu m^2 s^{-1}$. This theoretical value closely aligns with our experimental results, see **Table 3**.

In the second step (**B**), the LNP is attached to the cell membrane. The MSD curve shows along with the fit indicates confined motion. The free path length α was determined to be 0.6 µm, with a diffusion coefficient of 0.011 $\mu m^2 s^{-1}$. This is evident as well in the trajectory, and in the 2D projection, where the particle maintains a relatively constant distance from the nucleus. Please see here the supplementary movie **SM2** (**S10**).

In the third step (**C**), the LNP is diffusing inside the cell while encapsulated in the endosome. Here, the motion yields to a significantly lower diffusion coefficient of 0.13 $\mu m^2 s^{-1}$ compared to step **A**. This reduction can be attributed to the bigger size of the endosome and the denser intracellular environment[44]. By superimposing the trajectory over the image recorded with the third channel, it becomes clearly visible that the LNP is in large part moving around the nucleus. This can be seen in the supplementary movie **SM3** and in **S11**.

After approximately 1.5 h to 2 h, we observed very slow-moving LNPs accumulating near the cell nucleus (**Figure 3 - D**). As the number of LNPs increased, single-particle tracking became challenging. To address this, we conducted a 2D time-series of a single Z-plane and tracked the particles with post-processing. This analysis revealed a diffusion coefficient of 0.050 $\mu m^2 s^{-1}$. Because the colocalization of the intensity signal of the two color channels indicates a decreased Fluorescein fluorescence, the measured particles must be freely diffusing Cy3 flurophores entrapped in the endoplasmic reticulum. For the tracking videos and further analysis graphs please see the supplementary information **S5**.

Table 3. MSD Analysis of the LNP Tracks.

Location	Tracking Time [s]	Diffusion Coefficient [$\mu m^2/s$]	Diffusion Type
Outside Cell	60	1.95	Free Diffusion
cell membrane	45	0.13	Free Diffusion
Inside Cell	75	0.011 ($\alpha = 0.6$ µm)	Confined Diffusion
Endoplasmic Reticulum	60	0.012 - 0.050	Free Diffusion

Combining Tracking and Fluorescence Lifetime Imaging

After successfully testing the tracking method on a proof of principle sample system we wanted to extend the information content of the technique by combining time resolved measurements. A significant advantage of trajectory-based tracking methods is their ability to record the fluorescence lifetime of the tracked particle. While the feedback mechanism keeps the particle in focus, fluorescence can be recorded continuously, allowing for sufficiently long time-resolved measurements to extract the lifetime. This additional parameter provides valuable insights into microenvironmental properties, such as pH value, polarity, or temperature. In contrast, for image-based techniques, the pixel dwell time is often too short to capture meaningful lifetime data, rendering microenvironmental sensing impractical. However, lifetime data can offer crucial insights in imaging and help, for example to differentiate fluorophores with nearly identical emission spectra due to variations in their lifetimes. Using a novel FLIM technique called Speed-Up Fluorescence Lifetime Imaging Microscopy (SUPER-FLIM)[35,36], we can integrate lifetime measurements into SEMPA-Track. This is achieved through fast lifetime extraction based on a lock-in amplifier, enabling pixel dwell times of 102 ns, which align with the imaging speed of our setup.

For demonstration, we used standardized fluorescent beads with a known lifetime of 1.7 ns and 2.7 ns. A single bead was tracked for 128 s while freely diffusing in distilled water (see trajectory in **Figure 4 - a**). The time series contains 1000 images with a size of 1024x1024 pixels captured at 7.6 fps (128 ms per frame). By recording the signal of each pixel with a lock-in amplifier, we can use the demodulation and phase-shift information to extract the fluorescence lifetime. By post-processing the time series, a binary mask is applied to the individual images to only include the pixels that contain the particle at the center

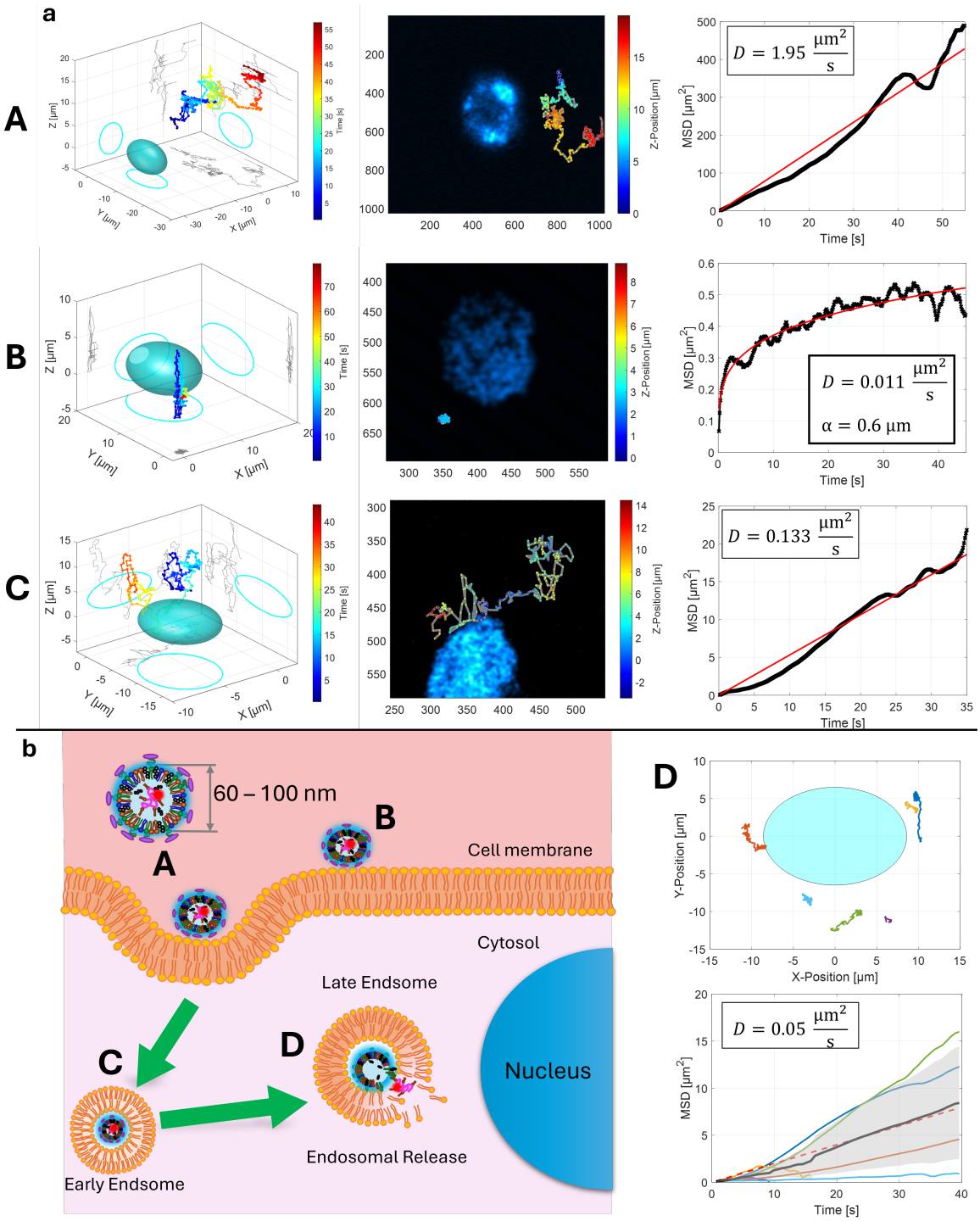

Figure 3. Tracking Results for Lipid Nanoparticles inside and outside of HuH7 Cells We show four different LNP movements. In **A** a free diffusing LNP outside of the cell, in **B** an entrapped particle at the cell membrane and in **C** a LNP moving inside the cell. The results in **a** show the 3D trajectories, together with the nucleus. In the middle section a 2D overlay image is represented and next to it the calculated MSD curve. The schematic of the LNP movement is shown in **b**. **C** after one to two hours, further 2D timelaps images were recorded showing the Cy3 signal diffusing around the nucleus

(see **Figure 4 - b**). By creating a histogram with all the lifetimes of the selected pixels, we determined an average fluorescence lifetime of $\tau = (2.68 \pm 0.50)$ ns, as shown in **Figure 4 - c**. The lifetime of the individual images is plotted against the recording

time to cover the entire trajectory in **Figure 4 - e**. Here, we also include the normalized intensity as a false color code to demonstrate that the lifetime value is independent of the intensity. Even when a particle leaves the image frame before the tracking algorithm can process it, the correct lifetime can still be detected. As long as a certain amount of photons are recorded. With this information the 3D trajectory is color coded with the lifetime data in **Figure 4 - d**. Finally, another histogram is created from the lifetimes of all 1000 images, which results in an average value of $\tau = (2.62 \pm 0.56)$ ns for the entire trajectory (see **Figure 4 - f**) The result matches well with literature (τ =2.7 ns)[45]. For the supplementary document we converted the time series into two movies, one with color coded intensity and the other with color coded lifetime (see supplementary movie **SM4** - **S12**).

The last experiment we present here shows a novelty in tracking combined with fluorescence lifetime measurement. By focusing the tracking algorithm on a smaller region (highlighted in magenta in **Figure 4 - g**), we can specifically target a portion of the image while excluding surrounding structures from the tracking process. However, the fluorescence lifetime of these excluded areas can still be analyzed, as shown in red in **Figure 4 - h**. When beads with different fluorophores are used, the system can detect distinct fluorescence lifetimes for each. This illustrates the dual advantage of the SEMPA-Track approach, where both the particle's trajectory and the surrounding environment can be imaged and analyzed based on their fluorescence lifetimes. For instance, the tracked bead exhibits a shorter lifetime of $\tau = (1.77 \pm 0.05)$ ns, while a longer lifetime ($\tau = (2.72 \pm 0.16)$ ns) is observed for the passive bead and closely matches with the literature values[45] of 1.7 ns and 2.7 ns. Although the intensity images do not reveal any obvious differences between the two particles, the fluorescence lifetime data distinctly sets them apart.

Discussion

The results achieved with our tracking method demonstrate a new way to monitor diffusing nanoparticles, which interact with their environment. The unique feature is, that it combines the advantages of tracking that is based on wide-field camera detection with tracking based on laser-scanning a probe volume. The advantages of the first type of methods coincide with the disadvantages of the second type. The first lacks high spatial resolution in the third dimension for optical sectioning and is difficult to combine with other microscopy techniques such as fluorescence lifetime microscopy. In the second type, the particle's environment is not recorded, only its trajectory, making it difficult to monitor the interactions between the particle and its environment. In contrast, SEMPA-track records both the trajectory and the environment in real time and has been shown to work well with fluorescence lifetime imaging. It is a hybrid technique in that it captures images like a confocal microscope, but never loses sight of the diffusing particle because it always keeps it at the center of the image thanks to the tracking process. Many microscopy techniques that are compatible with confocal or two-photon microscopy can also be integrated into SEMPA-Track to expand its performance capabilities. A detailed overview of and comparison with other 3D tracking techniques can be found in **S7**.

The controlled axial shift between the focal volumes of the two excitation lasers is achieved by a telescope that offers a high degree of flexibility to adapt to different optical setups and configurations. Thanks to the precise control, we were able to optimize the overlap of the volumes, increasing the robustness of the particle tracking process and resulting in artifact-free images. We emphasize the latter because other tracking methods also rely on intentionally introduced aberrations such as astigmatism, which in contrast affect image quality[25]. The theoretical simulations, based on Gaussian beam matrix methods, were well supported by experimental results in quantifying the introduced axial PSF shift (**Figure 1** and **S2**). It is crucial to maintain a high quality laser beam, as slight astigmatism can be exacerbated when applying axial PSF shifts. However, with the help of beam analysis tools and spatial light modulators (SLM), most known aberrations can be effectively compensated for[46,47].

The experiments with freely diffusing particles confirmed the robustness of the system under real conditions (**Figure 2**). Depending on the viscosity of the medium, the diffusion coefficient of the observed nanoparticles decreased from 2.58 $\mu m^2 s^{-1}$ in pure water to 1.50 $\mu m^2 s^{-1}$ in a 25% glycerol mixture. This led to an increase in observation time when tracking was active, which shows how well our algorithm can perform on these time scales typical of life processes. The observation time for the fastest diffusion was an order of magnitude longer with tracking than without. The measured diffusion coefficients agree well with the theoretical model, which further confirms the accuracy of our experimental results. Currently, the concentration of tracked particles must be low, but synchronization of the lock-in amplifier's data transfer to specific XY-regions could allow for higher concentrations. Challenges arise when tracked particles come into contact with others or when the Z-position changes drastically.

Our preliminary study of transfecting HuH7 cells with mRNA-loaded lipid nanoparticles demonstrates the importance of mapping the environment rather than just recording the trajectory. Taking a closer look at the trajectory depicted in **Figure 3 - C**, we observe that the motion starts in the top right corner. From this point, the trajectory exhibits random movement, followed by a more directed path towards the cell nucleus, before transitioning back to a random walk near the nucleus. The corresponding MSD curve shows an almost parabolic shape for 2-15 s. This indicates a more directed movement phase as the

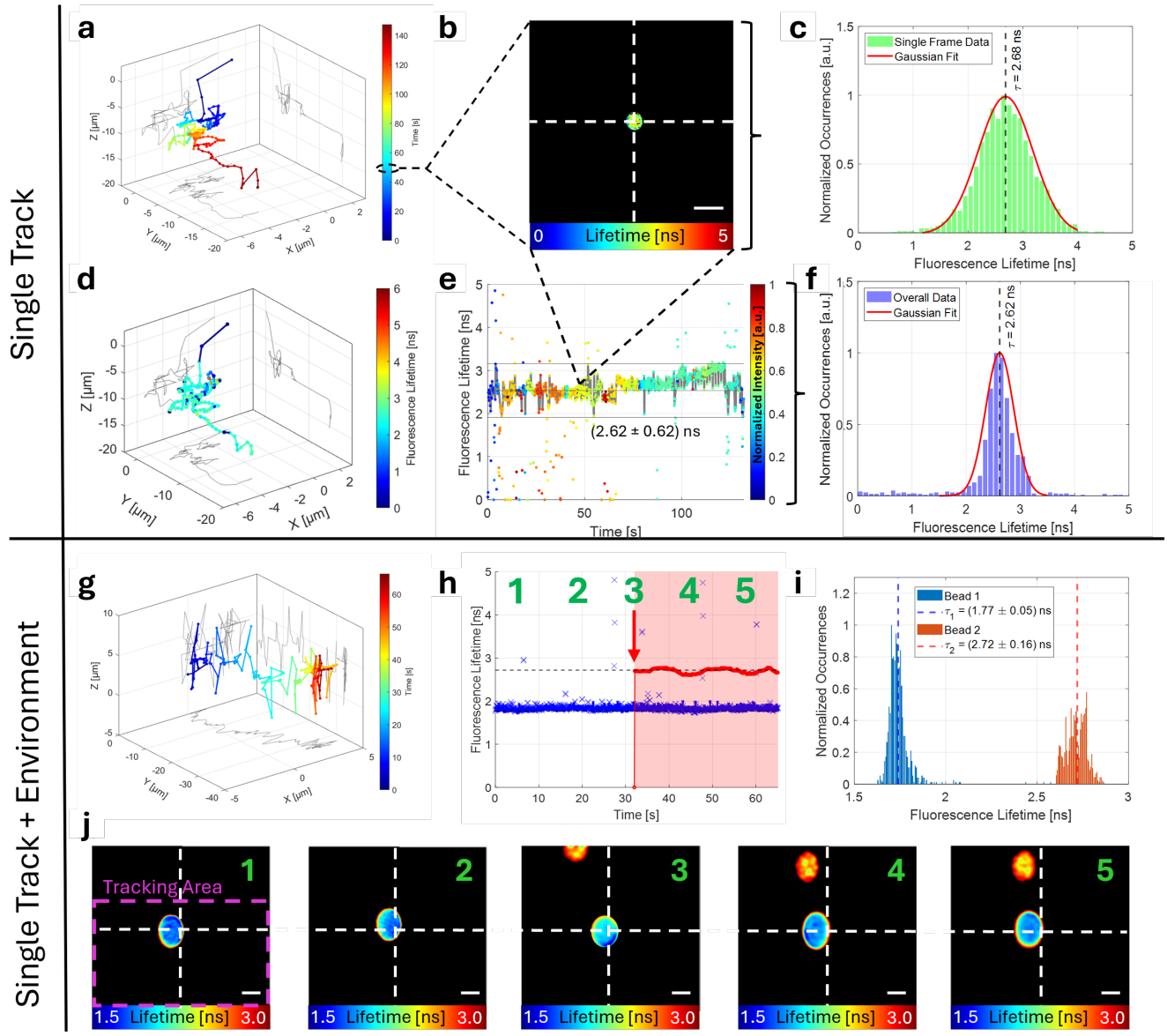

Figure 4. Combination of Tracking and Measuring the Fluorescence Lifetime. In **a** the three dimensional trajectory of the bead is visualized, where the time is false color coded. For a single frame the fluorescence lifetime image is shown in **b** (Scale bar: 10 µm) together with its lifetime histogram **c**. By repeating the evaluation of the lifetime for all 1000 images we achieve the lifetime course in **d** and used this statistic to get the overall lifetime in **e**. Also the trajectory can be used to represent the lifetime course in false color code in **f**. In **g** another track is shown. The difference is that the tracking window was decreased that another particle could be imaged but is not included in the tracking algorithm. The fluorescence lifetime of the two particles are separated and displayed in **h** and the overall lifetime histograms in **i**. Five different images of the track are shown in **j**. Scale bar: **b** - 10 µm, **j** - 5 µm

particle approaches the nucleus. Current literature reports that endosomes can show both slow and fast movements when using fast imaging techniques (frame rates > 30 fps), depending on the motor proteins involved[48]. To further differentiate the types of motion, additional parameters such as velocity can be extracted from our experimental data. This would allow a more robust statistical analysis in future studies, but is beyond the scope of our demonstration here.

Finally, SEMPA-track was extended by fluorescence lifetime imaging microscopy to increase its performance and to be able to observe changes in the microscopic environment.[49,50]. This is particularly valuable for biological and pharmaceutical applications, where environmental conditions such as pH, temperature, or viscosity can impact drug delivery systems. As a proof-of-principle we tracked a freely diffusing particle while simultaneously measuring its lifetime. Tracking in combination

with lifetime measurements as shown in **Figure 4 - a to f** was demonstrated already[15,21–23]. The novelty of our experiment is that the lifetime is not only measured for the tracked particle, but for each pixel of the entire image, so that the environment is also included. This is illustrated in **Figure 4- g to j**, where the distinction between two particle types is made possible by their different lifetimes. This feature represents a significant advancement in single particle tracking, which is demonstrated here for the first time.

In summary, the modification of the excitation geometry of a two-photon microscope in combination with the developed tracking algorithms provides a robust platform for recording particle trajectories as well as images of the environment in real time. The inclusion of fluorescence lifetime data opens up new possibilities for monitoring chemical and photophysical environmental conditions. This integration represents a significant advance for tracking applications in biological research and drug delivery systems, where analyzing the movement and interaction of nanoparticles and changes in the environment is critical to understanding therapeutic efficacy. The future potential of SEMPA-track may include further developments: for example, the overlap region of the focal volumes can be used to excite a third fluorophore with the sum frequency of the two lasers[51]. By adding a third detection channel, its signal could be used as a spatial reference for the particle movement.

Methods

Optical Setup

A detailed description of the optical setup can be found in the supplementary section **S1**.

Tracking Algorithm

To be able to image and track particles in real-time, a significant amount of image processing and data handling is required. This section explains and illustrates the flowcharts, as well as all the steps involved in image processing and data analysis. The algorithm was tested on predifined paths. For this tracking experiments, we validated our system by following a specific path using the microscope's built-in translation stage. The results, shown in the supplementary information (**S3** and **SM5**), confirm the accuracy of both the XY- and Z-tracking algorithms. Tracking letters and complex patterns in different axial regions demonstrated the system's reliability under dynamic conditions, which is promising for applications requiring precise following of complex trajectories.

XY-Detection

By synchronizing our tracking signal with the position signal of the resonant galvo scanner and utilizing the high data transfer rate of a lock-in amplifier, we were able to generate images while simultaneously tracking nanobeads. In **Figure 2 d**, the movement between consecutive images is clearly depicted. The red particle corresponds to image N, while the cyan particle represents image N+1. Overlaying these two images allows us to visualize the particle's movement. Additionally, our algorithm calculates the displacements δX, δY, and δZ between images N and N+1. This information is then used to reposition the entire sample, ensuring the particle is centered in the frame N+2.

To determine the XY-position of the target particle, image information is required. This can be acquired in several ways and depends on the image refresh rate and the necessary tracking speed. For instance, images can be loaded into the XY-program from a designated folder, or a screen recorder can be used to capture the image data what is done in these experiments. After this preliminary step, the active tracking process begins, which is depicted as a flowchart in the supplementary information **S6**.

Following hardware initialization, the region of interest (ROI) within the tracking will occur is cropped from the image. This can be either the entire field of view or a smaller selected area. For accurate image tracking, the software needs to know which objective magnification and scanner zoom factor are being used. With this information, it calculates the pixel size and the corresponding voltage steps required to adjust the image section via the piezoelectric stage.

Subsequently, image processing takes place. After the microscope image has been captured, the following filtering steps are performed: (i) a median filter to suppress pixel-like noise; (ii) a Gaussian filter to smooth the signal; (iii) thresholding to minimize background; (iv) generation of a binary image; (v) an algorithm to fill holes in the binary image; (vi) Hough transformation to determine edges and to detect circles.

After these processing steps, in addition to the two-photon image, we create another image that includes the diameters and center points of the detected particles. This information is also provided numerically to optimize the parameters required for the various filters.

Before the tracking algorithm is initiated, users can selectively decide whether to track a specific particle or to use the particle closest to the center of the ROI.

For every second image, a so-called Hungarian Linker is calculated[52]. This algorithm determines, through optimization steps, which particles between the first and second images correspond to each other and what their trajectory looks like. After establishing this relationship, the algorithm calculates the δX and δY from the target particle to the center of the image and

relays this information to the piezoelectric stage, which then adjusts its position accordingly. The piezoelectric stage position is queried and recorded with each image capture.

Once the particle is recentered in the image, the process repeats until the user terminates the tracking process or the boundaries of the piezoelectric stage are reached. Depending on how many particles are present in the image, this complete process takes around 75-150 ms. The user can choose to save computational resources when the particle is moving slowly by having the algorithm compare the particle's position changes only between every nth frame.

Throughout tracking, various graphs can be displayed, such as the history of the X-, Y-, and Z-stage positions in relation to time.

To minimize errors in the XY-tracking algorithm we also implemented a PI-Controller.

Z-Direction

To achieve accurate tracking of the Z-plane, various computations must be performed, as detailed in this section and visually represented as a flowchart in the supplementary information **S7**.

The initial step entails setting all necessary parameters within the lock-in amplifier. These include the detection of the reference signal and the acquisition and modulation of the signals from both photo multipliers (PMTs). By selecting the appropriate time constant for the filter, one can adjust over how many pixels the signal should be averaged. Outputs from the auxiliary ports of the lock-in amplifier provide the signals from both PMTs, as well as their difference, which can then be processed using a custom-written MATLAB script. Within this program, the two signals are normalized to account for the dark count rate and the individual signal maxima. The intersection point (center of the PSF overlap), at which the two signals cross, corresponds to the tracking point, which manifests as a zero value in the difference signal.

The user can further specify the precise moment for data capture, allowing for adjustments to the different image sizes and associated capture durations. The signal traces can also be smoothed, if necessary. Subsequently, the software evaluates whether the difference signal has increased or decreased. Based on this assessment, the previously read piezoelectric stage is then adjusted by a predetermined step size in the appropriate direction in the Z-position. This process is then iterated.

The difference signal is constantly monitored in order to avoid oscillation around the tracking point due to the stepwise adjustment. If this difference decreases, the set increment is successively reduced, thus mimicking an integral controller. In addition, a threshold value can be set below which the system should maintain its position.

SUPER-FLIM

The lifetime measurement utilizes a technique we have previously presented[35,36]. We employ a lock-in amplifier enabling frequency-domain FLIM detection despite using two-photon excitation. The method is based on the principle that by repetitive excitation at 80 MHz, our fluorescence is also modulated at this frequency. This allows the lock-in amplifier to perform a demodulation and measure the phaseshift between the signal (PMT) and the reference (laser), from which the lifetime can be extracted. However, to calculate valid and correct data, it is necessary to determine the system's offset phase at first, consisting of optical and electrical path lengths, and subtract it from the actual measurement. For this, we use a nonlinear sample that produces a Second Harmonic Generation (SHG) signal[53]. Since the used PMTs exhibit a nonlinear characteristics with respect to intensity fluctuations, two different phases must be recorded with the lock-in amplifier at 0° and 90°. These can then be used to eliminate the intensity dependence and thus obtain a correct fluorescence lifetime. A detailed description about this technique is currently in preparation. Preliminary work can be found here[35,36].

With this setup, depending on the concentration of the fluorophores, we are capable of determining a lifetime within 102 ns, making it ideally suited to be coupled with the tracking microscopy presented here using a pixel dwell time of 122.3 ns.

FCS Measurments

To determine the diffusion coefficient as well as the hydrodynamic radius of particles the FCS measurements were carried out on a LSM980 (LSM980, Zeiss) microscope. For the fitting algorithm the open source software PyCorrFit was used[54]. Here a single component 3D free diffusion fit was applied. Beforehand a calibration measurement on a 10 nM Cy3 solution was carried out to find the structural parameter of 5.7 at a wavelength of 550 nm.

Image Analysis

Image analysis were made with imageJ[43]. Further analysis like the MSD calculation, FLIM analysis and tracking representation was done by self written Matlab (R2020a, MathWorks, USA) scripts.

Fluorophores and Nanoparticles

Nanoparticles

For the free diffusion measurements, 151-200 nm beads (201 02 175, PolyAn GmbH) were utilized. A volume of 1 µL of the bead solution was mixed into 1000 µL of distilled water and underwent vortexing. The resultant sample was then placed into a

μ-Dish 35 mm (80137, ibidi) for the measurement process.

For setting different diffusion constants, the distilled water was preliminary mixed with glycerol (1.04095, Sigma-Aldrich) at the specified ratios of 0%, 10% and 25%.

For the PSF measurements we used 200 nm Crimson beads (F8806, Thermo Fisher). We diluted 1 µL of the bead solution with 10 mL destilled water. After sondicating the beads for 10 min to break up cluster we vortexed the solution and placed 10 µL on a clean coverslip (0107032, Marienfeld). After the solution was dried, we placed a drop of ProLong Diamond mounting media (P36965, Thermo Fisher) on a cleaned slide (MS10FS, Thorlabs) and placed the coverslip on top of it.

Lifetime Beads

For the lifetime measurements, beads with a specified lifetime of 1.7 ns (110 00 006, PolyAn GmbH) and 2.7 ns (110 10 006, PolyAn GmbH) were used. Also the concentration and preparation was the same as with the other beads described above. For the sample with both beads a one to one ratio was chosen.

Lipid Nanoparticles

To prepare lipid nanoparticles, the four lipids DLin-MC3-DMA (AMBH93D5393F, Merck), DSPC (850365, Avanti Polar Lipids), Cholesterol (700100, Avanti Polar Lipids), and DSPE-PEG2000 (880128, Avanti Polar Lipids) were dissolved in ethanol (5054.3, Roth) with a molar ratio of 50:10:38.5:1.5. ARCA Cy3 EGFP mRNA (R1008, APExBIO), Fluorescein (46955, Sigma Aldrich) and buffer (100 mM Citrate buffer, pH3) were prepared in water and combined with the lipid-containing organic phase using the microfluidic mixing device NanoAssemblrTM SparkTM (Cytivia, Precision NanoSystems). Mixing was conducted with a 2:1 aqueous to organic phase to reach an N/P ratio of 3 with 0.05 mg/mL mRNA concentration. After mixing, LNPs were incubated at room temperature for 15 min to allow self-assembly and subsequently dialyzed (Slide-A-Lyzer™ MINI dialysis cups 3.5 kDa molecular weight cut-off, 69550, ThermoFisher) against water to remove residual ethanol, Fluorescein and buffer.

Cell Culture and Cell-Patterning

Cell Culture

The human liver carcinoma cell line HuH7 was cultured in GibcoTM RPMI (Rosswell Park Memorial Institute) medium (61870010, ThermoFisher) supplemented with 10% (v/v) FBS (fetal bovine serum, ThermoFisher 10270106), 1 mM Na-Pyruvate (GibocTM, ThermoFisher, 11360070), and 5 mM HEPES (GibocTM, ThermoFisher, 15630080) at 37 °C, 5% CO_2. Cell cleavage was performed using Acutase (00-4555-56, Invitrogen) at 70-90% confluence. For single-cell experiments, cells were seeded in growth medium at a cell density of $5 \cdot 10^5$ cells/mL on the single-cell microarrays.

Cell-Patterning

PVA coated 6-channel ibidi µ-slides (80600, ibidi) were filled with 100 mM PLPP (Enamine), 2% (w/v) agarose (HP45.1, Roth) and calcium peroxide in ultra-pure water (1305-79-9, ThermoFisher). Using a silica photomask with 20x20 µm squares and a 85 µm spacing, channels were selectively exposed to UV light (365 nm) and PLPP mix was washed out by flushing with 50 mL water per channel, followed by 0.5 M HCl to remove residual agarose. After another washing step with water, the slide was dried and sterilized under UV light. Squares were coated with 20 µg mL^{-1} Laminin (524 LN, BioLamina).

References

1. Jonkman, J. E. et al. An introduction to the wound healing assay using live-cell microscopy. Cell adhesion & migration **8**, 440–451, DOI: https://doi.org/10.4161/cam.36224 (2014).
2. Deguchi, T. et al. Direct observation of motor protein stepping in living cells using minflux. Science **379**, 1010–1015, DOI: https://10.1126/science.ade2676 (2023).
3. Nguyen, T. D., Chen, Y.-I., Chen, L. H. & Yeh, H.-C. Recent advances in single-molecule tracking and imaging techniques. Annu. Rev. Anal. Chem. **16**, 253–284, DOI: https://doi.org/10.1146/annurev-anchem-091922-073057 (2023).
4. Hou, S., Johnson, C. & Welsher, K. Real-time 3d single particle tracking: towards active feedback single molecule spectroscopy in live cells. Molecules **24**, 2826, DOI: https://doi:10.3390/molecules24152826 (2019).
5. Zhou, Y., Handley, M., Carles, G. & Harvey, A. R. Advances in 3d single particle localization microscopy. APL Photonics **4**, DOI: https://doi.org/10.1063/1.5093310 (2019).
6. Gwosch, K. C. et al. Minflux nanoscopy delivers 3d multicolor nanometer resolution in cells. Nat. methods **17**, 217–224, DOI: https://doi.org/10.1038/s41592-019-0688-0 (2020).
7. Li, J., Tong, G., Pan, Y. & Yu, Y. Spatial and temporal super-resolution for fluorescence microscopy by a recurrent neural network. Opt. Express **29**, 15747–15763, DOI: https://doi.org/10.1364/OE.423892 (2021).

8. Hell, S. W. & Wichmann, J. Breaking the diffraction resolution limit by stimulated emission: stimulated-emission-depletion fluorescence microscopy. Opt. letters **19**, 780–782, DOI: https://doi.org/10.1364/OL.19.000780 (1994).

9. Betzig, E. et al. Imaging intracellular fluorescent proteins at nanometer resolution. science **313**, 1642–1645, DOI: https://10.1126/science.1127344 (2006).

10. Rust, M. J., Bates, M. & Zhuang, X. Sub-diffraction-limit imaging by stochastic optical reconstruction microscopy (storm). Nat. methods **3**, 793–796, DOI: https://10.1126/science.1127344 (2006).

11. Reiser, A., Woschée, D., Kempe, S. M. & Rädler, J. O. Live-cell imaging of single-cell arrays (lisca)-a versatile technique to quantify cellular kinetics. JoVE (Journal Vis. Exp. e62025, DOI: https://doi.org/10.3791/62025 (2021).

12. Goulian, M. & Simon, S. M. Tracking single proteins within cells. Biophys. journal **79**, 2188–2198, DOI: https://doi.org/10.1016/S0006-3495(00)76467-8 (2000).

13. Kamanzi, A. et al. Simultaneous, single-particle measurements of size and loading give insights into the structure of drug-delivery nanoparticles. ACS nano **15**, 19244–19255, DOI: https://doi.org/10.1021/acsnano.1c04862 (2021).

14. Kamanzi, A. et al. Quantitative visualization of lipid nanoparticle fusion as a function of formulation and process parameters. ACS nano **18**, 18191–18201, DOI: https://doi.org/10.1021/acsnano.3c12981 (2024).

15. Mieskes, F., Ploetz, E., Wehnekamp, F., Rat, V. & Lamb, D. C. Multicolor 3d orbital tracking. Small **19**, 2204726, DOI: https://doi.org/10.1002/smll.202204726 (2023).

16. Germann, J. A. & Davis, L. M. Three-dimensional tracking of a single fluorescent nanoparticle using four-focus excitation in a confocal microscope. Opt. express **22**, 5641–5650, DOI: https://doi.org/10.1364/OE.22.005641 (2014).

17. Liu, Y.-L. et al. Segmentation of 3d trajectories acquired by tsunami microscope: an application to egfr trafficking. Biophys. journal **111**, 2214–2227, DOI: https://doi.org/10.1016/j.bpj.2016.09.041 (2016).

18. Thompson, M. A., Casolari, J. M., Badieirostami, M., Brown, P. O. & Moerner, W. Three-dimensional tracking of single mrna particles in saccharomyces cerevisiae using a double-helix point spread function. Proc. Natl. Acad. Sci. **107**, 17864–17871, DOI: https://doi.org/10.1073/pnas.1012868107 (2010).

19. Hou, S., Lang, X. & Welsher, K. Robust real-time 3d single-particle tracking using a dynamically moving laser spot. Opt. Lett. **42**, 2390–2393, DOI: https://doi.org/10.1364/OL.42.002390 (2017).

20. Hou, S., Exell, J. & Welsher, K. Real-time 3d single molecule tracking. Nat. communications **11**, 3607, DOI: https://doi.org/10.1038/s41467-020-17444-6 (2020).

21. Wells, N. P. et al. Time-resolved three-dimensional molecular tracking in live cells. Nano letters **10**, 4732–4737, DOI: https://doi.org/10.1021/nl103247v (2010).

22. Perillo, E. P. et al. Deep and high-resolution three-dimensional tracking of single particles using nonlinear and multiplexed illumination. Nat. Commun. **6**, 7874, DOI: https://doi.org/10.1038/ncomms8874 (2015).

23. Bucci, A. et al. 4d single-particle tracking with asynchronous read-out single-photon avalanche diode array detector. Nat. Commun. **15**, 6188, DOI: https://doi.org/10.1038/s41467-024-50512-9 (2024).

24. Toprak, E., Balci, H., Blehm, B. H. & Selvin, P. R. Three-dimensional particle tracking via bifocal imaging. Nano letters **7**, 2043–2045, DOI: https://doi.org/10.1021/nl0709120 (2007).

25. Cierpka, C., Rossi, M., Segura, R. & Kähler, C. On the calibration of astigmatism particle tracking velocimetry for microflows. Meas. Sci. Technol. **22**, 015401 (2010).

26. Cullis, P. R. & Hope, M. J. Lipid nanoparticle systems for enabling gene therapies. Mol. Ther. **25**, 1467–1475, DOI: https://doi.org/10.1016/j.ymthe.2017.03.013 (2017).

27. Hou, X., Zaks, T., Langer, R. & Dong, Y. Lipid nanoparticles for mrna delivery. Nat. Rev. Mater. **6**, 1078–1094, DOI: https://doi.org/10.1038/s41578-021-00358-0 (2021).

28. Müller, J. A. et al. Kinetics of rna-lnp delivery and protein expression. Eur. J. Pharm. Biopharm. 114222, DOI: https://doi.org/10.1016/j.ejpb.2024.114222 (2024).

29. Maugeri, M. et al. Linkage between endosomal escape of lnp-mrna and loading into evs for transport to other cells. Nat. communications **10**, 4333, DOI: https://doi.org/10.1038/s41467-019-12275-6 (2019).

30. Wittrup, A. et al. Visualizing lipid-formulated sirna release from endosomes and target gene knockdown. Nat. biotechnology **33**, 870–876, DOI: https://doi.org/10.1038/nbt.3298 (2015).

31. Patel, S. et al. Boosting intracellular delivery of lipid nanoparticle-encapsulated mrna. Nano letters **17**, 5711–5718, DOI: https://doi.org/10.1021/acs.nanolett.7b02664 (2017).

32. Gilleron, J. et al. Image-based analysis of lipid nanoparticle–mediated sirna delivery, intracellular trafficking and endosomal escape. Nat. biotechnology **31**, 638–646, DOI: https://doi.org/10.1038/nbt.2612 (2013).

33. Katayama, Y. et al. Real-time nanomicroscopy via three-dimensional single-particle tracking. ChemPhysChem **10**, 2458–2464, DOI: https://doi.org/10.1002/cphc.200900436 (2009).

34. Kim, J. et al. Engineering lipid nanoparticles for enhanced intracellular delivery of mrna through inhalation. ACS nano **16**, 14792–14806, DOI: https://doi.org/10.1021/acsnano.2c05647 (2022).

35. Kellerer, T. et al. An image based real-time 3d particle tracking fluorescence lifetime imaging microscope to follow lipid nanoparticles. In Microscopy Histopathology and Analytics, MM5A–6, DOI: https://doi.org/10.1364/MICROSCOPY.2024.MM5A.6 (Optica Publishing Group, 2024).

36. Kellerer, T. et al. Rigorous investigation and comparison of different fluorescence lifetime imaging microscopy (flim) techniques analyzed using the phasor plot. In Multiphoton Microscopy in the Biomedical Sciences XXIV, vol. 12847, 177–187, DOI: https://doi.org/10.1117/12.3002648 (SPIE, 2024).

37. Zhang, T. et al. Toward quantitative bio-sensing with nitrogen–vacancy center in diamond. ACS sensors **6**, 2077–2107, DOI: https://doi.org/10.1021/acssensors.1c00415 (2021).

38. Janiak, F. et al. Divergent excitation two photon microscopy for 3d random access mesoscale imaging at single cell resolution. BioRxiv 821405, DOI: https://doi.org/10.1101/821405 (2019).

39. Valera, A. M., Neufeldt, F. C., Kirkby, P. A., Mitchell, J. E. & Silver, R. A. Precompensation of 3d field distortions in remote focus two-photon microscopy. Biomed. Opt. Express **12**, 3717–3728, DOI: https://doi.org/10.1364/BOE.425588 (2021).

40. Ries, J. & Schwille, P. Fluorescence correlation spectroscopy. BioEssays **34**, 361–368, DOI: https://doi.org/10.1002/bies.201100111 (2012).

41. Volk, A. & Kähler, C. J. Density model for aqueous glycerol solutions. Exp. Fluids **59**, 75, DOI: https://10.1007/s00348-018-2527-y (2018).

42. Murschhauser, A. et al. A high-throughput microscopy method for single-cell analysis of event-time correlations in nanoparticle-induced cell death. Commun. Biol. **2**, 35, DOI: https://doi.org/10.1038/s42003-019-0282-0 (2019).

43. Schindelin, J. et al. Fiji: an open-source platform for biological-image analysis. Nat. methods **9**, 676–682, DOI: doi.org/10.1038/nmeth.2019 (2012).

44. Nawrocki, G., Wang, P.-h., Yu, I., Sugita, Y. & Feig, M. Slow-down in diffusion in crowded protein solutions correlates with transient cluster formation. The J. Phys. Chem. B **121**, 11072–11084, DOI: https://doi.org/10.1021/acs.jpcb.7b08785 (2017).

45. Lin, Y., Mos, P., Ardelean, A., Bruschini, C. & Charbon, E. Coupling a recurrent neural network to spad tcspc systems for real-time fluorescence lifetime imaging. Sci. Reports **14**, 3286, DOI: https://doi.org/10.1038/s41598-024-52966-9 (2024).

46. Hampson, K. M. et al. Adaptive optics for high-resolution imaging. Nat. Rev. Methods Primers **1**, 68, DOI: https://doi.org/10.1038/s43586-021-00066-7 (2021).

47. Booth, M., Andrade, D., Burke, D., Patton, B. & Zurauskas, M. Aberrations and adaptive optics in super-resolution microscopy. Microscopy **64**, 251–261, DOI: https://doi.org/10.1093/jmicro/dfv033 (2015).

48. Granger, E., McNee, G., Allan, V. & Woodman, P. The role of the cytoskeleton and molecular motors in endosomal dynamics. In Seminars in cell & developmental biology, vol. 31, 20–29, DOI: https://doi.org/10.1016/j.semcdb.2014.04.011 (Elsevier, 2014).

49. Berezin, M. Y. & Achilefu, S. Fluorescence lifetime measurements and biological imaging. Chem. reviews **110**, 2641–2684, DOI: https://doi.org/10.1021/cr900343z (2010).

50. Kellerer, T. et al. Comprehensive investigation of parameters influencing fluorescence lifetime imaging microscopy in frequency-and time-domain illustrated by phasor plot analysis. Int. J. Mol. Sci. **23**, 15885, DOI: https://doi.org/10.3390/ijms232415885 (2022).

51. Mahou, P. et al. Multicolor two-photon tissue imaging by wavelength mixing. Nat. methods **9**, 815–818, DOI: https://doi.org/10.1038/nmeth.2098 (2012).

52. Tinevez, J.-Y. Hungarian based particle linking. https://www.mathworks.com/matlabcentral/fileexchange/33968-hungarian-based-particle-linking (2024). MATLAB Central File Exchange, retrieved October 4, 2024.

53. Mohler, W., Millard, A. C. & Campagnola, P. J. Second harmonic generation imaging of endogenous structural proteins. Methods **29**, 97–109, DOI: https://doi.org/10.1016/S1046-2023(02)00292-X (2003).

54. Müller, P., Schwille, P. & Weidemann, T. Pycorrfit—generic data evaluation for fluorescence correlation spectroscopy. Bioinformatics **30**, 2532–2533, DOI: https://doi.org/10.1093/bioinformatics/btu328 (2014).

Acknowledgements

This research was funded by the BMBF project "SEMPA-Track" (FKZ 13N16300) and the Bavarian Academic Forum (BayWISS)—Doctoral Consortium "Health Research". We thank Dr. Heidi Potts from Zurich Instruments for her great support in handling the lock-in amplifier. We also thank Bernhard Kichrmaier for the calibration measurements with FCS and Gerlinde Schwake for cell preparations and cell patterning samples. Last but not least we thank Cole Green for proofreading the manuscript.

Author contributions statement

T.K. conceived and conducted the experiments, analyzed the results and has written the manuscript. T.G and F.S. conducted experiments. J.A.M prepared the samples. J.O.R has supervised the project. T.H. has supervised the project and written the manuscript. All authors reviewed the manuscript.

Chapter 7

Conclusion

In this thesis, two innovative microscopy techniques were developed that can be employed individually or in combination. The first technique, **S**peed-**U**p **P**has**E** **R**esolved **F**luorescence **L**ifetime **I**maging **M**icroscopy is currently the fastest method for recording the fluorescence lifetime of molecules (see **Chapter 5**). Using a lock-in amplifier and a robust mathematical framework, lifetime values are extracted from the two demodulation parameters, G and S, within just 102 ns allowing for fluorescence intensity-, lifetime- and phasor streaming. Benchmarking measurements on fluorophore solutions demonstrated a smaller error margin than conventional methods (TD-FLIM, FD-FLIM and instant FLIM), validated by reference experiments using Rose Bengal dissolved in various solutions. Beyond spectroscopy, imaging capabilities were demonstrated, marking a milestone where a resonant galvo-scanner was used for lifetime extraction within a single frame. This approach was applied to investigate the stability of LNP at low pH values (~ 2.7). Further the pH-trace of endosomes in living cell were measured over a time period of one hour and revealed a significant acidification like proposed in the literature [31]. The pH sensing was done with carboxyfluorescein placed on the headgroup of the LNP lipid. Starting from the physiological pH value of ~ 7.4 down to ~ 4, we measured a linear pH drop associated with a lifetime change of 700 ps.

Unlike most microscopy techniques that rely on continuous-wave lasers, SUPER-FLIM was shown to be compatible with a variety of excitation sources, including intensity-modulated lasers (pulsed, sinusoidal, rectangular, etc.). This flexibility makes it an accessible technique for integration into any laser- or sample-scanning microscope, further facilitated by open-source software packages for image acquisition, including galvo-scanner control and lifetime/intensity image calculation. Additionally, SUPER-FLIM was successfully combined with fluorescence correlation spectroscopy, where the incorporation of lifetime information overcame the diffusion time limit of 1.6 for sample separation upon the auto correlation curves [179]. By leveraging lifetime-dependent intensity filtering, the technique was capable of distinguishing particles with nearly identical diameters and diffusion times showing the advantages of **m**ulti-**l**ifetime-**FCS**.

The second technique, **S**pectrally **E**ncoded **M**ultiphoton **PA**rticle-**Track**ing, is a novel real-time, image-based, 4D single-particle microscopy system (see **Chapter 6**). Through point spread function engineering, a two-photon excitation fluorescence microscope was adapted to track single particles in all three dimensions while simultaneously imaging their surroundings and recording fluorescence lifetimes. This technique extended the observation time of 170 nm fluorescent particles by a factor of 13 at a diffusion constant D=2.58 $\mu m^2\,s^{-1}$. Using SEMPA-Track in live-cell imaging, we visualized distinct LNP and endosome pathways, such as free LNP diffusion in the cell medium, slower endosome movement inside cells, and LNPs bound to the cell surface. Simultaneously, the technique provided contextual imaging of cellular structures, including the cell nucleus. Analyzing trajectories with this additional information revealed distinct movement phases, including random diffusion and directed motion towards the cell nucleus. These findings align with literature reports on endosomal transport mechanisms, suggesting further potential for extracting parameters such as velocity to differentiate motion types in future studies.

The integration of SUPER-FLIM with SEMPA-Track significantly enhances its capabilities. As a proof of principle, the system tracked a freely diffusing particle while simultaneously measuring fluorescence lifetimes across the entire image field. This novel feature allows the identification of particle types based on lifetime differences and represents a major advancement in single-particle tracking. Although SPT methods were already combined with FLIM the time-resolved analysis was limited to the trajectory only.

In addition to these new microscopy techniques, this dissertation contributes a comprehensive dataset of fluorescence lifetime measurements for a wide range of fluorophores in diverse environments [20, 213]. This database allows researchers to select fluorophores based on specific criteria, such as significant lifetime changes with pH (e.g. Fluorescein). By cross-referencing this dataset, potential confounding factors, such as temperature-induced lifetime variations, can be ruled out. In particularly, Fluorescein's lifetime was shown to remain unaffected by temperature fluctuations, ensuring reliable pH-sensing in future experiments.

Overall, the advancements presented in this thesis not only pushes the microscopy limits further but also lay the groundwork for further applications in biological systems and statistical studies, paving the way for future explorations in Biophotonics and nanoparticle research.

Chapter 8

Outlook

Time-resolved data has proven to be one of the most promising tools for advancing LNP research. Many of the changes that LNPs undergo alter their photophysical properties, which can be effectively monitored using fluorescence lifetime measurements. By investing in more advanced fluorophores, the amount of information gained from experiments can be increased or even expanded. For example, Förster pairs could be employed to measure environmental properties via the FRET mechanism.

Another important area is fluorescence anisotropy, which is particularly suited for detecting conformational changes during LNP fusion with endosomes—a process indicated by our results as the most likely mechanism. To enable anisotropy measurements, existing microscopy setups can be easily adapted by integrating polarization optics into both the excitation and emission paths.

Looking ahead, several improvements to the developed techniques can be considered. One area of focus is enhancing the tracking algorithms. In the current setup, many tasks are performed using MATLAB scripts, but future implementations could leverage real-time processing on a lock-in amplifier or field programmable gate array offering faster and more reliable feedback. Additionally, the potential of using the laser overlap region for expanded functionality should be explored further. Synchronizing the pulses of both lasers for sum frequency generation could allow the activation of another fluorophore, increasing the informational depth of experiments. Initial attempts to use the laser overlap for improved resolution yielded to results which warrant improvement and will require further optimization in the future but are theoretical not possible [214].

The SUPER-FLIM technique was extensively characterized and described through numerous measurements. However, its combination with FCS was only briefly explored and warrants more detailed investigations. In particular, the use of phasor plots could simplify the segmentation process in such combined analyses. Moreover, applying SUPER-FLIM to FRET samples could reveal new advantages, offering further insights into environmental dynamics and interactions at the molecular level.

To address key questions in LNP studies, our proof of principle measurements need to be further expanded. While our findings have already revealed many intriguing insights, a statistical analysis of a larger number of LNP trajectories, pH traces combined would be highly beneficial for advancing research in the field of novel drug delivery systems.

Appendix A

SUPER-FLIM

A.1 Supplementary Information to SUPER-FLIM

In this chapter the supplementary information to the publication *SUPER-FLIM* is presented.

Supplementary Information to "Speed-Up Phase Resolved Fluorescence Lifetime Imaging (SUPER-FLIM) for Real-Time Microenvironmental Sensing"

Thomas Kellerer[1,2], Lukas Moser[1], Judith A. Müller[2], Joachim O. Rädler[2], and Thomas Hellerer[1,*]

[1]Multiphoton Imaging Lab, Munich University of Applied Sciences, 80335 Munich, Germany
[2]Faculty of Physics and Center for NanoScience, Ludwig Maximilians-University, 80539 Munich, Germany
[*]Hellerer@hm.edu

ABSTRACT

Imaging cell biological processes while simultaneously sensing the microenvironment at high spatial and temporal resolution is a key goal in modern live-cell microscopy. However, adding parameters such as fluorescence lifetime compromises acquisition speed. To address this challenge, we introduce **S**peed-**U**p **P**has**E** **R**esolved **F**luorescence **L**ifetime **I**maging **M**icroscopy (SUPER-FLIM), an ultra-fast fluorescence lifetime imaging method that enables 3D live-imaging at unprecedented speed. Our approach combines digital lock-in detection with laser scanning excitation, allowing the simultaneous capture of fluorescence intensity, lifetime, and phasor data in real-time. With an acquisition time of $100\,\mathrm{ns}$, SUPER-FLIM is ten times faster than state of the art FLIM techniques and is, for the first time, integrated with resonant galvo-scanners. SUPER-FLIM is a major step forward in live imaging as it provides high spatial resolution in 3D that cannot be achieved with camera-based frequency domain FLIM. As a proof of concept, we demonstrate its utility in observing lipid-nanoparticle acidification within living cells. Beyond imaging, SUPER-FLIM's rapid lifetime acquisition unlocks new applications, including multi-lifetime fluorescence correlation spectroscopy (ml-FCS), a novel FCS mode that sorts and correlates fluorescence bursts from diffusing particles based on lifetime characteristics. The technique is compatible with virtually any modulated light source and can be easily integrated into any laser scanning microscope using our open-source software.

Keywords: Fluorescence Lifetime Imaging Microscopy, Fluorescence Correlation Spectroscopy, Two-Photon Excitation, Resonant Galvo Scanner, Lipid Nanoparticles, Endosomes

List Of Supplementary Files

In this supplementary file we will include following topics:

S1 Lock-in Amplifier Signal

A lock-in amplifier is an effective tool for detecting noisy or weak signals. It requires two inputs (**Figure 1**). The first is the reference signal, which is associated with the signal being measured or synchronized with it. The second input is the signal itself.

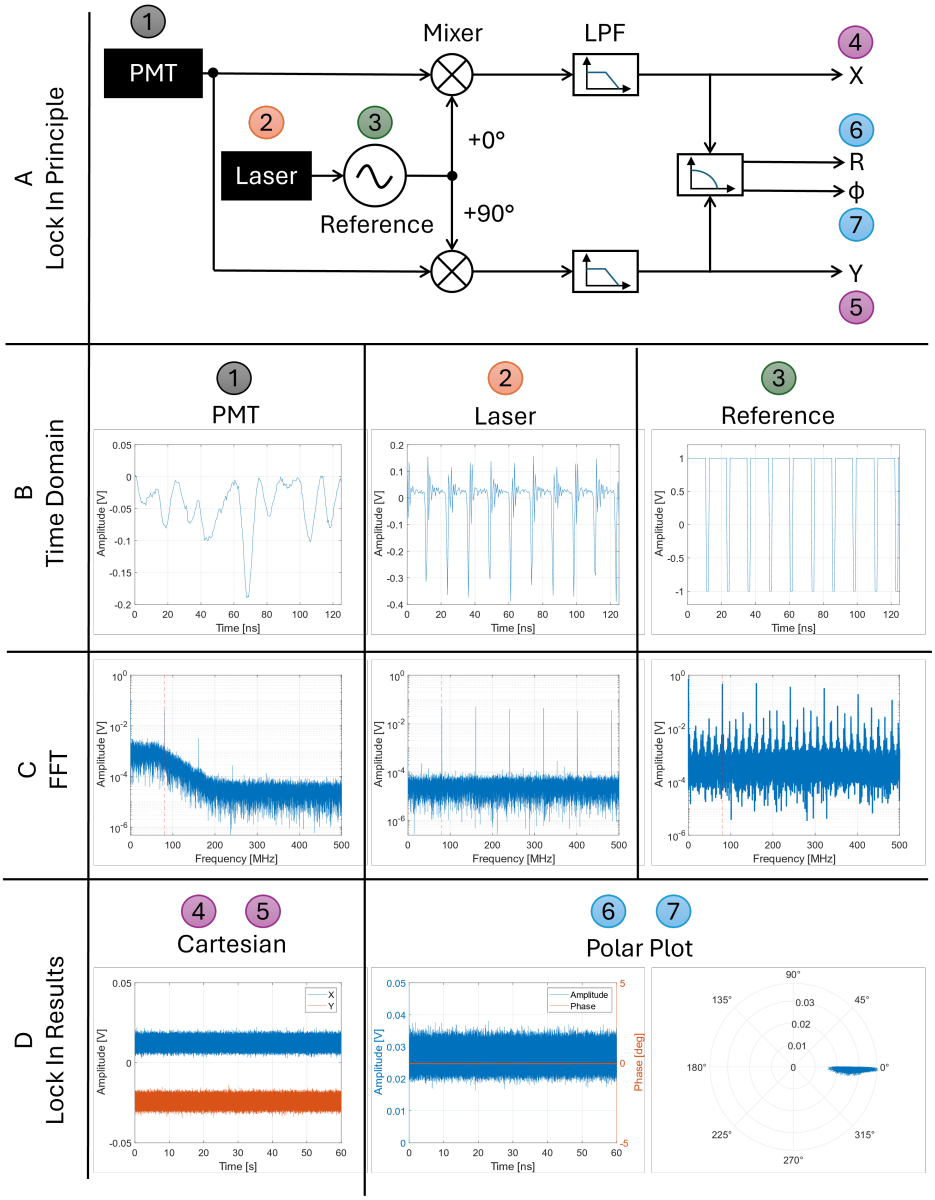

Figure 1. Principle of a lock-in Amplifier: In row **A**, the schematic setup of a lock-in amplifier signal chain is shown. The PMT signal (**1**) is multiplied with the laser reference (**2**), resulting in two output signals after filtering. These outputs are displayed in cartesian coordinates (**4** and **5**) and polar coordinates (**6** and **7**). In row **B**, the signals are shown in the time domain. Row **C** presents the FFT signals, and in row **D**, the results from the lock-in amplifier are displayed.

To describe the lock-in process for our technique mathematically we simplify the detected signal and reference as pure sine wave with an amplitude V, at a fixed frequency ω. The unknown initial phase of the signal is described as φ and for the reference as θ like in **Equation 1** and **2**.

$$V_S(t) = \hat{V}_S \cdot \sin(\omega_S t + \varphi) \tag{1}$$

$$V_R(t) = \hat{V}_R \cdot \sin(\omega_R t + \theta) \tag{2}$$

In the lock-in amplifier, the incoming weak and noisy signal V_S is mixed with the reference signal V_R, which is equivalent to a multiplication process. This multiplication results in a frequency spectrum comprising both the sum and difference of the frequencies of the reference and measurement signals. To facilitate the mathematical computation of this mixed signal, the exponential representation of a sine function, $\sin(x) = \frac{1}{2i}(e^{ix} - e^{-ix})$, can be utilized, allowing the two **Equations 1** and **2** to be formulated in complex notation.

$$V_S(t) = \hat{V_S} \cdot \frac{1}{2i}\left(e^{i(\omega_S t+\varphi)} - e^{-i(\omega_S t+\varphi)}\right) \tag{3}$$

$$V_R(t) = \hat{V_R} \cdot \frac{1}{2i}\left(e^{i(\omega_R t+\theta)} - e^{-i(\omega_R t+\theta)}\right) \tag{4}$$

By evaluating the multiplication of **Equation 3** with **Equation 4** we access the mixed signal V_{Mix_1}:

$$\begin{aligned} V_{Mix_1}(t) &= V_S(t) \cdot V_R(t) \\ &= \frac{\hat{V_S}\hat{V_R}}{-4}\left\{\left[e^{i(\omega_S t+\varphi+\omega_R t+\theta)} + e^{-i(\omega_S t+\varphi+\omega_R t+\theta)}\right] - \left[e^{i(\omega_S t+\varphi-\omega_R t-\theta)} + e^{-i(\omega_S t+\varphi-\omega_R t-\theta)}\right]\right\} \end{aligned} \tag{5}$$

Applying the Euler equation for the cosine, $\cos(x) = \frac{1}{2}(e^{ix} + e^{-ix})$ **Equation 5** is converted to a real signal shown in **Equation 6**:

$$V_{Mix_1}(t) = \frac{\hat{V_S}\hat{V_R}}{2}\{\cos[(\omega_S - \omega_R)t + \varphi - \theta] - \cos[(\omega_S + \omega_R)t + \varphi + \theta]\} \tag{6}$$

This expression can be further simplified if we assume that the frequency of the reference signal closely matches the frequency of the signal ($\omega_S \approx \omega_R = \omega$). By comparing the fast fourier transformed signal (FFT) of the input with the reference in **Figure 1** we see that this is the case for the fluorescence process created by periodic excitation (pulsed or intensity modulated) resulting in **Equation 7**.

$$V_{Mix_1}(t) = \frac{\hat{V_S}\hat{V_R}}{2} \cdot [\underbrace{\cos(\varphi - \theta)}_{\text{DC}} - \underbrace{\cos(2\omega t + \varphi + \theta)}_{\text{AC}}] \tag{7}$$

This mixed signal comprises a direct current (DC) component and a harmonic component at the frequency 2ω. Subsequently, the signal is fed into a low-pass filter configured with a cutoff frequency ω_c that is set to effectively eliminate the harmonic elements, resulting in the pure DC component, as expressed in **Equation 8**.

$$V_{Mix_1} = \frac{\hat{V_S}\hat{V_R}}{2} \cdot \cos(\varphi - \theta) \tag{8}$$

A low-pass filter allows frequencies below a certain cutoff frequency ω_c to pass while attenuating higher frequencies. The time constant (TC) of the filter is directly related to this cutoff frequency and defines the filter's response speed. For a first-order RC (resistor-capacitor) low-pass filter, the time constant is given by:

$$TC = \frac{1}{\omega_c} = R \cdot C \tag{9}$$

where R is the resistance and C is the capacitance in the filter circuit.

The cutoff frequency ω_c is the frequency at which the output power drops to half of the input power (or equivalently, the output amplitude drops by $\frac{1}{\sqrt{2}}$). By setting ω_c to be below 2ω, the filter suppresses the harmonic component effectively, allowing only the DC component of the signal to pass through.

The DC component contains the amplitudes of both the measured signal and the known reference signal, as well as a cosine term. The amplitude of the output signal can only be calculated from the measured signal level if the difference $\varphi - \theta$ is constant and known. However, this is not always the case in practice. The digital lock-in amplifier overcomes this issue by duplicating the reference signal without any loss and introducing a phase shift of $90° = \frac{\pi}{2}$.

The duplicated reference signal is then also mixed with the input signal. Knowing that $\cos(x-\frac{\pi}{2}) = \sin(x)$, and defining $x := [\omega_S - \omega_R]t + \varphi - \theta$, when substituted into Equation 7, results in the mixed signal V_{Mix_2} corresponding to Expression 10.

$$V_{Mix_2}(t) = \frac{\hat{V}_S \hat{V}_R}{2} \cdot [\underbrace{\sin(\varphi - \theta)}_{\text{DC}} - \underbrace{\sin(2\omega t + \varphi + \theta)}_{\text{AC}}] \tag{10}$$

Once again, high-frequency signal components are filtered out using a low-pass filter, resulting in a second DC component remaining, as laid out in Equation 11.

$$V_{Mix_2} = \frac{\hat{V}_S \hat{V}_R}{2} \cdot \sin(\varphi - \theta) \tag{11}$$

With those two DC voltages, the amplitude of the signal to be measured can ultimately be determined, independent of the phase difference $\varphi - \theta := \Delta\varphi$. This is achieved by squaring and then summing both signals as shown in Equation 12.

$$V_{Mix_1}^2 + V_{Mix_2}^2 = \left(\frac{\hat{V}_S \hat{V}_R}{2}\right)^2 \left[\sin(\Delta\varphi)^2 + \cos(\Delta\varphi)^2\right] = \left(\frac{\hat{V}_S \hat{V}_R}{2}\right)^2$$

$$\Rightarrow \hat{V}_S = \sqrt{V_{Mix_1}^2 + V_{Mix_2}^2} \cdot \frac{2}{\hat{V}_R} \tag{12}$$

The phase information is of significant importance for certain applications. By dividing the two obtained signals, this information can be extracted independently of the amplitudes of both signals, as delineated in Equation 13.

$$\frac{V_{Mix_2}}{V_{Mix_1}} = \frac{\frac{\hat{V}_S \hat{V}_R}{2} \sin(\Delta\varphi)}{\frac{\hat{V}_S \hat{V}_R}{2} \cos(\Delta\varphi)}$$

$$\Rightarrow \Delta\varphi = \arctan\left(\frac{V_{Mix_2}}{V_{Mix_1}}\right) \tag{13}$$

S2 Intensity Dependency

During measurements with a calibrated setup (**Figure 2**), significant phase fluctuations may be observed in response to changes in intensity. Such fluctuations could arise from nonlinear effects within the photomultiplier tube (PMT), leading to distorted signal outputs. Furthermore, as the PMT signal is not a perfect sinusoidal wave—which is the ideal signal type for lock-in amplification—the direct conversion of phase information to lifetime data is not straightforward. To circumvent this issue, one can compute a type of reference function that removes the intensity information, thereby producing a consistent phase. The mathematical derivation and subsequent application are demonstrated in the following:

To calculate the average intensity of the resulting mixed signal, an integration over one oscillation period $T = \frac{1}{f_{rep}}$ of the reference signal is performed, as shown in Equation 14.

$$V = \int_0^T \hat{a} e^{-\frac{t}{\tau}} \cdot \cos(\omega t + \theta)\, dt \tag{14}$$

To solve this integral double partial integration is required and leads to **Equation 15**.

$$\frac{V}{\hat{a}} = \int_0^T e^{-\frac{t}{\tau}} \cdot \cos(\omega t + \theta)\, dt = \Big| -\tau e^{-\frac{t}{\tau}} \cos(\omega t + \theta) \Big|_0^T - \int_0^T \tau e^{-\frac{t}{\tau}} \omega \sin(\omega t + \theta)\, dt \tag{15}$$

The right-hand side integral is resolved through another application of partial integration leading to **Equation 16**.

$$\frac{V}{\hat{a}} = \Big| -\tau e^{-\frac{t}{\tau}} \cos(\omega t + \theta) \Big|_0^T - \left\{ \Big| -\tau^2 e^{-\frac{t}{\tau}} \omega \sin(\omega t + \theta) \Big|_0^T - \int_0^T -\tau^2 e^{-\frac{t}{\tau}} \omega^2 \cos(\omega t + \theta)\, dt \right\} \tag{16}$$

The remaining integral on the right-hand side corresponds to the average intensity V multiplied by the factor $-\omega^2\tau^2$ (**Equation 17**):

$$\frac{V}{\hat{a}} = \Big| -\tau e^{-\frac{t}{\tau}} \cdot \cos(\omega t + \theta) \Big|_0^T - \left\{ \Big| -\omega\tau^2 e^{-\frac{t}{\tau}} \cdot \sin(\omega t + \theta) \Big|_0^T + \omega^2\tau^2 \cdot \frac{V}{\hat{a}} \right\} \tag{17}$$

Equation 18 provides the means to calculate the average intensity of the mixed signal:

$$V = \Big| \frac{\hat{a}\tau e^{-\frac{t}{\tau}} \cdot (\omega\tau \cdot \sin(\omega t + \theta) - \cos(\omega t + \theta))}{\omega^2\tau^2 + 1} \Big|_0^T \tag{18}$$

Applying the integral limits on **Equation 18** yields **Equation 19**:

$$V = \frac{\hat{a}\tau \cdot \left(e^{-\frac{T}{\tau}} \omega\tau \cdot \sin(\omega T + \theta) - e^{-\frac{T}{\tau}} \cos(\omega T + \theta) - \sin(\theta)\omega\tau + \cos(\theta) \right)}{\omega^2\tau^2 + 1} \tag{19}$$

Given that ωT equates to 2π since $\omega = \frac{2\pi}{T}$, it follows due to the periodicity of trigonometric functions that:

$$\sin(2\pi + \alpha) = \sin(\alpha)$$
$$\cos(2\pi + \beta) = \cos(\beta)$$

With this understanding, the integral for calculating V is fully solved, culminating in the final form as shown in **Equation 20**:

$$V = \frac{\hat{a}\tau}{\omega^2\tau^2 + 1} \cdot \left(e^{-\frac{T}{\tau}} \omega\tau \cdot \sin(\theta) - e^{-\frac{T}{\tau}} \cos(\theta) - \omega\tau \cdot \sin(\theta) + \cos(\theta) \right) \tag{20}$$

S3 Phase Calibration

To obtain accurate fluorescence lifetimes, it is necessary to establish the correct initial phase. To accomplish this calibration, three distinct methods, which are presented here, can be employed. The first method utilizes the immediate radiation from a second harmonic generation (SHG) signal[1]. An alternative approach involves using a calibration dye with a known lifetime, or positioning a mirror at the sample location. However, since the mirror method has already been described in[2], our discussion will focus on the first two techniques (**Figure** 2).

S3.A Nonlinear Signals

During the calibration step, we exploit the fact that the production of second harmonic generation radiation is based on a scattering process, rather than an absorption process as seen with fluorescence[1]. Consequently, the SHG signal has an effective lifetime of 0 ns, making it an ideal calibration standard[?]. When measuring the phase shift $\phi_{Measured}$ using an SHG sample (ϕ_{SHG}), the lock-in amplifier detects a phase shift that accurately reflects the optical ($\phi_{OpticalPath}$) and electronic path ($\phi_{ElectricalPath}$) lengths (**Figure** 2 - a, b). This is evidenced by Equation 21, which demonstrates this relationship:

$$\phi_{Measured} = \phi_{OpticalPath} + \phi_{ElectricalPath} + \underbrace{\phi_{SHG}}_{=0^\circ} \tag{21}$$

Once this phase shift is established as the initial phase in the lock-in amplifier, accurate lifetime measurements can be continuously obtained. This accuracy is maintained as long as there are no changes to the PMT gain, the optical setup, or the cables being used.

S3.B Fluoroscent Standard

Another method for calibration relies on a sample with a known fluorescence lifetime. One can use commercially available standards or samples that have been prepared in-house[3,4]. The procedure is as follows: The fluorescence from the sample is detected by the PMT, and the lock-in amplifier produces a demodulation as well as a phase shift. This phase shift now includes both the delay introduced by the optical and electronic setup and the phase shift attributable to the sample's fluorescence lifetime (**Figure** 2 - c, d). Thus, the resulting phase is determined as follows:

$$\phi_{\text{Measured}} = \phi_{\text{Optical Path}} + \phi_{\text{Electrical Path}} + \underbrace{\phi_{\text{Sample}}}_{\phi=\arctan(\omega\cdot\tau)} \tag{22}$$

By subtracting the known phase of the sample, denoted as ϕ_{Sample}, from the measured phase, we are able to isolate the phase shift induced by the setup.

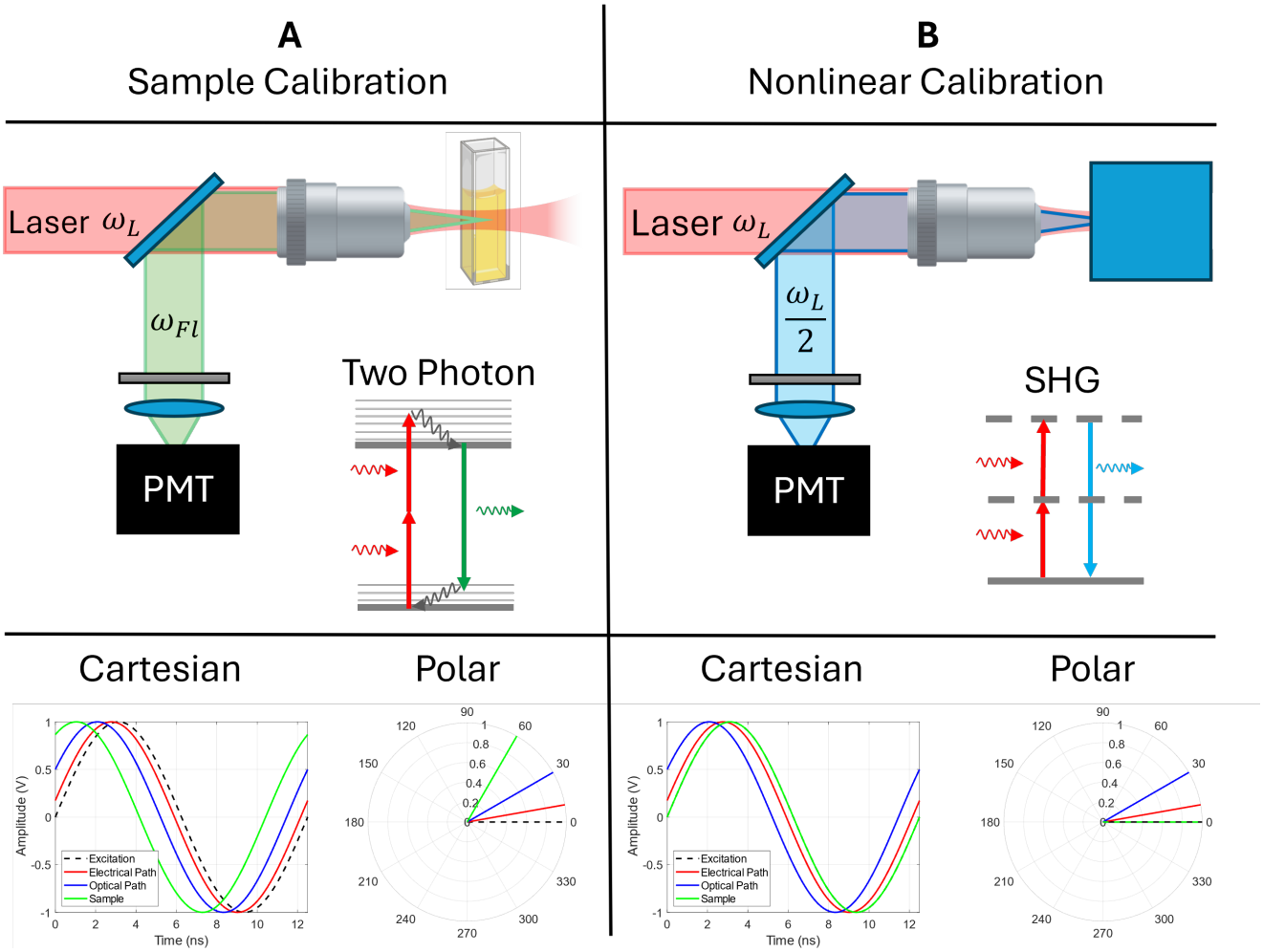

Figure 2. Calibration and Intensity Reference for SUPER-FLIM: Two calibration methods are demonstrated for this technique. In **a**, calibration is shown using a sample with a known fluorescence lifetime. The phase data of the electrical system, optical system, and sample are displayed in both Cartesian and polar coordinates in **b**. For nonlinear signals, such as SHG, the calibration process is shown in **c**, with corresponding Cartesian and polar representations in **d**.

S4 Setup Dependent Parameters

While the parameters set in the lock-in amplifier as well as the scanning mode influence the lifetime precision, we show the most important parameters. These are the TC-values and the image averaging.

S4.A Different TC-Values

In this chapter the results for a selection of flurophores at different TC-Values are represented. The smaller the TC-time is, the faster the fluorescence lifetime is extracted. For longer TC times the measurement duration is increased but also the error is decreasing. For each TC-value the measurement was carried out for 30 s and ten repetitions.

Rhodamine B

The first flurophore is Rhodamine B (**Figure - 3**) dissolved in dH_2O at a concentration of 1 mM.

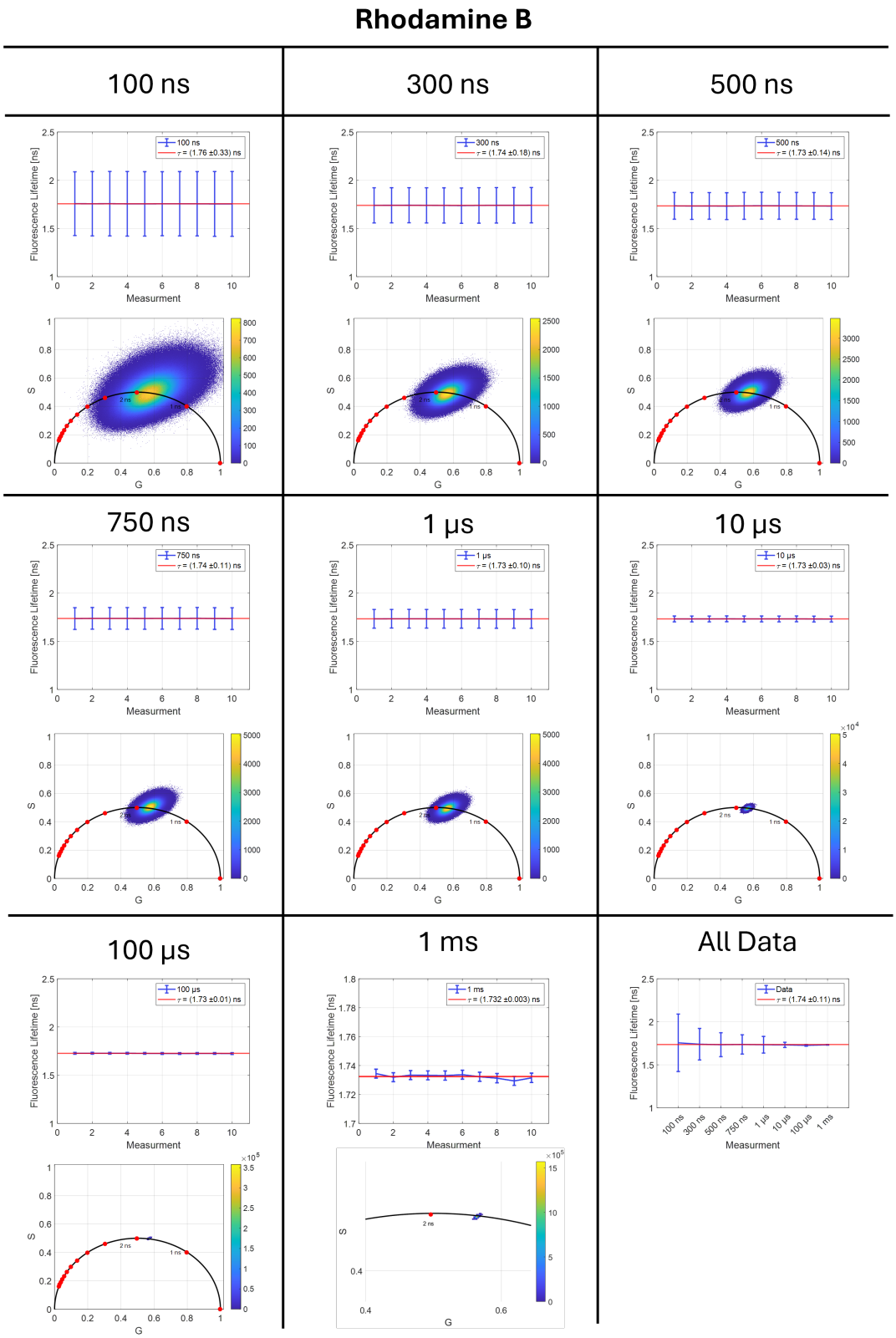

Figure 3. A 1 mM Rhodamine B solution in distilled water for eight different TC-values

Rose Bengal - Water

The second flurophore is Rose Bengal (**Figure - 4**) dissolved in dH_2O at a concentration of 1 mM.

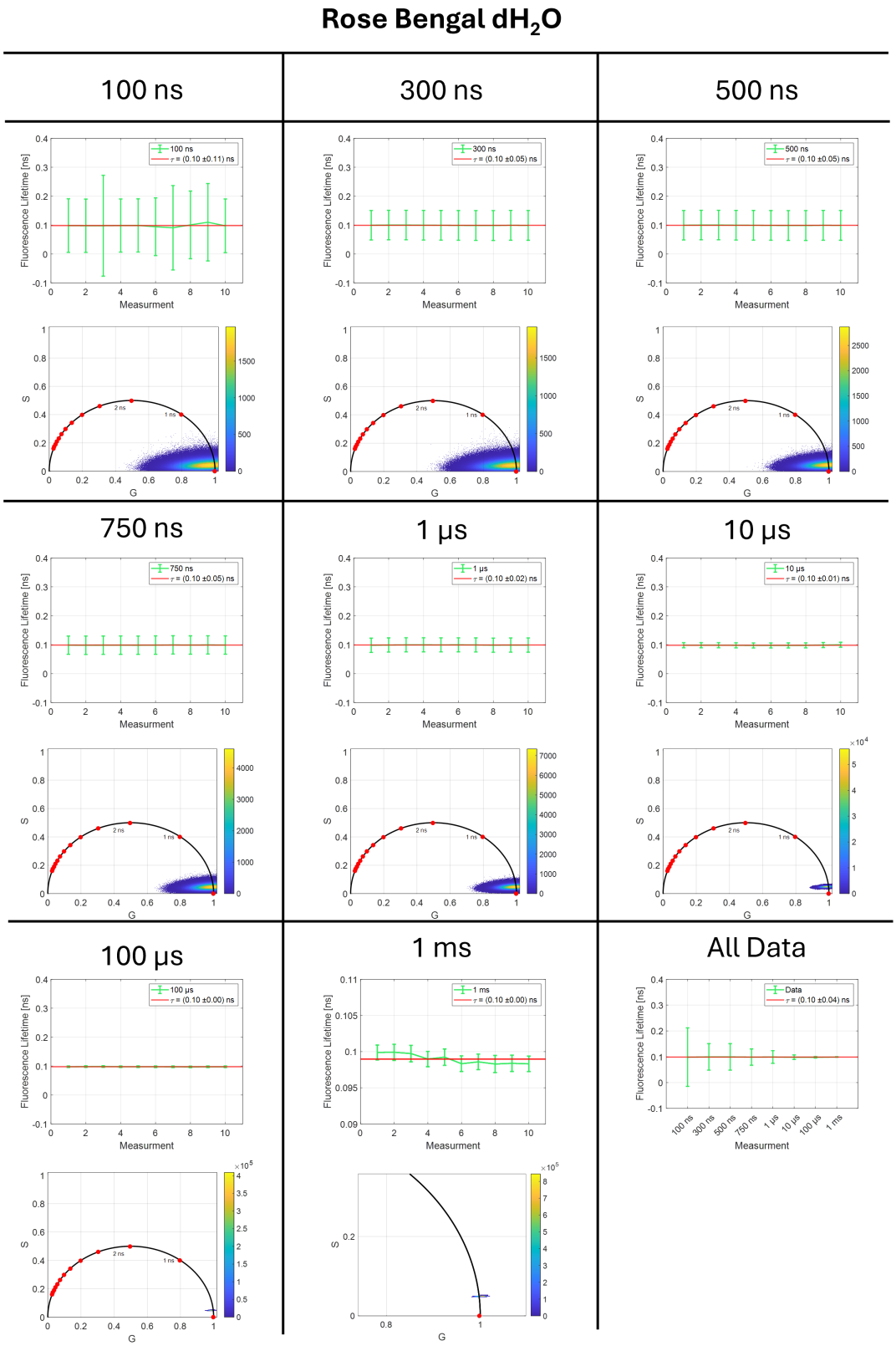

Figure 4. A 1 mM Rose Bengal solution in distilled water for eight different TC-values

Rose Bengal - Ethanol

The third flurophore is Rose Bengal (**Figure - 5**) dissolved in ethanol at a concentration of 1 mM.

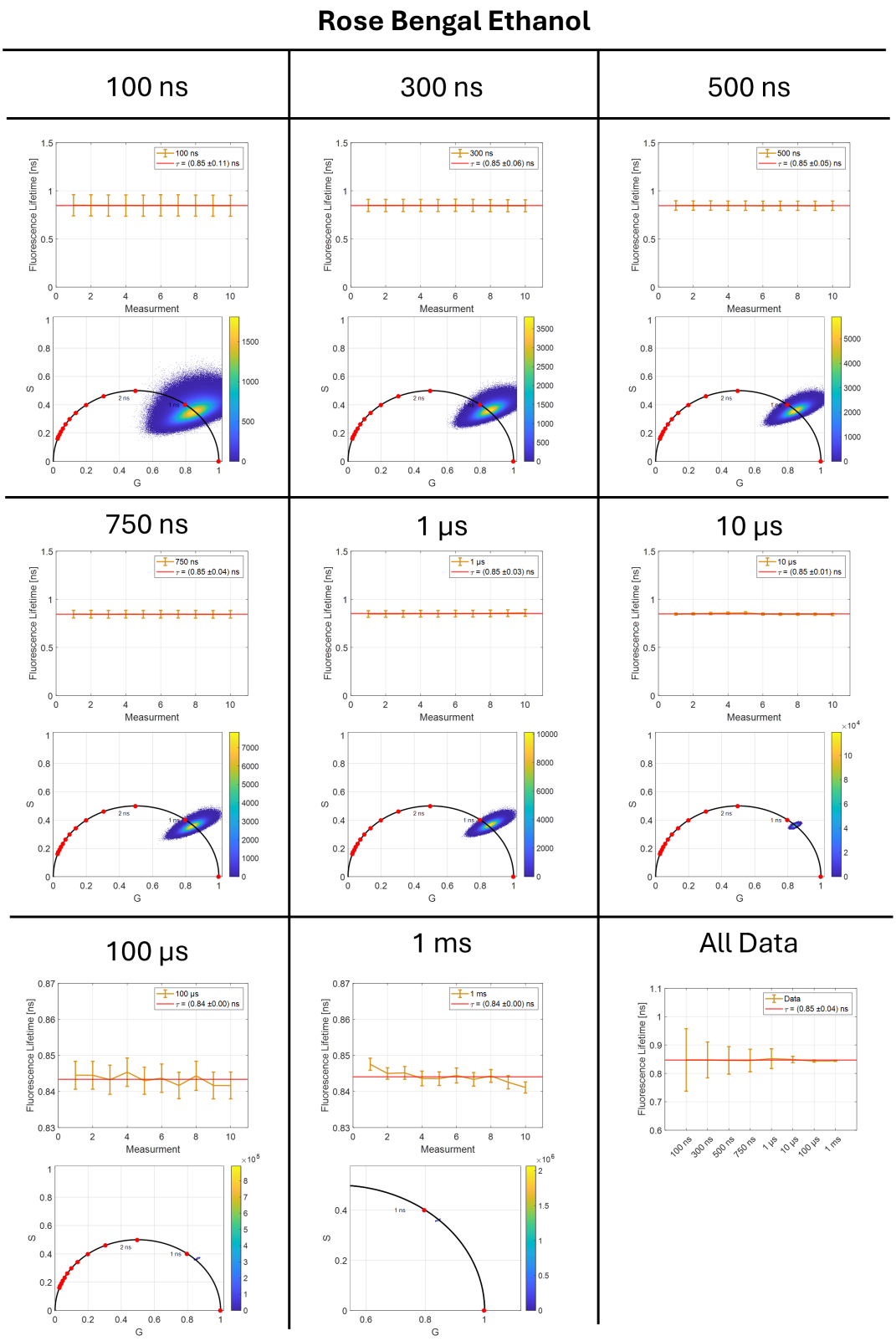

Figure 5. A 1 mM Rose Bengal solution in ethanol for eight different TC-values

Rose Bengal - Acetone

The fourth flurophore is Rose Bengal (**Figure - 6**) dissolved in Acetone at a concentration of 1 mM.

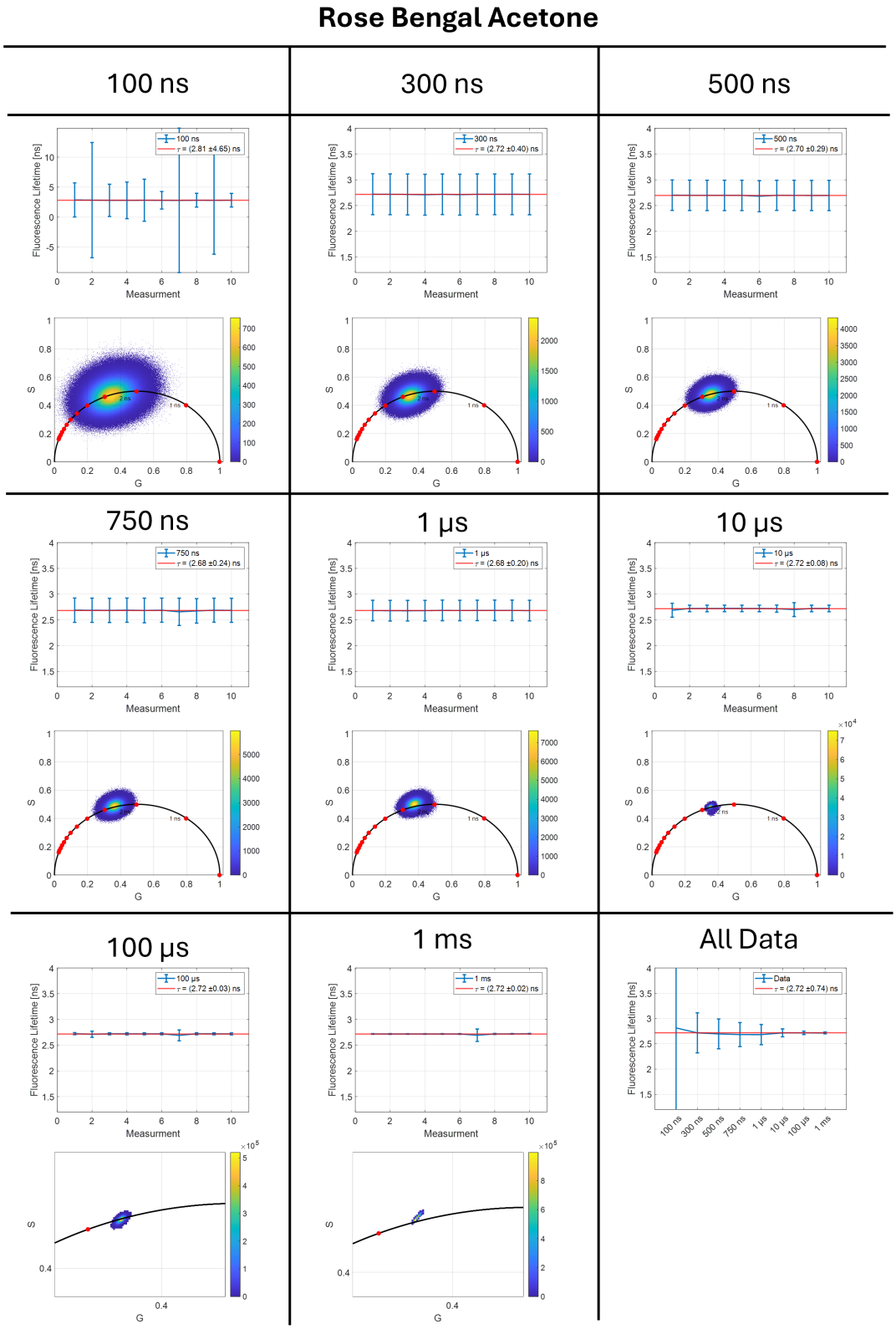

Figure 6. A 1 mM Rose Bengal solution in Acetone for eight different TC-values

S4.B Averaging

When low TC-times are necessary the lifetime precision can be increased by averaging. The image is therefore taken multiple times and for each pixel the average is calculated. Therefore the noise can be further minimized and the precision is increasing as it can be seen in **Figure 7**. For each averaging setting the recorded image was 1024x1024 pixel recorded with a TC time of 102 ns. For each averaging set ten measurements were carried out.

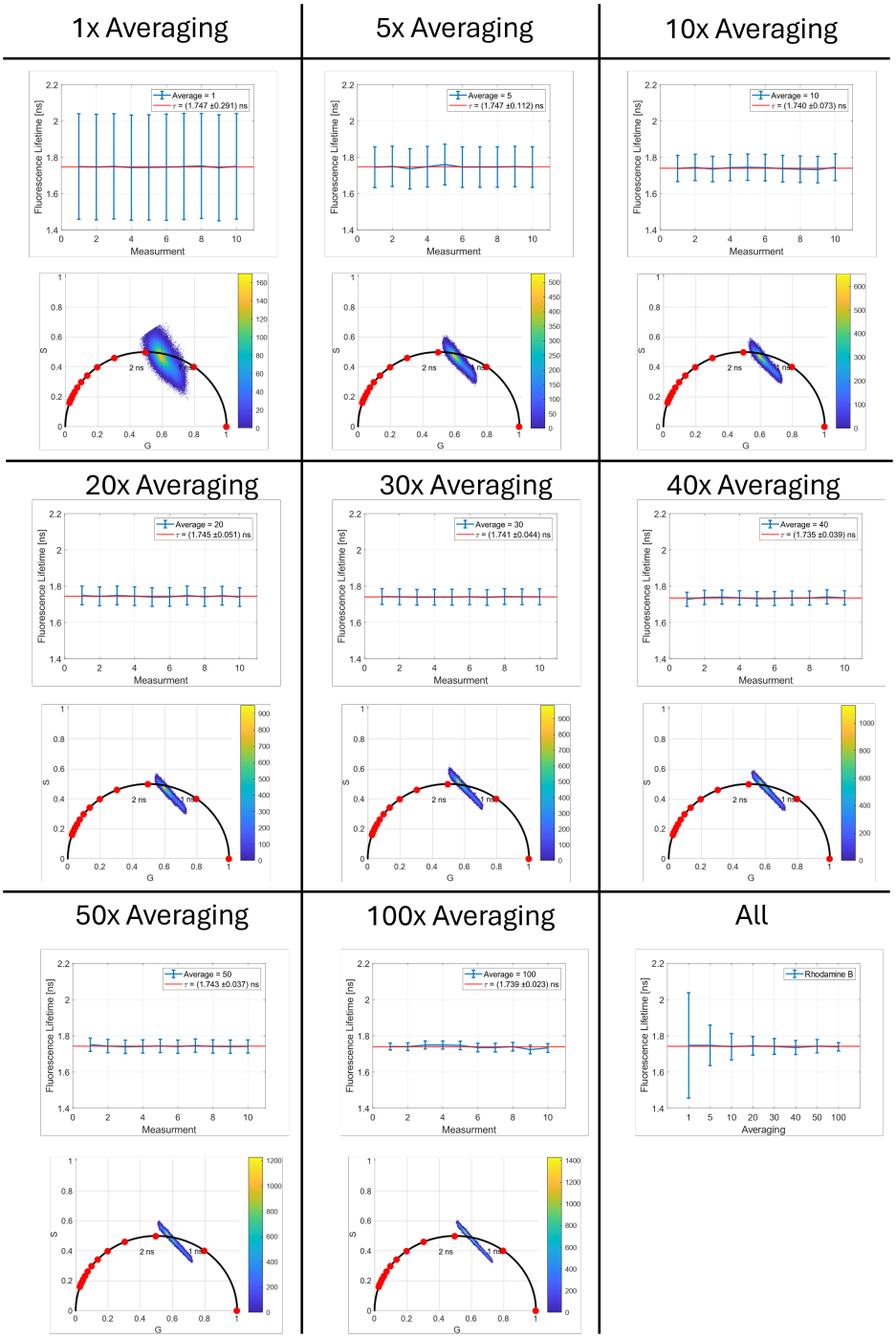

Figure 7. Averaging Effect on Fluorescence Lifetime of 1 mM Rhodamine B in Distilled Water (TC Time: 102 ns): Increasing the number of averaged images reveals an exponential decrease in both the mean fluorescence lifetime and its associated error, indicating improved measurement stability with greater averaging.

S5 Fluorescence Lifetime Benchmark

In this section we summarize the results from seven different samples that were statistically analyzed with our SUPER-FLIM technique. All results were displayed in **Table 1**.

Table 1. Results for the fluorescence lifetime measurements of various fluorophores with different modulation techniques. S = Sinusoidal Modulation, R = Rectangular Modulation.

Fluorophore	N	**Conc. C [mM]**	**Solvent**	**Relative Polarity**	**Excitation Wavelength [nm]**	**Excitation Frequency [MHz]**	**Fluorescence Lifetime Measured [ns]**	**Fluorescence Lifetime Literature [ns]**
Rhodamine 6G	10	1	dH_2O	1[5]	1030	80	4.06 ± 0.01	4.06 ± 0.17[6]
					561	3 (S)	4.06 ± 0.03	
					561	3 (R)	4.03 ± 0.05	
Rhodamine B	10	1	dH_2O	1[5]	1030	80	1.732 ± 0.001	1.74 ± 0.02[3]
					561	3 (S)	1.74 ± 0.37	
					561	3 (R)	1.75 ± 0.03	
Fluorescein	10	1	NaOH	—	780	80	3.984 ± 0.002	4.00 ± 0.20[7]
					561	3 (S)	4.01 ± 0.037	
					561	3 (R)	4.03 ± 0.04	
Rose Bengal	10	1	dH_2O	1[5]	780	80	0.098 ± 0.009	0.095 ± 0.015[8]
					561	3 (S)	0.10 ± 0.39	
					561	3 (R)	0.095 ± 0.012	
			Methanol	0.762[5]	780	80	0.650 ± 0.005	0.65 ± 0.012[9]
					561	3 (S)	0.64 ± 0.03	
					561	3 (R)	0.66 ± 0.02	
			Ethanol	0.654[5]	780	80	0.844 ± 0.002	0.85 ± 0.23[9]
					561	3 (S)	0.85 ± 0.03	
					561	3 (R)	0.85 ± 0.02	
			Acetone	0.355[5]	780	80	2.73 ± 0.02	2.73 ± 0.02[9]
					561	3 (S)	2.76 ± 0.04	
					561	3 (R)	2.77 ± 0.03	

Further the results for the benchmarking experiments to compare TD-FLIM, FD-FLIM instant FLIM and SUPER-FLIM are shown in the following table (**Table 2**).

Table 2. Benchmarking test of Rose Bengal dissolved in different solutions and measured with different FLIM methods.

	Rose Bengal			
Solvent	Acetone	Ethanol	Methanol	Water
Relative Polarity	0.355	0.654	0.762	1
TD-FLIM [ns]	2.82 ± 0.21	0.80 ± 0.06	0.61 ± 0.05	0.09 ± 0.05
FD-FLIM [ns]	2.73 ± 0.01	0.85 ± 0.01	0.65 ± 0.01	0.13 ± 0.01
instant FLIM [ns]	2.96 ± 0.07	0.96 ± 0.02	0.66 ± 0.02	0.13 ± 0.02
SUPER-FLIM [ns]	2.73 ± 0.06	0.85 ± 0.01	0.65 ± 0.01	0.1 ± 0.01

S6 Fluorescence Lifetime Correlation Spectroscopy

In traditional Fluorescence Correlation Spectroscopy, the factor of 1.6 is often cited as a rule of thumb for distinguishing two diffusing species[10]. This factor arises from the relationship between the diffusion times of two species in the observation volume. The diffusion time is determined by the size of the particle and its diffusion coefficient, and when two species have diffusion times that are close to each other (within a factor of 1.6), their fluorescence correlation signals start to overlap, making it difficult to distinguish them from one another.

Mathematically, this factor can be understood in terms of the autocorrelation function of the fluorescence intensity fluctuations. For two species with similar diffusion times, the resulting ACF from their combined signals will exhibit overlapping components. When the ratio of the diffusion times of the two species exceeds approximately 1.6, their individual contributions to the ACF can be more clearly separated, allowing for the distinct characterization of each species.

However, with the technique we have developed, we were able to overcome this limitation. By leveraging the fluorescence lifetime information of each species, our approach allows for the separation of species even when their diffusion times are nearly identical. This is possible because the fluorescence lifetime is an additional parameter that can be used to distinguish between species, in contrast to traditional FCS, which relies solely on the fluctuation patterns of the intensity. The fluorescence lifetime acts as an additional "dimension" for the measurement, enabling us to separate the two species based on this property, regardless of the similarities in their diffusion times.

As shown in **Figure 8**, we demonstrate how the combination of fluorescence lifetime with FCS data allows for the extraction of single ACF curves for each species, even when the diffusion times are very similar. This technique provides a significant improvement over conventional FCS, overcoming the 1.6 factor and enabling the accurate analysis of two species with closely matched diffusion coefficients.

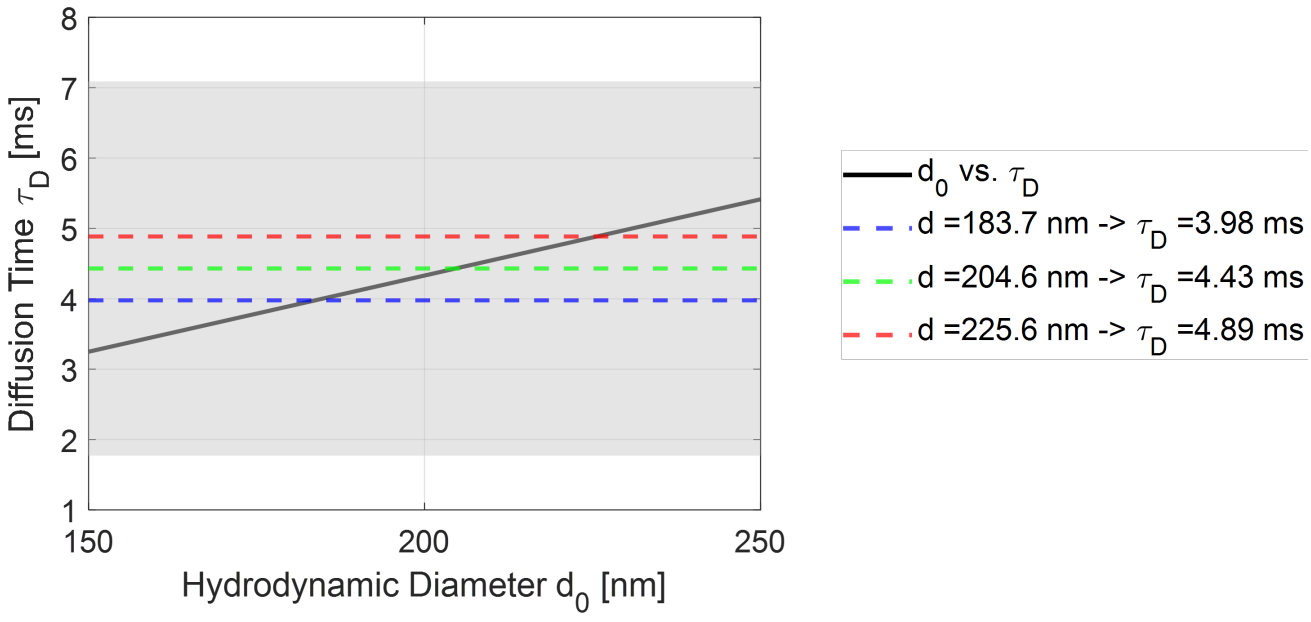

Figure 8. Results of the ml-FCS measurements and overcoming the factor of 1.6: The diffusion time is displayed against the hydrodynamic diameter. As stated in the Stokes-Einstein equation, the linear fit (black solid line) intersects the y-axis at (0|0), and the observed diameters align with this line. The grey shaded area represents the region where conventional FCS would struggle to differentiate between two particles due to overlapping diffusion times, a limitation often described by a factor of 1.6. Our technique clearly demonstrates that we are not constrained by this factor, allowing for the separation of particles with similar diffusion times.

S7 Monte Carlo Simulation TD-FLIM and SUPER-FLIM Comparison

Here we compare the SUPER-FLIM measurements with a monte carlo simulation of a TD-FLIM setup. The simulation was done for different numbers of pulse cycles (Repetition frequency of 80 MHz) to match the TC-times measured with the SUPER-FLIM setup. As Fluorophore we choose Rhodamine B. The experimental gained lifetime value for ten measurments of Rhodamine B resulted in $\tau_{SUPER-FLIM} = (1.76 \pm 0.33)$ ns and a TC-time of 102 ns while the TD simulations resulted in $\tau_{TD-FLIM} = (0.85 \pm 1.81)$ ns according to 8 photons. For the other extreme value uf 80000 photons in the TD-simulation and a TC-time of 1 ms the lifetime was $\tau_{TD-FLIM} = (1.741 \pm 0.006)$ ns and $\tau_{SUPER-FLIM} = (1.732 \pm 0.003)$ ns.

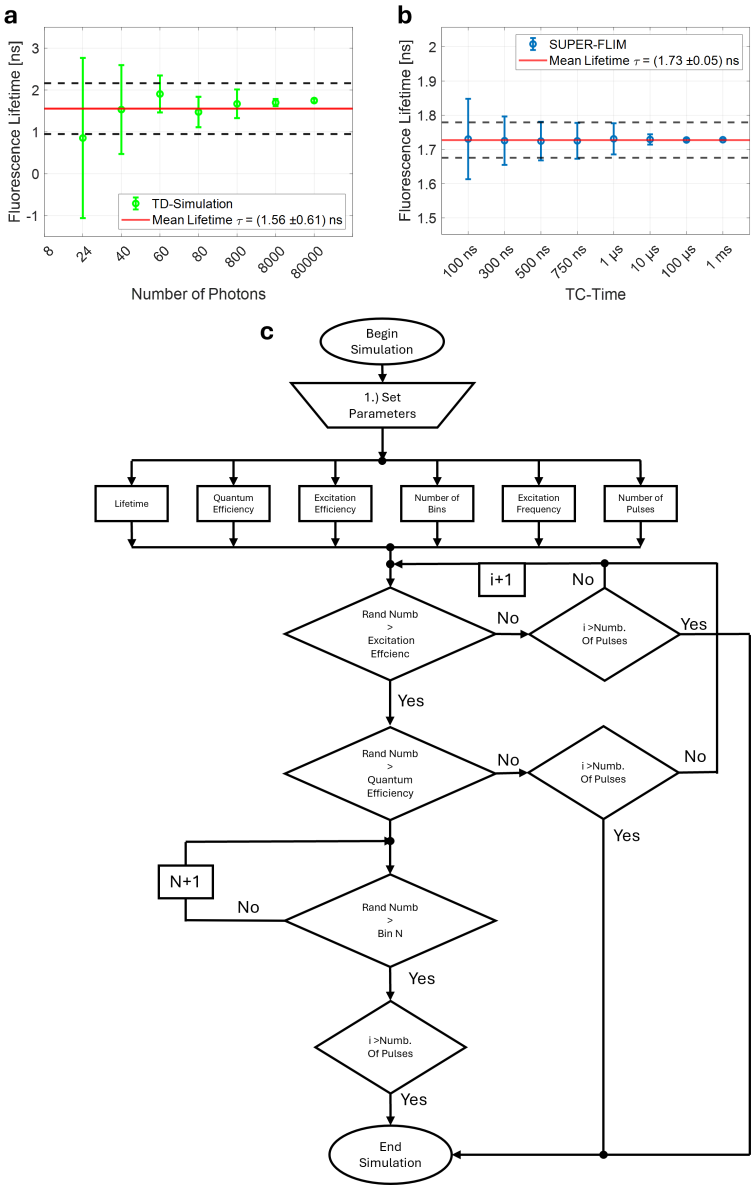

Figure 9. Monte Carlo Simulations Comparing TD-FLIM and SUPER-FLIM: We conducted Monte Carlo simulations to model TD-FLIM, based on a TCSPC system. Ten lifetimes were simulated at eight different photon count numbers, with mean lifetimes and standard deviations illustrated in **a.)**. These simulations were performed using a 1 mM Rhodamine B solution in distilled water (dH_2O) and are compared with experimental results from SUPER-FLIM in **b.)**. The workflow of the Monte Carlo simulation process is detailed in **c.)**.

S8 LNP-Stability

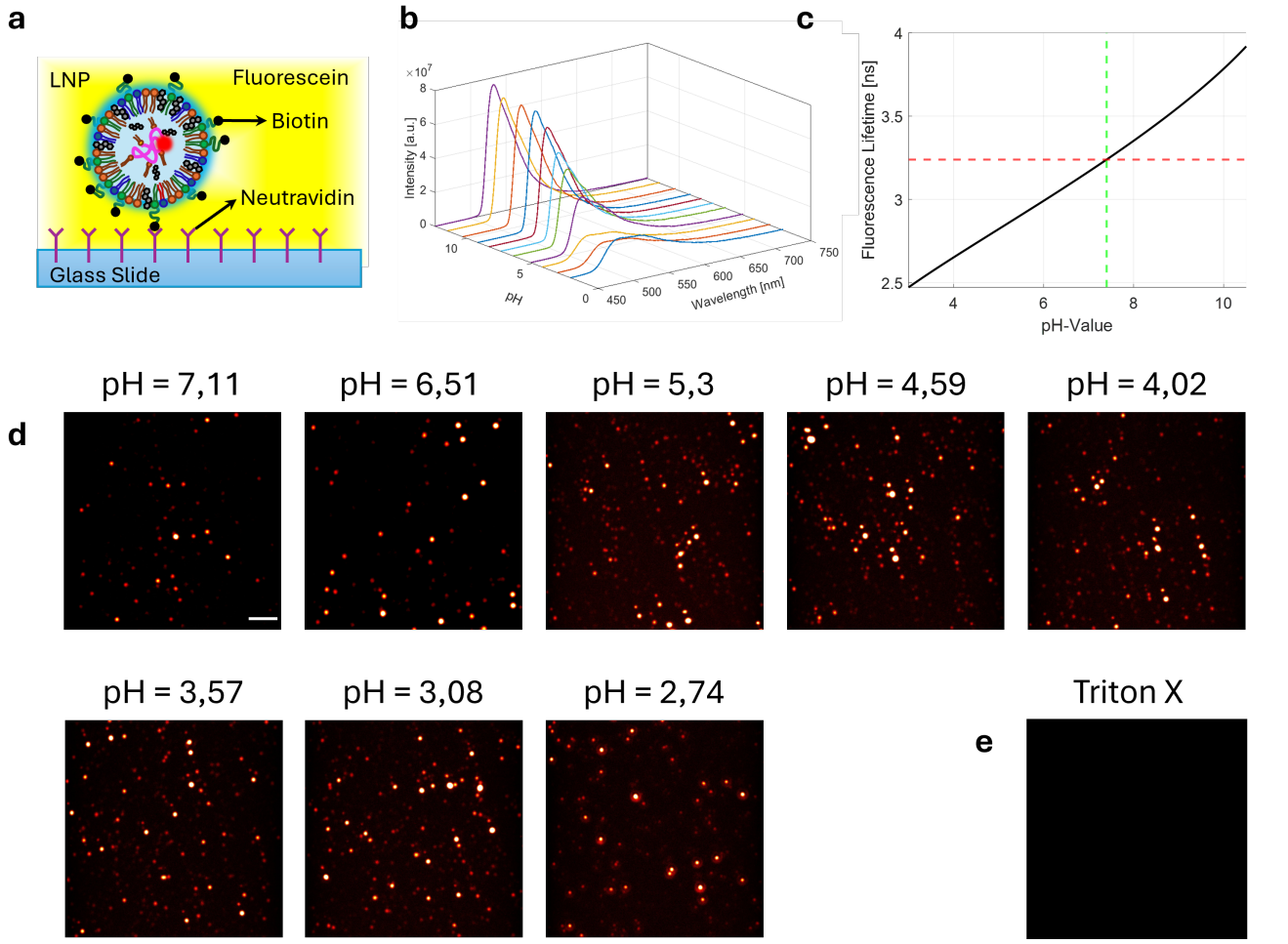

Figure 10. LNP Stability Across Different pH Values: **(a)** LNPs were anchored to the surface using a biotin–neutravidin linkage. The mRNA was stained with Cy3, while the surrounding solution contained 1 mM Fluorescein. The intensity of the obtained Fluorescein emission-spectra decreases with a pH-drop **(b)**, accompanied by alterations in fluorescence lifetime, as shown in **(c)**. At eight different pH-values, the mRNA was imaged to assess LNP stability, while fluorescence lifetime measurements were taken to determine pH-values according to **(c)**. For the anchored LNPs, Triton X was applied **(e)**, resulting in immediate LNP dissolution. Scale bar: **d,e** - 1 µm

S9 Comparison with Other FLIM Techniques

To provide a clearer comparison of SUPER-FLIM's performance relative to other FLIM techniques, we conducted an extensive literature review. Our aim was to gather a diverse set of approaches in fluorescence lifetime imaging microscopy and highlight key parameters and performance metrics. We have compiled what we believe are the most important aspects of these methods in a comparative format, emphasizing the distinctions in speed, sensitivity, and imaging capabilities.

Table 3. Technique comparison with already published techniques.

Correspondend Author	Akronym	Year	Excitation	Detection	Image Size	Pixel Dwell Time [μs]	fps
Thomas Hellerer	SUPER-FLIM	2024	2P	PMT	1024x1024	0.123	7.8
Scott S. Howard[11]	instantFLIM	2021	2P	PMT	360x360 - 540x540	1-12	N.A.
Yoshimasa Kawata[2]	Phase Resolved FLIM	2016	2P	PMT	1x1	$90 \cdot 10^6$	N.A.
Rainer Erdmann[12]	rapidFLIM	2016	1P & 2P	PMA Hybrid	128x128	4	6
Enrico Gratton[13]	DFD	2008	1P	PMT	256x256	40	N.A.
Bahram Jalali[14]	SLIDE	2020	2P	HPD	256x170	N.A.	N.A.
Stephen Boppart[15]	N.A.	2021	2P	PMT	256x256x2000	5	25
Graham Hungerford[16]	FLASH-FLIM	2021	1P	SPAD	192x128x120	N.A.	6
Xu Liu[17]	N.A.	2018	1P	6xAPD	N.A.	200	N.A.
Hsin-Chih Yeh[18]	PIE sFLIM	2024	1P	16xPMT	256x256	50	0.3
Andreas C. Hocke[19]	N.A.	2020	1P	16xPMT	512x512	1.5	N.A.
Dug Young Kim[20]	AMD-FLIM	2011	1P	PMT	158x127	6.4	7.7
Enrico Gratton[21]	pco.FLIM	2015	1P	Camera	1008x1008	1000	N.A.
Garth J. Simpson[22]	N.A.	2015	2P	PMT	512x512	2.54	15
Liang Gao[23]	Compressed FLIM	2021	1P	Streak Camera	500x400	10000	100

S10 Experimental Setup

S10.A Optical Setup

This section describes the optical and electronic configuration of the SUPER-FLIM technique. The system is constructed around a Nikon Eclipse Ti2 microscope stand, which has been modified with various 3D-printed components to create a Two-Photone Excited Fluorescence Microscope (TPEFM) with three color channels.

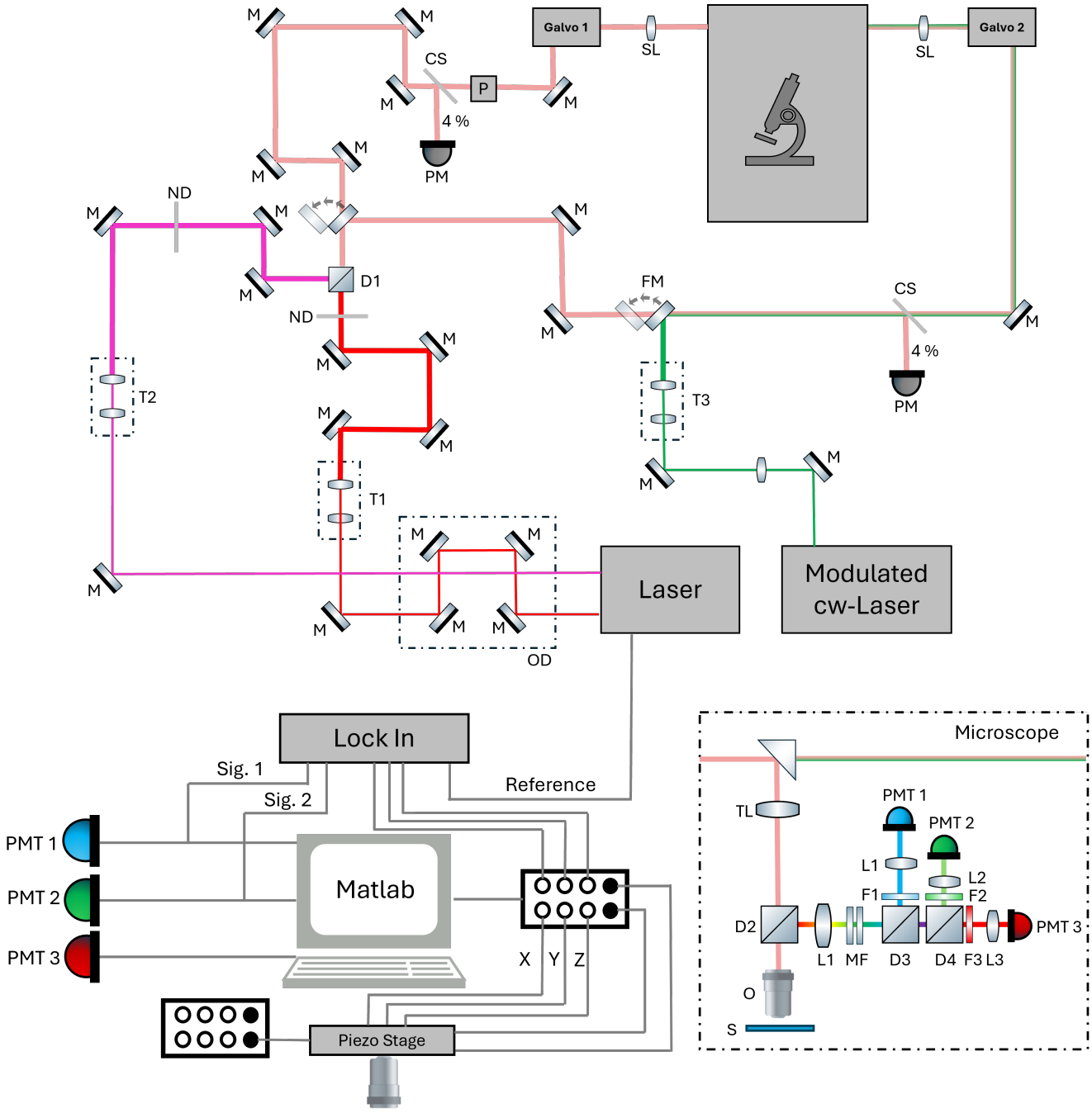

Figure 11. Optical Setup for the Tracking and Fluorescence Lifetime Imaging Measurements: The abbreviations are standing for M: Mirror, D: Dichroic, OD: Optical Delayline, FM: Flip Mirror, T: Telescope, ND: Neutral Density Filter, PM: Power Meter, CS: Coverslip, SL: Scan Lens, CL: Collimation Lens, TL: Tube Lens, O: Objective, S: Sample, MF: Multiphoton Filer, L: Lens, F: Filter, PMT: Photomultiplier

As the excitation source, an ultrafast pulse fiber laser (FemtoFiber Dichro Design, TOPTICA Photonics AG) with dual

central wavelengths at λ_1 = 780 nm and λ_2 = 1030 nm was employed. Both laser beams emit pulses of 100 fs at a repetition rate of 80 MHz, with a maximum power output of 100 mW each.

The laser beams are guided through several mirrors **M** to a dichroic beam splitter **D1** (F38-825, AHF Analysentechnik), which combines both beams. Before reaching this optical element, the laser beams pass through two telescopes that expand the beams to ensure the complete overfilling of the microscope objective's rear aperture, thereby obtaining optimal resolution and illumination. Telescope **T1** (87-570, Edmund Optics) results in a two-fold expansion for λ_1. The second telescope in the pathway of the λ_2 laser beam comprises a set of lenses with focal lengths L = 50 mm (LA1131-AB,Thorlabs) and L = 100 mm (LA1509-AB, Thorlabs), also achieving a two-fold beam expansion. A beam viewer unit (BC207VIS/M and M2MS, Thorlabs) allows monitoring of parameters, such as beam quality and size. Two neutral density filter **ND** (NDC-25C-2-B, Thorlabs) wheels positioned before the dichroic beam splitter enable continuous adjustment of the lasers' power, which is proportionally measured in the combined beam path using a coverslip (**CS**) induced 4% Fresnel reflection and a powermeter (843-R, Newport)

A resonant galvo scanner **Galvo 1** (MPM-2PKIT, Thorlabs), operating at a resonance frequency of 8 kHz, together with the scan lens **SL** (MPM-2PKIT, Thorlabs) and tube lens **TL**, forms a telecentric system. This system focuses the laser light onto the sample **S** through various objectives **O** (20x, 40x, 60x, 100x, Nikon) . The emitted fluorescence radiation is collected by the same objective, separated from the excitation light by a second dichroic beam splitter **D2** (F76-735, AHF Analysentechnik), and directed to the detection unit. The fluorescence light passes through another telecentric system composed of the objective, **L1** (LA1979-A-ML,Thorlabs), and corresponding PMT lenses **L2**, **L3**, and **L4** (LA1422-A, Thorlabs). Two multiphoton filters **MF** (F39-745, AHF Analysentechnik) remove potential laser reflections. The fluorescence light is then split by a third dichroic beam splitter **D3** (F38-495, AHF Analysentechnik) into a blue spectral component, with an additional bandpass filter **F1** (F34-450A, AHF Analysentechnik) directing the light to the first PMT detector , **PMT1** (PMT2101,Thorlabs). A fourth dichroic beam splitter **D4** (F38-593, Thorlabs) further separates the signal into green and red channels, with **PMT2** equipped with bandpass filter **F2** (F37-547, AHF Analysentechnik) for the green channel, and **F3** (F76-594, AHF Analysentechnik) for the red channel. For SHG detection the backscatterd signal was collected with **PMT2**

A flip mirror closely behind **D1** can be used to direct both laser beams to a second galvo-galvo scanner system denoted as **Galvo 2** (Saturn 5B, Edmund Optics). With this scanner the pixel dwell time can be set individual and can therefore be used to sync the image recording with the data transfer rate of the lock-in amplifier. The excitation and emission path is the same as with **Galvo 2**. Again a coverslip in the beampath can be used to measure the laser power for each laser.

To synchronize both laser beams in time and space at the location of the sample **S**, an optical delay line **OD** is integrated into the beam path of the 780 nm laser. This delay line consists of four mirrors **M** and a translation stage. In addition to facilitating sum frequency generation of a wavelength λ_3 = 443 nm, this arrangement ensures the system can be calibrated for simultaneous use with two detectors.

A second light source, a multi-laser engine (iChrome MLE, Toptica) with four distinct wavelengths (405, 488, 561 and 640 nm), was modulated using an external frequency generator (DG4162, Rigol) and employed in the experiment. The laser was expanded with **T3** and led to to **Galvo 2**.

S10.B Electrical Setup

For the electronic signal processing, all three photomultiplier tubes (PMTs) and the resonant galvanometer scanner **Galvo 1** are controlled via the ThorImage Software. For **Galvo 2** a self-written matlab code was used. The fluorescence signals captured by PMT1 and PMT2 are also fed into a lock-in amplifier using two T-junctions. This setup utilizes the output from an internal photodiode within the laser as the reference signal to facilitate accurate signal demodulation. The datacollection is done with the LabOne software. The further data process is done with self written Matlab scripts. For image recording and z-stacks the scanner-software of **Galvo 2** also generates various triggers (pixel, line and frame) with which the lock-in amplifier can generate images.

S11 Ancillary Measurements

S11.A Dynamic Light Scattering

Dynamic light scattering measurements where done on a DynaPro Nanostar (Wyatt). The temperature were set to 20°C and 10 µL where used as sample volume. Each measurement took 10 s and was measured with 660.5 nm.

S11.B FCS Measurements

To determine the diffusion coefficient and hydrodynamic radius of particles, Fluorescence Correlation Spectroscopy measurements were performed using a Zeiss LSM980 microscope. The fitting analysis was conducted with the open-source software PyCorrFit[24], applying a single-component 3D free diffusion model. Prior to these measurements, a calibration was performed on a 10 nM Cy5 solution to establish a structural parameter of 4.6 at a wavelength of 639 nm.

S11.C Fluorescence Absorption and Emission Spectra Measurements

The measurements of the emission and absorption spectra for all fluorophores were done on a Fluorolog 3 (Horiba). Here the dissolved dyes were placed in a clean cuvette and were measured with an excitation and emission slit of 2 nm and a 5 nm step width at a 1 s integration time.

S12 Software

Disclaimer:
This software has been developed with a focus on ease of integration and is provided as-is. While every effort has been made to ensure its functionality, it is not a perfect implementation and offers many opportunities for optimization and improvement. Users are encouraged to adapt and modify the code to suit their specific needs. For any questions, suggestions, or assistance, please feel free to reach out—I'm happy to help!

The SUPER-FLIM software can be used to control a laser-scanning microscope with up to two point-source detectors with the help of a data acquisition card (DAQ) and Matlab. Further it can be used for FCS measurements. If a lock-in amplifier is also available lifetime images as well as FLCS measurments can be done. At first a simplified setup is shown in **Figure 12**.

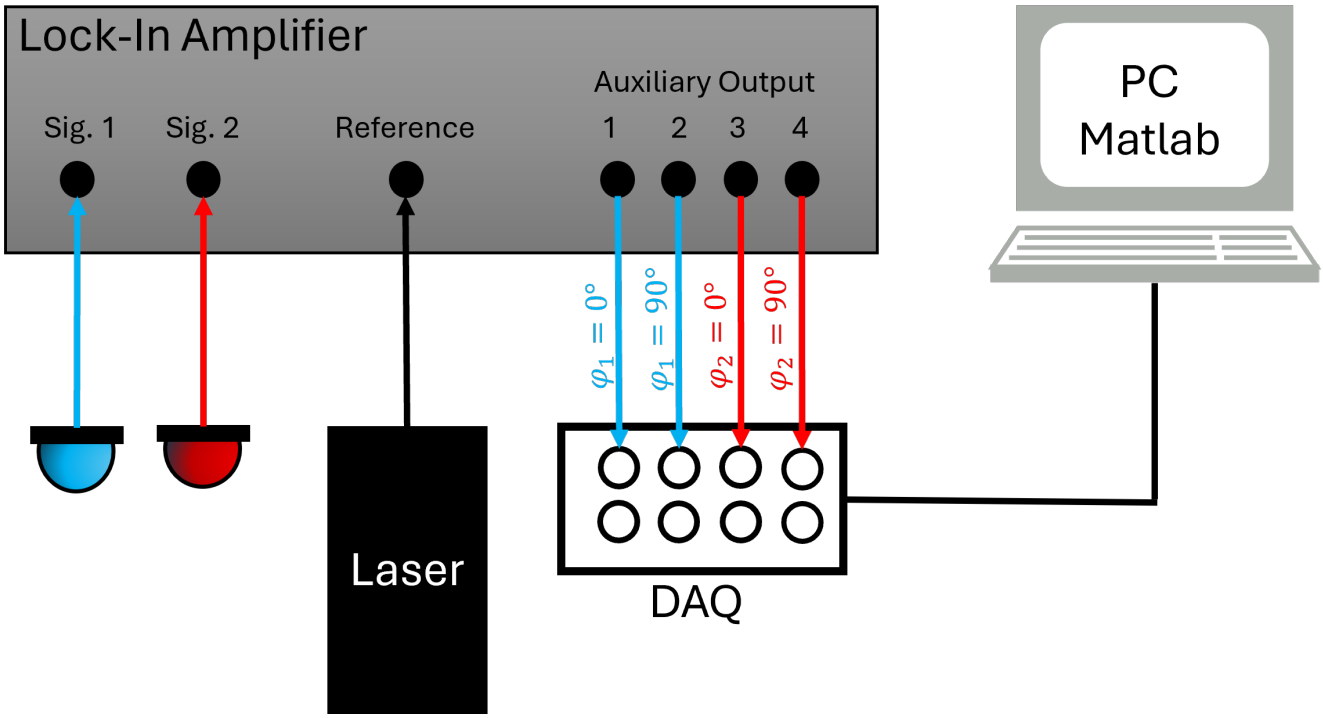

Figure 12. Simplified Setup of the SUPER-FLIM Technique: The SUPER-FLIM setup uses PMTs as the input source for the lock-in amplifier. The laser's photodiode signal serves as the reference. The lock-in amplifier software is responsible for setting the demodulation parameters. The system outputs four signals via auxiliary channels, with both the 0° and 90° phases provided for each channel. A data acquisition (DAQ) card records these signals, and a MATLAB script is used to process the data. The DAQ card is also used to control the scanning of the laser beam with a galvo scanner.

To use the provided Software packages Matlab R2016a or higher must be installed along with the image processing toolbox. A detailed description and a step by step instruction is given in the next section.

The software packages were developed alongside the evaluation and testing of the technique, so certain sections may benefit from further refinement. The packages are designed to enable immediate use of SUPER-FLIM. For integration into different setups or specific applications, the software may need to be adapted. We have included detailed descriptions and annotations to help make each step clear and understandable. If any issues arise, please feel free to reach out—we're happy to assist.

S12.A SUPER-FLIM Control Software

The *SUPER-FLIM Control Software* is designed for data acquisition, basic analysis, and data saving. It is organized into three main sections:

- **Two-Photon Imaging:** Facilitates the recording and display of two-photon images from two separate detectors.
- **SUPER-FLIM:** Enables the acquisition, analysis, and storage of FLIM images.
- **FCS and FLCS:** Allows for the recording of standard fluorescence correlation spectroscopy (FCS) curves, or fluorescence lifetime correlation spectroscopy (FLCS) curves. FLCS uses SUPER-FLIM to separate the autocorrelation function (ACF) by fluorescence lifetime.

The scanning settings for the first two sections are identical and are located at the top of the software interface, as shown in **Figure 13**.

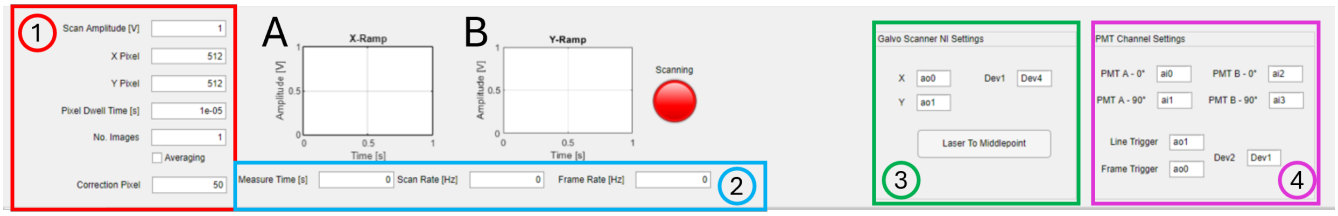

Figure 13. Scanning Settings of the SUPER-FLIM Control Software

Here are following the descriptions of the single panels.

1. The fields in this section allow adjustment of image size and zoom factor. To acquire SUPER-FLIM images, the pixel dwell time must be synchronized with the TC-time of the lock-in amplifier. The *Correction Pixel* option compensates for hysteresis effects, eliminating inaccurate pixel information at the image edges. The *Number of Images* setting can be increased for alignment and to locate the desired region of interest (ROI); here, the image is continuously refreshed. Selecting a lower pixel count and faster pixel dwell time increases the frames per second (fps). Enabling the *Averaging* checkbox averages the images, yielding improved signal-to-noise ratio (SNR) and more accurate lifetime values. Based on the scan amplitude, X-pixels, and Y-pixels, the voltage ramps are displayed in **A** and **B**.
2. This section displays essential image information, including measurement time, frame time, and scan rate.
3. The ports for the analog outputs of the galvo scanner can be modified here. Both the device name and output ports for the X-axis and Y-axis can be adjusted. Also by pressing the button *Laser To Middlepoint* the X-axis and Y-axis is set to 0 V.
4. The final box allows configuration of the device for signal inputs, as well as outputs for line and frame triggers. The line and frame trigger are optional and can be used to synchronize third-party devices.

S12.A.I Two-Photon Imaging

After the scanning and image settings have been set two photon images can be detected in the section showed in **Figure 14**.

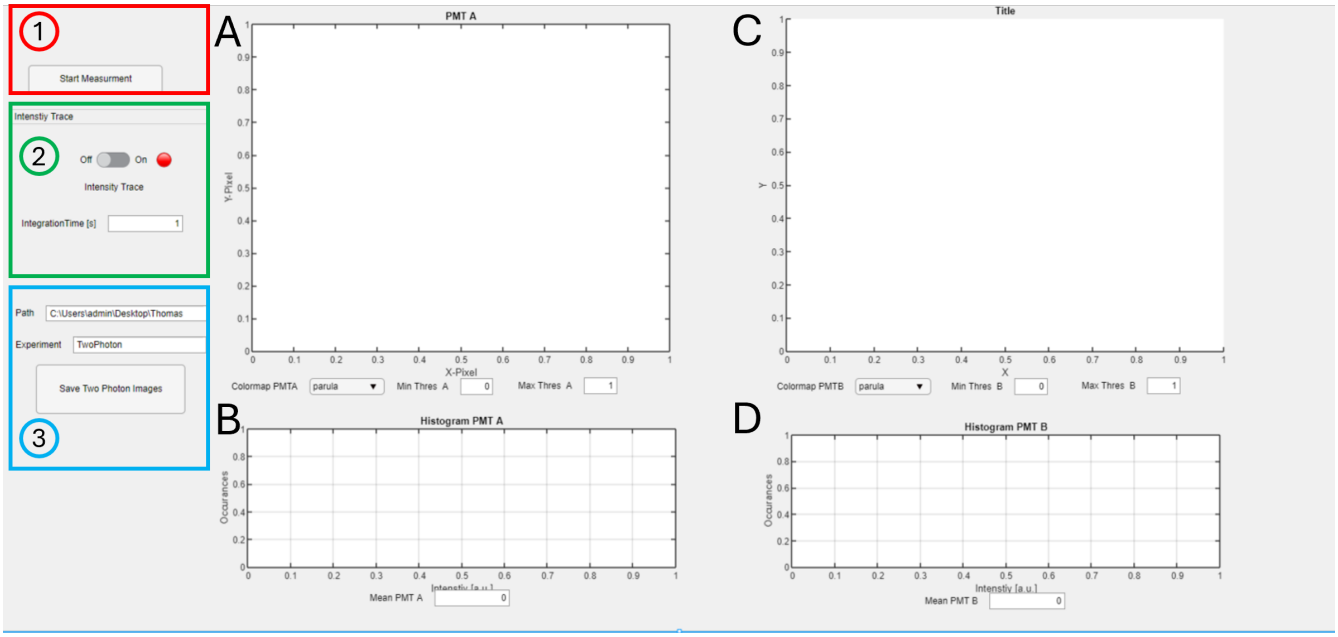

Figure 14. Overview of the Two-Photon Imaging Software Section.

1. Once the image settings are configured, press the *Start Measurement* button to begin acquisition. The scanning indicator in Figure XXX will light up green during acquisition and will turn off once the process is complete. After measurement, the laser returns to its default position at 0 V. If laser safety requirements prevent this, and the laser must be redirected to avoid entering the microscope, a modification to the program is necessary. The image from detector one is displayed in **A** with its histogram in **B**, while the image from detector two is displayed in **C** and its histogram in **D**. Below each image, the colormap and relevant image statistics are shown.

2. To facilitate quicker and easier focusing, an intensity trace can also be displayed. Based on the selected integration time, the intensity trace for detector one is shown in **B** and for detector two in **D**.

3. For saving images, the file path and experiment name can be specified. By pressing *Save Two Photon Images*, the images are saved as .mat files in a folder named according to the experiment. If a file with the same name already exists, a new folder is created with an incremented number appended.

S12.A.II SUPER-FLIM

If the lock-amplifier is set, also FLIM images can be generated in the second section of the *SUPER-FLIM Control Software* like shown in **Figure 15**

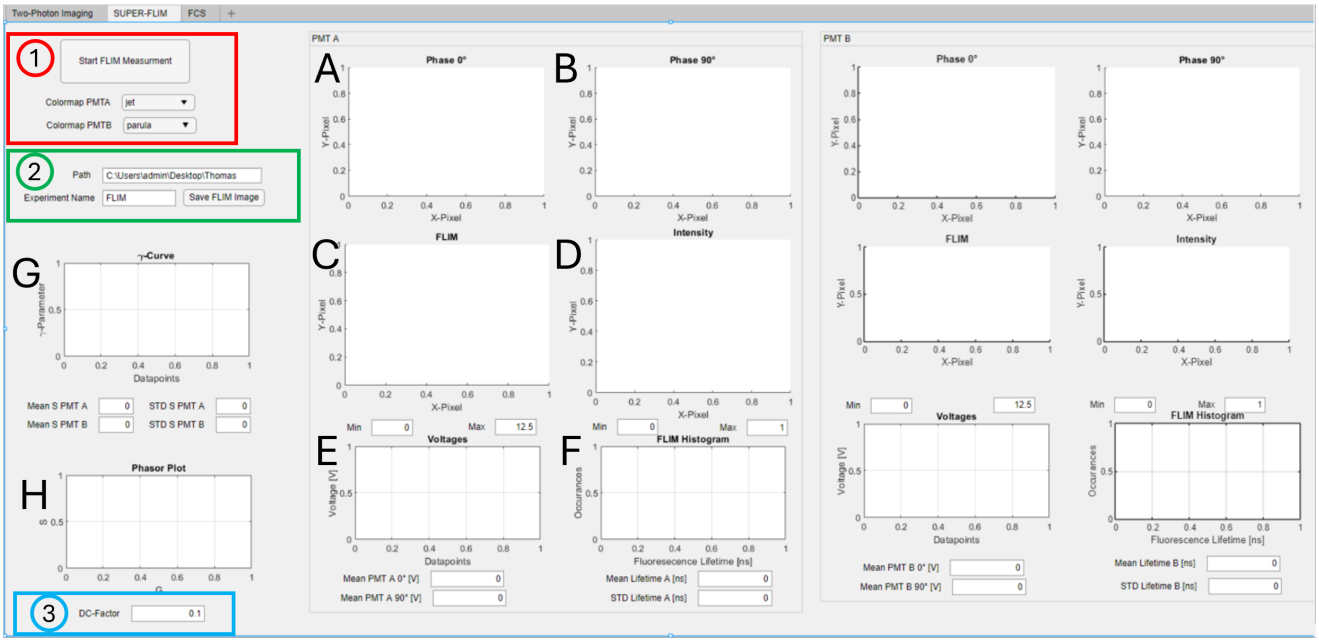

Figure 15. Overview of the SUPER-FLIM Software Section.

To record a FLIM image, follow these steps:

1. Press the *Start FLIM Measurement* button to initiate FLIM image acquisition. The scanning indicator in Figure XXX will light up green during acquisition and will turn off when the process is complete. After measurement, the laser returns to its default position at 0 V. If laser safety requirements prevent this, and the laser needs to be redirected to avoid entering the microscope, a program modification may be necessary. The image for the 0° phase appears in **A**, and the 90° phase image in **B**. The corresponding calculated FLIM image is displayed in **C** along with its intensity image in **D**. The recorded voltages for both phases per pixel are shown in **E**, and the FLIM histogram is shown in **F**. This setup is mirrored on the right side for the second detector. The γ traces for both detectors are displayed in **G**.

2. To save the images, specify the file path and experiment name. Pressing *Save FLIM Image* saves the images as .mat files in a folder named after the experiment. If a file with the same name already exists, a new folder is created with an incremented number appended.

3. The phasor plot is displayed in **H**. Since DC values are often recorded by detectors with digitized outputs, pixel values may require adjustment, which can be managed using the *DC-Factor*.

S12.A.III FCS and FLCS

In the last acquisition section FCS with additional lifetime information can be acquired. The GUI for this section is displayed in **Figure 16**:

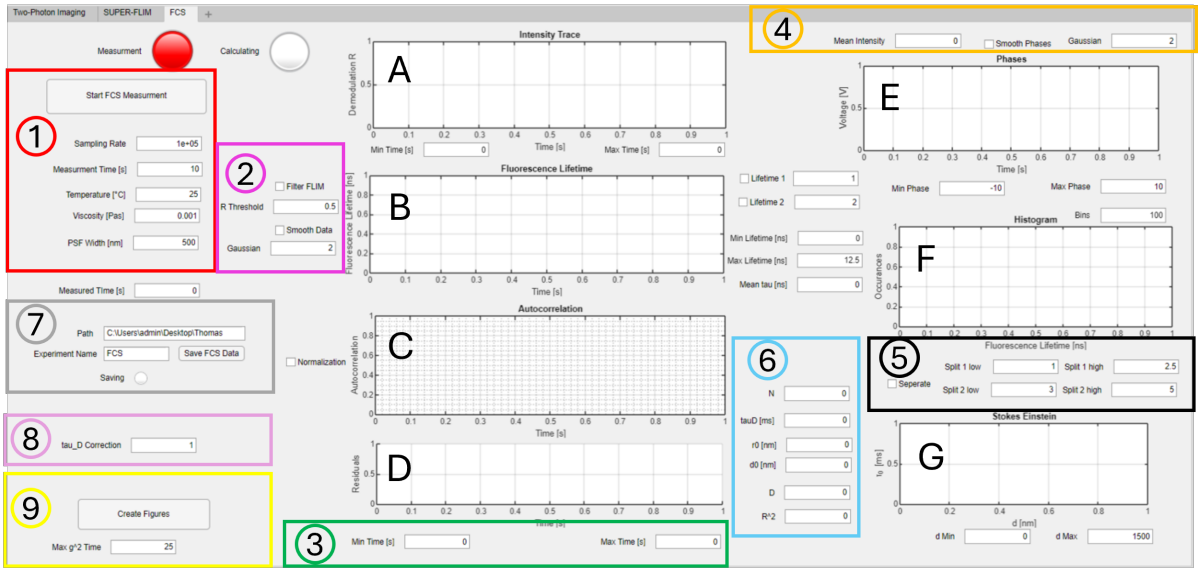

Figure 16. Overview of the FCS and FLCS Software Section.

The following steps must be performed to record a normal FCS measurement or an FCS with lifetime information in order to separate the intensity information and display the autocorrelation function (ACF) for two different species.

1. First, set the sampling rate. A higher sampling rate allows for the measurement of smaller diffusion times. The main parameters for the fit can be changed here also. If you wish to record the lifetime value, adjust the time constant (TC) of the lock-in amplifier accordingly. Upon pressing the *Start FCS Measurement* button, the measurement lamp will turn green, and the acquisition will proceed for the duration specified in *Measurement Time*. Once the measurement is complete, the ACF calculation and fitting process will commence, as indicated by the calculation lamp. The intensity trace will be displayed in **A**, alongside the ACF and its fit in **C**. (If desired, the normalized ACF can be displayed by activating the *Normalization* checkbox.) The fit is determined based on the initial parameters. If the fluorescence lifetime is also included, the results will appear in **B**. The hydrodynamic radius will be calculated and displayed in **G** based on the fitting parameters using the Stokes-Einstein equation.

2. To reduce noise or other intensity artifacts, activate the filter checkbox.

3. The fit can be adjusted by excluding values from the beginning or end of the trace by modifying the *Min Time* and *Max Time* fields under **D**. If the fit is inadequate, the *tau_D Correction* option can be utilized for fine-tuning adjustments.

4. If filtering of the FLIM values corresponding to the intensity trace is necessary, enable the *Smooth Data* checkbox. Adjusting the field below it will change the value of the Gaussian filter, and the modified trace will be displayed in **B** and **E**. The lifetime histogram in **F** will also update accordingly.

5. By enabling the *Split* checkbox, the separation of the ACF by the lifetime values specified in *Split 1 Low*, *Split 1 High*, *Split 2 Low*, and *Split 2 High* will be computed. The graphs will be distinguished by two colors, red and blue, representing the two different species.

6. Here the results of the fit are displayed. Note that this software is designed for two-photon absorption processes, which result in different equations and fit values compared to FCS measurements using single-photon absorption[25].

7. To save the FCS data, specify the file path and experiment name. Pressing *Save FCS Data* will save the data as .mat files in a folder named after the experiment. If a file with the same name already exists, a new folder will be created with an incremented number appended.

8. In some cases the ACF Fit is not calculated correctly. With the $tau_D Correction$ the fit can be changed manually until the desired accuracy is reached.

9. As an alternative to the save button, the *Create Figures* option can be pressed to save the current graphs as .fig files.

S12.B SUPER-FLIM Evaluation Software

When FLIM-images are generated in the *SUPER-FLIM Control Software* the *SUPER-FLIM Evaluation Software* can be used to analyse, process and save the images. The software is structured like shown in **Figure 17**.

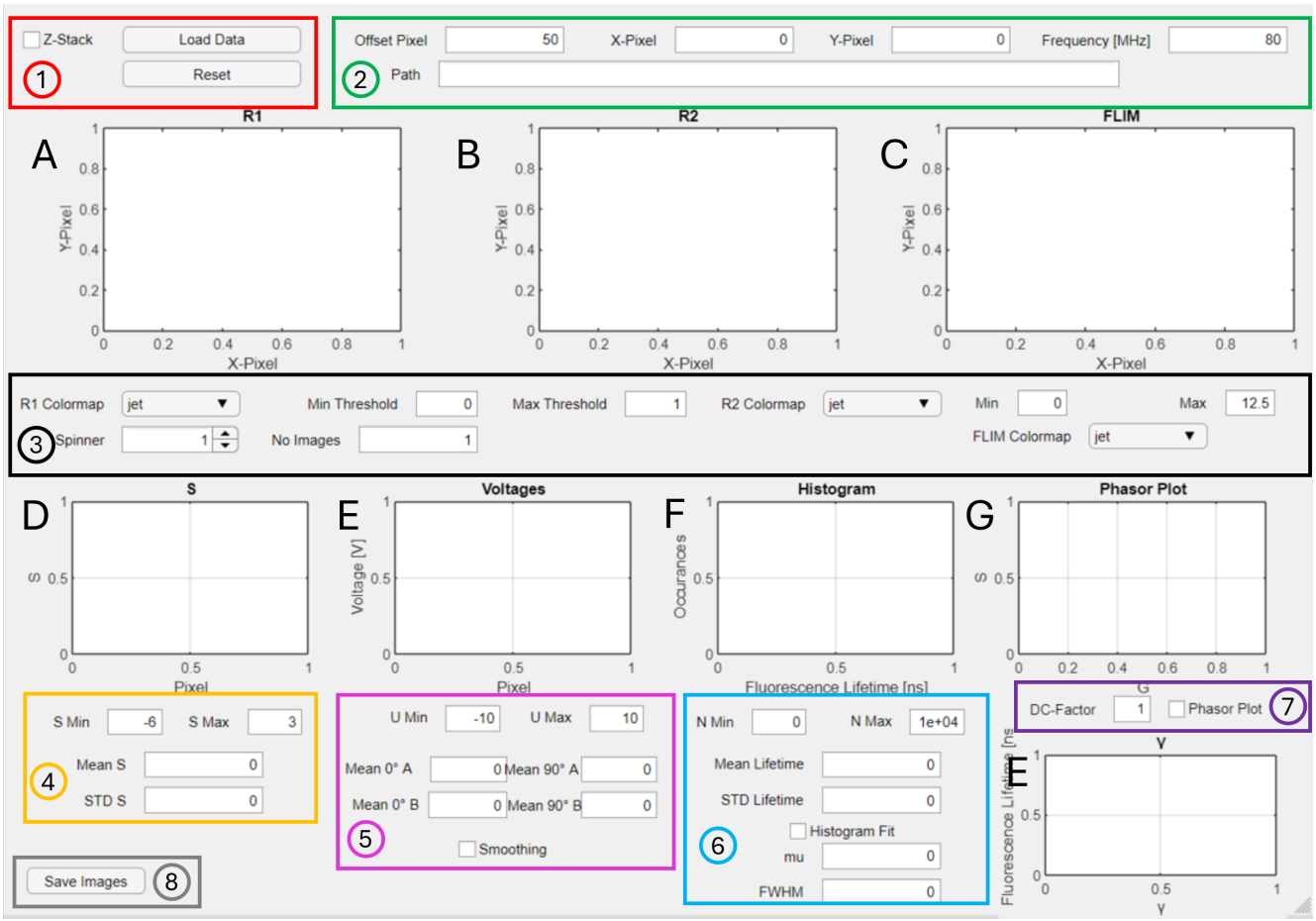

Figure 17. Overview of the SUPER-FLIM Evaluation Software.

Here is a step by step instruction to load, analyse and save the data:

1. Data can be loaded in this box by pressing *Load Data*. To load a Z-stack, select the corresponding checkbox. The *Reset* button restores all values to their default settings. After loading, the 0° image appears in **A**, the 90° signal in **B**, and the FLIM image in **C**. The γ trace for all pixels is shown in **D**. The corresponding voltage traces for 0° and 90° over time are displayed in **E**, with the lifetime histogram shown in **F** and the mean lifetime value annotated on the γ trace in **E**.

2. The image path and dimensions are displayed in this section. Since galvo scanners often exhibit some hysteresis, the first and last pixels may be distorted. Use the *Offset Pixel* option to exclude these edge pixels. Depending on the laser system, the frequency can be adjusted in the *Frequency [MHz]* field.

3. Intensity values can be adjusted here by setting the *Min Threshold* and *Max Threshold*. Pixels with values above *Max Threshold* or below *Min Threshold* are set to zero and displayed as black in **A** and **B**; they are also excluded from the FLIM image in **C**.

4. This section shows the mean γ trace value and standard deviation for the entire image. The graph in **D** can be adjusted by modifying *S Min* and *S Max*.

5. As in **4**, this section displays the mean values and standard deviations for the 0° and 90° phases. Selecting the *Smoothing* checkbox applies smoothing to these phases and, consequently, to the FLIM image.

6. Here, you can customize the appearance of the lifetime histogram. Selecting the *Histogram Fit* checkbox applies a Gaussian fit to the histogram in **F**, which is particularly useful for system calibration.

7. If a DC image is available, you can generate a phasor plot (**G**) by selecting the *Phasor Plot* checkbox. Since DC values are often recorded by detectors with digitized outputs, pixel values may need adjustment, which can be done using the *DC-Factor*.

8. This final box provides options for saving the data as .png files.

S12.C Resonant-Scanning Evaluation Software

To capture FLIM images using a resonant-galvo scanner, the lock-in signals must be recorded at an appropriate speed. There are three main options for achieving this:

1. **Custom Software:** One approach is to use custom software packages for galvo control and for recording the 0° and 90° lock-in signals. In this case, each pixel's value in the image should correspond directly to the voltage, recorded in units of volts.

2. **Imaging Control Software:** Another option is to utilize established imaging control software such as ScanImage, which can manage both the scanner and the acquisition of lock-in signals.

3. **ThorImage:** For recording SUPER-FLIM data, we employed ThorImage software in conjunction with a resonant-galvo scanner. In this setup, the lock-in signals were routed to the electronic control unit (ECU), typically used for photomultiplier tube (PMT) voltage signals.

Regardless of the option chosen, the *Resonant-Scanning Evaluation Software* can be used to analyze the images. In some cases, it may be necessary to reorder the images or make minor adjustments to ensure compatibility with the analysis code. The GUI is represented in **Figure 18**:

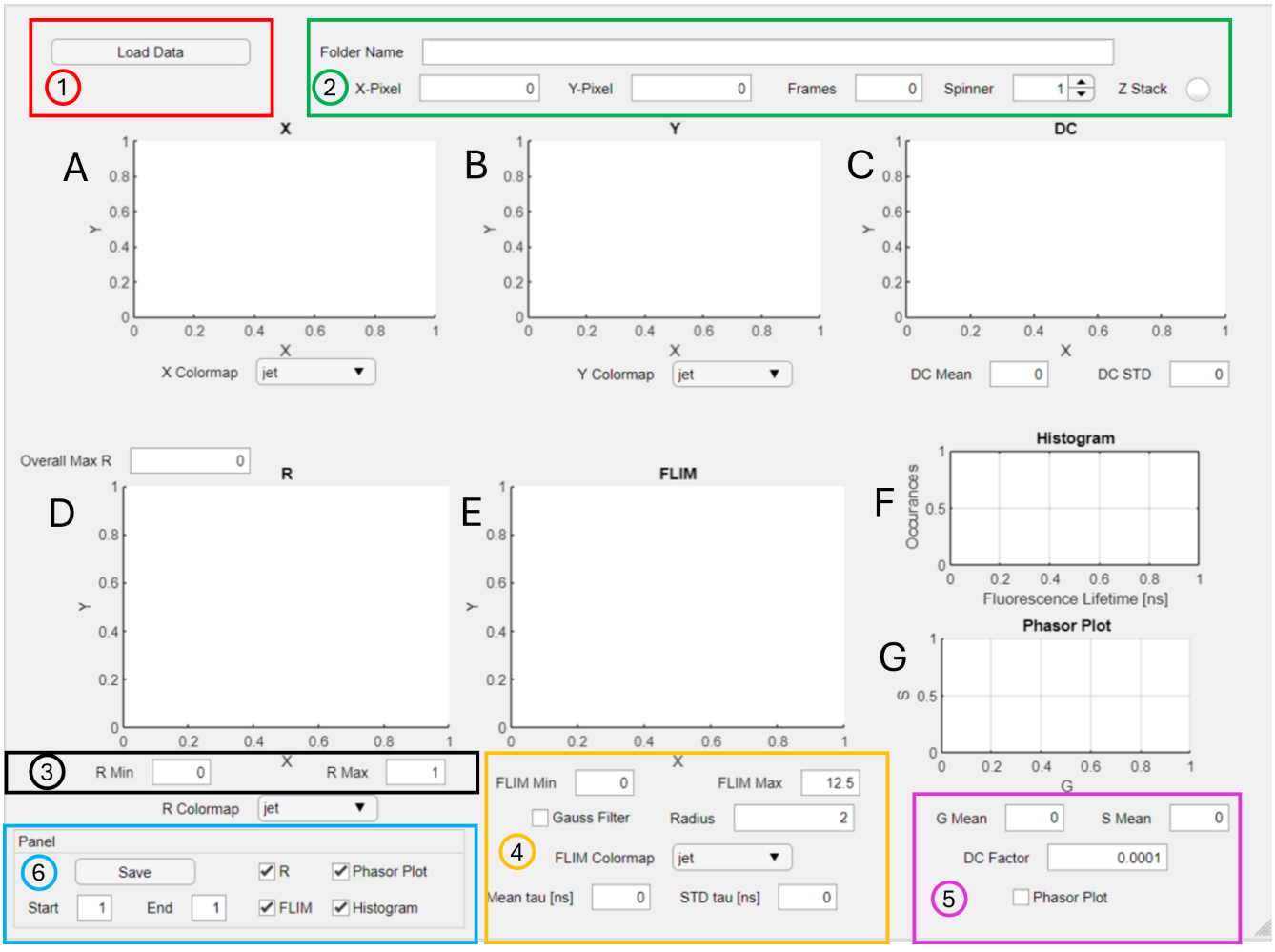

Figure 18. Overview of the Resonant-Scanning SUPER-FLIM Evaluation Software.

Here are the steps to load, analyse and save the data.

1. By pressing *Load Data* you can select the path to a folder containing either a single image or an image stack. The interface will display the images as follows: the 0° phase image in panel **A**, the 90° phase image in **B**, the DC image in

C, the demodulated intensity R image in **D**, the lifetime image in **E**, and its histogram in **F**. Each image's colormap can be adjusted using the dropdown menu located beneath the corresponding image.

2. In this section, the folder path and image dimensions are displayed. If a Z-stack is loaded, the *Z Stack* indicator will turn green, and you can navigate through the stack using the image number spinner.

3. Here, the intensity image in panel **D** (based on the demodulated R values) can be filtered by adjusting the *R Min* and *R Max* thresholds. Pixels with values above *R Max* or below *R Min* are set to zero (black), effectively excluding them from the lifetime image in panel **E**.

4. This section allows adjustment of the colormap for the FLIM image in **E** by setting *FLIM Min* and *FLIM Max*. The mean lifetime and its standard deviation are also displayed here.

5. If a DC image in panel **C** is available, a phasor plot (**G**) can be generated by selecting the *Phasor Plot* checkbox. Since DC values are typically recorded by detectors with digitized outputs, pixel values may need correction, which can be done by adjusting the *DC Factor*.

6. The final box provides options for saving the data. After selecting the desired data and image range, pressing *Start* will save the selected images as both .png and .mat files.

Figure 19. Overview of the FCS and FLCS Evaluation Software.

S12.D FLCS Evaluation Software

When FCS measurments have been made in the *SUPER-FLIM Control Software* (**S12.A**), the saved data can be read with the *FLCS Evaluation Software*. The GUI is represented in **Figure 19**.

1. The first step is to load the data by clicking the *Load Data* button. This action displays the folder path and sampling rate. The following figures are generated upon loading. The intensity trace is displayed in **A**, the phase and intensity in **B** (important for FLCS analysis later), and the ACF function along with the fitted curve in **C**. If lifetime data has also been recorded, the phases are shown in **D**, along with the lifetime histogram in **E** and the lifetime time trace in **F**. The fitting results are displayed in **G**, **H**, and **I**. If no lifetime separation is applied, only the overall ACF fit results are shown in **G**. The *Save Figures* button, located directly below *Load Data*, saves all figures to a new folder named "Results" in the data directory.

2. For 3D diffusion, parameters can be adjusted here. Note that this software is designed for two-photon absorption processes, which result in different equations and fit values compared to FCS measurements using single-photon absorption[25].

3. In this section, the intensity trace can be modified. For improved visualization, normalization can be applied to the trace. Selecting the *Threshold* option allows for excluding background noise or bursts unrelated to fluorescent particles, thereby enhancing the ACF in **C**.

4. The ACF can also be adjusted. By modifying the *Min Time* and *Max Time* settings, you can change the fit range. Normalization for both the ACF and the fit can be applied by selecting the corresponding checkbox. If lifetime separation is enabled, use the *Average*, *Species 1*, and *Species 2* checkboxes to display the individual graphs with their fit functions.

5. Lifetime separation can be applied by selecting the *Separate* checkbox and setting the lifetime ranges for species 1 and species 2. If preliminary filtering by lifetime or phase is required, use the filter checkboxes located above **D** and **E**.

S13 Resonant Scanning Videos

S13.A Description for movie SM1 (Resonant scanning - Rhodamine B)

In this movie we showed the resonant imaging ability of our technique. We imaged a dried sample of Rhodamine B with a known lifetime of 1.74 ns. In the movie the fluorescence lifetime image along with the lifetime histogram and phasor plot is shown.

S13.B Description for movie SM2 (Resonant scanning - HuH7 CellTracker)

In this movie we showed the resonant imaging ability of our technique. We imaged a timelapse of HuH7 cells stained with CellTracker green. In the movie the fluorescence lifetime image along with the lifetime histogram and the intensity image is shown.

S13.C Description for movie SM3 (Resonant scanning - Particle diffusion)

In this movie we showed the resonant imaging ability of our technique. We imaged a timelapse of two fluorescence lifetime bead standards with known lifetimes of 1.7 ns and 2.7 ns. In the movie the fluorescence lifetime image along with the lifetime histogram and the intensity image is shown.

References

1. Mohler, W., Millard, A. C. & Campagnola, P. J. Second harmonic generation imaging of endogenous structural proteins. *Methods* **29**, 97–109, DOI: https://doi.org/10.1016/S1046-2023(02)00292-X (2003).

2. Halip, H., Yoshimura, Y., Inami, W. & Kawata, Y. Ultrashort laser based two-photon phase-resolved fluorescence lifetime measurement method. *Methods Appl. Fluoresc.* **8**, 025003, DOI: https://10.1088/2050-6120/ab71c2 (2020).

3. Boens, N. *et al.* Fluorescence lifetime standards for time and frequency domain fluorescence spectroscopy. *Anal. chemistry* **79**, 2137–2149, DOI: https://doi.org/10.1021/ac062160k (2007).

4. Kristoffersen, A. S., Erga, S. R., Hamre, B. & Frette, Ø. Testing fluorescence lifetime standards using two-photon excitation and time-domain instrumentation: rhodamine b, coumarin 6 and lucifer yellow. *J. fluorescence* **24**, 1015–1024, DOI: https://doi.org/10.1007/s10895-014-1368-1 (2014).

5. Reichardt, C. & Welton, T. *Solvents and solvent effects in organic chemistry* (John Wiley & Sons, 2011).

6. Elder, A. D., Frank, J., Swartling, J., Dai, X. & Kaminski, C. Calibration of a wide-field frequency-domain fluorescence lifetime microscopy system using light emitting diodes as light sources. *J. microscopy* **224**, 166–180, DOI: https://doi.org/10.1111/j.1365-2818.2006.01689.x (2006).

7. Martin, M. M. Hydrogen bond effects on radiationless electronic transitions in xanthene dyes. *Chem. Phys. Lett.* **35**, 105–111, DOI: https://doi.org/10.1016/0009-2614(75)85598-9 (1975).

8. Fleming, G., Knight, A., Morris, J., Morrison, R. & Robinson, G. Picosecond fluorescence studies of xanthene dyes. *J. Am. Chem. Soc.* **99**, 4306–4311, DOI: https://doi.org/10.1021/ja00455a017 (1977).

9. Kellerer, T. *et al.* Comprehensive investigation of parameters influencing fluorescence lifetime imaging microscopy in frequency-and time-domain illustrated by phasor plot analysis. *Int. J. Mol. Sci.* **23**, 15885, DOI: https://doi.org/10.3390/ijms232415885 (2022).

10. Meseth, U., Wohland, T., Rigler, R. & Vogel, H. Resolution of fluorescence correlation measurements. *Biophys. journal* **76**, 1619–1631, DOI: https://doi.org/10.1016/S0006-3495(99)77321-2 (1999).

11. Zhang, Y. *et al.* Instant flim enables 4d in vivo lifetime imaging of intact and injured zebrafish and mouse brains. *Optica* **8**, 885–897, DOI: https://doi.org/10.1364/OPTICA.426870 (2021).

12. Orthaus-Mueller, S. *et al.* rapidflim: the new and innovative method for ultra fast flim imaging. *PicoQuant Appl. Note* 1–8, DOI: https://doi.org/10.1117/12.2249757 (2016).

13. Colyer, R. A., Lee, C. & Gratton, E. A novel fluorescence lifetime imaging system that optimizes photon efficiency. *Microsc. research technique* **71**, 201–213, DOI: https://doi.org/10.1002/jemt.20540 (2008).

14. Karpf, S. *et al.* Spectro-temporal encoded multiphoton microscopy and fluorescence lifetime imaging at kilohertz frame-rates. *Nat. communications* **11**, 2062, DOI: https://doi.org/10.1038/s41467-020-15618-w (2020).

15. Sorrells, J. E. *et al.* Real-time pixelwise phasor analysis for video-rate two-photon fluorescence lifetime imaging microscopy. *Biomed. optics express* **12**, 4003–4019, DOI: https://doi.org/10.1364/BOE.424533 (2021).

16. Sagoo, K., Cumberbatch, N., Holland, A. & Hungerford, G. Rapid (flash-flim) imaging of protoporphyrin ix in a lipid mixture using a cmos based widefield fluorescence lifetime imaging camera in real time for margin demarcation applications. *Methods Appl. Fluoresc.* **9**, 015002, DOI: https://doi.org/10.1088/2050-6120/abbcc6 (2021).

17. Liu, S. *et al.* Parallelized fluorescence lifetime imaging microscopy (flim) based on photon reassignment. *Opt. Commun.* **421**, 83–89, DOI: https://doi.org/10.1016/j.optcom.2018.03.060 (2018).

18. Nguyen, T. D. *et al.* Multiplexed imaging in live cells using pulsed interleaved excitation spectral flim. *Opt. Express* **32**, 3290–3307, DOI: https://doi.org/10.1364/OE.505667 (2024).

19. Wahl, M. *et al.* Photon arrival time tagging with many channels, sub-nanosecond deadtime, very high throughput, and fiber optic remote synchronization. *Rev. Sci. Instruments* **91**, DOI: https://doi.org/10.1063/1.5121412 (2020).

20. Won, Y. *et al.* High-speed confocal fluorescence lifetime imaging microscopy (flim) with the analog mean delay (amd) method. *Opt. express* **19**, 3396–3405, DOI: https://doi.org/10.1364/OE.19.003396 (2011).

21. Chen, H., Holst, G. & Gratton, E. Modulated cmos camera for fluorescence lifetime microscopy. *Microsc. research technique* **78**, 1075–1081, DOI: https://doi.org/10.1002/jemt.22587 (2015).

22. Dow, X. Y., Sullivan, S. Z., Muir, R. D. & Simpson, G. J. Video-rate two-photon excited fluorescence lifetime imaging system with interleaved digitization. *Opt. letters* **40**, 3296–3299, DOI: https://doi.org/10.1364/OL.40.003296 (2015).

23. Ma, Y., Lee, Y., Best-Popescu, C. & Gao, L. High-speed compressed-sensing fluorescence lifetime imaging microscopy of live cells. *Proc. Natl. Acad. Sci.* **118**, e2004176118, DOI: https://doi.org/10.1073/pnas.2004176118 (2021).

24. Müller, P., Schwille, P. & Weidemann, T. Pycorrfit—generic data evaluation for fluorescence correlation spectroscopy. *Bioinformatics* **30**, 2532–2533, DOI: https://doi.org/10.1093/bioinformatics/btu328 (2014).

25. Schwille, P., Haupts, U., Maiti, S. & Webb, W. W. Molecular dynamics in living cells observed by fluorescence correlation spectroscopy with one-and two-photon excitation. *Biophys. journal* **77**, 2251–2265, DOI: https://doi.org/10.1016/S0006-3495(99)77065-7 (1999).

Appendix B

SEMPA-Track

B.1 Supplementary Information to SEMPA-Track

In this chapter the supplementary information to the publication *SEMPA-Track* is presented.

Supplementary Information to "Spectrally Encoded Multiphoton Particle Tracking (SEMPA-Track): A Real-Time 4D-Single Particle Tracking Fluorescence Lifetime Imaging Microscope"

Thomas Kellerer[1,2], Tanja Grawert[1], Florian Schorre[1], Judith A. Müller[2], Joachim O. Rädler[2], and Thomas Hellerer[1,*]

[1]Multiphoton Imaging Lab, Munich University of Applied Sciences, 80335 Munich, Germany
[2]Faculty of Physics and Center for NanoScience, Ludwig Maximilians-University, 80539 Munich, Germany
[*]Hellerer@hm.edu

ABSTRACT

Image-based single particle tracking reveals specific movements or interactions of the particle under investigation with its surrounding. Existing methods often introduce optical aberrations, require multiple detectors, or rely on specific detection mechanisms to generate a feedback signal that keeps a particle in the field of view. These approaches are almost always camera-based, enabling rapid image acquisition but lacking fluorescence lifetime information and the high optical resolution associated with laser scanning microscopy. Using point spread function engineering, we modified the excitation geometry of two lasers by displacing their axial positions along the optical axis. These lasers were then scanned with a resonant galvo scanner in a two-photon laser scanning approach. The separated observation volumes enabled the extraction of the axial movement of the particle, while image information was used to detect XY-displacement. Both feedback values were fed into a piezoelectric stage to keep the observed particle in the field of view. By employing a digital lock-in amplifier for signal detection, the fluorescence could also be used to stream lifetime data by evaluating the phase shift in comparison to the two-photon excitation. We validated our tracking capabilities on lipid nanoparticles carrying messenger ribonucleic acid (mRNA) into HuH7 cells, analyzing diffusion coefficients and trajectories in intra- and extracellular environments. Subsequently, we combined the tracking approach with fluorescence lifetime measurements, adding an additional dimension to discriminate between different particles during tracking. We believe that this framework contributes to the advancement of real-time, image-based tracking technologies by integrating fluorescence lifetime data, thereby providing insights into the surrounding environment.

Keywords: Single-Particle Tracking, Fluorescence Lifetime Imaging Microsocpy, Two-Photon Excited Fluorescence Microscopy, Environmental Sensing, Lipid Nanoparticles, lock-in Amplifier, Transfection

List Of Supplememntary Files

In this supplementary file we will include following topics:

S8 Literature Research

S9 Description to movie SM1

S10 Description to movie SM2

S11 Description to movie SM3

S12 Description to movie SM4

S13 Description to movie SM5

S14 Description to movie SM6

S1 Experimental Setup

S1.A Optical Setup

The system is built around a Nikon Eclipse Ti2 microscope (Nikon, Japan) that has been modified with custom 3D-printed components to create a three-channel two-photon excitation fluorescence microscope.

For excitation, we use an ultrafast fiber laser (FemtoFiber Dichro Design, TOPTICA Photonics AG) emitting two beams with a center wavelength of 780 nm and 1030 nm. Both lasers emit 100 fs pulses at an 80 MHz repetition rate, with each laser providing up to 100 mW of power.

The beams are directed through a series of mirrors **M** to a dichroic beam splitter **D1** (F38-825, AHF Analysentechnik) that combines them. Before reaching **D1**, each laser beam passes through a telescope to expand the beam, ensuring optimal filling of the microscope objective's rear aperture for better resolution. The telescope **T1** (87-570, Edmund Optics) expands the 780 nm beam by a factor of two, while the 1030 nm beam passes through a lens pair (50 mm LA1131-AB and 100 mm LA1509-AB, Thorlabs) for similar expansion. A beam viewer (BC207VIS/M and M2MS, Thorlabs) monitors beam quality and size, while two neutral density filters **ND** (NDC-25C-2-B, Thorlabs) allow continuous adjustment of the laser power. Power measurements are made in the combined beam path via a 4% Fresnel reflection from a coverslip (**CS**) and a powermeter (843-R, Newport).

To create the axial offset of the two PSF in the beam path of the 780 nm a flip mirror is included that could be used to replace the Keppler telescope **T1** with a slightly misaligned Galilean telescope **GT**.

A resonant galvo scanner (MPM-2PKIT, Thorlabs), operating at 8 kHz, works with a scan lens **SL** (MPM-2PKIT, Thorlabs) and tube lens **TL** to create a telecentric system that focuses the laser light onto the sample **S**. The system uses various objectives **O** (20x, 40x, 60x, 100x, Nikon). The fluorescence emission is than collected through the same objective and separated from the excitation light by a second dichroic beam splitter **D2** (F76-735, AHF Analysentechnik). This emission is then directed towards the detection system.

The emitted fluorescence passes through a secondary telecentric system formed by the objective, **L1** (LA1979-A-ML, Thorlabs), and subsequent lenses **L2**, **L3**, and **L4** (LA1422-A, Thorlabs). Two multiphoton filters **MF** (F39-745, AHF Analysentechnik) block any laser reflections. A third dichroic beam splitter **D3** (F38-495, AHF Analysentechnik) divides the fluorescence into blue, green, and red channels. The blue channel is directed to a PMT detector **PMT1** (PMT2101, Thorlabs) through a bandpass filter **F1** (F34-450A, AHF Analysentechnik). Another dichroic splitter **D4** (F38-593, AHF Analysentechnik) separates the green and red channels, which are detected by **PMT2** with bandpass filters **F2** (F37-547, AHF Analysentechnik) for the green channel and **F3** (F76-594, AHF Analysentechnik) for the red channel. For second harmonic generation (SHG) detection, the backscattered signal is also collected by **PMT2**.

To synchronize the two laser beams in time and space at the sample **S**, an optical delay line **OD** is used in the 780 nm beam path. This delay line consists of four mirrors **M** mounted on a translation stage, which also enables sum-frequency generation at 443 nm and ensures proper calibration of both detectors for simultaneous use.

S1.B Electronical Setup

For electronic signal processing, all three photomultiplier tubes (PMTs) and the resonant galvanometer scanner, **Galvo 1**, are controlled using ThorImage Software. The fluorescence signals captured by **PMT1** and **PMT2** are routed into a Lock-in amplifier (UHFLI, Zurich Instruments) through two T-junctions. The internal photodiode of the laser serves as the reference signal for the Lock-in amplifier. The demodulation data is then processed in LabOne Software and output via the auxiliary outputs. A data acquisition (DAQ) card (PCIe-6323, National Instruments) collects the data, which is subsequently processed using a custom MATLAB script implementing the tracking algorithms. The piezoelectric stage (Nano-LPS, Mad City Labs) is placed on the microscope and controlled with two separate Matlab scripts. One is responsible for the Z-displacement and is controlled via the analog output signal of the DAQ card and receives the current position through the sensor port of the piezostage. The software that changes the XY position of the stage is controlled with a USB-DAQ card (USB-6002, National Instruments) and also receives the current position.

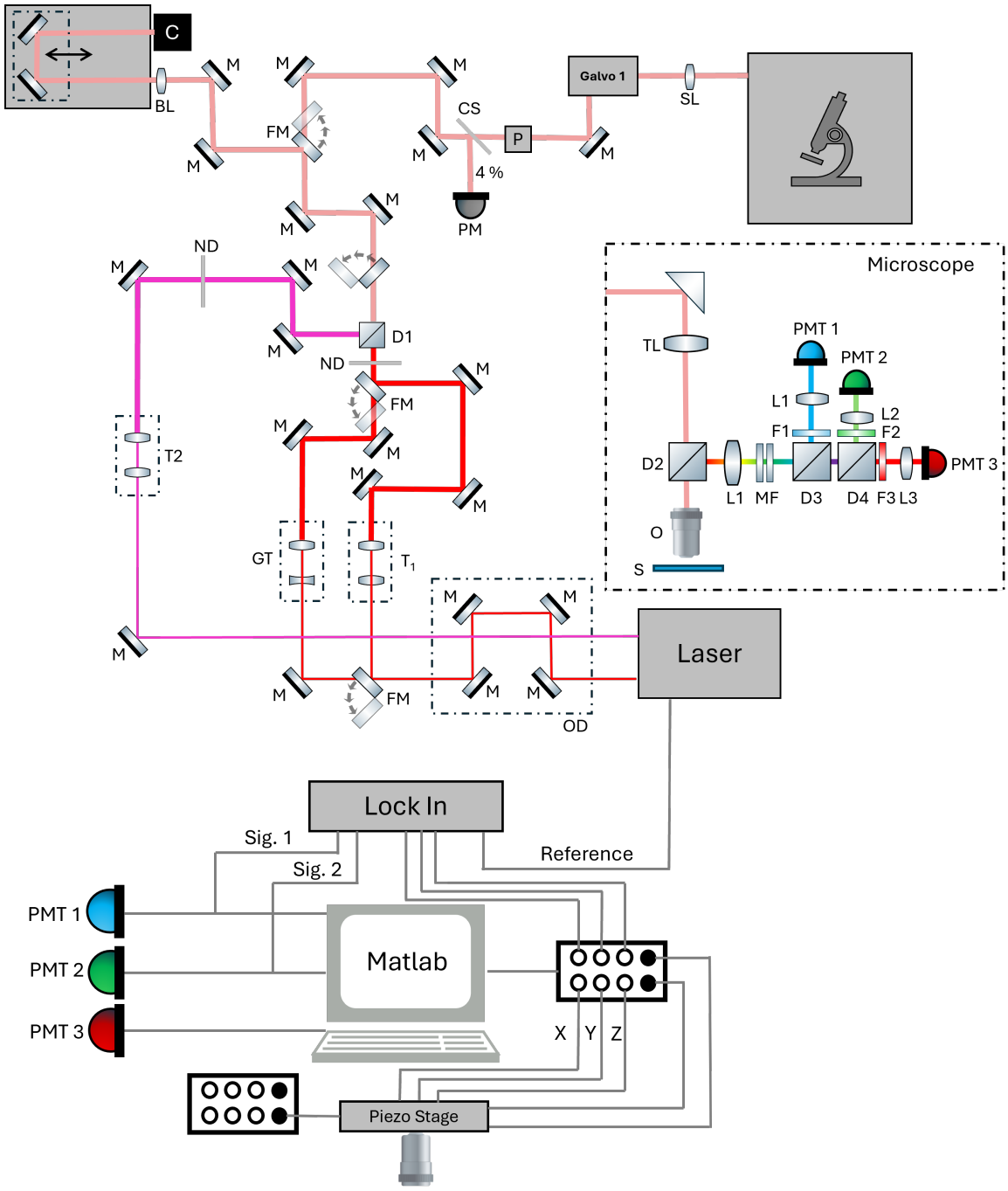

Figure 1. Optical Setup for the tracking and fluorescence lifetime imaging measurements: The abbreviations are standing for M: Mirror, D: Dichroic, OD: Optical Delayline, FM: Flip Mirror, T: Telescope, GT: Galilean Telescope, ND: Neutral Density Filter, PM: Power Meter, C: Camera, CS: Coverslip, SL: Scan Lens, TL: Tube Lens, O: Objective, S: Sample, MF: Multiphoton Filer, L: Lens, F: Filter, PMT: Photomultiplier

S2 Axial PSF-Shift

We simulated the point spread function (PSF) shift using the ABCD matrix for gaussian beams to identify optimal telescope settings (such as focal length and distance to the tube lens) for achieving the desired displacements, as illustrated in **Figure 2 - b**. To validate our simulations, we conducted PSF measurements on fluorescent nanobeads. The results for the initial setup without the Galilean telescope are presented in **Figure 2 - f**, followed by the PSF shifts observed for both the 60x and 100x objectives under three different conditions.

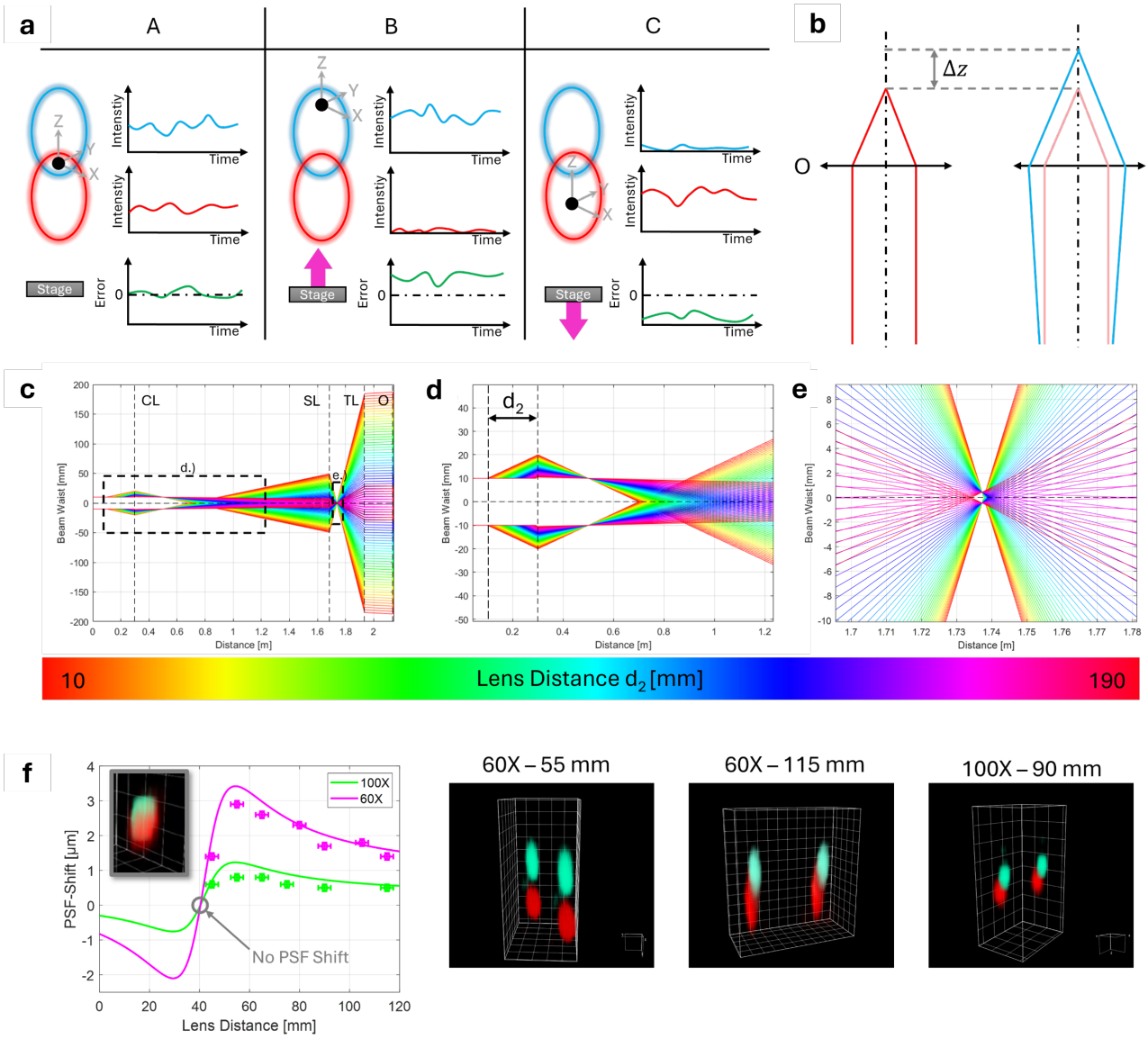

Figure 2. Axial PSF-Shift to create an axial error signal and track single particles: **a** Basic principle of the SEMPA-Track technique. The tracking-algorithm keeps the particle in the overlap region **A** so that the difference signal is zero. This point is referred to as the tracking point. When the particle is moving up (**B**) the difference signal is positive and the stage needs to drive up until it reaches again state **A**. In **C** the opposite situation is displayed. By creating a diverging beam in the backfocal aperture (**b**) the axial position of the PSF can be shifted. In **c** the simulations are shown for the complete system. In **d** and **e** the insets of **c** are displayed, where d_2 referes to the distance between the diverging lens and the collecting lens. The simulation results along with the experimental data are shown in **f**. CL: collecting lens, SL: scan lens, TL: tube lens, O: objective

S3 Tracking with Known Path

The initial XYZ-tracking measurements test the tracking algorithm for the 60x objective. First, a target particle is selected, then the tracking via a nanopositioning unit is activated. Last the microscope's built-in sample stage is used to displace the particle along the defined way. With this experiment both algorithms, can tested separately and jointly for optimization purposes. The final results are illustrated in **Figure 3**. For the videos of the tracking please see **SM5**.

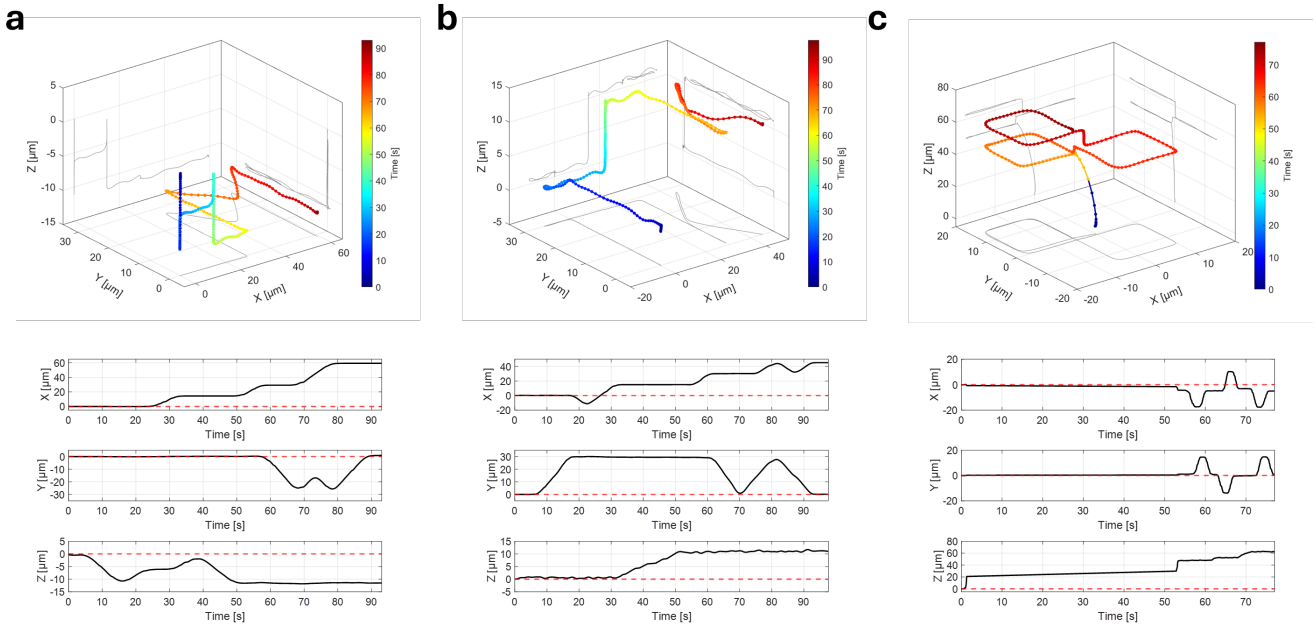

Figure 3. Tracking of nanoparticles for a predefined way. In **a** the two letters H and M, are tracked which are orthogonal to each other, i.e. one vertically aligned and the other horizontally. Underneath the 3D-trajectory the displacement of the piezoelectric stage in the X-,Y- and Z-direction is shown. In **b** again to initials were tracked but with a stronger focus on the Z-detection algorithm. In **c** a more complex pattern was used.

S4 FCS Experiments

Here we show the obtained FCS results (**Figure 4**). We were using a Zeiss LSM980 microsocpe together with PyCorrFit. The structure parameter was measured on a 10 nM Cy3 solution and resulted in 5.7.

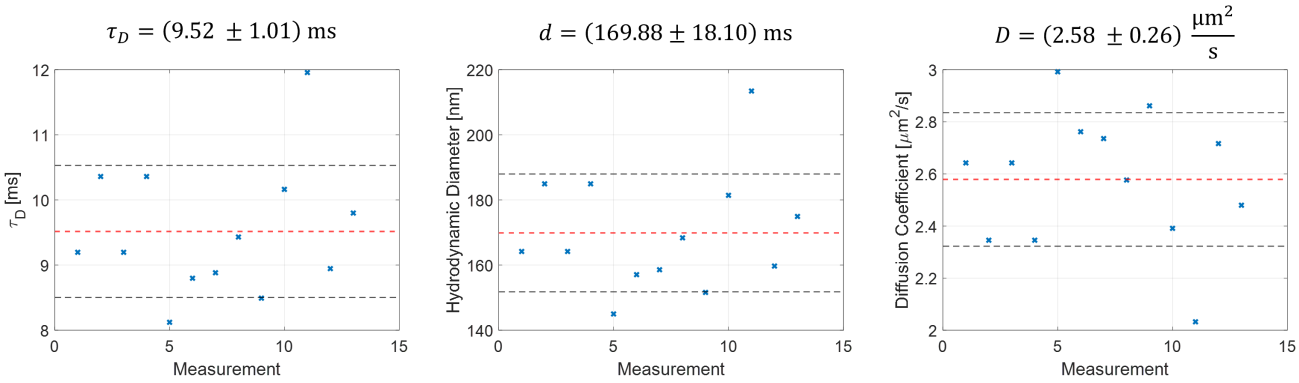

Figure 4. Results of the FCS experiments: We present the resulting diffusion times τ_D, hydrodynamic radii d, and diffusion coefficients D for pure distilled water.

S5 mRNA loaded Lipid Nanoparticles

As a biological application, we tracked lipid nanoparticles (LNPs) delivering mRNA into HuH7 cells. The cells were seeded on a patterned slide and transfected with Cy3-labeled mRNA encapsulated in LNPs, while a fluorescein solution served as a counterstain. Cell nuclei were stained with Höchst dye, providing a reference point for particle tracking. For the videos of the tracking please see **SM1 - SM3**.

In addition to the results presented in the main manuscript, further insights can be derived from the trajectories, such as the distance between the particles and the nuclei. Notably, in row **B** of **Figure 5 i** and **l**, the movement of the cells around the nuclei is clearly observable. Assuming a nucleus diameter of approximately 10 µm, the LNPs are expected to approach the nuclear membrane within about 5 µm from its center. The stage positions are displayed alongside the 2D tracks, with a color code indicating depth. Additionally, the mean square displacement (MSD) tracks are visualized separately in **Figure 5**.

After approximately 1.5 h two 2 h, we observed diffusing Cy3 accumulating near the cell nucleus **Figure 6**.

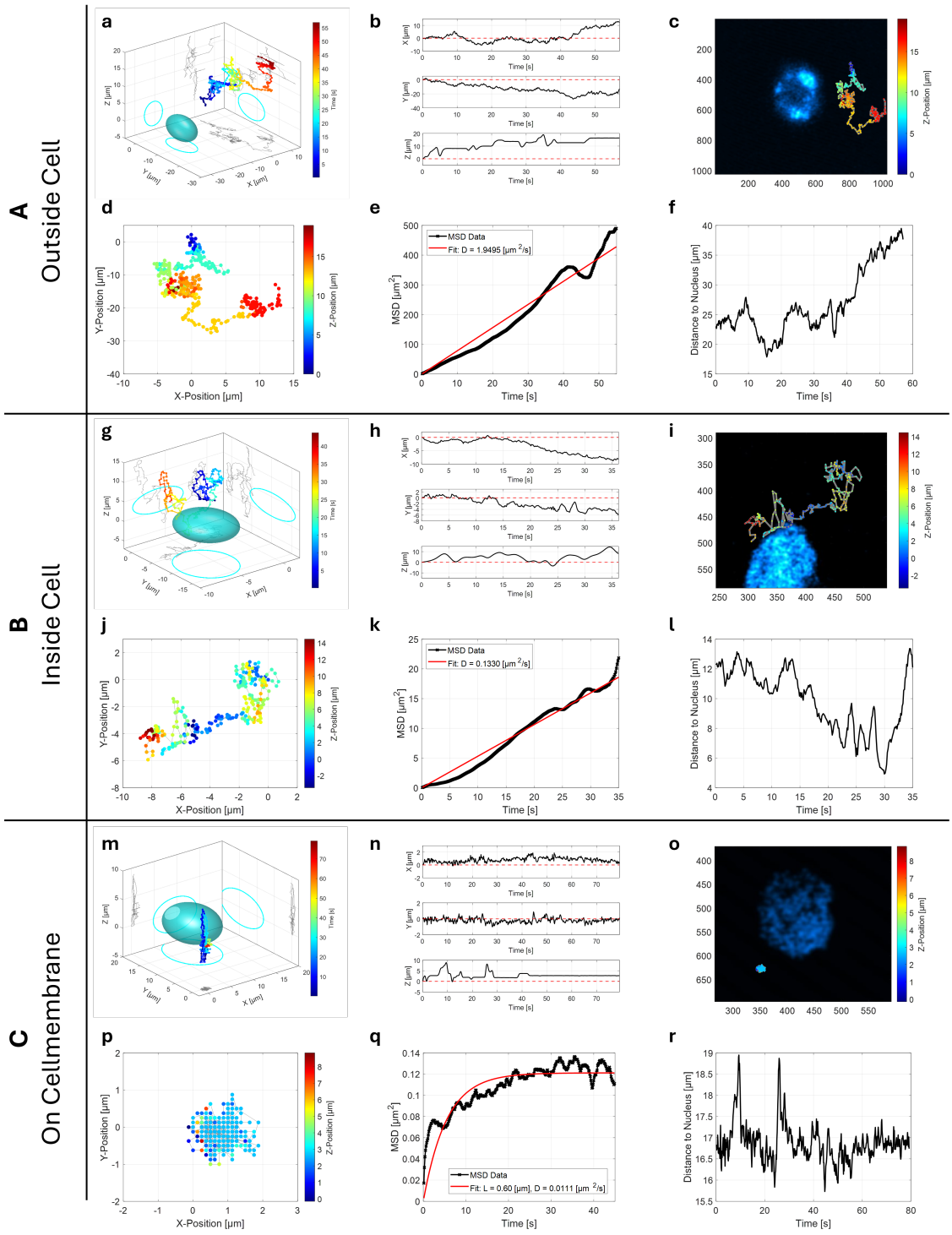

Figure 5. Tracking Results for Lipid Nanoparticle inside and outside of HuH7 Cells. In **A** a trajectory of a single lipid nanoparticle moving on the outside of the cell is shown. In **a** a trajectory along with the nucleus (cyan) is plotted along with the X-,Y- and Z-Position in **b** is shown. Further in **c** the first image of the track with the depth-color coded trajectory is shown and in **d** extracted. The MSD of the track is calculated and fitted in **e**. The distance from the nucleus to the particle is shown in **f**. The same informations are shown for a LNP inside a cell in **B**. Here the MSD shows a significant smaller diffusion coefficient and supports the statement that the LNP is in the higher viscous cytosol. In **C** the track for a LNP is shown that is trapped on the outside or the inside of the cell.

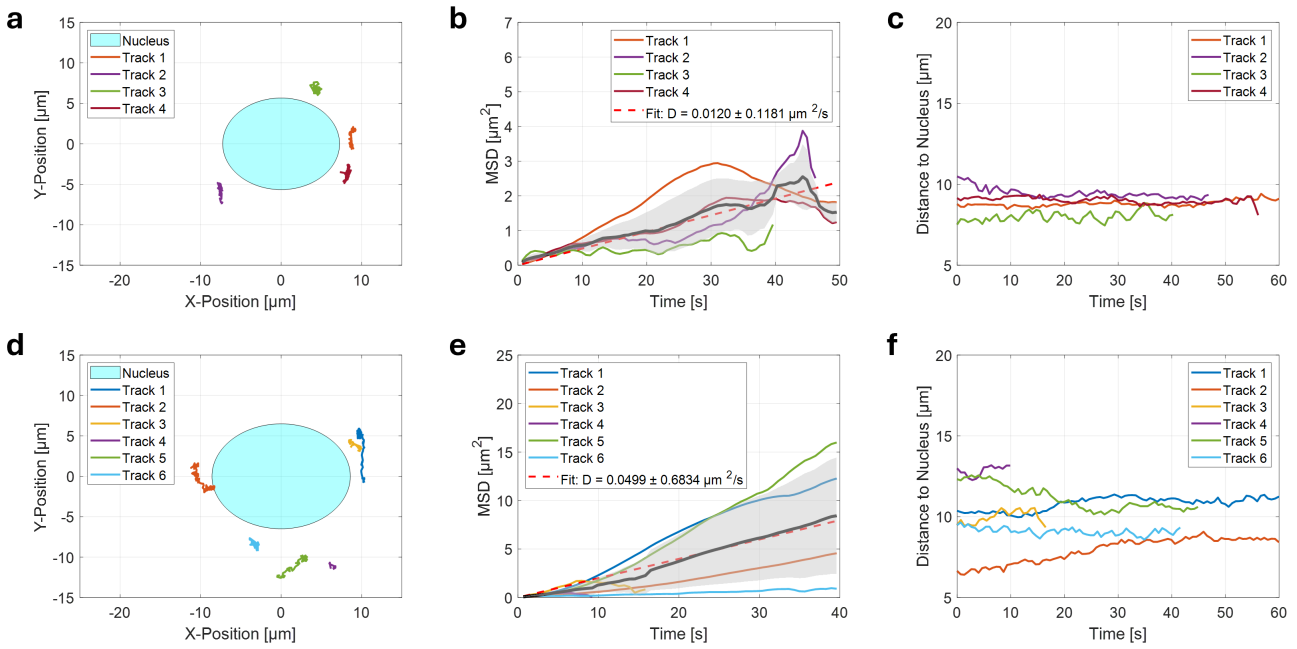

Figure 6. Slow Diffusion of LNP near the Nucleus after 1-2 h of the transfection process. In **a** the 2D trajectories in relation to the nucleus is shown. The MSD tracks of the single particles as well as the average (black curve) and its fit (red dashed line) is represented. The distance between the nucleus and the particles are displayed in **c**. For another measurement the same evaluations are shown in **d**, **e** and **f**

.

S6 XY-Tracking Algorithm

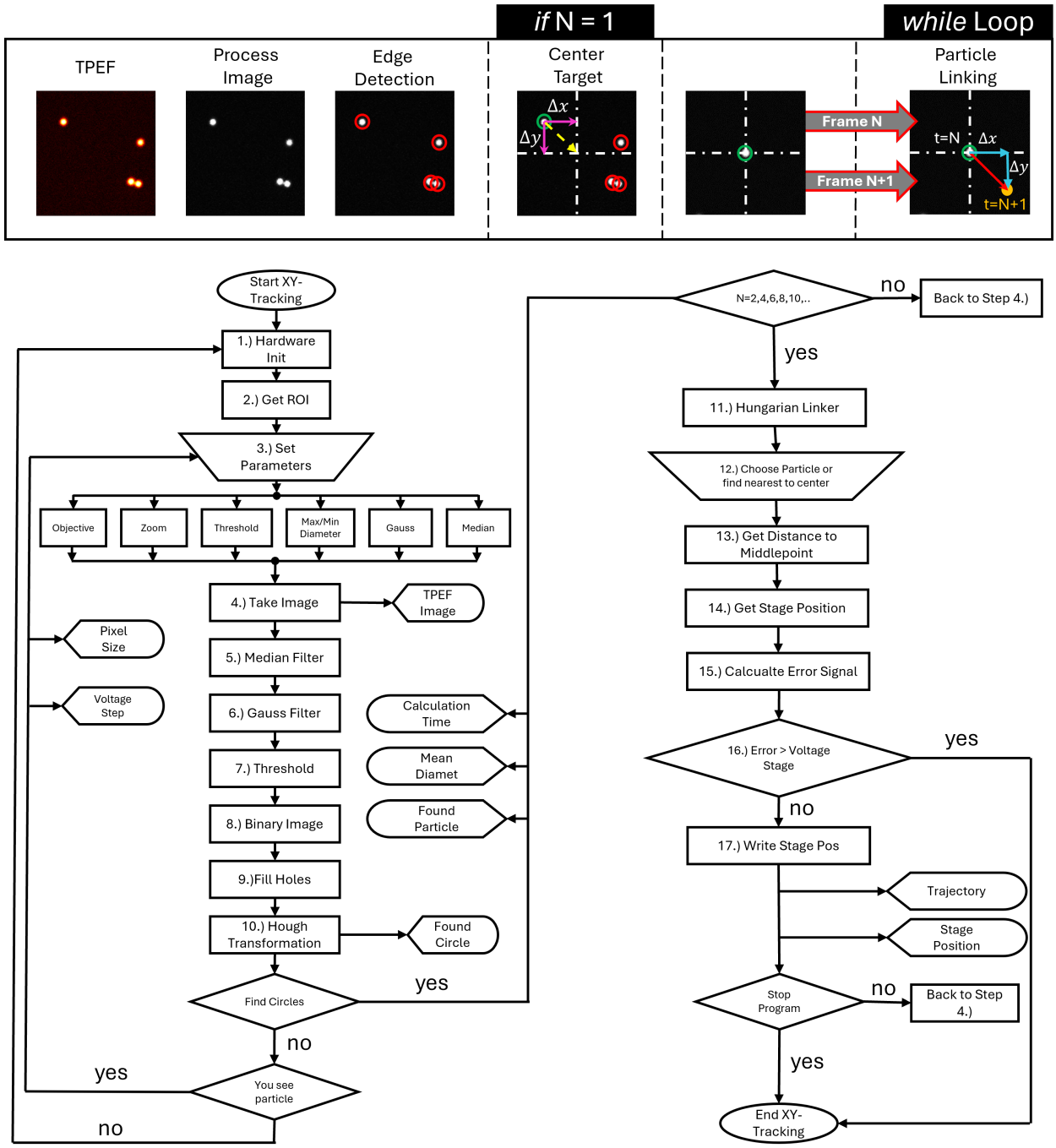

Figure 7. Graphical representation of XY-tracking and its algorithm flowchart. At the top, the graphical representation of the XY-algorithm is shown. It begins by capturing a TPEF image, which is then analyzed through background correction, filtering, and other processes until a Hough transformation detects the circles. If it is the first image, a target particle is selected and moved to the center of the frame. For each subsequent image (N and N+1), the displacement is calculated using a Hungarian linker, and the piezoelectric stage adjusts its position to return the particle to the center. Below, the flowchart with all individual steps is displayed.

S7 Z-Tracking Algorithm

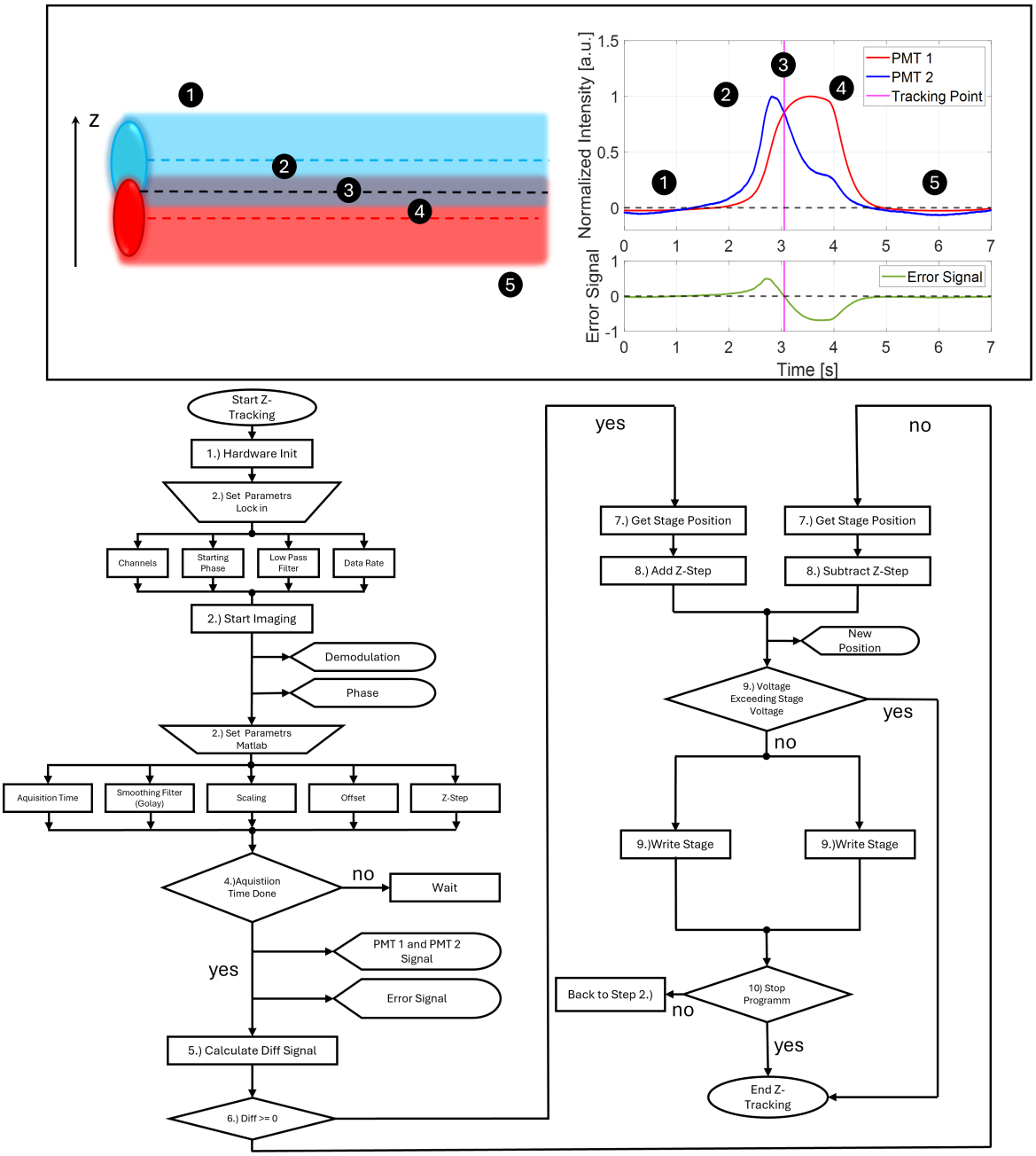

Figure 8. Graphical representation of the Z-tracking algorithm and its flowchart. At the top, the schematic working principle is shown, along with a real signal on the right. The tracking point and the areas where the algorithm decides whether to move up or down are indicated. Below this, the flowchart of the algorithm is displayed.

S8 Literature Research

To compare our technique with other tracking approaches, we conducted an extensive literature review. Building on the comprehensive analysis by[1], we extended their table with additional parameters and updated information. We also created **Figure** 9 to categorize and visualize various techniques systematically.

Single Particle Tracking (SPT) methods can broadly be classified into active and passive techniques. Active SPT methods employ feedback loops to maintain a specific particle within the observation volume, while passive methods rely on post-processing of acquired data to extract as much information as possible. Passive methods are typically applied in 2D tracking or for small Z-direction movements, where the axial position is inferred using optical aberrations that encode the Z-position based on their intensity.

Since our technique falls under the category of active SPT, we focus on this branch of the classification. Within active SPT, techniques can be further divided into trajectory-based and image-based approaches. As the names suggest, trajectory-based techniques track the movement path of a single particle over time, while image-based techniques rapidly capture images to localize the particle's XY-position and incorporate strategies to determine its Z-position, enabling real-time tracking of its movement.

Trajectory-based methods can be further subdivided based on how feedback is achieved, either through modified excitation or modified detection. While some techniques can also acquire images at specific time intervals, classifying them can sometimes be ambiguous, as differing criteria may lead to varying interpretations. Our classification approach aims to provide clarity while acknowledging the inherent overlap between certain methods.

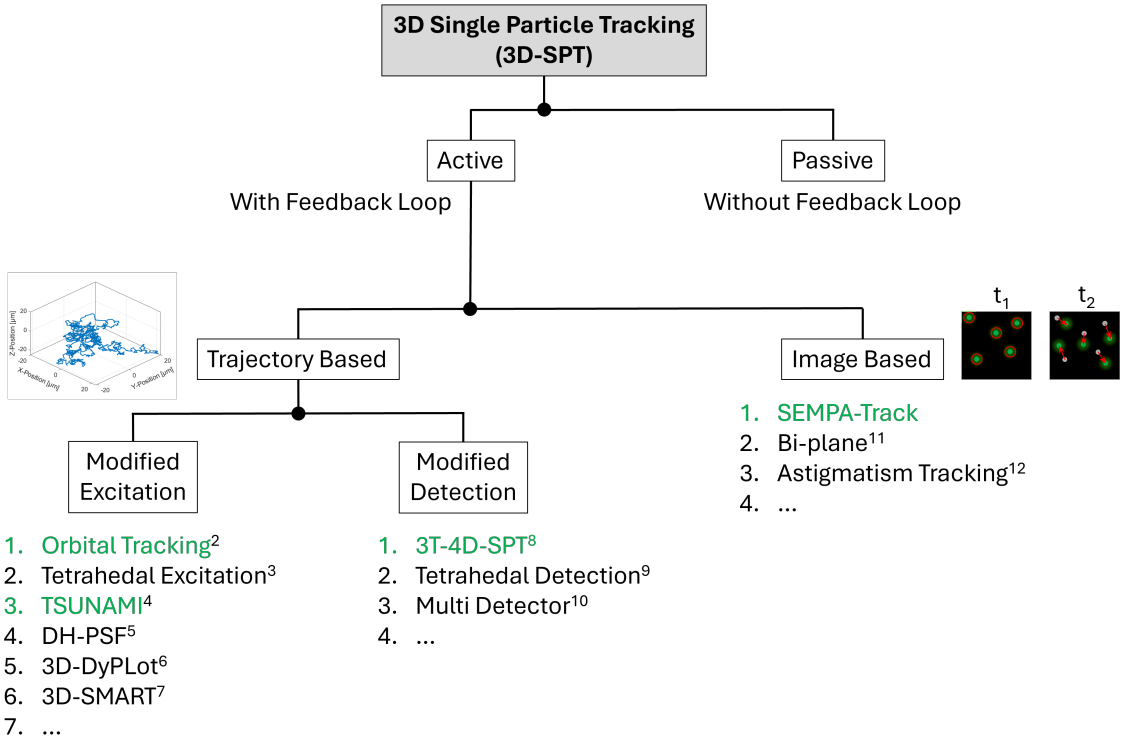

Figure 9. Classification of Different Tracking Mechanism: The figure categorizes 3D SPT techniques, with a focus on active methods incorporating feedback loops. Examples of trajectory-based techniques using modified excitation are listed, with references provided in the same order[2–7]. Techniques employing modified detection are also shown, with corresponding references available here[8–10]. Our SEMPA-Track approach is classified under image-based tracking methods, highlighting its place among various methodologies[11,12]. The with green marked methods represents where next to the trajectory also the fluorescence lifetime is detected.

Author	Akronym	Year	Diffusion-coefficient [$\mu m^2/s$]	Track Duration [s]	Imaging	FLIM	Trajectory	Sample System	Excitation
Thomas Hellerer	SEMPA-Track	2024	2.61	34.59	✓	✓	✓	Beads (160 nm), LNP	2P
Hideo Mabuchi[13]	Orbital Tracking	2007	20.0	20.0	X	X	✓	CdSe/ZnS quantum	1P
Giuseppe Vicidomini[8]	RT-4D-SPT	2024	11.51, 2.07	N.A, 120	X	✓	✓	Beads, Lysosomes	1P
Joerg Bewersdorf[14]	bi-plane	2010	2.4	3	✓	X	✓	Beads (200 nm)	1P
Kevin Welsher[6]	3D-DyPLoT	2017	8.9	30	X	X	✓	Beads, Quantum Dots, Virions	1P
Lloyd M. Davis[3]	Tetrahedral excitation	2014	12.2	0.078	X	X	✓	Beads (40 nm)	1P
Andrew K. Dunn[15]	TSUNAMI	2015	7.5, 2.1	N.A, 7	✓	✓	✓	Beads (100 nm), EGFR complexes	2P
James H. Werner[16,17]	Tetrahedral Detection	2008-2010	3	0.3	X	✓	✓	Quantum dots	1P
William E. Mörner[5]	DH-PSF	2010	0.04	10	X	X	✓	mRNP	1P
Don. C. Lamb[2]	3D Orbital Tracking	2023	1, 2	40, N.A.	X	✓	✓	Beads, dsDNA Oligos	1P
Kevin Welsher[7]	3D-SMART	2020	2.44	500	X	X	✓	dsDNA, RNA, Fluorophores	1P
Johan Elf[18]	—	2023	4.81, 10	0.7, N.A	X	X	✓	Beads, Trigger Factor protein	1P
Enrico Gratton[19]	—	2005	0.03	N.A	X (DIC each 15 s)	X	✓	Beads (500 nm)	2P
François Marquier[20]	3D-Red Shot	2023	1.07	85	X	X	✓	Nanocrystals	2P

S9 Description to movie SM1

Here we show a LNP moving on the outside of the cell. On the left, the 3D display is presented, while on the right, the intensity images are displayed.

S10 Description to movie SM2

Here we show a LNP bond to the cellmembrane. On the left, the 3D display is presented, while on the right, the intensity images are displayed.

S11 Description to movie SM3

In this video, the movement of an LNP within a cell is shown. On the left, the 3D display is presented, while on the right, the intensity images are displayed. The tracking mechanism is clearly visible on the right, as we observe intensity fluctuations in the cell nucleus due to changes in axial position.

S12 Description to movie SM4

In this video, we see a 6.5 µm fluorescent lifetime standard bead freely diffusing in distilled water. The intensity timelaps is shown on the top left, while the bottom left displays the 3D trajectory data. On the right side, instead of intensity, the fluorescence lifetime of the bead is represented.

S13 Description to movie SM5

In this video we show the three displayed trajectorys of the predefined way.

S14 Description to movie SM6

In this video we show exemplary tracks of the free diffusing 170 nm particles in 0%, 10% and 25% glycerol solutions.

References

1. Hou, S., Johnson, C. & Welsher, K. Real-time 3d single particle tracking: towards active feedback single molecule spectroscopy in live cells. *Molecules* **24**, 2826, DOI: https://doi:10.3390/molecules24152826 (2019).
2. Mieskes, F., Ploetz, E., Wehnekamp, F., Rat, V. & Lamb, D. C. Multicolor 3d orbital tracking. *Small* **19**, 2204726, DOI: https://doi.org/10.1002/smll.202204726 (2023).
3. Germann, J. A. & Davis, L. M. Three-dimensional tracking of a single fluorescent nanoparticle using four-focus excitation in a confocal microscope. *Opt. express* **22**, 5641–5650, DOI: https://doi.org/10.1364/OE.22.005641 (2014).
4. Liu, Y.-L. *et al.* Segmentation of 3d trajectories acquired by tsunami microscope: an application to egfr trafficking. *Biophys. journal* **111**, 2214–2227, DOI: https://doi.org/10.1016/j.bpj.2016.09.041 (2016).
5. Thompson, M. A., Casolari, J. M., Badieirostami, M., Brown, P. O. & Moerner, W. Three-dimensional tracking of single mrna particles in saccharomyces cerevisiae using a double-helix point spread function. *Proc. Natl. Acad. Sci.* **107**, 17864–17871, DOI: https://doi.org/10.1073/pnas.1012868107 (2010).
6. Hou, S., Lang, X. & Welsher, K. Robust real-time 3d single-particle tracking using a dynamically moving laser spot. *Opt. Lett.* **42**, 2390–2393, DOI: https://doi.org/10.1364/OL.42.002390 (2017).
7. Hou, S., Exell, J. & Welsher, K. Real-time 3d single molecule tracking. *Nat. communications* **11**, 3607, DOI: https://doi.org/10.1038/s41467-020-17444-6 (2020).
8. Bucci, A. *et al.* 4d single-particle tracking with asynchronous read-out single-photon avalanche diode array detector. *Nat. Commun.* **15**, 6188, DOI: https://doi.org/10.1038/s41467-024-50512-9 (2024).
9. DeVore, M. *et al.* Note: Time-gated 3d single quantum dot tracking with simultaneous spinning disk imaging. *Rev. Sci. Instruments* **86**, DOI: https://doi.org/10.1063/1.4937477 (2015).
10. Cang, H., Montiel, D., Xu, C. S. & Yang, H. Observation of spectral anisotropy of gold nanoparticles. *The J. chemical physics* **129**, DOI: https://doi.org/10.1063/1.2958912 (2008).
11. Toprak, E., Balci, H., Blehm, B. H. & Selvin, P. R. Three-dimensional particle tracking via bifocal imaging. *Nano letters* **7**, 2043–2045, DOI: https://doi.org/10.1021/nl0709120 (2007).
12. Cierpka, C., Rossi, M., Segura, R. & Kähler, C. On the calibration of astigmatism particle tracking velocimetry for microflows. *Meas. Sci. Technol.* **22**, 015401 (2010).
13. McHale, K., Berglund, A. J. & Mabuchi, H. Quantum dot photon statistics measured by three-dimensional particle tracking. *Nano letters* **7**, 3535–3539 (2007).
14. Juette, M. F. & Bewersdorf, J. Three-dimensional tracking of single fluorescent particles with submillisecond temporal resolution. *Nano letters* **10**, 4657–4663, DOI: https://doi.org/10.1021/nl1028792 (2010).
15. Perillo, E. P. *et al.* Deep and high-resolution three-dimensional tracking of single particles using nonlinear and multiplexed illumination. *Nat. Commun.* **6**, 7874, DOI: https://doi.org/10.1038/ncomms8874 (2015).
16. Wells, N. P., Lessard, G. A. & Werner, J. H. Confocal, three-dimensional tracking of individual quantum dots in high-background environments. *Anal. chemistry* **80**, 9830–9834, DOI: https://doi.org/10.1021/ac8021899 (2008).
17. Wells, N. P. *et al.* Time-resolved three-dimensional molecular tracking in live cells. *Nano letters* **10**, 4732–4737, DOI: https://doi.org/10.1021/nl103247v (2010).
18. Amselem, E., Broadwater, B., Hävermark, T., Johansson, M. & Elf, J. Real-time single-molecule 3d tracking in e. coli based on cross-entropy minimization. *Nat. Commun.* **14**, 1336, DOI: https://doi.org/10.1038/s41467-023-36879-1 (2023).
19. Levi, V., Ruan, Q. & Gratton, E. 3-d particle tracking in a two-photon microscope: application to the study of molecular dynamics in cells. *Biophys. journal* **88**, 2919–2928, DOI: https://doi.org/10.1529/biophysj.104.044230 (2005).
20. Semmer, F. *et al.* 3d real-time two-photon microscopy device for single-particle holographic tracking (3d-red shot). *ACS photonics* **10**, 3426–3434, DOI: https://doi.org/10.1021/acsphotonics.3c00949 (2023).

Appendix C

Microscopy Setup

C.1 Optical Setup

The optical setup for SUPER-FLIM and SEMPA-Track was described in the corresponding publications and is shown in **Figure C.2**. The main components in regard to the electronical and optical components will be listed in the following tables and displayed in **Figure C.1**.

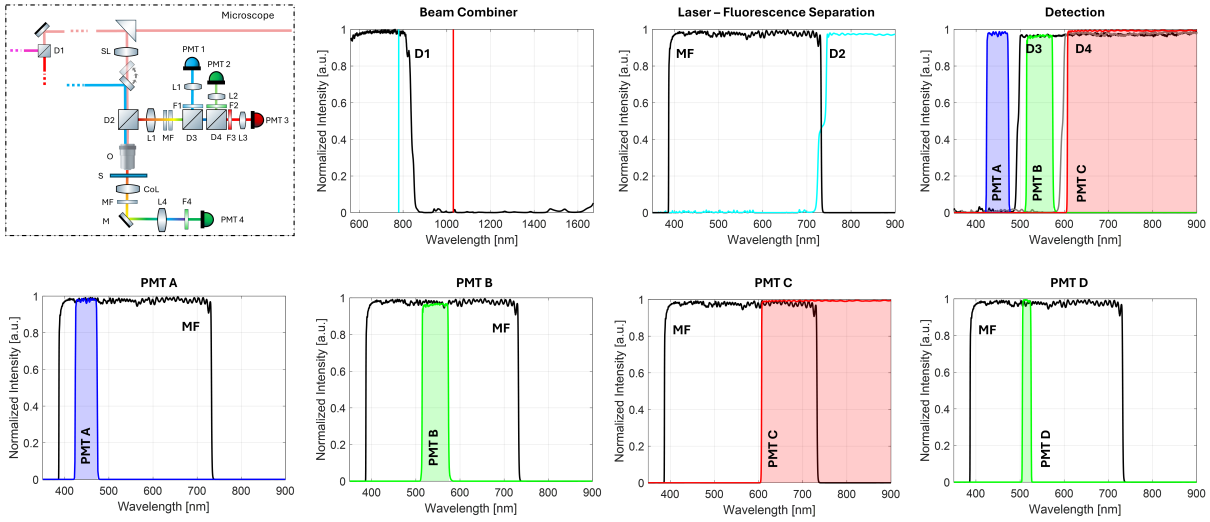

Figure C.1: Used Dichroic Mirrors and Fluorescence Filter: In this graphic the spectra of the different used filters are shown. Beginning from the beam combination to the separation of the laser light and the fluorescence. Finally the individual detections are shown for PMT A, PMT B and PMT C.

At first the different dichroic mirrors and filters are listed in **Table C.1**:

For the different techniques we can choose between four different multiphoton capable objective lenses. The used objectives are listed in **Table C.2**:

Table C.1: Used Dichroic Mirrors and Fluorescence Filters.

Filter	Company	Article Number	Type	Transmission	Reflection
D1	AHF	F38-825	Dichroic Mirror	565 - 800 nm > 90%	830 - 1200 nm > 96%
D2	AHF	F76-735	Dichroic Mirror	750 - 1600 nm > 90%	350 - 720 nm > 98%
D2*	AHF	F48-504	Dichroic Mirror	508 - 750 nm > 90%	380-500 nm > 90%
D2**	AHF	F38-538	Dichroic Mirror	547,7 - 950 nm > 90%	350 - 528,4 nm > 90%
D3	AHF	F38-495	Dichroic Mirror	503 - 950 nm > 93%	350 - 487.5 nm > 98%
D4	AHF	F38-593	Dichroic Mirror	601 - 950 nm > 93%	350 - 585 nm > 98%
MF	AHF	F39-745	Bandpass	392 - 725 nm > 93%	
F1	AHF	F34-450A	Bandpass	425 -475 nm $\geq$ 90%	
F2	AHF	F37-547	Bandpass	517.5 - 572.5 nm > 90%	
F3	AHF	F76-594	Longpass	610.6 - 900 nm > 93%	
F4	Omega	RPB500-530	Bandpass	500 - 530 nm 90%	
PB	AHF	F68-516	Pentaband		405, 442, 445, 514, 561, 640 nm

Table C.2: Used Objectives in this thesis. NA = Numerical Aperture, WD = Working Distance, BFP = Backfocal Aperture.

Magnification	Objective	Article Number	NA	WD [mm]	BFP [mm]	Immersion
20x	CFI Apo LWD Lambda S 20XC Wi	MRD77200	0.95	0.9 - 0.99	20	Water
40x	CFI Apo LWD Lambda S 40XC WI	MRD77410	1.15	0.61 - 0.59	12.5	Water
60x	CFI Plan APO 60XC Wi	MRD07650	1.27	0.18 - 0.16	10	Water
100x	CFI Apo TIRF 100XC Oil	MRD01991	1.49	0.16 -0.09	8	Oil

The complete setup with all beam paths and all possible microscopy techniques which were measured and tested in this thesis are shown in **Figure C.2**.

C.1.1 Nyquist criteria

For all measurements care was taken to work in agreement with the Nyquist criteria. By fulfilling this criteria artifact-free images can be generated [215, 216].

The Nyquist criteria in the XY-Direction for a multiphoton process is taken from [216] and is calculated like **Equation C.1**:

$$Nyquist_{XY} = \frac{0.541\lambda_{Exc}}{\sqrt{n}NA^{0.91}} \tag{C.1}$$

With the numerical aperture NA, the excitation wavelength λ_{Exc} (here 1030 nm) and the order of the multiphoton process n (here 2). The results are therefore depended on the used objective. Due to the use of a resonant scanner only specific zoom steps can be used. The results are shown in **Figure C.3** and are also summarized in the **Table C.3**:

Table C.3: In this table the Nyquist parameters for the different objectives are shown. The zoom factor represents at which factor the criteria is fulfilled.

Objective	20x	40x	60x	100x
NA	0.95	1.15	1.27	1.49
Nyquist Z [µm]	0.65	0.393	0.280	0.207
Nyquist XY [µm]	0.413	0.347	0.317	0.274
Zoom Factor 1024 x 1024	2	2	0.6	0.6
Zoom Factor 2048 x 2048	1	0.6	0.6	0.6

C.2 Electronical Setup

C.2.1 2P-Imaging

The TPEFM setup used in this work is based on the Thorlabs Multiphoton Essential Kit, which has been further modified. Currently, it consists of four PMTs, a resonant galvo-scanner operating at 8 kHz, and a galvo-scanner (Saturn 5B, Edmund Optics). Image acquisition and analysis are performed using a computer, referred to as the "ThorImage PC", which is equipped with an NI PCIe-6321 card and an AlazarTech ATS9440 card (see **Figure C.4**).

The DAQ card from NI is responsible for controlling the resonant galvo-scanner and generating the associated triggers (Frame, Line, and Pixel). The Alazar card is used to capture the PMT signals at a sampling rate of 80 MHz. The electronics for controlling and supplying power to the PMTs are housed in the **E**lectronic **C**ontrol **U**nit (ECU), which also contains the electronics for the resonant galvo-scanner. The ECU provides access to

individual triggers via its back panel. If third-party components need to be integrated, a breakout box must be inserted between the ThorImage PC and the ECU.

Currently, the setup employs two USB-PMTs and two PMTs with external **T**rans**i**mpedance **A**mplifier (TIA)s. For the latter, higher voltages are required, which are supplied by the ECU. It should be noted that the TIAs are not optimized for 80 MHz (designed for 60 MHz) operation and are therefore suboptimal for this setup. They will need to be replaced in the future.

Imaging is performed using the ThorImage software, which controls the resonant galvo-scanner based on user-defined parameters and adjusts the gain for the different PMTs. Images can be recorded individually, as part of a time series, or in streaming mode, fully leveraging the system's video-rate imaging capabilities.

C.2.2 Resonant Imaging with the Lock-In Amplifier

To record images using the lock-in amplifier and the resonant scanner system, certain modifications are required. This setup is necessary, for example, when the signal-to-noise ratio (SNR) needs improvement or when performing SUPER-FLIM. In summary, this configuration allows either the simultaneous acquisition of two lifetime images without a phasor plot or the use of a single detector for lifetime detection with the phasor plot.

To implement this setup, connect the **B**ayonet **N**eill **C**oncelman (BNC) output of the PMT to the input of the lock-in amplifier. The reference signal from the laser should be fed into the reference input of the lock-in amplifier. In the LabOne software, ensure that the appropriate demodulator is selected. If necessary, adjust the input level to detect the reference signal, as it is essential for demodulating the PMT signal.

The demodulated signals G (0°) and S (90°) are transmitted via the **Aux**iliary (AUX) outputs. Ensure that the amplification factor is the same for both channels. The AUX signals are then fed into the Alazar card, which is limited to an input range of 0 to 5 V. Take care not to exceed this voltage range. If the demodulated signal is negative—common for most PMT signals—it may need to be inverted.

Once this configuration is complete, the ThorImage software can be used as usual. For lifetime imaging, FCS, or 2P images, post-processing of the recorded images will be required. The schematic for this process is displayed in **Figure C.5**.

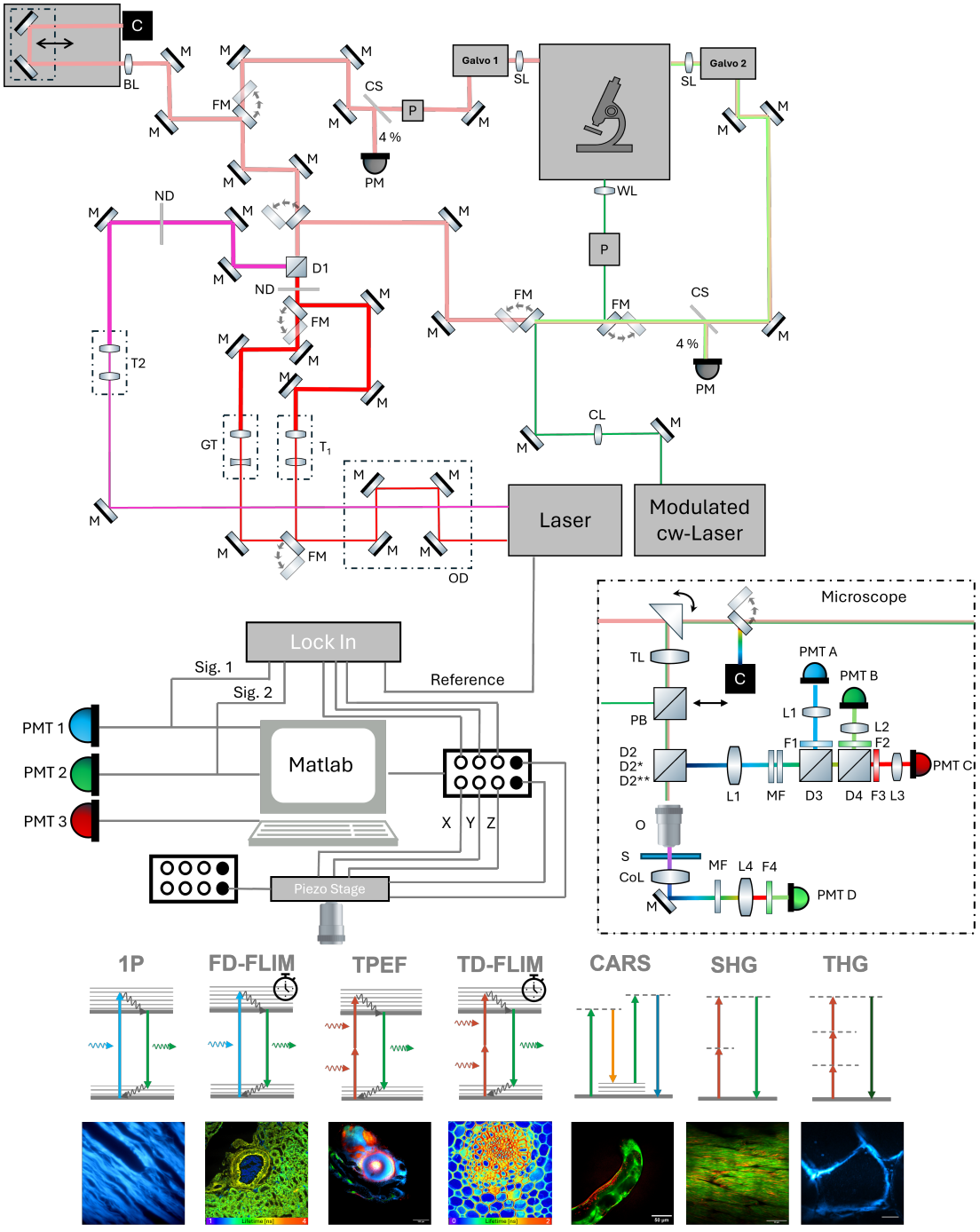

Figure C.2: Optical Setup for the Tracking and Fluorescence Lifetime Imaging Measurements: The abbreviations are standing for M: Mirror, D: Dichroic, OD: Optical Delayline, FM: Flip Mirror, T: Telescope, GT: Galilean Telescope, ND: Neutral Density Filter, PM: Power Meter, C: Camera, P: Periscope, CS: Coverslip, SL: Scan Lens, TL: Tube Lens, O: Objective, S: Sample, MF: Multiphoton Filer, WL: Wide-field Lens, PB: Pentaband Filter, L: Lens, F: Filter, CL: Collimation Lens, CoL: Condensor Lens, PMT: Photomultiplier

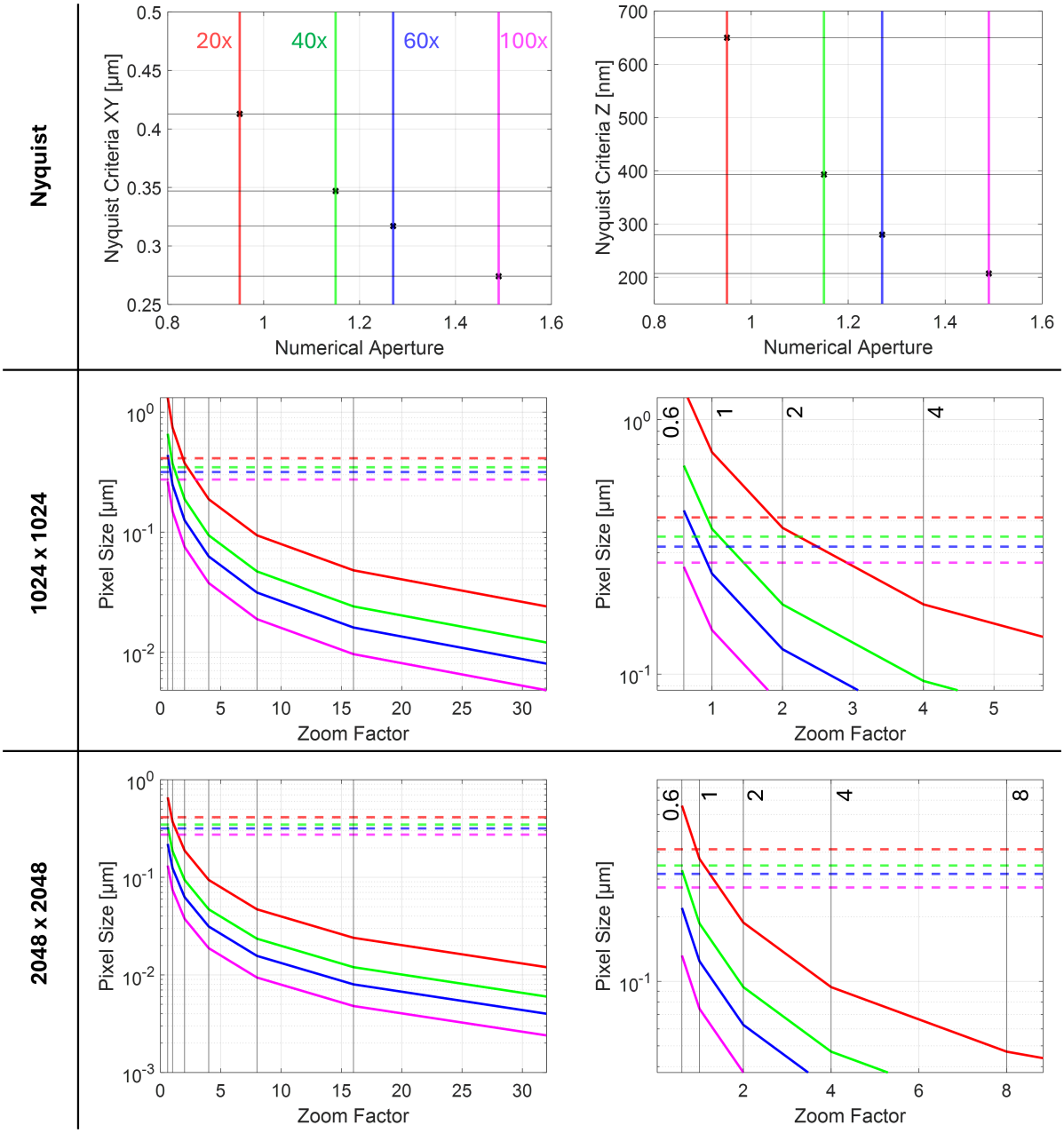

Figure C.3: Nyquist Criteria for the used Optical Setup: In the first row the pixel sizes are shown that fullfill the Nyquist criteria in the XY- and Z-direction for the four different used objectives. In the second row the pixel sizes for the imaging setup and the different objectives and zoom factors are presented with a zoomed figure on the right. This is done for a pixel number of 1024x1024 in the middle row and for 2048x2048 pixel in the last row.

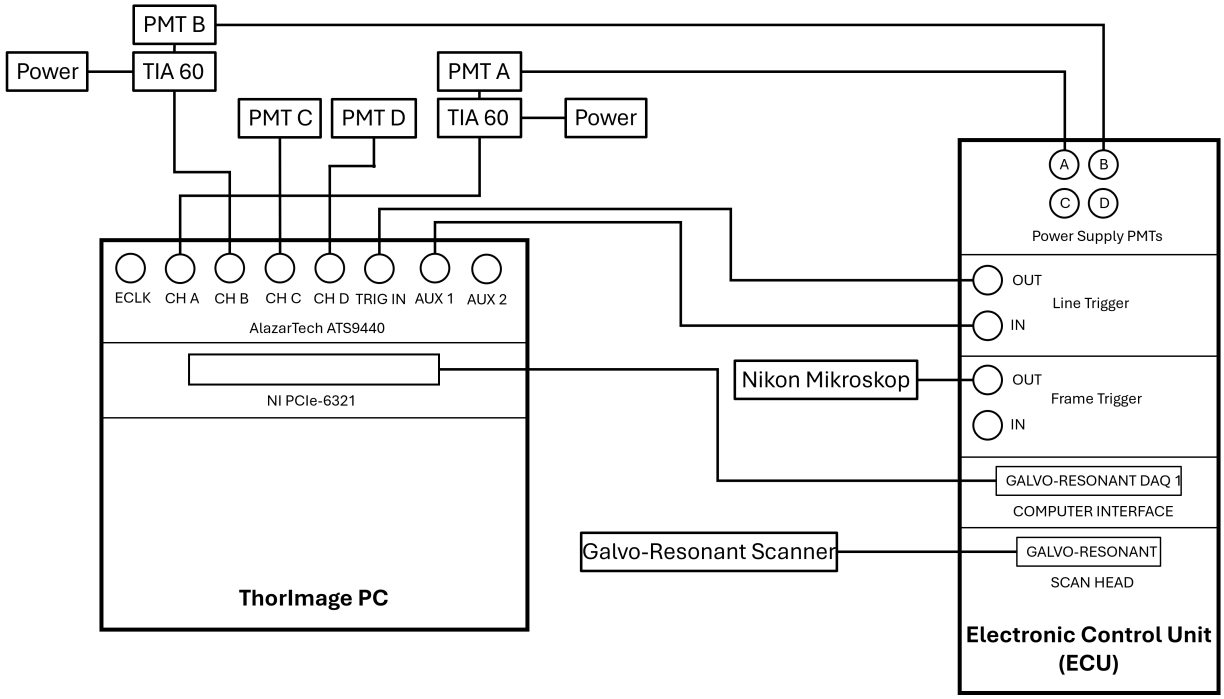

Figure C.4: Electornical Setup of the TPEFM System: Here the electronical setup of the TPEFM setup is shown. The Alazar card is used to detect the signal from the PMT signals as well as the trigger from the resonant galvo-scanner. The scanner is controlled with the ECU box that is also generating the power voltage for the PMTs.

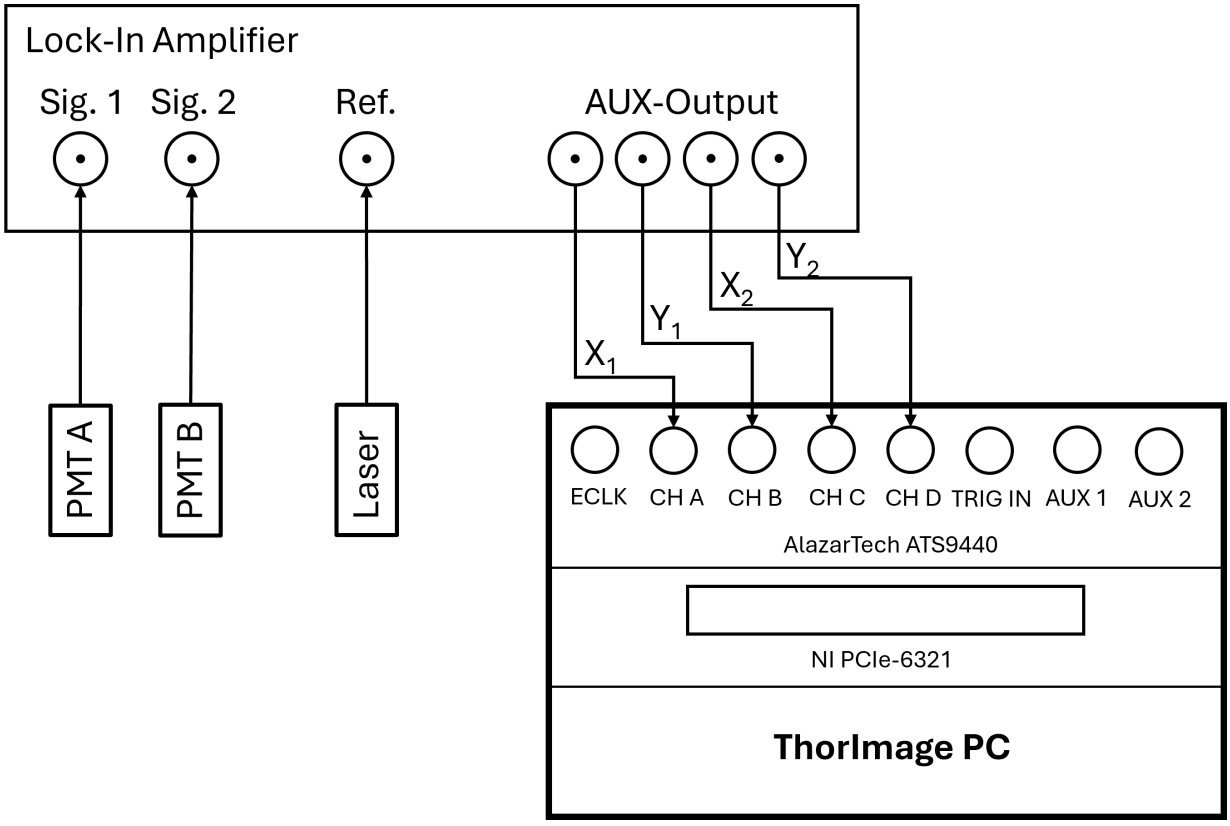

Figure C.5: Schematic Illustration of the Electronical Setup for SUPER-FLIM: As input for the lock-in amplifier the two PMTs are used together with the photodiode signal of the laser. The demodulation signals are transfered via the AUX-outputs and fed into the Alazar card. From here the signals are recorded with the ThorImage Software.

Bibliography

[1] L. Mockl and W. Moerner, "Super-resolution microscopy with single molecules in biology and beyond–essentials, current trends, and future challenges," *Journal of the American Chemical Society*, vol. 142, no. 42, pp. 17 828–17 844, 2020.

[2] L. Schermelleh, A. Ferrand, T. Huser, C. Eggeling, M. Sauer, O. Biehlmaier, and G. P. Drummen, "Super-resolution microscopy demystified," *Nature cell biology*, vol. 21, no. 1, pp. 72–84, 2019.

[3] J. C. Waters, "Accuracy and precision in quantitative fluorescence microscopy," *Journal of Cell Biology*, vol. 187, p. 1135–1148, 2009.

[4] P. R. Cullis and M. J. Hope, "Lipid nanoparticle systems for enabling gene therapies," *Molecular Therapy*, vol. 25, no. 7, pp. 1467–1475, 2017.

[5] L. Schoenmaker, D. Witzigmann, J. A. Kulkarni, R. Verbeke, G. Kersten, W. Jiskoot, and D. J. Crommelin, "mrna-lipid nanoparticle covid-19 vaccines: Structure and stability," *International journal of pharmaceutics*, vol. 601, p. 120586, 2021.

[6] E. Kon, N. Ad-El, I. Hazan-Halevy, L. Stotsky-Oterin, and D. Peer, "Targeting cancer with mrna–lipid nanoparticles: key considerations and future prospects," *Nature reviews clinical oncology*, vol. 20, no. 11, pp. 739–754, 2023.

[7] S. Kreiter, M. Diken, A. Selmi, Ö. Türeci, and U. Sahin, "Tumor vaccination using messenger rna: prospects of a future therapy," *Current opinion in immunology*, vol. 23, no. 3, pp. 399–406, 2011.

[8] J. D. Finn, A. R. Smith, M. C. Patel, L. Shaw, M. R. Youniss, J. van Heteren, T. Dirstine, C. Ciullo, R. Lescarbeau, J. Seitzer *et al.*, "A single administration of crispr/cas9 lipid nanoparticles achieves robust and persistent in vivo genome editing," *Cell reports*, vol. 22, no. 9, pp. 2227–2235, 2018.

[9] J. G. Rurik, I. Tombácz, A. Yadegari, P. O. Méndez Fernández, S. V. Shewale, L. Li, T. Kimura, O. Y. Soliman, T. E. Papp, Y. K. Tam *et al.*, "Car t cells produced in vivo to treat cardiac injury," *Science*, vol. 375, no. 6576, pp. 91–96, 2022.

[10] A. N. Kuhn, T. Beissert, P. Simon, B. Vallazza, J. Buck, B. P. Davies, O. Tureci, and U. Sahin, "mrna as a versatile tool for exogenous protein expression," *Current gene therapy*, vol. 12, no. 5, pp. 347–361, 2012.

[11] J. Gilleron, W. Querbes, A. Zeigerer, A. Borodovsky, G. Marsico, U. Schubert, K. Manygoats, S. Seifert, C. Andree, M. Stöter *et al.*, "Image-based analysis of lipid nanoparticle–mediated sirna delivery, intracellular trafficking and endosomal escape," *Nature biotechnology*, vol. 31, no. 7, pp. 638–646, 2013.

[12] A. Kamanzi, Y. Zhang, Y. Gu, F. Liu, R. Berti, B. Wang, F. Saadati, M. A. Ciufolini, J. Kulkarni, P. Cullis *et al.*, "Quantitative visualization of lipid nanoparticle fusion as a function of formulation and process parameters," *ACS nano*, vol. 18, no. 28, pp. 18 191–18 201, 2024.

[13] Y. Shav-Tal, R. H. Singer, and X. Darzacq, "Imaging gene expression in single living cells," *Nature Reviews Molecular Cell Biology*, vol. 5, no. 10, pp. 855–862, 2004.

[14] J. Kim, A. Jozic, Y. Lin, Y. Eygeris, E. Bloom, X. Tan, C. Acosta, K. D. MacDonald, K. D. Welsher, and G. Sahay, "Engineering lipid nanoparticles for enhanced intracellular delivery of mrna through inhalation," *ACS nano*, vol. 16, no. 9, pp. 14 792–14 806, 2022.

[15] M. O. Sonnaillon and F. J. Bonetto, "A low-cost, high-performance, digital signal processor-based lock-in amplifier capable of measuring multiple frequency sweeps simultaneously," *Review of Scientific Instruments*, vol. 76, no. 2, 2005.

[16] T. D. Nguyen, Y.-I. Chen, L. H. Chen, and H.-C. Yeh, "Recent advances in single-molecule tracking and imaging techniques," *Annual Review of Analytical Chemistry*, vol. 16, no. 1, pp. 253–284, 2023.

[17] S. Hou, C. Johnson, and K. Welsher, "Real-time 3d single particle tracking: towards active feedback single molecule spectroscopy in live cells," *Molecules*, vol. 24, no. 15, p. 2826, 2019.

[18] J. A. Müller, N. Schäffler, T. Kellerer, G. Schwake, T. S. Ligon, and J. O. Rädler, "Kinetics of rna-lnp delivery and protein expression," *European Journal of Pharmaceutics and Biopharmaceutics*, p. 114222, 2024.

[19] T. Kellerer, B. Sailer, P. Byers, R. Barnkob, O. Hayden, and T. Hellerer, "Two-photon microscopy of acoustofluidic trapping for highly sensitive cell analysis," *Lab on a Chip*, 2024.

[20] T. Kellerer, J. Janusch, C. Freymüller, A. Rühm, R. Sroka, and T. Hellerer, "Comprehensive investigation of parameters influencing fluorescence lifetime imaging microscopy in frequency-and time-domain illustrated by phasor plot analysis," *International Journal of Molecular Sciences*, vol. 23, no. 24, p. 15885, 2022.

[21] A. Coulter-Parkhill, S. McClean, V. A. Gault, and N. Irwin, "Therapeutic potential of peptides derived from animal venoms: current views and emerging drugs for diabetes," *Clinical Medicine Insights: Endocrinology and Diabetes*, vol. 14, p. 11795514211006071, 2021.

[22] O. Péterfi, F. Boda, Z. Szabó, E. Ferencz, and L. Bába, "Hypotensive snake venom components—a mini-review," *Molecules*, vol. 24, no. 15, p. 2778, 2019.

[23] S. P. Jackson and J. Bartek, "The dna-damage response in human biology and disease," *Nature*, vol. 461, no. 7267, pp. 1071–1078, 2009.

[24] B. K. Armstrong, "How sun exposure causes skin cancer: an epidemiological perspective," *Prevention of skin cancer*, pp. 89–116, 2004.

[25] S. Preston-Martin, M. C. Pike, R. K. Ross, P. A. Jones, and B. E. Henderson, "Increased cell division as a cause of human cancer," *Cancer research*, vol. 50, no. 23, pp. 7415–7421, 1990.

[26] V. Gambardella, N. Tarazona, J. M. Cejalvo, P. Lombardi, M. Huerta, S. Roselló, T. Fleitas, D. Roda, and A. Cervantes, "Personalized medicine: recent progress in cancer therapy," *Cancers*, vol. 12, no. 4, p. 1009, 2020.

[27] C. E. Dunbar, K. A. High, J. K. Joung, D. B. Kohn, K. Ozawa, and M. Sadelain, "Gene therapy comes of age," *Science*, vol. 359, no. 6372, p. eaan4672, 2018.

[28] F. Crick, "Central dogma of molecular biology," *Nature*, vol. 227, no. 5258, pp. 561–563, 1970.

[29] H. Yin, R. L. Kanasty, A. A. Eltoukhy, A. J. Vegas, J. R. Dorkin, and D. G. Anderson, "Non-viral vectors for gene-based therapy," *Nature reviews genetics*, vol. 15, no. 8, pp. 541–555, 2014.

[30] A. K. Varkouhi, M. Scholte, G. Storm, and H. J. Haisma, "Endosomal escape pathways for delivery of biologicals," *Journal of Controlled Release*, vol. 151, no. 3, pp. 220–228, 2011.

[31] S. Chatterjee, E. Kon, P. Sharma, and D. Peer, "Endosomal escape: A bottleneck for lnp-mediated therapeutics," *Proceedings of the National Academy of Sciences*, vol. 121, no. 11, p. e2307800120, 2024.

[32] M. R. Hunter, L. Cui, B. T. Porebski, S. Pereira, S. Sonzini, U. Odunze, P. Iyer, O. Engkvist, R. L. Lloyd, S. Peel *et al.*, "Understanding intracellular biology to improve mrna delivery by lipid nanoparticles," *Small methods*, vol. 7, no. 9, p. 2201695, 2023.

[33] C. Chen, C. Chen, Y. Li, R. Gu, and X. Yan, "Characterization of lipid-based nanomedicines at the single-particle level," *Fundamental Research*, vol. 3, no. 4, pp. 488–504, 2023.

[34] S. Patel, J. Kim, M. Herrera, A. Mukherjee, A. V. Kabanov, and G. Sahay, "Brief update on endocytosis of nanomedicines," *Advanced drug delivery reviews*, vol. 144, pp. 90–111, 2019.

[35] C. C. Miller, "The stokes-einstein law for diffusion in solution," *Proceedings of the Royal Society of London. Series A, Containing Papers of a Mathematical and Physical Character*, vol. 106, no. 740, pp. 724–749, 1924.

[36] C. Manzo and M. F. Garcia-Parajo, "A review of progress in single particle tracking: from methods to biophysical insights," *Reports on progress in physics*, vol. 78, no. 12, p. 124601, 2015.

[37] M. Kaksonen and A. Roux, "Mechanisms of clathrin-mediated endocytosis," *Nature reviews Molecular cell biology*, vol. 19, no. 5, pp. 313–326, 2018.

[38] C. Lorenz, M. Fotin-Mleczek, G. Roth, C. Becker, T. C. Dam, W. P. Verdurmen, R. Brock, J. Probst, and T. Schlake, "Protein expression from exogenous mrna: Uptake by receptor-mediated endocytosis and trafficking via the lysosomal pathway," *RNA biology*, vol. 8, no. 4, pp. 627–636, 2011.

[39] E. J. Sayers, S. E. Peel, A. Schantz, R. M. England, M. Beano, S. M. Bates, A. S. Desai, S. Puri, M. B. Ashford, and A. T. Jones, "Endocytic profiling of cancer cell models reveals critical factors influencing lnp-mediated mrna delivery and protein expression," *Molecular Therapy*, vol. 27, no. 11, pp. 1950–1962, 2019.

[40] M. J. Munson, G. O'Driscoll, A. M. Silva, E. Lázaro-Ibáñez, A. Gallud, J. T. Wilson, A. Collén, E. K. Esbjörner, and A. Sabirsh, "A high-throughput galectin-9 imaging assay for quantifying nanoparticle uptake, endosomal escape and functional rna delivery," *Communications biology*, vol. 4, no. 1, p. 211, 2021.

[41] G. Nawrocki, P.-h. Wang, I. Yu, Y. Sugita, and M. Feig, "Slow-down in diffusion in crowded protein solutions correlates with transient cluster formation," *The Journal of Physical Chemistry B*, vol. 121, no. 49, pp. 11 072–11 084, 2017.

[42] X. Hou, T. Zaks, R. Langer, and Y. Dong, "Lipid nanoparticles for mrna delivery," *Nature Reviews Materials*, vol. 6, no. 12, pp. 1078–1094, 2021.

[43] P. A. Vanlandingham and B. P. Ceresa, "Rab7 regulates late endocytic trafficking downstream of multivesicular body biogenesis and cargo sequestration," *Journal of Biological Chemistry*, vol. 284, no. 18, pp. 12 110–12 124, 2009.

[44] J. Shin, C. J. Douglas, S. Zhang, C. P. Seath, and H. Bao, "Targeting recycling endosomes to potentiate mrna lipid nanoparticles," *Nano Letters*, vol. 24, no. 17, pp. 5104–5109, 2024.

[45] L. M. Vermeulen, S. C. De Smedt, K. Remaut, and K. Braeckmans, "The proton sponge hypothesis: Fable or fact?" *European Journal of Pharmaceutics and Biopharmaceutics*, vol. 129, pp. 184–190, 2018.

[46] S. C. Semple, A. Akinc, J. Chen, A. P. Sandhu, B. L. Mui, C. K. Cho, D. W. Sah, D. Stebbing, E. J. Crosley, E. Yaworski *et al.*, "Rational design of cationic lipids for sirna delivery," *Nature biotechnology*, vol. 28, no. 2, pp. 172–176, 2010.

[47] N. Sonawane, F. C. Szoka, and A. Verkman, "Chloride accumulation and swelling in endosomes enhances dna transfer by polyamine-dna polyplexes," *Journal of Biological Chemistry*, vol. 278, no. 45, pp. 44 826–44 831, 2003.

[48] J. A. Kulkarni, M. M. Darjuan, J. E. Mercer, S. Chen, R. Van Der Meel, J. L. Thewalt, Y. Y. C. Tam, and P. R. Cullis, "On the formation and morphology of lipid nanoparticles containing ionizable cationic lipids and sirna," *ACS nano*, vol. 12, no. 5, pp. 4787–4795, 2018.

[49] G. Tesei, Y.-W. Hsiao, A. Dabkowska, G. Grönberg, M. Yanez Arteta, D. Ulkoski, D. J. Bray, M. Trulsson, J. Ulander, M. Lund *et al.*, "Lipid shape and packing are key for optimal design of ph-sensitive mrna lipid nanoparticles," *Proceedings of the National Academy of Sciences*, vol. 121, no. 2, p. e2311700120, 2024.

[50] J. Philipp, A. Dabkowska, A. Reiser, K. Frank, R. Krzysztoń, C. Brummer, B. Nickel, C. E. Blanchet, A. Sudarsan, M. Ibrahim *et al.*, "ph-dependent structural transitions in cationic ionizable lipid mesophases are critical for lipid nanoparticle function," *Proceedings of the National Academy of Sciences*, vol. 120, no. 50, p. e2310491120, 2023.

[51] A. Akinc, M. A. Maier, M. Manoharan, K. Fitzgerald, M. Jayaraman, S. Barros, S. Ansell, X. Du, M. J. Hope, T. D. Madden *et al.*, "The onpattro story and the clinical translation of nanomedicines containing nucleic acid-based drugs," *Nature nanotechnology*, vol. 14, no. 12, pp. 1084–1087, 2019.

[52] M. J. Evers, J. A. Kulkarni, R. van der Meel, P. R. Cullis, P. Vader, and R. M. Schiffelers, "State-of-the-art design and rapid-mixing production techniques of lipid nanoparticles for nucleic acid delivery," *Small methods*, vol. 2, no. 9, p. 1700375, 2018.

[53] J. A. Kulkarni, D. Witzigmann, J. Leung, Y. Y. C. Tam, and P. R. Cullis, "On the role of helper lipids in lipid nanoparticle formulations of sirna," *Nanoscale*, vol. 11, no. 45, pp. 21 733–21 739, 2019.

[54] D. Paolino, M. L. Accolla, F. Cilurzo, M. C. Cristiano, D. Cosco, F. Castelli, M. G. Sarpietro, M. Fresta, and C. Celia, "Interaction between peg lipid and dspe/dspc phospholipids: An insight of pegylation degree and kinetics of de-pegylation," *Colloids and Surfaces B: Biointerfaces*, vol. 155, pp. 266–275, 2017.

[55] J. S. Suk, Q. Xu, N. Kim, J. Hanes, and L. M. Ensign, "Pegylation as a strategy for improving nanoparticle-based drug and gene delivery," *Advanced drug delivery reviews*, vol. 99, pp. 28–51, 2016.

[56] X. Zhu, W. Tao, D. Liu, J. Wu, Z. Guo, X. Ji, Z. Bharwani, L. Zhao, X. Zhao, O. C. Farokhzad *et al.*, "Surface de-pegylation controls nanoparticle-mediated sirna delivery in vitro and in vivo," *Theranostics*, vol. 7, no. 7, p. 1990, 2017.

[57] J. R. McIntosh, "Electron microscopy of cells: a new beginning for a new century," *The Journal of cell biology*, vol. 153, no. 6, pp. F25–F32, 2001.

[58] C. Malburet, L. Leclercq, J.-F. Cotte, J. Thiebaud, E. Bazin, M. Garinot, and H. Cottet, "Size and charge characterization of lipid nanoparticles for mrna vaccines," *Analytical Chemistry*, vol. 94, no. 11, pp. 4677–4685, 2022.

[59] T. N. Vigil, D. Zhang-Hulsey, J. L. Santos, and G. P. Hussmann, "Expediting in vitro characterization of mrna-based gene therapies via high-content fluorescent imaging," *Analytical Biochemistry*, vol. 627, p. 114259, 2021.

[60] S. W. Hell and J. Wichmann, "Breaking the diffraction resolution limit by stimulated emission: stimulated-emission-depletion fluorescence microscopy," *Optics letters*, vol. 19, no. 11, pp. 780–782, 1994.

[61] E. Betzig, G. H. Patterson, R. Sougrat, O. W. Lindwasser, S. Olenych, J. S. Bonifacino, M. W. Davidson, J. Lippincott-Schwartz, and H. F. Hess, "Imaging intracellular fluorescent proteins at nanometer resolution," *science*, vol. 313, no. 5793, pp. 1642–1645, 2006.

[62] M. J. Rust, M. Bates, and X. Zhuang, "Sub-diffraction-limit imaging by stochastic optical reconstruction microscopy (storm)," *Nature methods*, vol. 3, no. 10, pp. 793–796, 2006.

[63] M. G. Gustafsson, "Surpassing the lateral resolution limit by a factor of two using structured illumination microscopy," *Journal of microscopy*, vol. 198, no. 2, pp. 82–87, 2000.

[64] S. Pujals, N. Feiner-Gracia, P. Delcanale, I. Voets, and L. Albertazzi, "Super-resolution microscopy as a powerful tool to study complex synthetic materials," *Nature Reviews Chemistry*, vol. 3, no. 2, pp. 68–84, 2019.

[65] J. Vogelsang, C. Steinhauer, C. Forthmann, I. H. Stein, B. Person-Skegro, T. Cordes, and P. Tinnefeld, "Make them blink: Probes for super-resolution microscopy," *ChemPhysChem*, vol. 11, no. 12, pp. 2475–2490, 2010.

[66] M. Minoshima and K. Kikuchi, "Photostable and photoswitching fluorescent dyes for super-resolution imaging," *JBIC Journal of Biological Inorganic Chemistry*, vol. 22, pp. 639–652, 2017.

[67] S. Manley, J. M. Gillette, G. H. Patterson, H. Shroff, H. F. Hess, E. Betzig, and J. Lippincott-Schwartz, "High-density mapping of single-molecule trajectories with photoactivated localization microscopy," *Nature methods*, vol. 5, no. 2, pp. 155–157, 2008.

[68] S. Jeong, J. Widengren, and J.-C. Lee, "Fluorescent probes for sted optical nanoscopy," *Nanomaterials*, vol. 12, no. 1, p. 21, 2021.

[69] Z. Zhao, D. Roy, J. Steinkühler, T. Robinson, R. Lipowsky, and R. Dimova, "Super-resolution imaging of highly curved membrane structures in giant vesicles encapsulating molecular condensates," *Advanced Materials*, vol. 34, no. 4, p. 2106633, 2022.

[70] E. Sezgin, F. Schneider, S. Galiani, I. Urbančič, D. Waithe, B. C. Lagerholm, and C. Eggeling, "Measuring nanoscale diffusion dynamics in cellular membranes with super-resolution sted–fcs," *Nature protocols*, vol. 14, no. 4, pp. 1054–1083, 2019.

[71] S. Li, Y. Hu, A. Li, J. Lin, K. Hsieh, Z. Schneiderman, P. Zhang, Y. Zhu, C. Qiu, E. Kokkoli *et al.*, "Payload distribution and capacity of mrna lipid nanoparticles," *Nature communications*, vol. 13, no. 1, p. 5561, 2022.

[72] S. Hou, X. Lang, and K. Welsher, "Robust real-time 3d single-particle tracking using a dynamically moving laser spot," *Optics Letters*, vol. 42, no. 12, pp. 2390–2393, 2017.

[73] R. Pepperkok and J. Ellenberg, "High-throughput fluorescence microscopy for systems biology," *Nature reviews Molecular cell biology*, vol. 7, no. 9, pp. 690–696, 2006.

[74] J. A. Müller, G. Schwake, and J. O. Rädler, "Einzelzellmikroskopie im hochdurchsatz auf mikrostrukturen," *BIOspektrum*, vol. 28, no. 7, pp. 723–725, 2022.

[75] J. A. Mueller, G. Schwake, A. Reiser, D. Woschee, Z. Alirezaeizanjani, J. O. Raedler, and S. Rudorf, "Less is more: Slow-codon windows enhance egfp mrna resilience against rna interference," *bioRxiv*, pp. 2024–09, 2024.

[76] A. Reiser, D. Woschée, S. M. Kempe, and J. O. Rädler, "Live-cell imaging of single-cell arrays (lisca)-a versatile technique to quantify cellular kinetics," *JoVE (Journal of Visualized Experiments)*, no. 169, p. e62025, 2021.

[77] A. Kamanzi, Y. Gu, R. Tahvildari, Z. Friedenberger, X. Zhu, R. Berti, M. Kurylowicz, D. Witzigmann, J. A. Kulkarni, J. Leung *et al.*, "Simultaneous, single-particle measurements of size and loading give insights into the structure of drug-delivery nanoparticles," *ACS nano*, vol. 15, no. 12, pp. 19 244–19 255, 2021.

[78] D. M. Jameson, *Introduction to fluorescence*. Taylor & Francis, 2014.

[79] C. K. Payne, "Imaging gene delivery with fluorescence microscopy," *Nanomedicine*, vol. 2, no. 6, pp. 847–860, 2007.

[80] P. Luu, S. E. Fraser, and F. Schneider, "More than double the fun with two-photon excitation microscopy," *Communications Biology*, vol. 7, no. 1, p. 364, 2024.

[81] W. R. Zipfel, R. M. Williams, and W. W. Webb, "Nonlinear magic: multiphoton microscopy in the biosciences," *Nature biotechnology*, vol. 21, no. 11, pp. 1369–1377, 2003.

[82] P. T. So, C. Y. Dong, B. R. Masters, and K. M. Berland, "Two-photon excitation fluorescence microscopy," *Annual review of biomedical engineering*, vol. 2, no. 1, pp. 399–429, 2000.

[83] M. Pawlicki, H. A. Collins, R. G. Denning, and H. L. Anderson, "Two-photon absorption and the design of two-photon dyes," *Angewandte Chemie International Edition*, vol. 48, no. 18, pp. 3244–3266, 2009.

[84] K. A. Foster, C. G. Oster, M. M. Mayer, M. L. Avery, and K. L. Audus, "Characterization of the a549 cell line as a type ii pulmonary epithelial cell model for drug metabolism," *Experimental cell research*, vol. 243, no. 2, pp. 359–366, 1998.

[85] M. Renz, "Fluorescence microscopy—a historical and technical perspective," *Cytometry Part A*, vol. 83, no. 9, pp. 767–779, 2013.

[86] T. H. Maiman *et al.*, "Stimulated optical radiation in ruby," 1960.

[87] E. Abbe, "Beiträge zur theorie des mikroskops und der mikroskopischen wahrnehmung," *Archiv für mikroskopische Anatomie*, vol. 9, no. 1, pp. 413–468, 1873.

[88] C. Chi, Y. Du, J. Ye, D. Kou, J. Qiu, J. Wang, J. Tian, and X. Chen, "Intraoperative imaging-guided cancer surgery: from current fluorescence molecular imaging methods to future multi-modality imaging technology," *Theranostics*, vol. 4, no. 11, p. 1072, 2014.

[89] M. Jermyn, J. Mercier, K. Aubertin, J. Desroches, K. Urmey, J. Karamchandiani, E. Marple, M.-C. Guiot, F. Leblond, and K. Petrecca, "Highly accurate detection of cancer in situ with intraoperative, label-free, multimodal optical spectroscopy," *Cancer research*, vol. 77, no. 14, pp. 3942–3950, 2017.

[90] J. W. Lichtman and J.-A. Conchello, "Fluorescence microscopy," *Nature methods*, vol. 2, no. 12, pp. 910–919, 2005.

[91] J.-A. Conchello and J. W. Lichtman, "Optical sectioning microscopy," *Nature methods*, vol. 2, no. 12, pp. 920–931, 2005.

[92] M. Minsky, "Memoir on inventing the confocal scanning microscope," *Scanning*, vol. 10, no. 4, pp. 128–138, 1988.

[93] P. O. Bayguinov, D. M. Oakley, C.-C. Shih, D. J. Geanon, M. S. Joens, and J. A. Fitzpatrick, "Modern laser scanning confocal microscopy," *Current protocols in cytometry*, vol. 85, no. 1, p. e39, 2018.

[94] J. Icha, M. Weber, J. C. Waters, and C. Norden, "Phototoxicity in live fluorescence microscopy, and how to avoid it," *BioEssays*, vol. 39, no. 8, p. 1700003, 2017.

[95] J. Mertz, "Nonlinear microscopy: new techniques and applications," *Current opinion in neurobiology*, vol. 14, no. 5, pp. 610–616, 2004.

[96] D. L. Coutu and T. Schroeder, "Probing cellular processes by long-term live imaging–historic problems and current solutions," *Journal of cell science*, vol. 126, no. 17, pp. 3805–3815, 2013.

[97] M. Göppert-Mayer, "Über elementarakte mit zwei quantensprüngen," *Annalen der Physik*, vol. 401, no. 3, pp. 273–294, 1931.

[98] R. S. Fischer, Y. Wu, P. Kanchanawong, H. Shroff, and C. M. Waterman, "Microscopy in 3d: a biologist's toolbox," *Trends in cell biology*, vol. 21, no. 12, pp. 682–691, 2011.

[99] R. R. Anderson and J. A. Parrish, "The optics of human skin," *Journal of investigative dermatology*, vol. 77, no. 1, pp. 13–19, 1981.

[100] J. Squier and M. Müller, "High resolution nonlinear microscopy: A review of sources and methods for achieving optimal imaging," *Review of Scientific Instruments*, vol. 72, no. 7, pp. 2855–2867, 2001.

[101] B. Sailer, R. Barnkob, and O. Hayden, "Acoustophoretic particle motion in a spherical microchamber," *Physical Review Applied*, vol. 22, no. 4, p. 044034, 2024.

[102] F. Rehfeldt and M. Weiss, "The random walker's toolbox for analyzing single-particle tracking data," *Soft Matter*, 2023.

[103] N. Gal, D. Lechtman-Goldstein, and D. Weihs, "Particle tracking in living cells: a review of the mean square displacement method and beyond," *Rheologica Acta*, vol. 52, pp. 425–443, 2013.

[104] P. J. Campagnola and C.-Y. Dong, "Second harmonic generation microscopy: principles and applications to disease diagnosis," *Laser & Photonics Reviews*, vol. 5, no. 1, pp. 13–26, 2011.

[105] B. Weigelin, G.-J. Bakker, and P. Friedl, "Third harmonic generation microscopy of cells and tissue organization," *Journal of Cell Science*, vol. 129, no. 2, pp. 245–255, 2016.

[106] P. Mahou, M. Zimmerley, K. Loulier, K. S. Matho, G. Labroille, X. Morin, W. Supatto, J. Livet, D. Débarre, and E. Beaurepaire, "Multicolor two-photon tissue imaging by wavelength mixing," *Nature methods*, vol. 9, no. 8, pp. 815–818, 2012.

[107] B. Torrado, B. Pannunzio, and M. A. Malacrida, Leonel andDigman, "Fluorescence lifetime imaging microscopy," *Nature Reviews Methods Primers*, vol. 4, no. 80, 2024.

[108] R. Datta, T. M. Heaster, J. T. Sharick, A. A. Gillette, and M. C. Skala, "Fluorescence lifetime imaging microscopy: fundamentals and advances in instrumentation, analysis, and applications," *Journal of biomedical optics*, vol. 25, no. 7, pp. 071 203–071 203, 2020.

[109] J.-X. Cheng and X. S. Xie, "Coherent anti-stokes raman scattering microscopy: instrumentation, theory, and applications," pp. 827–840, 2004.

[110] L. G. Rodriguez, S. J. Lockett, and G. R. Holtom, "Coherent anti-stokes raman scattering microscopy: A biological review," *Cytometry Part A: The Journal of the International Society for Analytical Cytology*, vol. 69, no. 8, pp. 779–791, 2006.

[111] H. Yuen, J. Princen, J. Illingworth, and J. Kittler, "Comparative study of hough transform methods for circle finding," *Image and vision computing*, vol. 8, no. 1, pp. 71–77, 1990.

[112] R. C. Gonzalez, *Digital image processing*. Pearson education india, 2009.

[113] J. Chen, "Hungarian-based particle linking," https://de.mathworks.com/matlabcentral/fileexchange/33968-hungarian-based-particle-linking, 2021, accessed: 2024-11-29.

[114] K. Suhling, P. M. French, and D. Phillips, "Time-resolved fluorescence microscopy," *Photochemical & Photobiological Sciences*, vol. 4, no. 1, pp. 13–22, 2005.

[115] M. Y. Berezin and S. Achilefu, "Fluorescence lifetime measurements and biological imaging," *Chemical reviews*, vol. 110, no. 5, pp. 2641–2684, 2010.

[116] H. Szmacinski and J. R. Lakowicz, "Fluorescence lifetime-based sensing and imaging," *Sensors and Actuators B: Chemical*, vol. 29, no. 1-3, pp. 16–24, 1995.

[117] K. Okabe, N. Inada, C. Gota, Y. Harada, T. Funatsu, and S. Uchiyama, "Intracellular temperature mapping with a fluorescent polymeric thermometer and fluorescence lifetime imaging microscopy," *Nature communications*, vol. 3, no. 1, p. 705, 2012.

[118] H. Zhang, H. Huang, S. He, H. Zeng, and A. Pralle, "Monodisperse magnetofluorescent nanoplatforms for local heating and temperature sensing," *Nanoscale*, vol. 6, no. 22, pp. 13 463–13 469, 2014.

[119] A. Colom, E. Derivery, S. Soleimanpour, C. Tomba, M. D. Molin, N. Sakai, M. González-Gaitán, S. Matile, and A. Roux, "A fluorescent membrane tension probe," *Nature chemistry*, vol. 10, no. 11, pp. 1118–1125, 2018.

[120] J. Lakowicz, "Principles of fluorescence spectroscopy," *University of Maryland School of Medicine Baltimore*, vol. 132, 2006.

[121] R. C. Hilborn, "Einstein coefficients, cross sections, f values, dipole moments, and all that," *Am. J. Phys*, vol. 50, no. 11, pp. 982–986, 1982.

[122] D. J. Griffiths and D. F. Schroeter, *Introduction to quantum mechanics*. Cambridge university press, 2019.

[123] C. M. Marian, "Understanding and controlling intersystem crossing in molecules," *Annual review of physical chemistry*, vol. 72, no. 1, pp. 617–640, 2021.

[124] K. Jahn, V. Buschmann, and C. Hille, "Simultaneous fluorescence and phosphorescence lifetime imaging microscopy in living cells," *Scientific reports*, vol. 5, no. 1, p. 14334, 2015.

[125] J. V. Caspar and T. J. Meyer, "Application of the energy gap law to nonradiative, excited-state decay," *The Journal of Physical Chemistry*, vol. 87, no. 6, pp. 952–957, 1983.

[126] A. Jablonski, "Efficiency of anti-stokes fluorescence in dyes," *Nature*, vol. 131, no. 3319, pp. 839–840, 1933.

[127] LibreTexts Chemistry, "Jablonski diagram," 2024, accessed: 2024-12-05. [Online]. Available: https://chem.libretexts.org/Bookshelves/Physical_and_Theoretical_Chemistry_Textbook_Maps/Supplemental_Modules_(Physical_and_Theoretical_Chemistry)/Spectroscopy/Electronic_Spectroscopy/Jablonski_diagram

[128] M. Kasha, "Characterization of electronic transitions in complex molecules," *Discussions of the Faraday society*, vol. 9, pp. 14–19, 1950.

[129] J. J. Fisz, "Another look at magic-angle-detected fluorescence and emission anisotropy decays in fluorescence microscopy," *The Journal of Physical Chemistry A*, vol. 111, no. 50, pp. 12 867–12 870, 2007.

[130] C. C. Gradinaru, D. O. Marushchak, M. Samim, and U. J. Krull, "Fluorescence anisotropy: from single molecules to live cells," *Analyst*, vol. 135, no. 3, pp. 452–459, 2010.

[131] C. Freymüller, S. Kalinina, A. Rück, R. Sroka, and A. Rühm, "Quenched coumarin derivatives as fluorescence lifetime phantoms for nadh and fad," *Journal of Biophotonics*, vol. 14, no. 7, p. e202100024, 2021.

[132] L. Assies, J. García-Calvo, F. Piazzolla, S. Sanchez, T. Kato, L. Reymond, A. Goujon, A. Colom, J. Lopez-Andarias, K. Straková *et al.*, "Flipper probes for the community," 2021.

[133] X.-X. Chen, F. Bayard, N. Gonzalez-Sanchis, K. K. P. Pamungkas, N. Sakai, and S. Matile, "Fluorescent flippers: Small-molecule probes to image membrane tension in living systems," *Angewandte Chemie*, vol. 135, no. 20, p. e202217868, 2023.

[134] L. Yu, Y. Lei, Y. Ma, M. Liu, J. Zheng, D. Dan, and P. Gao, "A comprehensive review of fluorescence correlation spectroscopy," *Frontiers in physics*, vol. 9, p. 644450, 2021.

[135] J. Ries and P. Schwille, "Fluorescence correlation spectroscopy," *BioEssays*, vol. 34, no. 5, pp. 361–368, 2012.

[136] O. Krichevsky and G. Bonnet, "Fluorescence correlation spectroscopy: the technique and its applications," *Reports on Progress in Physics*, vol. 65, no. 2, p. 251, 2002.

[137] C. Reichardt, "Solvatochromic dyes as solvent polarity indicators," *Chemical reviews*, vol. 94, no. 8, pp. 2319–2358, 1994.

[138] D. Magde, G. E. Rojas, and P. G. Seybold, "Solvent dependence of the fluorescence lifetimes of xanthene dyes," *Photochemistry and photobiology*, vol. 70, no. 5, pp. 737–744, 1999.

[139] G. G. Stokes, "Xxx. on the change of refrangibility of light," *Philosophical transactions of the Royal Society of London*, no. 142, pp. 463–562, 1852.

[140] M. Baruah, W. Qin, C. Flors, J. Hofkens, R. A. Vallée, D. Beljonne, M. Van der Auweraer, W. M. De Borggraeve, and N. Boens, "Solvent and ph dependent fluorescent properties of a dimethylaminostyryl borondipyrromethene dye in solution," *The Journal of Physical Chemistry A*, vol. 110, no. 18, pp. 5998–6009, 2006.

[141] L. Onsager, "Electric moments of molecules in liquids," *Journal of the American Chemical Society*, vol. 58, no. 8, pp. 1486–1493, 1936.

[142] T. Jue, *Fundamental concepts in biophysics*. Springer, 2009.

[143] J. R. Lakowicz and J. R. Lakowicz, "Quenching of fluorescence," *Principles of fluorescence spectroscopy*, pp. 257–301, 1983.

[144] M. H. Gehlen, "The centenary of the stern-volmer equation of fluorescence quenching: From the single line plot to the sv quenching map," *Journal of Photochemistry and Photobiology C: Photochemistry Reviews*, vol. 42, p. 100338, 2020.

[145] O. Stern and M. Volmer, "Über die abklingungszeit der fluoreszenz," *Physikalische Zeitschrift*, vol. 20, no. 1, pp. 183–188, 1919.

[146] E. A. Jares-Erijman and T. M. Jovin, "Fret imaging," *Nature biotechnology*, vol. 21, no. 11, pp. 1387–1395, 2003.

[147] Y. Shibasaki, T. Suenobu, T. Nakagawa, and R. Katoh, "Effect of reabsorption of fluorescence on transient absorption measurements," *Spectrochimica Acta Part A: Molecular and Biomolecular Spectroscopy*, vol. 220, p. 117127, 2019.

[148] K. König, "1 brief history of fluorescence lifetime imaging," *Multiphoton Microscopy and Fluorescence Lifetime Imaging*, pp. 3–16, 2018.

[149] M. A. Digman, V. R. Caiolfa, M. Zamai, and E. Gratton, "The phasor approach to fluorescence lifetime imaging analysis," *Biophysical journal*, vol. 94, no. 2, pp. L14–L16, 2008.

[150] L. Malacrida, S. Ranjit, D. M. Jameson, and E. Gratton, "The phasor plot: a universal circle to advance fluorescence lifetime analysis and interpretation," *Annual Review of Biophysics*, vol. 50, no. 1, pp. 575–593, 2021.

[151] A. Vallmitjana, B. Torrado, and E. Gratton, "Phasor-based image segmentation: machine learning clustering techniques," *Biomedical optics express*, vol. 12, no. 6, pp. 3410–3422, 2021.

[152] Y. Zhang, T. Hato, P. C. Dagher, E. L. Nichols, C. J. Smith, K. W. Dunn, and S. S. Howard, "Automatic segmentation of intravital fluorescence microscopy images by k-means clustering of flim phasors," *Optics Letters*, vol. 44, no. 16, pp. 3928–3931, 2019.

[153] F. Fereidouni, A. N. Bader, and H. C. Gerritsen, "Spectral phasor analysis allows rapid and reliable unmixing of fluorescence microscopy spectral images," *Optics express*, vol. 20, no. 12, pp. 12 729–12 741, 2012.

[154] P. N. Hedde, R. Cinco, L. Malacrida, A. Kamaid, and E. Gratton, "Phasor-based hyperspectral snapshot microscopy allows fast imaging of live, three-dimensional tissues for biomedical applications," *Communications biology*, vol. 4, no. 1, p. 721, 2021.

[155] W. Becker, "Fluorescence lifetime imaging–techniques and applications," *Journal of microscopy*, vol. 247, no. 2, pp. 119–136, 2012.

[156] S. P. Counting, "Time-correlated single photon counting," 2009.

[157] W. Becker, H. Hickl, C. Zander, K. Drexhage, M. Sauer, S. Siebert, and J. Wolfrum, "Time-resolved detection and identification of single analyte molecules in microcapillaries by time-correlated single-photon counting (tcspc)," *Review of scientific instruments*, vol. 70, no. 3, pp. 1835–1841, 1999.

[158] M. Adhikari, R. Houhou, J. Hniopek, and T. Bocklitz, "Review of fluorescence lifetime imaging microscopy (flim) data analysis using machine learning," *Journal of Experimental and Theoretical Analyses*, vol. 1, no. 1, pp. 44–63, 2023.

[159] N. Boens, W. Qin, N. Basarić, J. Hofkens, M. Ameloot, J. Pouget, J.-P. Lefevre, B. Valeur, E. Gratton, M. Vandeven *et al.*, "Fluorescence lifetime standards for time and frequency domain fluorescence spectroscopy," *Analytical chemistry*, vol. 79, no. 5, pp. 2137–2149, 2007.

[160] H. Chen, G. Holst, and E. Gratton, "Modulated cmos camera for fluorescence lifetime microscopy," *Microscopy research and technique*, vol. 78, no. 12, pp. 1075–1081, 2015.

[161] T. W. Gadella Jr, T. M. Jovin, and R. M. Clegg, "Fluorescence lifetime imaging microscopy (flim): spatial resolution of microstructures on the nanosecond time scale," *Biophysical chemistry*, vol. 48, no. 2, pp. 221–239, 1993.

[162] A. Esposito, H. C. Gerritsen, and F. S. Wouters, "Fluorescence lifetime heterogeneity resolution in the frequency domain by lifetime moments analysis," *Biophysical journal*, vol. 89, no. 6, pp. 4286–4299, 2005.

[163] S.-C. Liao, Y. Sun, and U. Coskun, "Flim analysis using the phasor plots," *ISS Inc.: Champaign, IL, USA*, vol. 61822, 2014.

[164] V. Mannam, Y. Zhang, X. Yuan, C. Ravasio, and S. S. Howard, "Machine learning for faster and smarter fluorescence lifetime imaging microscopy," *Journal of Physics: Photonics*, vol. 2, no. 4, p. 042005, 2020.

[165] F. Cutrale, V. Trivedi, L. A. Trinh, C.-L. Chiu, J. M. Choi, M. S. Artiga, and S. E. Fraser, "Hyperspectral phasor analysis enables multiplexed 5d in vivo imaging," *Nature methods*, vol. 14, no. 2, pp. 149–152, 2017.

[166] J. J. Rennick, C. J. Nowell, C. W. Pouton, and A. P. Johnston, "Resolving subcellular ph with a quantitative fluorescent lifetime biosensor," *Nature communications*, vol. 13, no. 1, p. 6023, 2022.

[167] G. C. Kemmer, S. A. Bogh, M. Urban, M. G. Palmgren, T. Vosch, J. Schiller, and T. G. Pomorski, "Lipid-conjugated fluorescent ph sensors for monitoring ph changes in reconstituted membrane systems," *Analyst*, vol. 140, no. 18, pp. 6313–6320, 2015.

[168] P. Paramasivam, C. Franke, M. Stöter, A. Höijer, S. Bartesaghi, A. Sabirsh, L. Lindfors, M. Y. Arteta, A. Dahlén, A. Bak *et al.*, "Endosomal escape of delivered mrna

from endosomal recycling tubules visualized at the nanoscale," *Journal of Cell Biology*, vol. 221, no. 2, p. e202110137, 2021.

[169] J. Lee, B. Kim, B. Park, Y. Won, S.-Y. Kim, and S. Lee, "Real-time cancer diagnosis of breast cancer using fluorescence lifetime endoscopy based on the ph," *Scientific Reports*, vol. 11, no. 1, p. 16864, 2021.

[170] A. Esposito, M. Gralle, M. A. C. Dani, D. Lange, and F. S. Wouters, "phlameleons: a family of fret-based protein sensors for quantitative ph imaging," *Biochemistry*, vol. 47, no. 49, pp. 13 115–13 126, 2008.

[171] Y. Zhang, I. H. Guldner, E. L. Nichols, D. Benirschke, C. J. Smith, S. Zhang, and S. S. Howard, "Instant flim enables 4d in vivo lifetime imaging of intact and injured zebrafish and mouse brains," *Optica*, vol. 8, no. 6, pp. 885–897, 2021.

[172] H. Halip, Y. Yoshimura, W. Inami, and Y. Kawata, "Ultrashort laser based two-photon phase-resolved fluorescence lifetime measurement method," *Methods and Applications in Fluorescence*, vol. 8, no. 2, p. 025003, 2020.

[173] S. Orthaus-Mueller, B. Kraemer, R. Dowler, A. Devaux, A. Tannert, T. Roehlicke, M. Wahl, H.-J. Rahn, and R. Erdmann, "rapidflim: the new and innovative method for ultra fast flim imaging," *PicoQuant Appl. Note*, pp. 1–8, 2016.

[174] X. Liu, D. Lin, W. Becker, J. Niu, B. Yu, L. Liu, and J. Qu, "Fast fluorescence lifetime imaging techniques: A review on challenge and development," *Journal of Innovative Optical Health Sciences*, vol. 12, no. 05, p. 1930003, 2019.

[175] H. C. Gerritsen, M. Asselbergs, A. Agronskaia, and W. Van Sark, "Fluorescence lifetime imaging in scanning microscopes: acquisition speed, photon economy and lifetime resolution," *Journal of microscopy*, vol. 206, no. 3, pp. 218–224, 2002.

[176] A. Ghosh, N. Karedla, J. C. Thiele, I. Gregor, and J. Enderlein, "Fluorescence lifetime correlation spectroscopy: Basics and applications," *Methods*, vol. 140, pp. 32–39, 2018.

[177] P. Kapusta, M. Wahl, A. Benda, M. Hof, and J. Enderlein, "Fluorescence lifetime correlation spectroscopy," *Journal of Fluorescence*, vol. 17, pp. 43–48, 2007.

[178] P. Kapusta, R. Macháň, A. Benda, and M. Hof, "Fluorescence lifetime correlation spectroscopy (flcs): concepts, applications and outlook," *International journal of molecular sciences*, vol. 13, no. 10, pp. 12 890–12 910, 2012.

[179] U. Meseth, T. Wohland, R. Rigler, and H. Vogel, "Resolution of fluorescence correlation measurements," *Biophysical journal*, vol. 76, no. 3, pp. 1619–1631, 1999.

[180] K. Bacia, S. A. Kim, and P. Schwille, "Fluorescence cross-correlation spectroscopy in living cells," *Nature methods*, vol. 3, no. 2, pp. 83–89, 2006.

[181] P. Montero Llopis, R. A. Senft, T. J. Ross-Elliott, R. Stephansky, D. P. Keeley, P. Koshar, G. Marqués, Y.-S. Gao, B. R. Carlson, T. Pengo *et al.*, "Best practices and tools for reporting reproducible fluorescence microscopy methods," *Nature Methods*, vol. 18, no. 12, pp. 1463–1476, 2021.

[182] T. Kellerer, T. Grawert, F. Schorre, L. Moser, P. Byers, J. Rädler, and T. Hellerer, "An image based real-time 3d particle tracking fluorescence lifetime imaging microscope to follow lipid nanoparticles," in *Microscopy Histopathology and Analytics*. Optica Publishing Group, 2024, pp. MM5A–6.

[183] S. Quentmeier, S. Denicke, J.-E. Ehlers, R. A. Niesner, and K.-H. Gericke, "Two-color two-photon excitation using femtosecond laser pulses," *The Journal of Physical Chemistry B*, vol. 112, no. 18, pp. 5768–5773, 2008.

[184] S. Quentmeier, S. Denicke, and K.-H. Gericke, "Two-color two-photon fluorescence laser scanning microscopy," *Journal of fluorescence*, vol. 19, pp. 1037–1043, 2009.

[185] C. Stringari, L. Abdeladim, G. Malkinson, P. Mahou, X. Solinas, I. Lamarre, S. Brizion, J.-B. Galey, W. Supatto, R. Legouis *et al.*, "Multicolor two-photon imaging of endogenous fluorophores in living tissues by wavelength mixing," *Scientific reports*, vol. 7, no. 1, p. 3792, 2017.

[186] C. Polzer, S. Ness, M. Mohseni, T. Kellerer, M. Hilleringmann, J. Rädler, and T. Hellerer, "Correlative two-color two-photon (2c2p) excitation sted microscopy," *Biomedical Optics Express*, vol. 10, no. 9, pp. 4516–4530, 2019.

[187] J. O. Wirth, L. Scheiderer, T. Engelhardt, J. Engelhardt, J. Matthias, and S. W. Hell, "Minflux dissects the unimpeded walking of kinesin-1," *Science*, vol. 379, no. 6636, pp. 1004–1010, 2023.

[188] V. Briane, M. Vimond, and C. Kervrann, "An overview of diffusion models for intracellular dynamics analysis," *Briefings in bioinformatics*, vol. 21, no. 4, pp. 1136–1150, 2020.

[189] A. N. Kapanidis, S. Uphoff, and M. Stracy, "Understanding protein mobility in bacteria by tracking single molecules," *Journal of molecular biology*, vol. 430, no. 22, pp. 4443–4455, 2018.

[190] B. Van Heerden, N. A. Vickers, T. P. Krüger, and S. B. Andersson, "Real-time feedback-driven single-particle tracking: A survey and perspective," *Small*, vol. 18, no. 29, p. 2107024, 2022.

[191] F. Mieskes, E. Ploetz, F. Wehnekamp, V. Rat, and D. C. Lamb, "Multicolor 3d orbital tracking," *Small*, vol. 19, no. 17, p. 2204726, 2023.

[192] J. A. Germann and L. M. Davis, "Three-dimensional tracking of a single fluorescent nanoparticle using four-focus excitation in a confocal microscope," *Optics express*, vol. 22, no. 5, pp. 5641–5650, 2014.

[193] Y.-L. Liu, E. P. Perillo, C. Liu, P. Yu, C.-K. Chou, M.-C. Hung, A. K. Dunn, and H.-C. Yeh, "Segmentation of 3d trajectories acquired by tsunami microscope: an application to egfr trafficking," *Biophysical journal*, vol. 111, no. 10, pp. 2214–2227, 2016.

[194] M. A. Thompson, J. M. Casolari, M. Badieirostami, P. O. Brown, and W. Moerner, "Three-dimensional tracking of single mrna particles in saccharomyces cerevisiae using a double-helix point spread function," *Proceedings of the National Academy of Sciences*, vol. 107, no. 42, pp. 17 864–17 871, 2010.

[195] S. Hou, J. Exell, and K. Welsher, "Real-time 3d single molecule tracking," *Nature communications*, vol. 11, no. 1, p. 3607, 2020.

[196] A. Bucci, G. Tortarolo, M. O. Held, L. Bega, E. Perego, F. Castagnetti, I. Bozzoni, E. Slenders, and G. Vicidomini, "4d single-particle tracking with asynchronous read-out single-photon avalanche diode array detector," *Nature Communications*, vol. 15, no. 1, p. 6188, 2024.

[197] M. DeVore, D. Stich, A. Keller, C. Cleyrat, M. Phipps, J. Hollingsworth, D. Lidke, B. Wilson, P. Goodwin, and J. Werner, "Note: Time-gated 3d single quantum dot tracking with simultaneous spinning disk imaging," *Review of Scientific Instruments*, vol. 86, no. 12, 2015.

[198] H. Cang, D. Montiel, C. S. Xu, and H. Yang, "Observation of spectral anisotropy of gold nanoparticles," *The Journal of chemical physics*, vol. 129, no. 4, 2008.

[199] E. Toprak, H. Balci, B. H. Blehm, and P. R. Selvin, "Three-dimensional particle tracking via bifocal imaging," *Nano letters*, vol. 7, no. 7, pp. 2043–2045, 2007.

[200] C. Cierpka, M. Rossi, R. Segura, and C. Kähler, "On the calibration of astigmatism particle tracking velocimetry for microflows," *Measurement Science and Technology*, vol. 22, no. 1, p. 015401, 2010.

[201] K. McHale, A. J. Berglund, and H. Mabuchi, "Quantum dot photon statistics measured by three-dimensional particle tracking," *Nano letters*, vol. 7, no. 11, pp. 3535–3539, 2007.

[202] J. Enderlein, "Tracking of fluorescent molecules diffusing within membranes," *Applied Physics B*, vol. 71, pp. 773–777, 2000.

[203] A. Dupont and D. C. Lamb, "Nanoscale three-dimensional single particle tracking," *Nanoscale*, vol. 3, no. 11, pp. 4532–4541, 2011.

[204] P. Annibale, A. Dvornikov, and E. Gratton, "Electrically tunable lens speeds up 3d orbital tracking," *Biomedical optics express*, vol. 6, no. 6, pp. 2181–2190, 2015.

[205] Y. Katayama, O. Burkacky, M. Meyer, C. Bräuchle, E. Gratton, and D. C. Lamb, "Real-time nanomicroscopy via three-dimensional single-particle tracking," *ChemPhysChem*, vol. 10, no. 14, pp. 2458–2464, 2009.

[206] H. Cang, C. M. Wong, C. S. Xu, A. H. Rizvi, and H. Yang, "Confocal three dimensional tracking of a single nanoparticle with concurrent spectroscopic readouts," *Applied physics letters*, vol. 88, no. 22, 2006.

[207] "Astigmatism particle tracking velocimetry for macroscopic flows," in *PIV13; 10th International Symposium on Particle Image Velocimetry, Delft, The Netherlands, July 1-3, 2013*. Citeseer, 2013.

[208] M. F. Juette and J. Bewersdorf, "Three-dimensional tracking of single fluorescent particles with submillisecond temporal resolution," *Nano letters*, vol. 10, no. 11, pp. 4657–4663, 2010.

[209] E. P. Perillo, Y.-L. Liu, K. Huynh, C. Liu, C.-K. Chou, M.-C. Hung, H.-C. Yeh, and A. K. Dunn, "Deep and high-resolution three-dimensional tracking of single particles using nonlinear and multiplexed illumination," *Nature Communications*, vol. 6, no. 1, p. 7874, 2015.

[210] N. P. Wells, G. A. Lessard, P. M. Goodwin, M. E. Phipps, P. J. Cutler, D. S. Lidke, B. S. Wilson, and J. H. Werner, "Time-resolved three-dimensional molecular tracking in live cells," *Nano letters*, vol. 10, no. 11, pp. 4732–4737, 2010.

[211] G. Lazarev, A. Hermerschmidt, S. Krüger, and S. Osten, "Lcos spatial light modulators: trends and applications," *Optical Imaging and Metrology: Advanced Technologies*, pp. 1–29, 2012.

[212] S. R. P. Pavani, M. A. Thompson, J. S. Biteen, S. J. Lord, N. Liu, R. J. Twieg, R. Piestun, and W. E. Moerner, "Three-dimensional, single-molecule fluorescence imaging beyond the diffraction limit by using a double-helix point spread function," *Proceedings of the National Academy of Sciences*, vol. 106, no. 9, pp. 2995–2999, 2009.

[213] T. Kellerer, J. Janusch, L. Moser, T. Grawert, P. Byers, T. Spellauge, J. Rädler, and T. Hellerer, "Rigorous investigation and comparison of different fluorescence lifetime imaging microscopy (flim) techniques analyzed using the phasor plot," in *Multiphoton Microscopy in the Biomedical Sciences XXIV*, vol. 12847. SPIE, 2024, pp. 177–187.

[214] T. Hellerer, "Cars-mikroskopie: Entwicklung und anwendung," Ph.D. dissertation, lmu, 2004.

[215] H. Nyquist, "Certain topics in telegraph transmission theory," *Transactions of the American Institute of Electrical Engineers*, vol. 47, no. 2, pp. 617–644, 1928.

[216] B. J. Borah, J.-C. Lee, H.-H. Chi, Y.-T. Hsiao, C.-T. Yen, and C.-K. Sun, "Nyquist-exceeding high voxel rate acquisition in mesoscopic multiphoton microscopy for full-field submicron resolution resolvability," *Iscience*, vol. 24, no. 9, 2021.

List of Figures

List of Tables

Danksagung

666 → 999

Die Retrospektive auf die letzten fünf Jahre zeigte mir, mit wie vielen Menschen ich in Kontakt treten, kennenlernen und arbeiten durfte. Bei allen möchte ich mich für diese prägenden Jahre sehr herzlich bedanken und wünsche jedem Einzelnen viel Erfolg auf dem weiteren Weg.

Die wohl längste Zeit habe ich mit **Thomas Hellerer** verbringen dürfen. Beginnend mit dem ersten Praktikum während meiner Bachelorzeit, in dem wir unsere Namensverwandtschaft erkannt hatten, bis zu den diversen Abschlussarbeiten, die ich unter seiner Leitung anfertigen durfte. Ich habe von dir sehr viel gelernt, und du hast mir eine riesige Möglichkeit mit der Dissertation in deinem Labor eröffnet, wofür ich mich herzlichst bedanken möchte. Neben unserer Arbeit werde ich unsere diversen Trips, zum einzig wahren Wolfgangsee, nicht vergessen, auf dem die erste Idee zu meiner Doktorarbeit entstanden ist, während Peter Alexander im Hintergrund lief, bis hin zu unseren Konferenzausflügen nach Italien oder Amerika. Vielen Dank für deine Betreuung und ein noch größeres Dankeschön für deine Freundschaft und dem Aushalten meiner schlechten Witze.

Ein weiteres großes Dankeschön möchte ich an **Joachim Rädler** richten. Neben dem unfassbar spannenden Thema, den faszinierenden Gesprächen und theoretischen Ausflügen möchte ich mich bei dir auch vor allem dafür bedanken, in einer hervorragenden Gruppe promovieren zu können und dass du mir diese Möglichkeit ermöglicht hast.

Selbstverständlich möchte ich mich bei all meinen Mitstreitern bedanken, die sowohl in den Höhen als auch in den Tiefen, bei Erfolgsbieren oder dem Notfallschnaps, stets bei mir waren. Vor allem möchte ich mich hier bei **Judith Müller** und **Gerlinde Schwake** bedanken, die mir als Biologieexpertinnen und immer als offene Ansprechstelle an der LMU zur Seite gestanden sind. Auch an den gesamten Lehrstuhl Rädler, vielen Dank für die gemeinsame Zeit.

Jemand, der mich in die Welt der Mikroskopie eingearbeitet hat und von dem ich sehr viel lernen konnte, ist mein Vorgänger **Christoph Polzer**. Vielen Dank für deine Unterweisungen und die Möglichkeit, deinen Platz im Labor zu übernehmen. Liebe **Stefanie**

Kiderlen, tausend Dank geht auch an dich – nicht nur für die stetige Unterstützung mit spannenden Proben, Biologieunterweisungen, Tipps und Tricks für Probensysteme und die gemeinsamen Kooperationen, sondern auch für die wunderbare Freundschaft. Die gemeinsamen Ausflüge im Rahmen diverser Konferenzen werde ich nicht vergessen.

Fünf Jahre haben auch bedeutet, dass einige Abschlussarbeiten bei uns im Multiphoton Imaging Lab bearbeitet wurden, die ich immer mit Freude betreut habe. Dabei durfte ich viele Studierende kennenlernen, denen ich hoffentlich etwas auf ihren weiteren Weg mitgeben konnte und von denen ich auch einiges gelernt und Unterstützung erhalten habe. Bei euch allen möchte ich mich sehr herzlich bedanken! Especially for your great friendship, **Cole Green**!

Auch an meine Box- und Freundesgruppe, **Rainer, Ines, Inga** und **Dirk** der **Boxschule Knoch**. Vielen Dank für alle Sport- und Freizeitaktionen. Sie waren der ideale und vor allem nötige ausgleich. Das Reaggy-Boot wird dabei Tradition bleiben.

Liebe Familie, über uns könnte man mehr als nur eine Dissertation schreiben, und es würde sicherlich einige Zeit in Anspruch nehmen. Liebe **Mum**, lieber **Dad**, Zahlen können viel beschreiben und Worte bekanntlich auch, doch bei meinem Dank an euch würden vermutlich auch diese an ihre Grenzen kommen. Vielen Dank für alles – sei es gemeinsame Urlaube, die Zeit am Wolfgangsee, die Unterstützung und alles andere. Einfach nur Danke!

An **Michi**: Deine Art, Menschen zu motivieren und zu begeistern, ist einzigartig und der Grund, warum diese Arbeit ihren Abschluss gefunden hat. Ohne dich würde ich heute nicht an diesem Punkt stehen, deshalb danke ich dir von Herzen und kann nur sagen: *'Strength and Honor'*.

Der kleine, große Bruder **Alexander**: Danke für unseren geteilten Wahnsinn in Prüfungszeiten und deine Unterstützung durch deinen einmaligen Charakter in allen Lebenslagen. Deine Musiktipps und vor allem unser gemeinsamer Miami-Trip werde ich immer mit dieser Zeit verbinden.

Liebe **Andrea**, auch an dich ein enormes Dankeschön für deine stetige Unterstützung und deine Hilfe in schweren Zeiten. Deine Art war immer mein Vorbild, die Dinge positiv zu sehen und weiterzumachen. Damit es auch in dieser Abschlussarbeit steht: Waschmaschine und Gartenzwerg. Auch an dich, **Timo**, tausend Dank für unsere diversen Ausflüge zum Kiten, die wir meist ohne Wind bei guten Gesprächen verbracht haben. Ich freue mich vor allem schon auf **X** – ich verspreche, euren Nachwuchs nicht zu sehr zu verderben. Bei Einschlafschwierigkeiten könnte diese Arbeit eventuell noch wahre Wunder vollbringen.

666 → 999